Universitat Internacional de Catalunya
Facultat de Medicina i Ciències de la Salut
Departament de Ciències Bàsiques

uLc
barcelona

Tesi doctoral

CPT1C-ABHD6 interaction in hypothalamic neurons: implications for bis (monoacylglycero) phosphate metabolism and the endolysosomal system

Ana Cristina Reguera Moreno

ulc barcelona

UNIVERSITAT INTERNACIONAL DE CATALUNYA

MEDICINE AND HEALTH SCIENCE FACULTY

BASIC SCIENCE DEPARTMENT

CPT1C-ABHD6 INTERACTION IN HYPOTHALAMIC NEURONS: IMPLICATIONS FOR BIS(MONOACYLGLYCERO)PHOSPHATE METABOLISM AND THE ENDOLYSOSOMAL SYSTEM

Ana Cristina Reguera Moreno

2023

uic
barcelona

CPT1C-ABHD6 INTERACTION IN HYPOTHALAMIC NEURONS: IMPLICATIONS FOR BIS(MONOACYLGLYCERO)PHOSPHATE METABOLISM AND THE ENDOLYSOSOMAL SYSTEM

Doctoral thesis manuscript presented by Ana Cristina Reguera Moreno to opt for the degree of Doctor on Philosophy (PhD) awarded by the Universitat Internacional de Catalunya.

This thesis has been conducted in the Basic Science Department from the Medicine and Health Science Faculty of the Universitat Internacional de Catalunya, under the co-direction of Dr. Núria Casals Farré and Dr. Rosalía Rodríguez Rodríguez.

This thesis is part of the Doctoral program of Health Sciences, included in the Neuroscience Research line of Universitat Internacional de Catalunya.

Sant Cugat del Vallès, 2023

Dr. Núria Casals Farré	**Dr. Rosalía Rodríguez Rodríguez**	**Ana Cristina Reguera Moreno**
Director	Director	PhD student

A mis padres y a mi hermana,

Por su apoyo incondicional.

The endolysosomal system plays a critical role in neuronal function and has emerged as a potential target for treating various neuronal diseases, such as neurodegenerative disorders and even obesity. The main components of the endolysosomal system, endosomes and lysosomes, have been traditionally regarded as simple sorting and lytic bodies, but nowadays they are recognized as advanced organelles and are considered crucial regulators of neuronal homeostasis. Within late endosomes (LEs) and lysosomes, a unique lipid named bis(monoacylglycero)phosphate (BMP) has been found to exert significant functions in endolysosomal processes, including cholesterol trafficking, endosome maturation, and lysosomal activity. Nonetheless, the metabolism of BMP remains poorly understood. Recent research has reported that α/β-hydrolase domain-containing 6 (ABHD6), initially characterized as an endocannabinoid hydrolase, is a key regulator of BMP hydrolysis. Additionally, our group has identified carnitine palmitoyltransferase 1C (CPT1C) as the first negative regulator of ABHD6 activity depending on the nutritional status, particularly in the hypothalamus. Taken together, these findings position CPT1C as a potential regulator of BMP metabolism and endolysosomal function, which could be crucial in the context of obesity.

This thesis focuses on how the interaction between CPT1C and ABHD6 might regulate BMP metabolism and, therefore, endolysosomal function, and how this regulation is affected in a context of lipid overload. To address these questions, we have generated a hypothalamic cell model lacking CPT1C using CRISPR technology, in which we have analyzed the consequences of CPT1C deletion on BMP metabolism and BMP-related functions in both basal conditions and after exposure to fatty acids (FA). Moreover, the impact of dietary lipid overload on BMP metabolism was also assessed in wild-type (WT) and CPT1C-knock-out (KO) animal models. Lastly, we aimed to elucidate the subcellular location where the CPT1C-ABHD6 interaction might occur and the structural domains of CPT1C and ABHD6 involved in their interaction and modulation of ABHD6 hydrolase activity.

Our results demonstrate, on the one hand, that CPT1C regulates BMP metabolism through its interaction with ABHD6 in the hypothalamus, and that this regulation is dependent on lipid sensing. Furthermore, we found that CPT1C is necessary for many BMP-related functions and for the formation of contact sites between the endoplasmic reticulum (ER) and endosomes in their latest stages of maturity, playing a crucial role in the functionality of the endolysosomal system. On the other hand, we observed that CPT1C and ABHD6 colocalize in the ER, where their interaction is likely to take place, in close proximity to LEs and lysosomes where ABHD6 may hydrolyze BMP. Finally, we also report that the interaction of both proteins and the modulation of ABHD6 activity by CPT1C occur through their C-terminal domains.

Overall, our findings confirm the involvement of CPT1C in BMP metabolism and the endolysosomal system, providing new insights in the regulatory mechanisms of endolysosomal function in the context of a lipid overload.

TABLE OF CONTENT

INTRODUCTION

1. The endolysosomal system in neuronal homeostasis

The endolysosomal system is present in all cell types. It performs a series of essential roles for maintaining cellular homeostasis, such as trafficking and sorting of membrane cargo, intracellular signaling, control of metabolism and degradation of macromolecules (Ivanova & Cousin, 2022).

1.1. Components and dynamics of the endolysosomal system

The endolysosomal system comprises a cellular network of dynamic membrane-bounded organelles where the endocytic, autophagic and secretory pathways intersect. The highly heterogeneous collection of organelles that constitutes the endolysosomal system is generally classified into several compartments, including early endosomes (EEs), recycling endosomes (REs), late endosomes (LEs), as well as different maturation stages of lysosomes. These elements are distinguished by their morphologies and composition and are interconnected through maturation and fusion/fission processes *(Figure 1)* (Ivanova & Cousin, 2022; Kuijpers et al., 2021; Winckler et al., 2018).
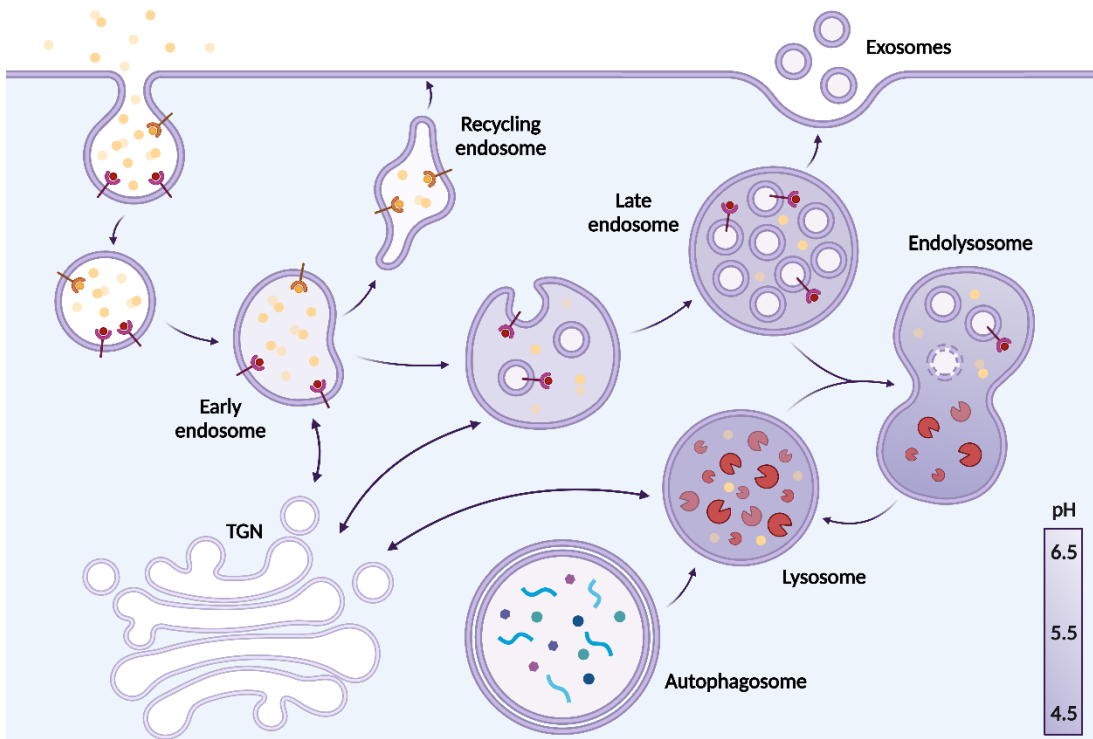
Figure 1. Schematic view of the endolysosomal system. The primary endocytic vesicles deliver their contents and their membranes to EEs in the peripheral cytoplasm. Cargo within EEs can be recycled to the plasma membrane (PM) via REs or sorted into intraluminal vesicles (ILVs). EEs mature into LEs as they accumulate more

ILVs. LEs deliver their ILVs to lysosomes for degradation, or fuse with the PM to secrete the ILVs as exosomes. The fusion of an endosome with a lysosome generates a transient hybrid organelle, the endolysosome. Lysosomes also receive cargo from autophagosomes. The TGN interacts with endosomes and lysosomes throughout all the endocytic pathways. EE: Early endosome; RE: Recycling endosome: LE: Late endosome; TGN: Trans-Golgi network.

EEs are formed from the plasma membrane (PM) through endocytosis of cargo molecules, such as receptors, ligands, and other extracellular material. Most of them are relatively small and have a complex structure with tubular and vacuolar domains. They are usually located at the peripheral cytoplasm close to the PM, where they serve as the initial sorting station for the internalized material (Appelqvist et al., 2013; Huotari & Helenius, 2011). EEs receive endocytic cargo through the clathrin-mediated pathway, but also through clathrin-independent mechanisms such as the caveolae- or lipid raft-mediated endocytosis (Mayor & Pagano, 2007). Then, cargo in EEs is either sorted into the recycling pathway back to the cell surface via a RE, routed toward the trans-Golgi network (TGN) for further processing, or directed to the lysosomes for degradation (Appelqvist et al., 2013; Scott et al., 2014).

Cargo destined for degradation is retained in EEs and are progressively sorted into intraluminal vesicles (ILVs), which are formed through the invagination of the endosomal membrane (Winckler et al., 2018; Woodman & Futter, 2008). Protein sorting into ILVs and ILV formation depend on endosomal sorting complexes required for transport (ESCRT). Moreover, bis(monoacylglycero)phosphate (BMP), an atypical lipid present in the membranes of ILVs has been also described to play a critical role in this process (Gruenberg, 2020). Then, EEs undergo gradual maturation towards LEs, also known as multivesicular bodies due to the high content of ILVs. Within LEs, cargo undergo further sorting between the limiting membrane and ILVs, and is transported to other organelles, including the TGN (Appelqvist et al., 2013; Huotari & Helenius, 2011). In some cases, LEs can also fuse with the plasmatic membrane (PM), and secrete the ILVs to the extracellular space as exosomes (Yakovlev, 2023).

During the maturation process, LEs move from the cell periphery to the perinuclear area, where lysosomes are located. Lysosomes are acidic compartments containing hydrolytic enzymes such as cathepsins. LEs interact with lysosomes, either through direct fusion or kiss-and-run mechanisms, to facilitate cargo degradation (Appelqvist et al., 2013; Woodman & Futter, 2008). The fusion of a LE with a lysosome generates a transient hybrid organelle, the endolysosome. Within endolysosomes, the endosomal content mix with the hydrolytic enzymes present in the lysosome, and active degradation of internalized material takes place (Huotari & Helenius, 2011). Lysosomes are then re-formed by the retrieval of LE components (Pryor & Luzio, 2009).

Lysosomes represent the ultimate destination of the degradative pathway. They play a pivotal role in the degradation and recycling of macromolecules delivered not only by

endocytosis but also by autophagy. Autophagy is the cellular process by which cytoplasmic components, such as organelles and proteins, are enclosed in a double membrane structure called autophagosome, and subsequently degraded and recycled to maintain cellular homeostasis together with the endolysosomal system (Appelqvist et al., 2013).

Throughout the whole endocytic pathway, the vesicular traffic between the endolysosomal system and the TGN is a continuously ongoing process that ensures the correct transport of molecules within the cell. At the endosome level, the TGN is responsible for the retrieval of protein cargo from endosomes for reuse, while at the lysosomal level, the TGN provides newly synthesized hydrolytic enzymes to ensure the optimal activity within lysosomes (Chia et al., 2013; Huotari & Helenius, 2011).

The maturation process from EE to lysosome takes around 40 min. During this time, the vesicle undergoes a multitude of changes, including exchange of membrane components, movement to the perinuclear area, formation of ILVs, a decrease in luminal pH and acquisition of lysosomal components (Appelqvist et al., 2013; Huotari & Helenius, 2011). Regarding membrane proteins, maturation involves association with particular sets of RabGTPases (hereafter referred to as Rab proteins). Rab proteins are considered to be markers of membrane identity and function as central organizers of vesicle-mediated transport between organelles along the endolysosomal pathway. Several Rab proteins are known to be involved in different stages of the endolysosomal pathway, such as Rab5 for the EEs, Rab7 for the LEs and lysosomes and Rab11 for RE. In fact, one of the critical events for maturation of EEs into LEs is that Rab5 is replaced by Rab7. This allows the recruitment of a new set of effectors to the endosomal membrane, which will change the fate of the endosome (Langemeyer et al., 2018; Naslavsky & Caplan, 2018). Other membrane proteins such as early endosomal antigen 1 (EEA1) or lysosome-associated membrane protein 1 (LAMP1) are also widely used as markers of EEs or LE/lysosomes, respectively (Appelqvist et al., 2013).

Moreover, there is also a progressively decrease in pH along the endocytic pathway. The organelles of the endolysosomal system become more acidic as they enter the maturation process due to the activity of the ATP-dependent proton pumps present in the membrane of both endosomes and lysosomes. The membrane bilayer of these organelles creates an enclosed environment allowing an acidic pH, which is critical for the function of many hydrolases and other enzymes. Compared to a cytoplasmic pH (of about 7.0), the endosomal and lysosomal lumen pH is maintained in a range below 6.5. EE maintain a pH at about 6.5, LE at about 5.5 and lysosomes at about 4.5 (Hu et al., 2015).

Finally, dynamics of the endolysosomal system involve interaction with other organelles such as the endoplasmic reticulum (ER) or mitochondria through membrane contact sites (MCS).

These contact sites facilitate vital cellular processes, including cargo sorting, calcium signaling, endosome positioning and membrane remodeling, thus contributing to endolysosomal maturation and membrane dynamics. MCS ensure, then, efficient communication and coordination between organelles, ultimately governing various cellular functions essential for maintaining cellular homeostasis (Prinz et al., 2020).

1.2. Functions of the endolysosomal system in neurons

Endosomes and lysosomes, the main components of this system, have been traditionally regarded as simple sorting and lytic bodies, but nowadays they are recognized as advanced organelles involved in numerous cellular processes and are considered crucial regulators of cellular homeostasis (Appelqvist et al., 2013; Ivanova & Cousin, 2022).

Neurons are highly polarized post-mitotic cells, consisting of a cell body, intricate dendritic arbors, and a single long axon with extensive branches and terminals that can span several tens to hundreds of centimeters. In comparison to other cell types, neurons exhibit a significantly elevated level of morphological complexity and possess a relatively large intracellular volume. Additionally, neurons are extremely active, generating action potentials at rates up to 50-100 impulses per second, a demand they must sustain for nearly a century. Given these factors, neurons have adapted their endolysosomal system to accommodate their intricate morphology, their elevated activity as well as their longevity (Winckler et al., 2018).

The endolysosomal system in neurons is tightly regulated and cooperates with the autophagic pathway to ensure neuronal homeostasis through three key functions: degradation, secretion and signaling (Settembre et al., 2013).

1.2.1. Degradation of macromolecules

The Greek word lysosome means digestive body, and in accordance, a well-known function of lysosomes is degradation (Appelqvist et al., 2013). Lysosomes are involved in the degradation and recycling of extracellular material, via endocytosis, and intracellular material, via autophagy. This degradation process contributes significantly to neuronal homeostasis by eliminating protein aggregates and damaged organelles, while also facilitating neurotransmitter recycling. The resultant breakdown products serve then to generate new cellular components and as a source of energy in response to the nutritional needs of the cell (Giovedì et al., 2020; Roney et al., 2022; Settembre et al., 2013).

Both the endolysosomal system and autophagy function very efficiently due to its high degree of spatial compartmentalization. While endosomes and autophagosomes are found throughout nerve terminals, including distal portions, mature lysosomes with high

degradative capacity are located primarily in the soma and proximal neurites, but not distally (Cheng et al., 2018; Kuijpers et al., 2021; Yap et al., 2018). EEs are formed from fusion of endocytosed vesicles, and autophagosomes from progressive assembly of cellular components such as damaged organelles or protein aggregates targeted for destruction. After endosomes and autophagosomes are formed at distal neurites, they are transported retrogradely toward the cell soma as they undergo a series of maturation steps, and despite sequestering their cargos via different mechanisms, they converge at the levels of lysosomes as their common degradative endpoint *(Figure 2)* (Ferguson, 2019; Kuijpers et al., 2021; Winckler et al., 2018). Surprisingly, although degradative lysosomes are found primarily in cell bodies, live imaging studies in the *Drosophila* brain have revealed degradation of PM and synaptic proteins locally in axon terminals, suggesting that some substrates can be degraded distally in axons as well (Jin et al., 2018).
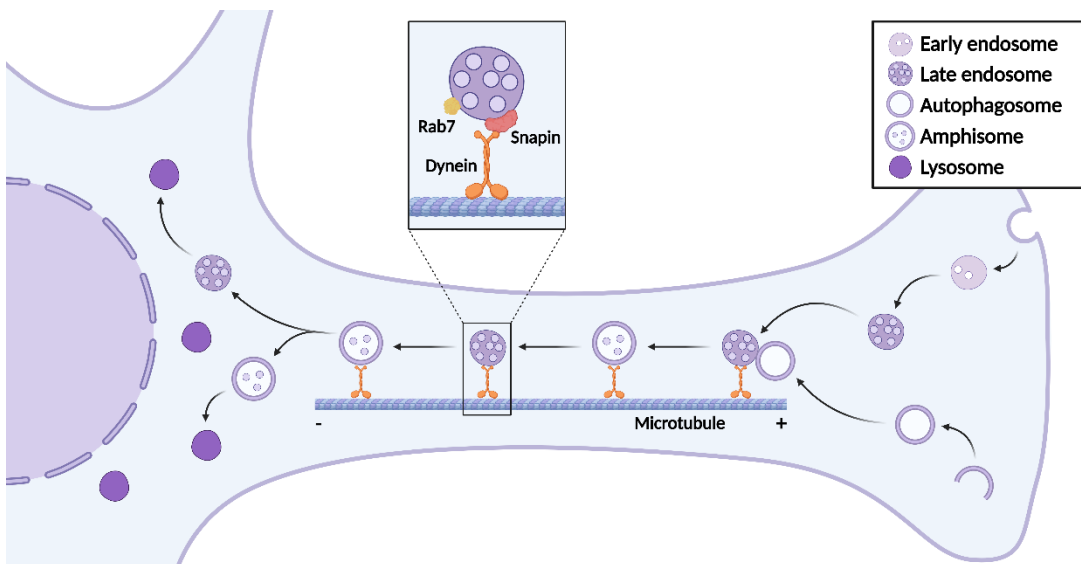
Figure 2. Degradation of macromolecules in neurons. In neurons, mature lysosomes with high degradative capacity are located primarily in the soma or proximal neurites. Endosomes and autophagosomes initiate in distal regions of the axon and are transported retrogradely toward the cell soma as they undergo a series of maturation steps. During this process, autophagosomes may fuse with late endosomes to form amphisomes. The retrograde transport of late endosomes or amphisomes is mediated by dynein motor proteins, snapin or Rab7 among others, and once near the soma, they fuse with lysosomes for cargo degradation.

Regarding retrograde transport, a variety of factors have been implicated in the transport of LE, autophagosomes or amphisomes (formed through fusion of autophagosomes with LE) towards the soma. These include small GTPases such as Rab7, dynein-dynactin adaptor proteins, and snapin among others (Kuijpers et al., 2021).

1.2.2. Secretion of molecules

Neuronal endosomes and lysosomes also undergo regulated exocytosis to secrete their content into the extracellular space, thereby playing different key roles *(Figure 3)* (Settembre et al., 2013). Some ILVs, along with their cargo, do not appear to be destined for degradation; instead, they are released as exosomes into the extracellular space after fusion of LEs with the PM (Scott et al., 2014). Within the central nervous system (CNS), exosomes function as critical mediators of intercellular communication. Exosomes are secreted by neurons in response to synaptic activity, carrying their molecular cargo to recipient cells to regulate their functions (Huo et al., 2021).
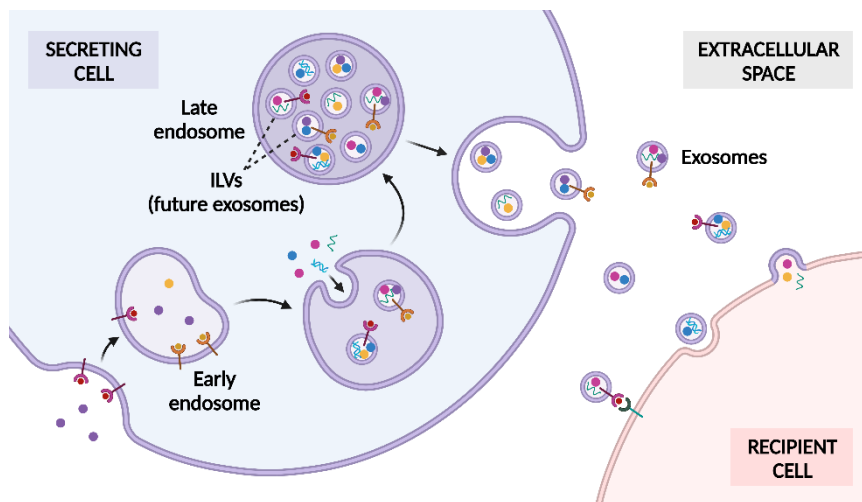
Figure 3. Biogenesis and secretion of exosomes. Exosomes are vesicles originating from the endolysosomal system. The EEs are formed by endocytosis and PM invagination. During this process, some extracellular constituents can enter the EEs along with cell-surface proteins. Then the EEs mature into LEs. Following the specific cargos (proteins, lipids, or nucleic acids) accumulating at the endosomal membrane, the limiting membrane of LEs further bud inward to generate the ILVs which are future exosomes. LEs can be transported to the PM and release exosomes by exocytosis. Because of the double invagination processes, the exosomal membrane maintains the same topological orientation as the PM of cells. Exosomes can be taken up by recipient cells in different ways, including endocytosis, receptor-ligand interaction, and fusion with the recipient cell membrane (Huo et al., 2021). EE: Early endosome; PM: Plasma membrane; LE: Late endosomes; ILVs: Intraluminal vesicles.

The exocytosis of lysosomes has been linked to the regulation of synaptic plasticity, involving enzymes such as matrix metalloproteinase 9 (MMP-9). Padamsey et al. demonstrated that back-propagating action potential induce Ca^{2+} release from lysosomes in neurons, triggering the exocytosis of the lysosomal protease cathepsin B. As a result, the local release of cathepsin B activates MMP-9, which remodels the extracellular matrix to facilitate spine growth (Padamsey et al., 2017).

1.2.3. Signaling in response to nutrient sensing

More recently, lysosomes have been identified as signaling organelles that can sense nutrient availability to regulate energy metabolism via mTORC1, a master growth regulator. When nutrients are available, mTORC1 is activated and recruited to the lysosomal surface, where it phosphorylates downstream proteins such as the transcription factor EB (TFEB) to induce cell growth and protein synthesis while inhibiting autophagy. Conversely, during nutrient depletion, mTORC1 is released and deactivated, preventing the phosphorylation of TFEB. Dephosphorylated TFEB translocates then to the nucleus and activates then the expression of genes required for lysosome biogenesis and autophagy induction, facilitating cellular adaptation to starvation *(Figure 4)*. (Cabukusta & Neefjes, 2018; Lie & Nixon, 2019; Napolitano & Ballabio, 2016). Importantly, enhancing the lysosomal-autophagic pathway by TFEB activation has been suggested as a potential therapy for the treatment of neurodegenerative diseases (Settembre et al., 2013).
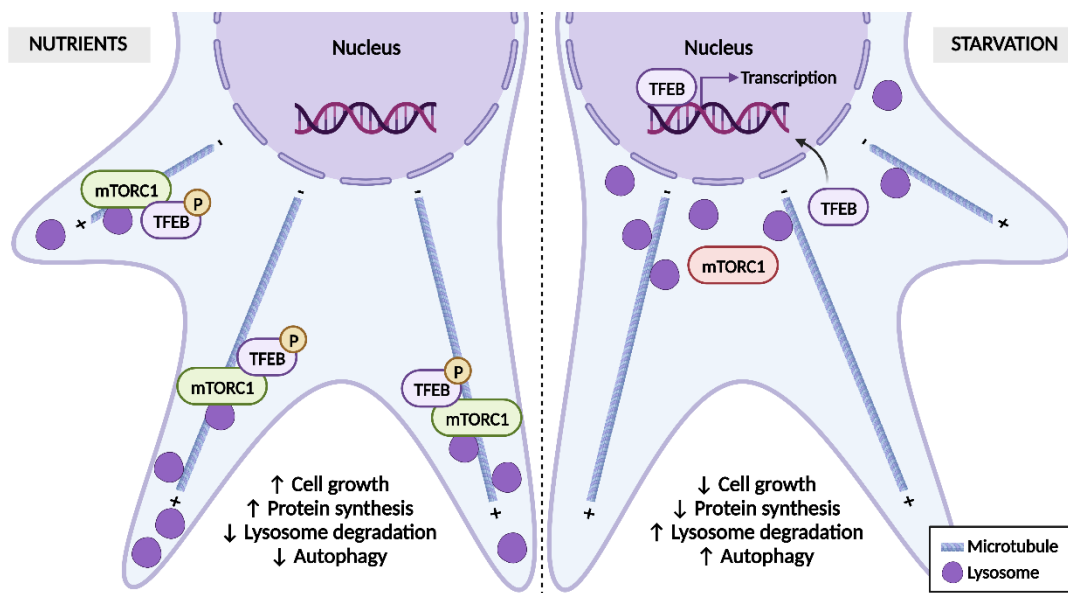
Figure 4. The mTORC1 signaling pathway regulates lysosomal function in response to nutrients. Under normal nutrient-rich conditions, lysosomes are located in the periphery, mTORC1 is activated and recruited to the lysosomal surface, and TFEB is phosphorylated and sequestered in the cytoplasm by mTORC1. Upon starvation, lysosomes are clustered in the perinuclear region and mTORC1 is inactivated, leading to the dephosphorylation of TFEB, which translocates to the nucleus to activate the transcription of genes required for lysosomal function and autophagy.

Furthermore, nutrient sensing also regulates lysosomal positioning. Under nutrient-rich conditions, the activation of mTORC1 causes scattering of lysosomes to the periphery, whereas upon starvation peripheral lysosomes move toward the perinuclear region, where autophagosomes fuse with them *(Figure 4)* (Cabukusta & Neefjes, 2018). Additionally,

nutrient sensing via carnitine palmitoyltransferase 1C (CPT1C) plays an important role in the anterograde transport of LE/lysosomes, influencing axon growth. When nutrients are available, CPT1C, through its interaction with protrudin, enhances the transport of these organelles towards the periphery, thus promoting axonal growth. However, in nutrient-deprived conditions, this process is disrupted, causing LE/lysosomes to remain in the perinuclear area (Palomo-Guerrero et al., 2019).

1.3. Impact of lipid overload in endolysosomal functionality

The previous section delves into how nutrients can regulate endolysosomal functionality. Nutrient sensing by lysosomes is necessary to maintain cellular homeostasis. Nevertheless, is important to note that an excessive presence of specific nutrients, particularly those present in a high-fat diet (HFD), may be detrimental for the correct function of the endolysosomal system.

Morselli's group has extensively studied the impact of saturated fatty acids (SFA) on endolysosomal dynamics. First, they observed that long-term HFD increased the presence of palmitic acid (PA) and sphingolipids in the hypothalamus of male mice, which led to a reduction in autophagic flux. Importantly, the inhibited autophagic flux was found to trigger hypothalamic inflammation, resulting in metabolic imbalance and further promoting obesity (Morselli et al., 2015). Subsequently, they confirmed that exposure to PA inhibits the autophagic flux in hypothalamic neurons, and demonstrated that the impairment in autophagy was not the result of a reduction in lysosomal activity but rather of an alteration in endolysosomal dynamics (Hernández-Cáceres et al., 2020). In their research, they observed that PA exposure induced lysosomal swelling without affecting the pH or impairing the activity of cathepsin B, and reduced autophagosome-lysosome fusion in hypothalamic cells. Furthermore, they demonstrated by live-cell imaging that PA affects the dynamics of endolysosomal structures, by decreasing their velocity and their traveled distance within the cell. In agreement with this, they found that PA induced a hyper-activation of Rab7, an important protein in endolysosomal transport, impairing the later phases of the autophagic process ultimately leading to a decrease in autophagic flux.

1.4. Endolysosomal dysfunction in the pathogenesis of neuronal diseases

Given the particular challenges that the endolysosomal system must face in neurons, its dysfunction has been linked to the pathogenesis of various neuronal diseases, including neurodegeneration associated to lysosomal storage disorders (LSD), neurodegenerative diseases (Alzheimer's disease (AD) and Parkinson's disease (PD), among others), certain types of cancer (glioblastoma multiforme (GBM)), and even obesity (Afghah et al., 2020; Halcrow et al., 2019; Hernández-Cáceres et al., 2020; Marques & Saftig, 2019).

The canonical view is that defects in endolysosomal function lead to reduction in autophagic flux, alterations in lipid transfer and information between organelles, mitochondrial dysfunction and oxidative stress, and accumulation of toxic proteins prone to form aggregates, ultimately resulting in cellular pathologies defining these disorders (Afghah et al., 2020; Miranda & Di Paolo, 2018).

Regarding LSD, these are a group of inherited metabolic disorders that are caused by mutations in the genes encoding for lysosomal hydrolases, accessory proteins, membrane transporters or trafficking proteins within the endolysosomal system, leading to intralysosomal accumulation of undegraded substrates. This accumulation gives rise to a broad spectrum of clinical manifestations, including neurological effects in two-thirds of LSD. Examples of LSD causing neuronal disorders are mucopolysaccharidoses, caused by deficiencies in the lysosomal enzymes necessary for the degradation of glycosaminoglycans; Niemann-Pick type C (NPC) disease, caused by deficiencies in the lysosomal cholesterol export machinery; and neuronal ceroid lipofuscinoses, caused by mutations in genes encoding for lysosomal soluble and membrane proteins (Marques & Saftig, 2019; Sun, 2018).

In the context of neurodegenerative diseases, common hallmarks are the accumulation of toxic protein aggregates (e.g., amyloid-β plaques and hyperphosphorylated tau in AD, and α-synuclein in PD) and reduced autophagy within neurons, caused by dysfunction in multiple steps of the endolysosomal network. Even though the exact mechanisms vary in each disease, impairment of endolysosomal pathways represents a converging factor that ultimately leads to neuronal cell death (Afghah et al., 2020; Wang et al., 2018).

Less often, endosomes and lysosomes have also been linked to the pathogenesis of GBM. Specifically, they participate in the acidification of the tumor microenvironment, which increases resistance to apoptosis, promotes tumor cell invasion and increases angiogenesis, among others (Halcrow et al., 2019). v-ATPase, the main regulator of H^+ ions in endolysosomes, has been found to be upregulated in GBM, being responsible for the acidification near GBM tumors by pumping protons through the extracellular space. In fact, treatment of GBM organotypic cultures with the selective v-ATPase inhibitor bafilomycin A1, results in increased levels of tumor cell death (Cristofori et al., n.d.).

Finally, dysfunction of the endolysosomal system can also be induced by chronic consumption of HFDs, rich in SFA like PA, ultimately leading to obesity. Morselli and colleagues demonstrated that HFD impairs endolysosomal dynamics, resulting in decreased autophagic flux in hypothalamic cells, and that the reduced autophagic flux triggered hypothalamic inflammation potentially promoting obesity, as described in *Section 1.3* (Hernández-Cáceres et al., 2020; Morselli et al., 2015). Accordingly, Singh's group demonstrated that loss of autophagy in hypothalamic POMC neurons promotes adiposity,

impairs lipolysis and alters glucose homeostasis through modulation of α-MSH levels (Kaushik et al., 2012).

2. BMP: the intriguing phospholipid of LE

Certain lipids have emerged as key components of the endolysosomal system and consequently, as essential regulators of cellular homeostasis. Amongst them, BMP has garnered significant attention for research. BMP, originally named lyso-*bis*-phosphatidic acid (LBPA), was first identified in 1967 after isolation from a lipid extract of pig lungs (Body & Gray, 1967). Following its discovery, literature on this intriguing lipid was relatively sparse. However, in recent years, there has been a significant increase in BMP-related publications, reflecting the growing recognition of the functional importance of BMP in membrane biology (Showalter et al., 2020). In the following sections, we will delve into the structure, localization, metabolism, and contribution of this significant phospholipid in maintaining cellular homeostasis.

2.1. Structure and composition

BMP is a negatively charged phospholipid that belongs to the group of polyglycerophospholipids, a class of phospholipids characterized for having multiple glycerol units in their structure (Hostetler, 1982). It consists of a phosphodiester group, two glycerol molecules and two fatty acyl chains *(Figure 5)* (Goursot et al., 2010).

Figure 5. Comparison of PG and BMP structures. BMP exhibits an unusual sn-1:sn-1' stereoconfiguration based on the position of the phosphate on each glycerol moiety, different from the sn-3:sn-1' configuration of its precursor PG. In native BMP, the acyl chains are esterified on the sn-2:sn-2' positions whereas in PG, they are in sn-1 and sn-2 of the same glycerol molecule. PG: phosphatidylglycerol; BMP: bis(monoacylglycero)phosphate.
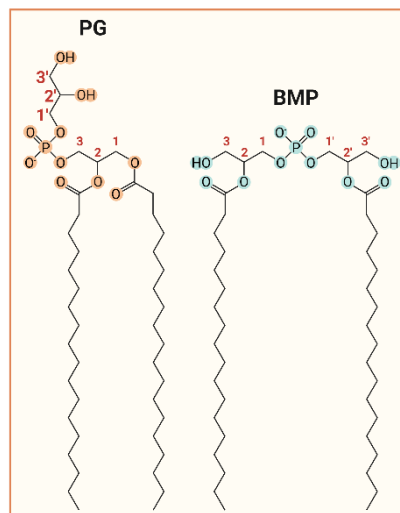
BMP is an unconventional phospholipid because it exhibits an unusual structural characteristic. Whereas all other mammalian glycerophospholipids, such as its precursor phosphatidylglycerol (PG), have a sn-3-glycerophosphate stereoconfiguration (the phosphodiester group is bonded to the carbon 3 of the glycerol backbone), BMP displays a sn-1-glycerophosphate-sn-1'-glycerol (sn-1:sn-1') stereoconfiguration (the phosphodiester group is bonded to the carbon 1 of each glycerol molecule) *(Figure 5)* (Goursot et al., 2010; Hullin-Matsuda et al., 2009). Furthermore, it is important to note that BMP is not a single

compound, but rather represents a family of compounds differing in the length and saturation of their acyl chains. The acyl chains in BMP are esterified on the sn-2 position of both glycerol backbones, although it has been stablished that they can move to the sn-3 position by acyl migration (Gallala & Sandhoff, 2011).

BMP seems to be ubiquitously distributed in all mammalian cells and tissues of high eukaryotic cells (Gruenberg, 2020). As for BMP acyl chains, different fatty acid (FA) compositions have been described, depending on the species or tissue being considered. Biochemical analysis of BMP purified from BHK cells revealed that oleic acid (OA, 18:1), the most common monounsaturated fatty acid (MUFA), accounted for more than 90% of BMP fatty acyl chains (Kobayashi et al., 2002). Conversely, in U_{III} rat uterine stromal cells, OA constituted only 30% of BMP species, being polyunsaturated fatty acids (PUFA), particularly docosahexaenoic acid (DHA, 22:6n-3), the major constituent of BMP species (Luquain et al., 2000). In THP-1 macrophages, SFA constituted almost 50 % of BMP species, while MUFA and PUFA accounted for 30 % and 20 % of BMP acyl chains, respectively. Moreover, in mouse liver and brain tissues, BMP species were found primarily esterified with PUFA (Moreau et al., 2019). Taken together, this variation in the FA content of BMP is important for its biophysical properties, and is considered to play a crucial role in its biochemical function (Gallala & Sandhoff, 2011; Hullin-Matsuda et al., 2009).

2.2. Localization

In the early studies following its discovery, BMP was primarily associated with lysosomes (Brotherus & Renkonen, 1977). However, after characterization of LE membranes and a considerable contribution of Gruenberg's group, it is now well established that BMP is localized almost exclusively in the internal membranes of LEs, representing about 15 % of the total phospholipid content of these organelles and up to 70 % in specific domains of internal membranes (Kobayashi et al., 1998, 2001, 2002). Indeed, Kobayashi et al. generated the only monoclonal antibody (6C4) able to specifically recognize BMP using endosomal membranes from BHK cells as antigens (Kobayashi et al., 1998). This antibody allowed them to reveal the localization of BMP, and has since been used by numerous researchers, contributing significantly to a better understanding of BMP in physiology and disease.

The distribution of BMP in LEs is unique compared to other phospholipids, which are not confined to specific subsets of membranes within endocytic and secretory organelles (Gruenberg, 2020). BMP-rich domains are predominantly confined to the luminal side of LEs (Kobayashi et al., 2001). However, it is noteworthy that BMP can also appear on the limiting membrane of LE following the back-fusion of the BMP-containing ILVs. This back-fusion mechanism serves as a route for recycling proteins and lipids from the endosomal lumen,

allowing them to be exported to destinations beyond lysosomes (Falguières et al., 2009). Moreover, since LE are very dynamic organelles that also fuse with lysosomes, the presence of BMP has been also described in these latter compartments (Gallala & Sandhoff, 2011).

Finally, it is noteworthy to mention that not all LEs contain BMP. It has been suggested that there might be more than one class of LE or more than one type of internal membrane within LEs. Wubbolts et al. found that purified exosomes derived from the ILVs of LEs were enriched in CD63 but lacked BMP (Wubbolts et al., 2003). Additionally, Futter's group discovered that LEs containing activated epidermal growth factor receptors (EGFRs) were distinct from those containing BMP, despite appearing morphologically identical (White et al., 2006), therefore confirming the existence of different LE subpopulations.

2.3. BMP metabolism

Despite being discovered more than fifty years ago, the enzymes responsible for regulating the metabolism of BMP remain to be fully elucidated. Unlike other phospholipids that are synthesized in the early secretory pathway, BMP is believed to be synthesized in late endocytic compartments from PG, which is in turn synthetized from phosphatidic acid (PAc) in the mitochondrial membrane through a series of enzymatic reactions (Hullin-Matsuda et al., 2007; Mayr, 2015). Although the latter steps are yet to be demonstrated, in the prevailing model of BMP biosynthesis, the first rate-limiting step involves the conversion of sn-3:sn-1' PG to sn-3:sn-1' lysophosphatidylglycerol (LPG) by the lysosomal phospholipase A2 (LPLA2) enzyme, and after a couple of transacylation steps, the sn-3:sn-1' LPG is converted into the final product, sn-1:sn-1' BMP *(Figure 6)* (Chen et al., 2023; Heravi & Waite, 1999).
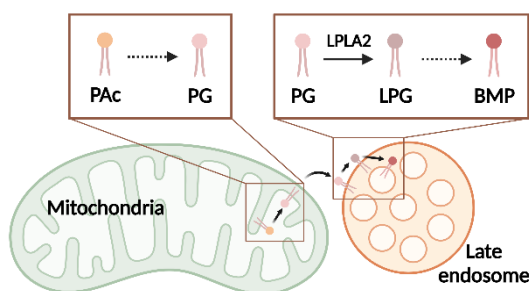
Figure 6. Biosynthesis of BMP. PG, the precursor of BMP, is synthesized in the mitochondria by phosphatidic acid (PAc). PG is transferred to endosomes where the synthesis of BMP takes place. First, the enzyme LPLA2 converts PG into LPG, and then LPG is converted into BMP. Dashed black arrows indicate that the reaction involves more than one step. PAc: phosphatidic acid; PG: phosphatidylglycerol; LPG: lysophosphatidylglycerol; BMP: bis(monoacylglycero)phosphate; LPLA2: lysosomal phospholipase A2.

Regarding its catabolism, different studies have identified potential enzymes responsible for BMP hydrolysis over the years. An early study from Matsuzawa and Hostetler showed that BMP was substantially hydrolyzed to monoglyceride and lysophosphatidic acid by a lysosomal phosphodiesterase (Matsuzawa & Hostetler, 1979). Later in 1989 Cochran et al. showed that BMP could be hydrolyzed upon macrophage activation by a putative lysosomal phospholipase A1 (LPLA1) (Cochran et al., 1987), and in the 2000s it was suggested that BMP was also a substrate for LPLA2 (Abe & Shayman, 2009; Ito et al., 2002).

More recently, two proteins from the α/β-hydrolase domain (ABHD) family, ABHD12 and particularly ABHD6, have emerged as BMP hydrolases. ABHD12 was found to contribute to BMP degradation after analyzing BMP hydrolase activity in both ABHD12-overexpressed cells and brain homogenates from mice lacking ABHD12 (Blankman et al., 2013). Similarly, ABHD6 has also been identified as a BMP hydrolase with high specific activity. Zimermann's group showed that ABHD6 is responsible for 90 % and 50 % of the BMP hydrolase activity in liver and brain, respectively, highlightin the key role of ABHD6 in BMP catabolism (Pribasnig et al., 2015). Intriguingly, ABHD6 is thought to be located at the cytosolic side of membranes, while BMP is enriched in the lumen of LE. The authors then suggested that ABHD6 may degrade BMP after the back-fusion of BMP-enriched ILVs with the limiting membrane of LEs *(Figure 7)*.
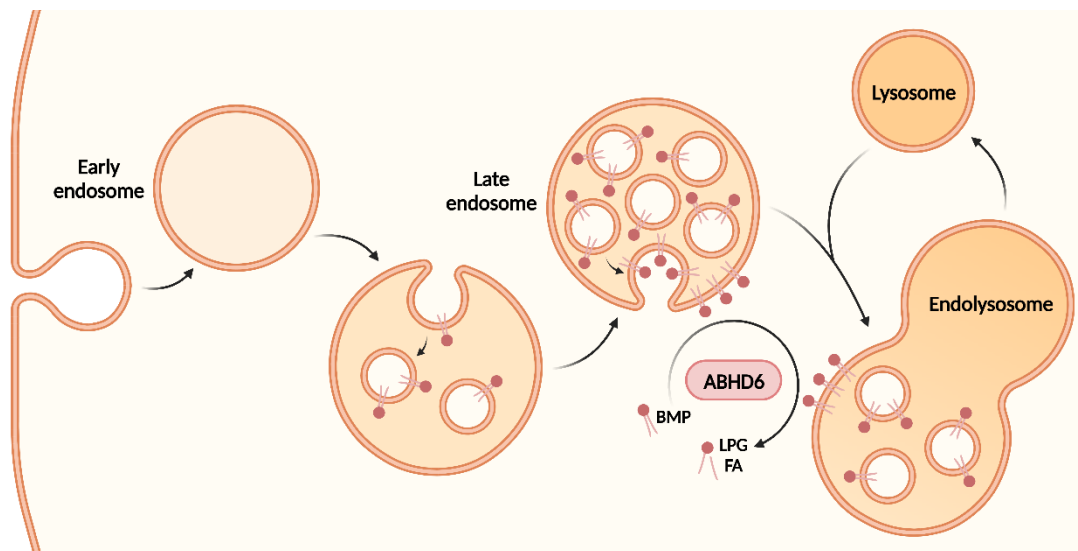
Figure 7. Proposed model for BMP hydrolysis by ABHD6. EEs formed in the peripheral cytoplasm move toward the perinuclear area along microtubules. Their conversion into LE involves the formation of BMP-containing ILVs. BMP-rich ILVs of LE and endolysosomes can fuse with the limiting membrane, allowing the export of ILV contents. After back-fusion, BMP appears on the limiting membrane and is degraded by ABHD6 into LPG and FA (Pribasnig et al., 2015). EE: Early endosome; LE: Late endosome; BMP: bis(monoacylglycero)phosphate; LPG: lysophosphatidylglycerol; FA: Fatty acid.

Despite the growing body of literature on BMP metabolism, controversies persist regarding the enzymes involved in BMP degradation and the specific conditions under which BMP is hydrolyzed. Many have argued that BMP's unusual stereoconfiguration and negative charge protects it from degradation by lysosomal enzymes, but further research and application of modern methods will be necessary for a full understanding of its metabolism (Showalter et al., 2020).

2.4. Cellular functions of BMP

Several lines of evidence have shown that BMP is not only a constitutive lipid of LEs but also a key player in the dynamics and functions of the endolysosomal system. Its main functions include the formation of ILVs, the modulation of lysosomal proteins activity and the regulation of cholesterol homeostasis within the cell (Showalter et al., 2020).

2.4.1. Role of BMP in endosome biogenesis and dynamics

As previously described, cargo destined for degradation undergoes selective sorting into ILVs following endocytosis. ILVs are formed through the invagination of the endosomal membrane. The current view is that ILV formation depends on ESCRT proteins and the ESCRT-associated protein Alix (Falguières et al., 2009).

A more recent view includes the participation of BMP. It was discovered that BMP specifically interacts with Alix (Bissig et al., 2013), suggesting that both BMP and Alix may play a direct role in the ESCRT-dependent ILV formation within LE. In fact, Matsuo et al. demonstrated that BMP can induce membrane invagination and the formation of internal vesicles within acidic liposomes, resembling the structures found in multivesicular LEs. Importantly, this phenomenon was dependent on the same pH gradient that exists across endosome membranes in vivo and was controlled, at least in part, by transient interactions between BMP membranes and Alix (Matsuo et al., 2004). Furthermore, the same group demonstrated afterwards that Alix knock-down led to a decrease in BMP levels and a concomitant reduction in the luminal membrane content of LEs, which was restored by the addition of exogenous BMP (Chevallier et al., 2008).

Additionally, BMP is predicted to have a cone-shaped structure with a small head group, which may confer to BMP-rich domains the capacity to induce membrane asymmetry and favor the invagination process, hence facilitating the formation of ILVs (Hullin-Matsuda et al., 2009).

2.4.2. Role of BMP in the degradative pathway

Recent studies have underscored the importance of BMP for lipid and membrane catabolism. BMP's negative charge allows it to act as a docking site and essential cofactor for various proteins of the endolysosomal system that contain positively charged domains. Notably, BMP has garnered significant attention for its involvement in sphingolipid metabolism by stimulating the activity of sphingolipid degradative enzymes (Gallala & Sandhoff, 2011; Showalter et al., 2020).

Among these enzymes, BMP has been reported to stimulate the activity of several key players, including acid sphingomyelinase, acid ceramidase, and saposin activating proteins, among others (Linke, Wilkening, Lansmann, et al., 2001; Linke, Wilkening, Sadeghlar, et al., 2001; Oninla et al., 2014; Wilkening et al., 2000).

2.4.3. Role of BMP in cholesterol homeostasis

BMP also plays a crucial role in controlling the fate of endosomal cholesterol. Most cells acquire cholesterol from circulating LDL endocytosed by the LDL receptor. Once inside endosomes, cholesteryl esters are de-esterified and free cholesterol is rapidly incorporated into nearby membranes, including BMP-containing membranes. Cholesterol then reaches the limiting membrane of endosomes and is further exported to the ER for cholesterol sensing (Gruenberg, 2020).

Within endosomes, cholesterol transfer to the limiting membrane depends on NPC1 and NPC2 proteins (Garver & Heidenreich, 2005), and loss-of-function mutations in either of these proteins leads to NPC disease, which is characterized by cholesterol accumulation in late endocytic compartments. Remarkably, BMP has been found to accumulate together with cholesterol in NPC cell models, concomitantly with an increase in the size of LE compartments, presumably as a compensatory mechanism to accommodate excess cholesterol (Sobo et al., 2007).

More recently, different studies have highlighted BMP as a critical regulator of cholesterol trafficking within the endolysosomal system through its interaction with NPC2 *(Figure 8)* (Enkavi et al., 2017; McCauliff et al., 2019). On the one hand, Chevallier et al. suggested that BMP controls the cholesterol capacity of endosomes. They found that Alix down-expression decreased both BMP levels and ILVs within LEs, as well as cellular cholesterol levels, presumably because of the storage capacity of endosomes. Moreover, they observed that addition of exogenous BMP to NPC cells reduced the pathological accumulation of cholesterol, partially reverting the NPC phenotype (Chevallier et al., 2008). And on the other hand, in the study conducted by McCauliff et al., supplementation of NPC1-deficient cells with the BMP precursor PG increased BMP levels and concomitantly reversed cholesterol

accumulation in a NPC2-dependent manner (McCauliff et al., 2019). The same group revealed later the mechanisms underlying the reduction in cholesterol storage after PG/BMP enrichment. They found that PG incubation significantly enhanced the late stages of autophagy, providing a route for NPC1-independent endolysosomal cholesterol mobilization (Ilnytska et al., 2021).

Figure 8. BMP regulates cholesterol export from endosomes through its interaction with NPC2. After endocytosis, cholesterol is incorporated in BMP-containing membranes. Then, cholesterol is transferred to the limiting membrane of endosomes by the cooperation of BMP, NPC2 and NPC1.
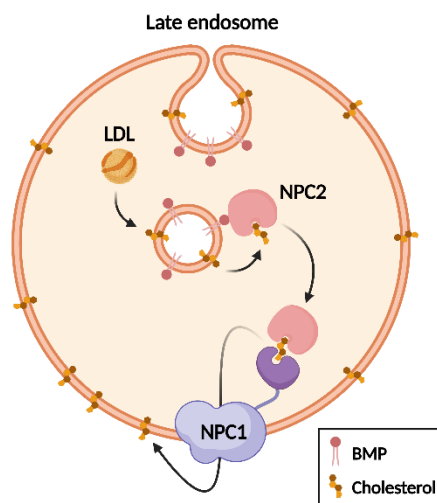
Altogether, BMP in late endocytic compartments serves as a platform to accommodate endosomal cholesterol, controlling both the cholesterol storage capacity of LEs and the flux of cholesterol through these organelles (Gruenberg, 2020).

2.5. BMP as a biomarker in disease

BMP has been extensively characterized as a biomarker for LSD (reviewed in Showalter et al., 2020). However, it has been less frequently described as a biomarker in obesity and neurodegenerative diseases, conditions that have also been associated to endolysosomal dysfunction.

Published work suggests that dietary lipid overload increase the hepatic, renal and circulating BMP concentrations in mice (d'Avignon et al., 2018; Grabner et al., 2019; Pribasnig et al., 2015; Rampanelli et al., 2018). Considering that BMP is crucial for proper endolysosomal function in lipid sorting and catabolism, HFD-induced alterations in BMP are thought to reflect lysosomal stress triggered by an increased lipid influx (Grabner et al., 2019).

Accordingly, a later comprehensive study investigated the effects of nutritional and metabolic factors on BMP profiles of whole tissues and parenchymal and nonparenchymal cells from mice under different conditions. The obtained results confirmed that BMP content and species adapt to the nutritional and metabolic state in a tissue- and cell-type-specific manner (Grabner et al., 2020).

In the context of neurodegenerative disorders, BMP was described as a biomarker linked to neuronal endolysosomal dysfunction in a study conducted by Di Paolo's group. They observed that inhibition of Vps34, an enzyme involved in endolysosomal and autophagic

functions, caused endolysosomal dysfunction and promoted the secretion of exosomes enriched in APP fragments, specific sphingolipids and BMP. Hence, they suggested that exosomal APP fragments and BMP could serve as potential diagnostic biomarkers of endolysosomal dysfunction associated with neurodegenerative disorders (Miranda et al., 2018).

Altogether, changes in the cellular BMP content reflect an altered metabolic activity of the endolysosomal system, thereby positioning BMP as a potential biomarker of diseases associated with endolysosomal dysfunction.

3. The hydrolase ABHD6

One of the most characterized enzymes of BMP catabolism in the last years has been ABHD6 (Pribasnig et al., 2015). ABHD6 belongs to the α/β-hydrolase superfamily, a diverse class of serine hydrolases that is recognized by a common structural motif, the α/β-hydrolase fold, which consists of eight mostly parallel strands connected by helices and loops (Lord et al., 2013).

3.1. Structure and localization of ABHD6

While the structure and subcellular localization of ABHD6 remains to be fully elucidated, several studies have provided valuable insights into these aspects. The experimental structure of human ABHD6 has been recently obtained by X-ray crystallography (PDB code 7OTS) (Nawrotek et al., 2021) and has also been predicted by AlphaFold (Jumper et al., 2021; Varadi et al., 2022). As deduced from these models, ABHD6 is an integral membrane protein consisting of a single N-terminal transmembrane domain and a globular cytosolic domain, the latter containing the active site comprised by the catalytic triad Ser148-Asp278-His306 (Navia-Paldanius et al., 2012) *(Figure 9)*.
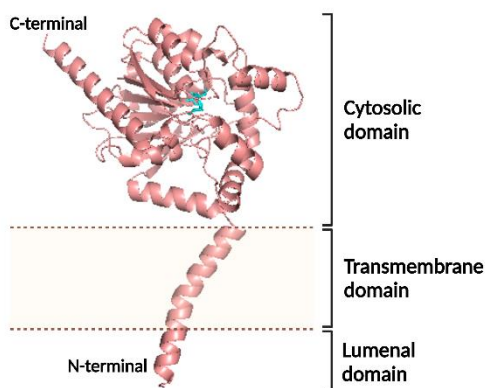
Figure 9. Structure of ABHD6. ABHD6 consists of a N-terminal domain facing the lumen, one transmembrane domain and a globular C-terminal domain facing the cytosol. The catalytic triad comprised by Ser148-Asp278-His306 is colored in cyan.

Based on the current models, Pusch et al. generated a first model of ABHD6 embedded in a phospholipid-containing membrane. The electrostatic surface properties of their model revealed a rather positively charged face of the protein, suggesting that ABHD6 could attach to charged membrane surfaces, which could explain the preference for negatively charged lipid substrates such as BMP (Pusch et al., 2022). However, this model must be interpreted with caution since it is based on predictions and needs experimental verification on different membranes.

Concerning its subcellular localization, very few studies have reported differing data in this regard. First, ABHD6 was detected in cellular fractions enriched in mitochondria (Marrs et al., 2010). Then, it was described to colocalize with LE/lysosomes (Pribasnig et al., 2015), and one last study found ABHD6 to be present in ER membranes (Schwenk et al., 2019).

3.2. ABHD6 hydrolase activity

ABHD6 was first characterized as a 2-arachidonoylglycerol (2-AG) hydrolase in 2007, in a functional proteomic study aimed to unravel the enzymes responsible for 2-AG hydrolysis (Blankman et al., 2007). In this study, the authors described that ABDH6 was responsible for around 4% of 2-AG hydrolysis in mouse brain homogenates. However, further studies have revealed that ABHD6 is able to hydrolyze other substrates such as LPG or BMP with even more affinity (Pribasnig et al., 2015; Thomas et al., 2013). In fact, when Zimmerman's group described BMP as a substrate for ABHD6 for the first time, they demonstrated that ABHD6 was responsible for around 90 % and 50 % of the BMP hydrolase activity in mouse liver and brain lysates, respectively (Pribasnig et al., 2015).

Finally, how ABHD6 activity is regulated is an ongoing area of research. To date, only one protein, the brain specific CPT1C, has been identified by our research group as a negative regulator of ABHD6 hydrolase activity (Miralpeix et al., 2021).

3.3. Functions of ABHD6

ABHD6 is an ubiquitously expressed enzyme, with its highest expression observed in brain, brown adipose tissue (BAT), small intestine and liver (Thomas et al., 2013). Its widely expression confers ABHD6 a wide range of functions in both physiological and pathological processes. It has been described to play a role in the control of metabolism and energy homeostasis, cognition processes, the inflammatory response, various neurological disorders, and even cancer *(Figure 10)* (Deng & Li, 2020; Poursharifi et al., 2017). These functions have been elucidated through the generation of animal models with global or tissue-specific ABHD6 deletion (Pusch et al., 2022) and the use of small molecule inhibitors,

which have been employed to inhibit ABHD6 activity in both *in vitro* and *in vivo* studies (Bononi et al., 2021).
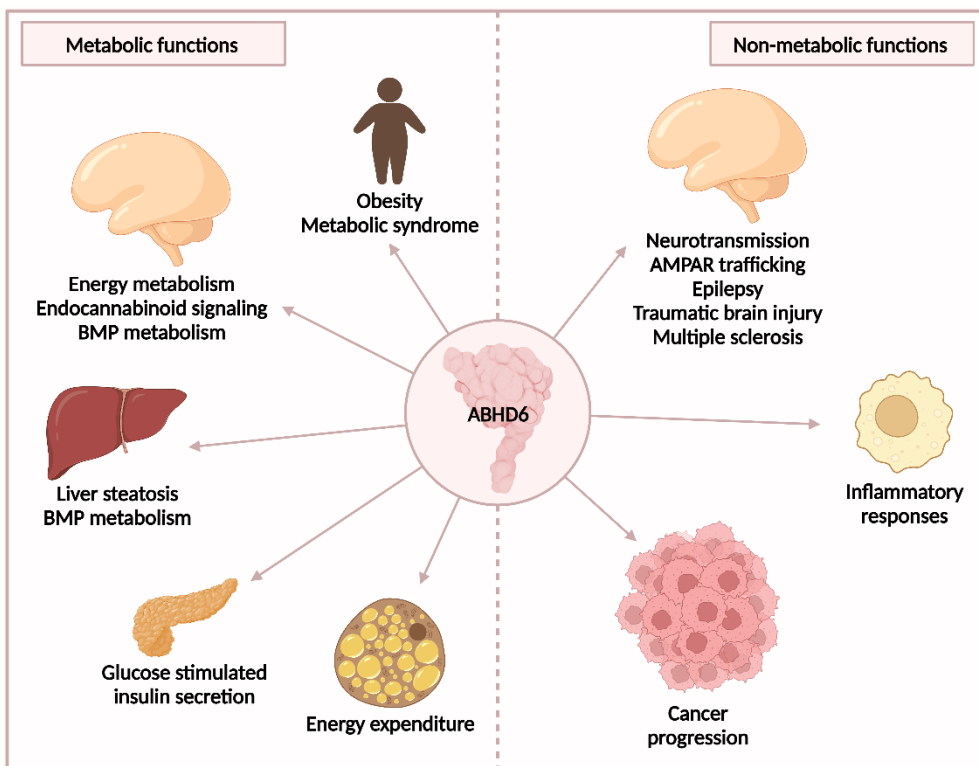
Figure 10. ABHD6 functions. Involvement of ABHD6 in metabolic and non-metabolic (patho)-physiological processes.

3.3.1. Metabolic functions of ABHD6

ABHD6 has been implicated in metabolic functions in both the CNS and the periphery *(Figure 10)*.

Regarding the functions of ABHD6 in the CNS, it has been demonstrated that ABHD6 regulates energy metabolism flexibility through the regulation of 2-AG levels in the ventromedial hypothalamus (VMH) (Fisette et al., 2016). Specifically, knocked-down mice for ABHD6 in the VMH displayed increased hypothalamic 2-AG levels and an impaired adaptative response to different metabolic challenges, including HFD feeding, dieting and cold exposure.

The role of ABHD6 in the peripheral energy metabolism was first established by Thomas et al. using antisense oligonucleotides to knock-down the enzyme in peripheral tissues. In their study, selective knock-down of ABHD6 in metabolic tissues protected mice from diet-induced obesity (DIO), hepatic steatosis and systemic insulin resistance, therefore positioning ABHD6 as a critical regulator in the development of the metabolic syndrome (Thomas et al., 2013).

Accordingly, further studies conducted by Zhao et al. reported that suppression of ABHD6 promotes glucose-stimulated insulin secretion (GSIS) in pancreatic β cells (Zhao et al., 2014, 2015) and protects from DIO through different mechanisms (Zhao et al., 2016). Deletion of ABHD6, both globally and specifically in pancreatic β-cells, as well as ABHD6 inhibition in diabetic mice resulted in an enhanced GSIS and improved glucose tolerance. This effect was ascribed to reduced hydrolysis of lipolysis-derived 1-monoacylglycerol (1-MAG), which activated the exocytotic regulator Munc13-1, thereby triggering insulin secretion (Zhao et al., 2014, 2015). Moreover, global deletion of ABHD6 in mice fed with a HFD protected them from obesity and diabetes. These mice exhibited reduced weight gain and liver steatosis, improved glucose tolerance and insulin sensitivity, increased locomotor activity and energy expenditure, and white adipose tissue browning compared to their wild-type (WT) littermates. In particular, the mechanism of adipose browning behind ABHD6 suppression seems to be mediated via PPARα/γ activation by 1-MAG (Zhao et al., 2016).

Finally, Zimmermann's group demonstrated that ABHD6 also has a fundamental role in BMP metabolism. In their initial study, ABHD6 was found to hydrolyze BMP in liver and brain with high specificity. They also observed that knocking-down ABHD6 in liver of chow diet-fed mice increased total hepatic BMP levels, being that effect even greater in mice fed a HFD. Considering the central role of BMP in degradation and sorting of lipids within the endolysosomal system, the authors of the study proposed a role for ABHD6 in the LE/lysosome lipid sorting-machinery (Pribasnig et al., 2015). Later on, they demonstrated that ABHD6 affected circulating BMP levels both in mice and humans. On the one hand, they observed that global deletion of ABHD6 in mice increased BMP levels in plasma while hepatic BMP levels remained unchanged, which suggested that ABHD6 deficiency promotes BMP release into the circulation without promoting LSD. And on the other hand, they identified a patient with a loss-of-function mutation in the Abhd6 gene, who exhibited increased DHA-containing BMP subspecies (Grabner et al., 2019).

Taken together, ABHD6 exerts different metabolic effects depending on its site of action, thus becoming a potential therapeutic target for common metabolic diseases.

3.3.2. Non-metabolic functions of ABHD6

ABHD6 has also been implicated in other functions related to cognition, inflammation, neurological disorders, and cancer *(Figure 10)*.

ABHD6 regulates long-term depression in the prefrontal cortex in an activity-dependent manner. There, ABHD6 controls the accumulation and efficiency of 2-AG at cannabinoid receptors, thus regulating cannabinoid-dependent long-term depression (Marrs et al., 2010). Moreover, ABHD6 has a role in receptor trafficking. In 2012, ABHD6 was identified as a

component of α-amino-3-hydroxy-5-methyl-4-isoxazolepropionic acid receptor (AMPAR) complexes in the CNS (Schwenk et al., 2012), and subsequent studies revealed that ABHD6 negatively regulates their surface delivery to the cell surface and affected their synaptic function independently of its hydrolase activity (Wei et al., 2016, 2017).

ABHD6 is also involved in the regulation of inflammatory responses by controlling the hydrolysis of 2-AG. 2-AG hydrolysis releases arachidonic acid, which is the precursor for prostaglandins, some of which contribute to inflammatory processes (Poursharifi et al., 2017). For instance, pharmacological blockade of ABHD6 in macrophages has been reported to increase the COX-2-mediated synthesis of prostaglandin-D2-glycerol ester, which has anti-inflammatory effects both *in vitro* and *in vivo* (Alhouayek et al., 2013).

Related to neurological disorders, ABHD6 has emerged as a promising therapeutic target for the treatment of epilepsy, traumatic brain injury and multiple sclerosis. Blockade of ABHD6 exerted antiepileptic effects in mouse models of pentylenetetrazole-induced seizures or Dravet Syndrome (Naydenov et al., 2014; Westenbroek et al., 2023). In the mouse model of traumatic brain injury, pharmacological inhibition of ABHD6 had multiple positive effects: it improved motor coordination and working memory performance due to a reduction of brain lesions, neuroinflammation, neurodegeneration and blood-brain dysfunctions (Tchantchou & Zhang, 2013). Inhibition of ABHD6 was also protective in a mouse model of experimental autoimmune encephalomyelitis, a model for multiple sclerosis. In this model, treatment of mice with an ABHD6 inhibitor elevated 2-AG levels in the cerebral cortex, downregulated the expression of pro-inflammatory markers, and attenuated macrophage and T cell infiltration in the spinal cord. However, more recent studies indicate that ABHD6 blockade exerts only modest therapeutic effects against autoimmune-mediated diseases and call into question its utility as novel drug target in multiple sclerosis (Manterola et al., 2018).

Finally, some investigations have also identified ABHD6 as an interesting target for the development of anti-metastatic and anti-tumor therapies. ABHD6 expression is reported to link with the pathogenesis of Epstein Barr virus (EBV) associated malignancies (Maier et al., 2006). Moreover, increased ABHD6 expression was identified in various tumor cells including Jurkat (leukocyte), U2OS (bone), PC-3 (prostate) (Li et al., 2009), as well as in Ewing tumors (Max et al., 2009). And based on RNAseq data and screening of differential genes in liver tumors, ABHD6 was found to be a potential marker of hepatocellular carcinoma prognosis (Yu et al., 2016). These studies implicate the expression of ABHD6 in different tumors but did not clearly elucidate the role of ABHD6 in the pathogenesis of these tumors. Interestingly, ABHD6 was found to be highly expressed in pancreatic ductal adenocarcinoma tumors, and inhibition of ABHD6 was able to reduce cancer cell proliferation *in vitro* and tumor metastasis *in vivo* (Grüner et al., 2016). Evidence for a prooncogenic function of ABHD6 also came from

a study investigating the role of ABHD6 in the pathogenesis of non-small cell lung carcinoma. ABHD6 silencing and pharmacological inhibition reduced migration and invasion of tumorous cells *in vitro* and blunted metastatic seeding and tumor growth in mice (Tang et al., 2020). However, further research is required to better characterize the role of ABHD6 in the pathogenesis of these tumors and its use as a potential diagnostic marker and a therapeutic target for the treatment of these malignancies.

4. CPT1C, the first negative regulator of ABHD6

CPT1C was the last and most enigmatic isoform of the CPT family to be identified, the others being CPT2, CPT1A and CPT1B. CPT2, CPT1A and CPT1B are located in the mitochondrial membrane, where they catalyze the reversible transesterification of acyl-CoA esters (specifically long-chain fatty acids, LCFA) and carnitine to form acylcarnitine esters and coenzyme A, thus facilitating the transport of LCFA inside mitochondria to undergo β-oxidation *(Figure 11).* In contrast, CPT1C is located in the ER and has no catalytic activity (Casals et al., 2016).
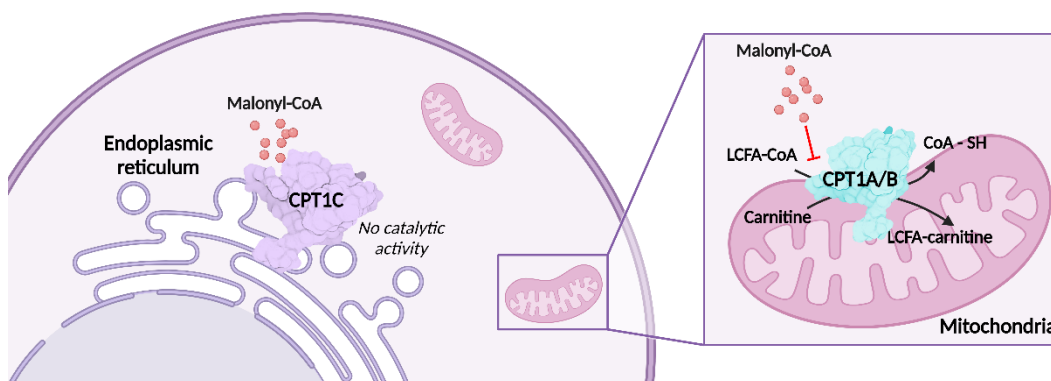
Figure 11. Schematic representation of subcellular localization and function of CPT1 isoforms. CPT1C is expressed in the ER and has no catalytic activity, whereas CPT1A and CPT1B are located in the mitochondrial membrane, where they facilitate the transport of LCFA into the mitochondria to undergo β-oxidation. Malonyl-CoA binds to all three isoforms. It acts as a nutrient indicator for CPT1C, while it inhibits CPT1A and CPT1B activity. ER: Endoplasmic reticulum; LCFA: Long-chain fatty acids.

CPT1C also differs from the canonical isoforms in tissue expression. CPT1A is ubiquitously expressed in the body, particularly in the liver, and CPT1B is mainly expressed in muscle and BAT (McGarry & Brown, 1997). However, CPT1C is specifically expressed in neurons of different brain areas. Nonetheless, all three CPT1 isoforms share a common feature, they are able to bind malonyl-CoA, an intermediate precursor of the FA synthesis that acts as an energy sensor (Casals et al., 2016).

4.1. General features of CPT1C

CPT1C was first discovered in a study by Price and colleagues two decades ago (Price et al., 2002) and still remains the less characterized. Although its genetic sequence shares a 52% identity with CPT1A and 51% with CPT1B (Samanta et al., 2014), CPT1C exhibits a unique expression profile, being primarily found in mammalian neurons, testicular tissue (Price et al., 2002) and tumor cells (Zaugg et al., 2011). Further investigations delving into the localization of CPT1C in brain revealed its widespread expression within the CNS, with a major concentration in hippocampus (involved in learning and cognition), hypothalamic nuclei (involved in feeding behavior and energy expenditure), and amygdala (which coordinates autonomic and endocrine responses to emotional states) (Dai et al., 2007). Later, it was demonstrated that CPT1C is also expressed in the peripheral nervous system (Rinaldi et al., 2015). Notably, this expression appears to be neuron-specific, as it has not been observed in glial or endothelial cells (Sierra et al., 2008).

One defining characteristic that distinguishes CPT1C from the other CPT1s is its subcellular localization within the ER, in contrast to the mitochondria, where CPT1A and CPT1B reside. In a first study, CPT1C was reported in microsomal fractions of mouse brain and yeast (Price et al., 2002), and a later co-localization study from our group with specific markers confined the distribution of this protein in the ER. Moreover, this same study also established that the N-terminal region of CPT1C was responsible for its subcellular localization (Sierra et al., 2008).

Concerning the structure of CPT1C, it has not been achieved experimentally yet, probably because of its membrane association. Only the 3D structure of N-terminal domain encompassing the first 50 amino acids have been obtained (Samanta et al., 2014). Nonetheless, its domains and structure have been predicted by sequence homology with other carnitine acyltransferases and informatic predictions. CPT1C have a short N-terminal domain and a globular C-terminal domain separated by two transmembrane domains and a short connecting loop. Both terminal domains are facing the cytoplasm while the connecting loop is within the ER lumen *(Figure 12)* (Casals et al., 2016). One interesting feature is the spatial structure of the N-terminal domain. A first study on CPT1A postulated that its N-terminal domain can adopt two different conformations, termed Nα and Nβ, which are inhibitory and non-inhibitory, respectively (Rao et al., 2011). A second study observed that the CPT1C N-terminal domain adopted only the inhibitory Nα state, which could explain its lack of catalytic activity (Samanta et al., 2014). Lastly, CPT1C C-terminal tail is around 30 residues longer than the C-terminal domain of the canonical CPT1 isoforms (Casals et al., 2016).
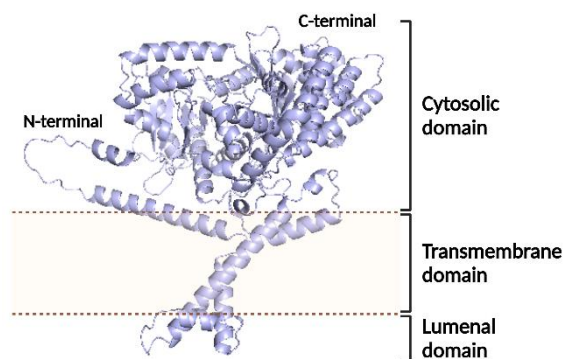
Figure 12. Structure of CPT1C. CPT1C consists of a short N-terminal domain and a globular C-terminal domain facing the cytosol, and two transmembrane domains connected by a loop facing the lumen.

Despite conserving all the motifs required for catalytic activity and the binding site for acyl-CoAs, CPT1C has very low catalytic efficiency with carnitine and acyl-CoA as substrates (Price et al., 2002; Wolfgang et al., 2006). Notably, it displayed a relatively high affinity for palmitoyl-CoA, although its catalytic efficiency remained 20-300 times lower than that of CPT1A (Sierra et al., 2008). Accordingly, CPT1C-knock-out (KO) mice exhibited no differences in acyl-Coa and acyl-carnitine levels when compared to WT mice, confirming that CPT1C does not contribute to fatty acid oxidation (FAO) in neuronal cells (Wolfgang et al., 2006). As mentioned above, Samanta et al. attributed the low catalytic activity of CPT1C to the N-terminal domain conformation, which was found to adopt the same inhibitory state previously observed in CPT1A (Samanta et al., 2014).

4.2. Malonyl-CoA sensing

Despite of its lack of catalytic activity, CPT1C is still able to bind malonyl-CoA, a metabolic intermediate that acts as an energy sensor (Price et al., 2002). Malonyl-CoA is synthesized by acetyl-CoA carboxylase (ACC) from acetyl-CoA, and is then metabolized by the fatty acid synthase (FAS) to generate FA. The main kinase that regulates ACC activity, and therefore malonyl-CoA synthesis, is the AMP-activated protein kinase (AMPK). In conditions of energy deprivation such as fasting or in response to certain hormones like glucagon or ghrelin, AMPK is activated. AMPK then phosphorylates and inactivates ACC, resulting in a decrease of malonyl-CoA levels and FA synthesis and thus leading to significant savings in cell energy expenditure (Hardie, 2015). On the contrary, in conditions of nutrient abundance, especially high glucose availability, ACC is activated and triggers the synthesis of FA to store excess nutrients in form of fat *(Figure 13)* (Brownsey et al., 2006). Lastly, ACC is also modulated allosterically by two important substrates, citrate and palmitoyl-CoA. Citrate is an allosteric activator of ACC and hence promotes the synthesis of malonyl-CoA, whereas palmitoyl-CoA, as an allosteric inhibitor, decreases its synthesis (Hunkeler et al., 2018).
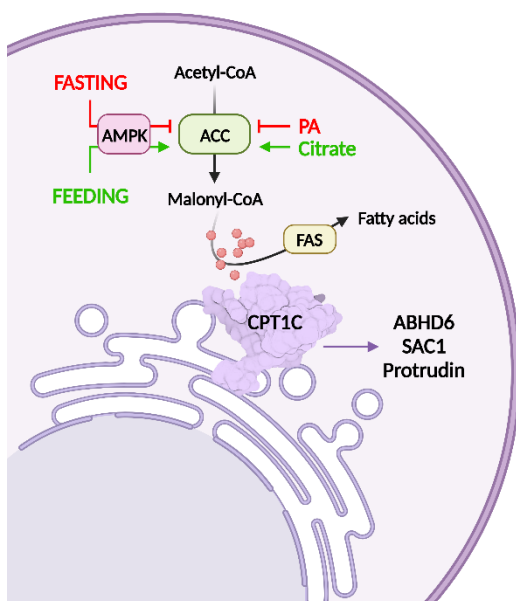
Malonyl-CoA levels, which fluctuate depending on the nutritional state of the cell, are sensed by CPT1 proteins. Regarding the canonical CPT1 isoforms, malonyl-CoA acts as a physiological inhibitor of CPT1A and CPT1B proteins, therefore inhibiting the entry of LCFA to the mitochondria for β-oxidation. Interestingly, malonyl-CoA is not an inhibitor of CPT1C. Instead, malonyl-CoA is sensed by CPT1C to regulate the function of other proteins (e.g. ABHD6, SAC1 and protrudin) depending on the nutritional status of the cell *(Figure 13)* (Fadó et al., 2021). How CPT1C regulates other protein functions depending on malonyl-CoA sensing will be described in detail later.

4.3. Functions of CPT1C

Although the molecular function of CPT1C is not completely understood, it has been described to play critical roles in energy homeostasis, cognition, motor function and cancer (Casals et al., 2016).

4.3.1. CPT1C in energy homeostasis

Based on CPT1C-KO mouse models, CPT1C has demonstrated important relevance in hypothalamic regulation of energy homeostasis. The first model was developed and characterized in 2006 by Wolfgang and colleagues and revealed for the first time the physiological role of CPT1C in energy homeostasis. In their study, they showed that, under basal conditions, deletion of CPT1C resulted in lower body weight (BW) and food intake (FI). However, under a HFD, CPT1C-KO mice were more susceptible to obesity in terms of BW gain while maintaining a lower FI (Wolfgang et al., 2006). In agreement with these data, overexpression of CPT1C in the hypothalamus of WT mice resulted in protection from BW gain when fed a HFD (Dai et al., 2007), therefore confirming that CPT1C is protective against the effects of fat feeding.

Subsequent studies conducted by our research group delved into the underlying mechanism of CPT1C in the control of FI, whose findings demonstrated that CPT1C is crucial in the hypothalamic regulation of FI through leptin and ghrelin signaling (S. Gao et al., 2011; Ramírez et al., 2013). Overexpression of CPT1C in the arcuate nucleus of the hypothalamus increased FI while counteracting the anorexigenic effects of leptin. Furthermore, both the orexigenic and anorexigenic actions after administration of ghrelin and leptin, respectively, were totally blunted in CPT1C-KO mice (S. Gao et al., 2011; Ramírez et al., 2013). In both studies, the impaired effects of the appetite-related hormones were linked to the involvement of CPT1C in ceramide metabolism within the hypothalamus (S. Gao et al., 2011; Ramírez et al., 2013).

Additionally, hypothalamic CPT1C was also found to regulate energy homeostasis through peripheral signaling to the liver and muscle under metabolic challenges. After HFD, CPT1C-KO mice developed a more severe insulin resistance phenotype than WT mice, which was attributable to elevated hepatic gluconeogenesis and decreased glucose uptake in skeletal muscle. These effects correlated with a lower rate of FAO in liver and muscle of CPT1C-KO mice, which resulted in higher levels of triglycerides in these tissues (X. F. Gao et al., 2009). Interestingly, studies from our lab and other groups revealed that fasted CPT1C-KO mice also showed defective FAO (Pozo et al., 2017; Wolfgang et al., 2006).

The observed decreased in FAO in CPT1C-KO mice is indicative of reduced energy expenditure, which would explain the increased BW gain observed in CPT1C-KO animals after HFD (Wolfgang et al., 2006). Likewise, we have demonstrated that CPT1C in the VMH is necessary for BAT thermogenesis following HFD (Rodríguez-Rodríguez et al., 2019). Specifically, CPT1C-KO mice showed impaired BAT thermogenesis activation after short-term HFD, which was restored after the expression of CPT1C in the VMH. Noteworthy, these mice also evidenced disrupted hypothalamic leptin signaling in terms of BAT thermogenesis activation.

Finally, hypothalamic CPT1C is also crucial for fuel selection (Pozo et al., 2017) and food preference determination (Okamoto et al., 2018) under fasting conditions. In a study conducted by our group, CPT1C-KO mice were unable to properly regulate the peripheral switch on fuel substrate selection after 48 h of fasting, while CPT1C overexpression in the mediobasal hypothalamus reversed the observed phenotype (Pozo et al., 2017). Regarding food preference, Okamoto et al. found that CPT1C in the paraventricular hypothalamus mediates the fasting-induced increase in high-carbohydrate diet selection (Okamoto et al., 2018).

Taken together, hypothalamic CPT1C is essential for maintaining energy homeostasis by coordinating various metabolic processes through hypothalamic signaling to peripheral tissues.

4.3.2. Non-metabolic functions of CPT1C

Beyond its involvement in metabolic functions, CPT1C has proved relevance in cognition and motor function processes, as well as in the pathogenesis of cancer (Casals et al., 2016).

Concerning cognition processes, CPT1C has been related to hippocampus-dependent spatial learning. In a study conducted by our group, CPT1C-KO mice showed impaired spatial learning when subjected to the Morris water maze test. This deficiency was associated with poor maturation of dendritic spines, a process that was found to be dependent on the capacity of CPT1C to regulate ceramide levels (Carrasco et al., 2012). However, proper spine maturation could be also related to the interaction of CPT1C with AMPAR (Brechet et al., 2017; Schwenk et al., 2012).

Accordingly, subsequent studies revealed the role of CPT1C in controlling AMPAR synthesis and trafficking to the postsynaptic membrane, thereby influencing synaptic plasticity (Casas et al., 2020; Fadó et al., 2015; Gratacòs-Batlle et al., 2015). CPT1C was found to regulate both the post-transcriptional regulation of GluA1 protein synthesis, the most abundant subunit of AMPAR, and the trafficking of AMPAR to the cell surface (Fadó et al., 2015; Gratacòs-Batlle et al., 2015). More recently, our group elucidated that this AMPAR trafficking was regulated by the interaction of CPT1C with the phosphatase SAC1 depending on malonyl-CoA sensing (Casas et al., 2020).

CPT1C deficiency has been also associated with motor function impairment. On the one hand, a battery of neurological tests on CPT1C-KO mice revealed impaired coordination and gait, severe muscle weakness, and reduced daily locomotor activity. The motor impairment and hypoactivity increased progressively with age and was associated with the role of CPT1C in neuronal ceramide metabolism (Carrasco et al., 2013). And on the other hand, Rinaldi and colleagues described a mutation in CPT1C associated with a specific form of hereditary spastic paraplegia (HSP), an inherited neurological disorder characterized by progressive spasticity and weakness in lower limbs caused by dysfunction of corticospinal motor neurons (Rinaldi et al., 2015). Importantly, CPT1C has recently been linked to axonal growth, as it enhances LE/lysosome anterograde transport in response to malonyl-CoA changes by interacting with the ER protein protrudin. In line with the pathogenesis of HSP, the CPT1C mutation described by Rinaldi was found to be associated with decreased axonal length in cortical neurons (Palomo-Guerrero et al., 2019).

Lastly, CPT1C has emerged as a key factor in tumor cell survival in certain types of cancer (Reilly & Mak, 2012). A first study showed that the expression of CPT1C is unusually increased in many human breast and lung cancers (Zaugg et al., 2011), and a study performed by Reilly and Mak in a wide array of human tumor types revealed an increased expression of CPT1C in brain cancers such as neuroblastoma and an unusual expression in several sarcomas of soft-tissues and lung (Reilly & Mak, 2012). The role of CPT1C in cancer cells is not fully elucidated yet. Zaugg et al. observed that constitutive overexpression of CPT1C in breast cancer cells increased FAO, ATP production and resistance to glucose deprivation or hypoxia (Zaugg et al., 2011). Additionally, our group has reported that CPT1C in breast cancer cells is involved in PM lipid remodeling and anthracycline resistance, becoming a potential biomarker for breast cancer chemotherapy (Muley et al., 2023).

Likewise, our group described that CPT1C in human mesenchymal stem cells protects them against glucose deprivation through the modulation of autophagy (Roa-Mansergas et al., 2018), therefore confirming the role of CPT1C in cell survival and highlighting CPT1C as a potential target in cancer therapy.

4.4. Interaction of CPT1C with other proteins

It is worth noting that that some of the functions described above are mediated by the interaction of CPT1C with other proteins. Different studies conducted by our group have described that, even though CPT1C does not have catalytic activity, it is able to modulate the activity of other proteins depending on malonyl-CoA sensing (Casas et al., 2020; Fadó et al., 2021; Miralpeix et al., 2021; Palomo-Guerrero et al., 2019).

Firstly, CPT1C was known to regulate LE/lysosome anterograde transport through its interaction with protrudin depending on the nutritional status of the cell, being this anterograde transport of LE/lysosomes crucial for proper axon growth (Palomo-Guerrero et al., 2019). Under normal nutrient conditions, CPT1C senses malonyl-CoA and enhances the transfer of kinesin-1 from protrudin to FYCO1 at the LE/lysosome membrane, hence favoring the plus-end transport of LE/lysosomes and axon growth. By contrast, under energy stress conditions CPT1C does not enhance the transfer of kinesin-1 to FYCO1, and in consequence, the anterograde transport of LE/lysosomes is not promoted, and axon growth arrested *(Figure 14)*. The interaction between CPT1C and protrudin occurs in both situations, but the nature of their interaction changes depending on malonyl-CoA sensing. Although protrudin was found to be an important effector of CPT1C, other mechanisms may also be involved. Notably, these results revealed for the first time the implication of malonyl-CoA in the regulation of LE/lysosome transport and gave insight into how axon growth is regulated by nutrients.
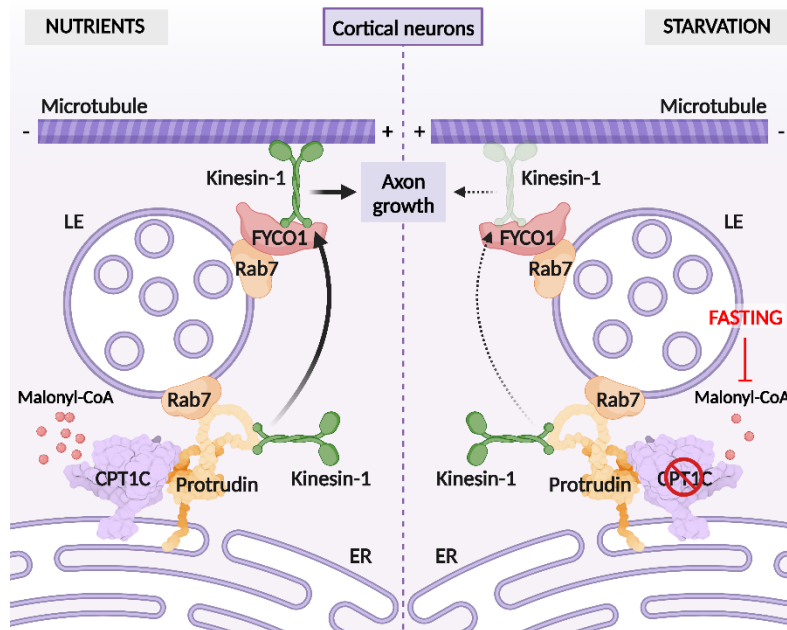
Figure 14. Model for the role of CPT1C in LE/Lys anterograde transport and axon growth. In normal nutrient conditions, CPT1C is bound to malonyl-CoA and its N-terminal domain acquires the folded conformation (Nα), which enhances the transfer of kinesin-1 from protrudin to FYCO1, which promotes the plus-end transport of LE/lysosomes and axon growth. However, under energy stress, such as glucose depletion or the activation of AMPK pathway, N-regulatory domain of CPT1C switches to its extended conformation (Nβ). In this state, CPT1C does not enhance the transfer of kinesin-1 to FYCO1, and in consequence, the anterograde transport of LE/lysosomes is not promoted, and axon growth arrested. Based on (Palomo-Guerrero et al., 2019). ER: Endoplasmic reticulum; LE: Late endosome.

Then, SAC1 was described as an interactor of CPT1C. On the one hand, CPT1C was found forming part of the AMPAR macrocomplexes at the ER of neurons together with SAC1 and ABHD6 (Brechet et al., 2017; Schwenk et al., 2012). On the other hand, CPT1C was found to regulate AMPAR trafficking through its interaction with the phosphatidylinositol-4-phosphate (PI(4)P) phosphatase SAC1 depending on nutrient sensing (Casas et al., 2020). Regarding the latter, CPT1C down-regulates SAC1 catalytic activity under normal nutrient conditions, which leads to the accumulation of PI(4)P at the TGN. This favors the trafficking of GluA1-containing AMPARs from the TGN to the PM through the secretory pathway. However, under low malonyl-CoA levels, such as glucose depletion, CPT1C-dependent inhibition of SAC1 is released, facilitating SAC1's translocation to ER-TGN contact sites to decrease TGN PI(4)P pools and trigger GluA1 retention at the TGN *(Figure 15)*. Since AMPAR trafficking is necessary for synaptic plasticity, this study shed light on how nutrients can affect synaptic function and cognition through the interplay of CPT1C.
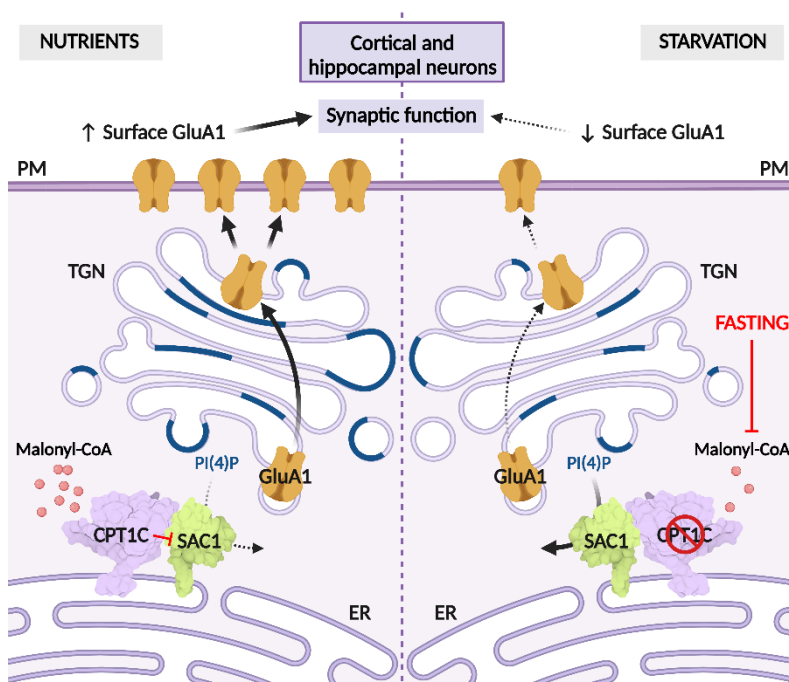
Figure 15. Model for CPT1C regulation of GluA1 trafficking. CPT1C and SAC1 form part of the AMPAR complex at the ER of neurons. In normal nutrient conditions, malonyl-CoA–bound CPT1C down-regulates SAC1 activity, allowing the accumulation of PI(4)P at the TGN. This favors the trafficking of GluA1-containing AMPARs from the TGN to the PM through the secretory pathway. In energy stress conditions that decrease malonyl-CoA levels, such as glucose deficiency, ER-TGN contacts are increased and CPT1C favors the transport of SAC1 to these junctions. At the same time, malonyl-CoA–free CPT1C releases its inhibition on SAC1 activity. This results in dephosphorylation of PI(4)P at the TGN by SAC1 in trans, which halts GluA1-containing AMPAR trafficking. Based on (Casas et al., 2020). ER: Endoplasmic reticulum; PM: Plasma membrane; TGN: Trans-Golgi network.

A subsequent study from our group confirmed the interaction of CPT1C with ABHD6 and revealed that CPT1C is a key regulator of ABHD6 activity depending on malonyl-CoA sensing (Miralpeix et al., 2021). Under normal conditions, CPT1C was found to inhibit ABHD6 hydrolase activity in both neuronal cells and in brain tissues from WT and CPT1C-KO mice. Conversely, overnight deprivation of food induced a significant increase in ABHD6 activity in both hypothalamic and hippocampal tissues of WT mice, whereas no differences were apparent in brain tissues from the CPT1C-KO mice, indicating that CPT1C inhibition of ABHD6 is blunted when malonyl-CoA levels drop. Furthermore, as ABHD6 is a hydrolase of the endocannabinoid 2-AG, the inhibitory effect of CPT1C on ABHD6 activity was found to impact 2-AG downstream signaling *(Figure 16)*. The importance of this interaction stands with ABHD6 playing a wide range of functions in both metabolic and neurological processes. CPT1C, as a negative regulator of ABHD6 activity, could therefore indirectly control all those functions and become an interesting target in combating ABHD6-related pathologies.
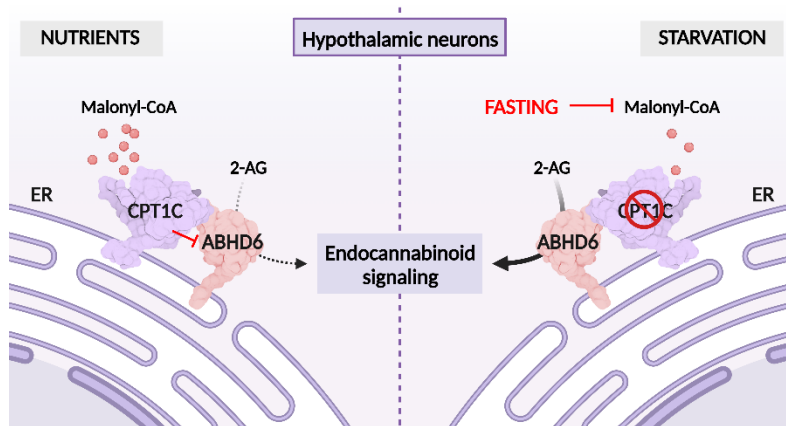
Figure 16. Model for CPT1C regulation of ABHD6 activity. Under normal conditions, CPT1C senses malonyl-CoA and inhibits ABHD6 activity in hypothalamic neurons, thus regulating 2-AG levels and endocannabinoid signaling. This regulation is affected in CPT1C-KO mice or under fasting conditions, where inhibition of ABHD6 is released thus increasing the hydrolysis of 2-AG. ER: Endoplasmic reticulum.

HYPOTHESIS

We hypothesize that CPT1C, through its interaction with ABHD6, regulates BMP metabolism and endolysosomal function in hypothalamic neurons in response to dietary FA. This regulation could be crucial for neuronal homeostasis and metabolic diseases such as DIO.

OBJECTIVES

To validate our hypothesis, the following objectives have been established:

1. To investigate the role of CPT1C in BMP metabolism through the regulation of ABHD6 activity.

2. To explore the consequences of CPT1C-mediated regulation of BMP levels on endolysosomal function.

3. To determine whether the roles of CPT1C on BMP metabolism and endolysosomal function are dependent on the nutritional status.

4. To elucidate the subcellular localization of CPT1C and ABHD6.

5. To characterize the structural motifs involved in both the CPT1C-ABHD6 interaction and the modulation of ABHD6 activity by CPT1C.

Objectives 1, 2 and 3 will be addressed in Chapter I, while objectives 4 and 5 will be covered in chapter II.

METHODOLOGY

1. Cell lines and procedures

GT1-7 (SCC116, Merck Millipore, Burlington, USA), HEK293T (kindly provided by Dr. Ramon Trullàs, IDIBAPS) and HeLa P (kindly provided by Dr. Harald Stenmark, Institute for Cancer Research, University of Oslo) cell lines have been used in this thesis. GT1-7 are mouse hypothalamic neuronal cells that have been mainly used to study the role of CPT1C on BMP metabolism and LE/Lys functionality (Chapter I). Otherwise, HEK293T and HeLa cells have been used for CPT1C-ABHD6 interaction studies and colocalization experiments (Chapter II), respectively.

GT1-7, HEK293T and HeLa cells were maintained in high-glucose Dulbecco's modified Eagle's medium (D5671, Sigma-Aldrich, Madrid, Spain) supplemented with 10% fetal bovine serum (FBS, FBS-12A, Labclinics, Barcelona, Spain), 1% Penicillin/Streptomycin (P0781, Sigma-Aldrich, Madrid, Spain) and 1% Glutamine (X0551, Labclinics, Barcelona, Spain). GT1-7 cells medium was also supplemented with 1mM sodium pyruvate. All cells were grown at 37ºC in a humidified atmosphere and 5% CO_2, were passed before reaching complete confluence and were regularly tested for mycoplasma contamination.

1.1. Gene editing by CRISPR-Cas9

The CRISPR-Cas9 system was used to generate WT and CPT1C-KO cells from the hypothalamic GT1-7 cell line. CRISPR-Cas is a microbial adaptive immune system that uses RNA-guided nucleases to cleave foreign genetic elements. Different CRISPR systems have been identified, being the CRISPR-Cas9 derived from *Streptococcus pyogenes* one of the best characterized and the one used in this thesis (Ran et al., 2013).

In the CRISPR-Cas9 system, the Cas9 nuclease promotes gene editing by stimulating a double-stranded break (DSB) at a target genomic locus *(Figure 17)*. Cas9 is targeted to genomic DNA by an sgRNA consisting of a 20-nt guide sequence. The guide sequence pairs with the DNA target, directly upstream of a requisite 5'-NGG adjacent motif (protospacer adjacent motif, PAM). There, Cas9 mediates a DSB around 3 bp upstream the PAM sequence. DBS is then repaired by non-homologous end joining which results in random indel mutations at the site of junction. Since DSB is guided to occur within a coding exon, it usually leads to frameshift mutations and the creation of a premature stop codon, resulting in gene KO.
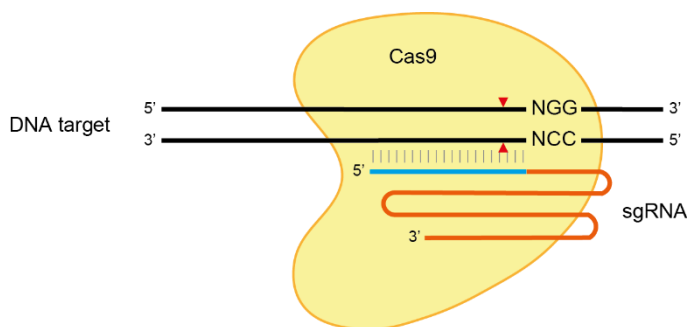
Figure 17. Scheme of the CRISPR-Cas9 system. The Cas9 nuclease (in yellow) is targeted to genomic DNA (in black) by an sgRNA consisting of a 20-nt guide sequence (in blue) and a scaffold (in orange). The guide sequence pairs with the DNA target directly upstream of the PAM sequence (NGG). Cas9 mediates a DSB ~3 bp upstream of the PAM sequence (red triangle) (Ran et al., 2013).

Based on that, we designed different sgRNAs to target the Cpt1c gene and cloned them into a CRISPR plasmid bearing the Cas9 nuclease. Then, since GT1-7 cells are not easy to transfect, we produced lentiviral particles containing the resultant CRISPR plasmids and infected them into GT1-7 cells to generate our hypothalamic cell model. The performed steps are further detailed below.

1.1.1. sgRNA design and plasmid construction

First, custom sgRNAs for Cpt1c were designed *in silico* via the online CRISPR Guide RNA Design Tool (https://www.benchling.com/crispr; Gene: Cpt1c (ENSMUSG00000007783)). The 20-nt guide sequences *(Table 1)* were selected depending on the on- and off-target scores given by the software.

Primer	Sequence (5'-3')	Purpose
mCpt1c_exon1_sgRNA-top	CACCGTTTGTGGACTCATTACACG	To clone sgRNA targeting the exon 1 of Cpt1c into lentiCRISPR v2.
mCpt1c_exon1_sgRNA-bottom	AAACCGTGTAATGAGTCCACAAAC	
mCpt1c _exon6_sgRNA-top	CACCgCATTTGCCAGCGCTGTAGCG	To clone sgRNA targeting the exon 6 of Cpt1c into lentiCRISPR v2; appended guanine and cytosine (complementary to appended guanine) in lowercase.
mCpt1c_exon6_sgRNA-bottom	AAACCGCTACAGCGCTGGCAAATGc	
mCpt1c _exon9_sgRNA-top	CACCGAACATCCTCTCATACTGGG	

mCpt1c_exon9_sgRNA-bottom	AAACCCCAGTATGAGAGGATGTTC	To clone sgRNA targeting the exon 9 of Cpt1c into lentiCRISPR v2.
mCpt1c_exon10_sgRNA-top	CACCgCACGTGGCTGTCTTCCACCG	To clone sgRNA targeting the exon 10 of Cpt1c into lentiCRISPR v2; appended guanine and cytosine (complementary to appended guanine) in lowercase.
mCpt1c_exon10_sgRNA-bottom	AAACCGGTGGAAGACAGCCACGTGc	

Table 1. sgRNAs used for targeting the Cpt1c gene by CRISPR-Cas9. All oligonucleotides were bought at Integrated DNA Technologies (IDT™).

Then, the sgRNA guide sequences were cloned into the expression plasmid lentiCRISPR v2 (52961, Addgene (Sanjana et al., 2014)) *(Figure 18)* following the method described in (Ran et al., 2013).
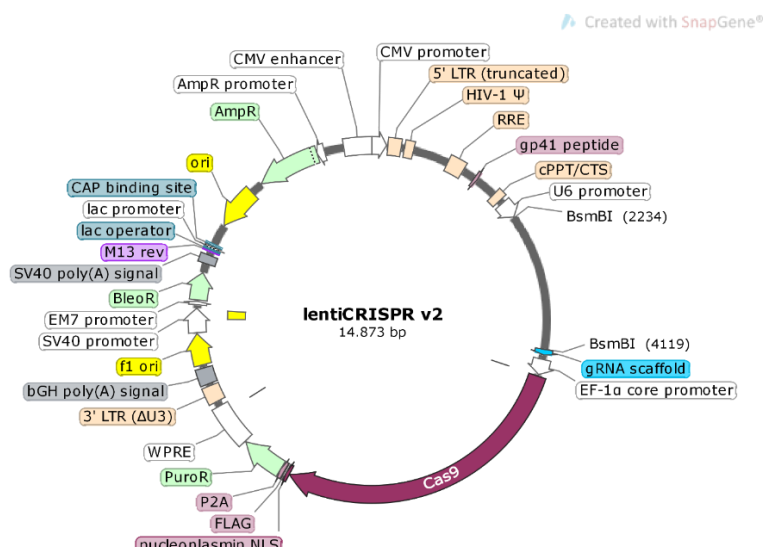
Figure 18. lentiCRISPR v2 plasmid structure. sgRNA guide sequences were cloned upstream the gRNA scaffold (in blue) using the BsmBI restriction enzyme. This plasmid contains, among others, the gene cassette for the Cas9 nuclease (in purple) and the puromycin resistance gene (in green). Map created with SnapGene® from the vector sequence (52961, Addgene).

In order to do that, each pair of oligos (top and bottom strands) were phosphorylated and annealed by mixing the following components and incubating the reaction in a thermocycler under the parameters detailed below *(Table 2)*.

Reaction mix		
Component	**Amount**	**Source or reference**
sgRNA top (100 μM)	1 μl	*Table 1*
sgRNA bottom (100 μM)	1 μl	*Table 1*
10X T4 DNA ligase buffer	1 μl	B69, Thermo Fisher Scientific, Waltham, USA
T4 Polynucleotide Kinase	1 μl	M0201, New England Biolabs, Ipswich, USA
ddH$_2$O	6 μl	
Total	10 μl	

Thermocycler conditions	
Temperature	**Time**
37 ºC	30 min
95 ºC	5 min
Ramp down to 25 ºC	5 ºC/min

Table 2. Reaction mix (up) and conditions (down) for annealing sgRNA top and bottom oligos.

Once the oligos were annealed and phosphorylated, they were diluted 1:200 in ddH$_2$O and cloned into the lentiCRISPR v2 vector at BsmBI. For each sgRNA, the ligation reaction described in *Table 3* was performed.

Reaction mix		
Component	**Amount**	**Source or reference**
lentiCRISPR v2	100 ng	52961, Addgene (Sanjana et al., 2014)
Diluted oligo duplex	2 μl	
10X FastDigest Buffer	2 μl	B64, Thermo Fisher Scientific, Waltham, USA
10 mM DTT	1 μl	
10 mM ATP	μl	
FastDigest BsmBI	1 μl	FD0454, Thermo Fisher Scientific, Waltham, USA
T4 ligase	0.5 μl	EL0014, Thermo Fisher Scientific, Waltham, USA
ddH$_2$O	to 20 μl	
Total	20	

Thermocycler conditions		
Temperature	**Time**	
37 ºC	5 min	x2
21 ºC	5 min	

Table 3. Reaction mix (up) and conditions (down) for cloning the sgRNA into the lentiCRISPR v2 vector at BsmBI.

Finally, the plasmids listed in *Table 4* were obtained.

Plasmid	Target	Application
CRISPR_EV	-	Generation of WT GT1-7 cells
CRISPR_exon1-mCpt1c	Exon 1 of Cpt1c	Generation of CPT1C-KO GT1-7 cells by disrupting the exon 1 of the Cpt1c gene
CRISPR_exon6-mCpt1c	Exon 6 of Cpt1c	Generation of CPT1C-KO GT1-7 cells by disrupting the exon 6 of the Cpt1c gene
CRISPR_exon9-mCpt1c	Exon 9 of Cpt1c	Generation of CPT1C-KO GT1-7 cells by disrupting the exon 9 of the Cpt1c gene
CRISPR_exon10-mCpt1c	Exon 10 of Cpt1c	Generation of CPT1C-KO GT1-7 cells by disrupting the exon 10 of the Cpt1c gene

Table 4. Plasmids used to generate WT and CPT1C-KO GT1-7 cells. WT cells were generated by infecting GT1-7 cells with the CRISPR plasmid empty vector (EV), and CPT1C-KO cells were generated by infecting GT1-7 cells with the CRISPR plasmid bearing sgRNA sequences targeting different exons of the Cpt1c gene.

1.1.2. Bacterial transformation

The different resulting plasmids were transformed by thermal shock into DH5α competent *E. coli* cells produced in our lab. 50 µl of DH5α were incubated with 5 µl of ligated construct on ice for 30 min. Heat-shock was carried out in a 42 ºC water bath for 75 s followed by 3 min incubation on ice. Then, 500 µl of SOC medium (2 % Tryptone, 0.5 % Yeast Extract, 10 mM NaCl, 2.5 mM KCl, 10 mM MgCl$_2$, 10 mM MgSO$_4$ and 20 mM glucose) was added, and cells were incubated for 1 h at 37 ºC under agitation. Finally, transformed cells were plated in antibiotic-containing LB plates and incubated at 37 ºC overnight.

1.1.3. Plasmid isolation and sequencing

After transforming the plasmids, an isolated colony of each plasmid was inoculated into 3 ml of liquid antibiotic-containing LB medium and incubated at 37 ºC overnight under agitation.

The isolation and purification of the plasmids was done using the NucleoSpin TriPrep (740966.250, Macherey-Nagel, Barcelona, Spain), and then the plasmids were verified by sequencing using the U6-Fwd primer (5'-3': GAGGGCCTATTTCCCATGATTCC).

1.1.4. Lentivirus production

For lentivirus production, HEK293T cells were seeded in 100 mm plates at 5.000.000 cells/plate. 24 h after seeding, cells were transfected with the corresponding CRISPR plasmid (15 µg per plate) and lentiviral packaging plasmids (5.3 µg of psPAX2 and 9.7 µg of pMD2.G per plate) using calcium-phosphate as later described in *Section 1.2*.

After 16 h of transfection, the medium of each plate was replaced carefully with 5 ml of fresh medium, and the supernatant was collected at 24 h, 40 h and 48 h post-transfection. Then, the supernatant was filtered using 0.45 µm filters (257201, DD Biolab, Barcelona, Spain) and lentivirus were concentrated by centrifugation at 3000 rcf and 4 ºC for 1 h using centrifugal concentrators (Vivaspin™ 20 (100.000 MWCO PES), Fisher Scientific, Madrid, Spain). Obtained lentivirus were then used to infect GT1-7 cells.

1.2. Cell transfection

For fluorescence resonance energy transfer (FRET) and ABHD6 Activity Assays HEK293T cells were transfected using calcium-phosphate, whereas for colocalization experiments HeLa cells were transfected using FuGENE® HD Transfection Reagent (E2312, Promega, Madison, USA) following the manufacturer's instructions.

Regarding the transfection by calcium-phosphate, the following procedure was performed. For each condition, a mix consisting of the corresponding plasmids, 0.1X TE (1 mM Tris-HCl pH 8.0 and 0.1 mM EDTA), buffered water (2.5 mM HEPES pH 7.3) and 2.5 M $CaCl_2$ was vigorously vortexed while 2X HBS (0.28 M NaCl, 0.05 M HEPES, 1.5 mM $Na_2HPO_4·7H_2O$ pH 7.0) was added drop by drop. Then, the mix was incubated for 15 min at room temperature and added evenly to each well. The volume of each reagent as well as the volume to be added per well is detailed in *Table 5*.

Component	Amount per 6-well plates	Amount per 10 mm plates
Plasmid(s)	X µg[1]	X µg[1]
0.1X TE	87 µl	433 µl
Buffered water	48 µl	242 µl
2.5 M CaCl$_2$	15 µl	75 µl
2X HBS	150 µl	750 µl
Total amount per well	300	1.5 ml

Table 5. Components and corresponding amounts for cell transfection using calcium-phosphate. Listed amounts are per well. [1]The number and quantity of plasmid(s) vary depending on the experiment.

1.3. MTT viability assay

The MTT viability assay was performed to assess cell viability when infecting the GT1-7 cells with the lentiviral vectors harboring CRISPR plasmids. The CRISPR plasmid used in this thesis contains a puromycin resistance gene (PuroR in *Figure 18*), enabling selection of infected cells by exposing them to puromycin. To test the lentiviral vectors in GT1-7 cells, the cells were infected with the different lentiviral vectors and selected with puromycin (P8833, Sigma-Aldrich, Madrid, Spain) 72 h post-infection. Another 72 hours later, the viability assay was conducted to determine the percentage of infected cells.

For the MTT viability assay, infected GT1-7 cells were incubated with MTT solution (11312727, Fisher Scientific, Madrid, Sapin) for 1 h at 37 ºC. The resulting formazan crystals were then dissolved in DMSO, and the absorbance was measured at 570 nm using a Synergy HT microplate reader (BioTek, Winooski, USA). Cell viability percentage was calculated by relativizing the absorbance of puromycin-treated cells to non-treated cells.

1.4. Cell treatments

1.4.1. Inhibition of ABHD6

To study how BMP levels changed depending on ABHD6 activity, inhibition of ABHD6 activity was conducted in GT1-7 cells incubated for 1 h with the specific hydrolase inhibitor WWL70 (10011213, Cayman Chemicals) (Blankman et al., 2007) at a final concentration of 10 µM. Incubation with 1 % DMSO (vehicle of WWL70) was used as control. After ABHD6 inhibition, both ABHD6 activity and BMP levels were analyzed by the 4-MUH assay *(Section 6)* and anti-BMP immunocytochemistry *(Section 8.1.1)*, respectively.

1.4.2. PG supplementation

PG supplementation was done in WT and CPT1C-KO cells using liposomes to study the correlation between BMP and cholesterol (McCauliff et al., 2019). Liposomes of 100 mol % phosphatidylcholine (PC) and 100 % mol PG were generated in collaboration of Dr. Ramon Barnadas at the Universitat Autònoma de Barcelona. PC liposomes were used as control.

PC and PG liposomes were prepared with soy PC (840054, Avanti Polar Lipids, Birmingham, USA) and 1,2-dioleoyl-sn-glycero-3-phospho-(1'-rac-glycerol) (DOPG) (840475, Avanti Polar Lipids, Birmingham, USA), respectively, by reverse phase evaporation. First, lipids were dissolved in 2:1 chloroform:methanol. Then, lipids were dried using a rotary evaporator and incubated under vacuum overnight. The remaining yield lipid film after evaporation was redissolved in phosphate-buffered saline (PBS). The mixture was agitated for 30 min to ensure the dissolution of lipids and then sonicated continuously for 2 min on ice so small unilamellar vesicles (30-40 nm) would form. Finally, liposomes were sterilized by extrusion through a 200 nm membrane.

For PG supplementation, WT and CPT1C-KO cells were incubated with 100 µM PC or PG liposomes for 24 h, and BMP and cholesterol levels were measured thereafter by immunofluorescence *(Sections 8.1.1 and 8.1.2)*.

1.4.3. Palmitate treatment

To explore the impact of the nutritional status of neurons in BMP-cholesterol metabolism, WT and CPT1C-KO cells were exposed to PA or OA. For PA and OA treatment, sodium palmitate (P9767, Sigma-Aldrich, Madrid, Spain) or sodium oleate (O3880, Sigma-Aldrich, Madrid, Spain) were complexed to free FA bovine serum albumin (BSA) (126575, Merck Millipore, Burlington, USA). First, palmitate or oleate were diluted in 0.1 M NaOH at 80 ºC for 5 min and free FA BSA was diluted at 100 mg/ml in 0.9% NaCl at 37 ºC. Then, the palmitate or oleate solution were mixed with the BSA solution and incubated for 5 min at 37 ºC. The same procedure was done to prepare unconjugated BSA as control. The final concentration for PA and OA was 3 mM and all PA-BSA, OA-BSA and BSA solutions were passed through 0.45 µm filters (257201, DD Biolab, Barcelona, Spain) before being supplemented to the cells.

To evaluate the response to PA and OA, cells were incubated with DMEM high glucose supplemented with 1% of FBS 1 h before treatment and then exposed to 300 µM palmitate-BSA for 16 h. BSA treatment was used as a control.

2. Expressing vectors

Different plasmid constructs required to overexpress proteins in FRET assays, the ABHD6 activity assay, and colocalization experiments have been developed.

The different backbones and constructs that have been used in this thesis and their applications are shown in *Table 6*.

Plasmid	Encoded proteins	Application	Source or reference
EYFP-N1	YFP	Backbone used for cloning YFP-tagged proteins and as empty vector (EV) in ABHD6 Activity Assay	6006-1, Takara Bio, Mountain View, USA
mTurquoise2-N1	mTurq2	Backbone used for cloning mTurquoise2-tagged proteins and as EV in ABHD6 Activity Assay	54843, Addgene, Teddington, UK
p_m_ABHD6_YFP	ABHD6-YFP	FRET and ABHD6 Activity Assay	(Miralpeix et al., 2021)
p_m_Δ8ABHD6_YFP	Δ8ABHD6-YFP	FRET and ABHD6 Activity Assay	This study
p_m_Δ29ABHD6_YFP	Δ29ABHD6-YFP	ABHD6 Activity Assay	This study
p_m_ABHD6ΔCter_YFP	ABHD6ΔCter-YFP	FRET and ABHD6 Activity Assay	This study
p_h_CPT1C_ mTurquoise2	CPT1C-mTurq2	FRET and ABHD6 Activity Assay	(Palomo-Guerrero et al., 2019)
p_h_Δ26CPT1C_ mTurquoise2	Δ26CPT1C-mTurq2	FRET and ABHD6 Activity Assay	This study
p_h_Δ52CPT1C_ mTurquoise2	Δ52CPT1C-mTurq2	FRET and ABHD6 Activity Assay	This study
pmturquoise_ h_calnexin	Calnexin-mTurq2	FRET	55539, Addgene, Teddington, UK
pcDNA3.1/myc-His A	-	Backbone used for cloning ABHD6-mCherry	V80020, Invitrogen
pcDNA3.1_myc-His_A_ m_ABHD6_mCherry	ABHD6-mCherry	Colocalization	This study
pcDNA3.1_myc-His_A_ h_CPT1C_EGFP	CPT1C-EGFP	Colocalization	Our lab

Table 6. Plasmids used in this thesis. YFP: yellow fluorescent protein. mTurq2: mTurquoise2. EGFP: enhanced green fluorescent protein.

The EYFP-N1, mTurquoise2-N1, which have the same basic structure *(Figure 19)*, and pcDNA3.1/myc-His A *(Figure 20)* vectors were cloned at BamHI as it is described below to obtain the following fusion proteins: Δ8ABHD6-YFP, Δ29ABHD6-YFP, ABHD6ΔCter-YFP, Δ26CPT1C-mTurquoise2, Δ52CPT1C-mTurquoise2 and ABHD6-mCherry. YFP- and mTurquoise2-tagged proteins were overexpressed in HEK293T cells to analyze which structural motifs of ABHD6 and CPT1C were involved in the interaction of both proteins. And mCherry- and EGFP-tagged proteins were overexpressed in HeLa cells for colocalization studies. All proteins were fluorescently tagged at the C-terminal end.
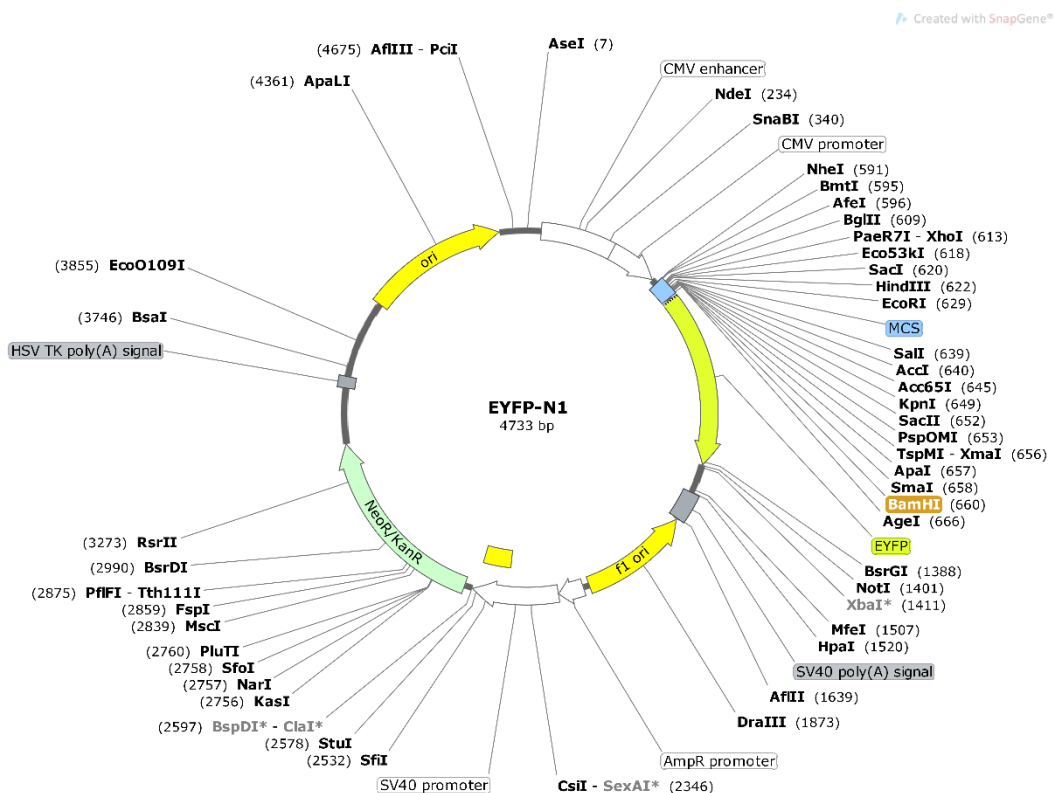
Figure 19. Structure of plasmid EYFP_N1 used in plasmid constructs. BamHI, the restriction site where the genes of the different proteins have been cloned, is highlighted. Image created with SnapGene® from the vector sequences.
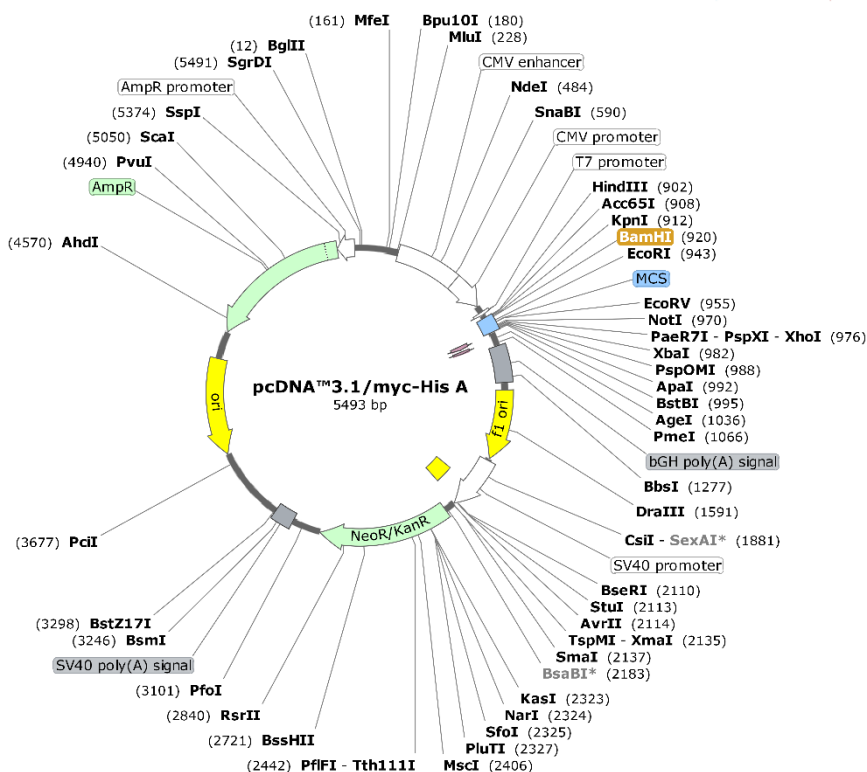
Figure 20. Structure of plasmid pcDNA3.1/myc-His A used in plasmid constructs. BamHI, the restriction site where the genes of the different proteins have been cloned, is highlighted. Image created with SnapGene® from the vector sequences.

2.1. DNA cloning

The gene cassettes for Δ8ABHD6, Δ29ABHD6, ABHD6ΔCter, Δ26CPT1C and Δ52CPT1C were amplified by polymerase chain reaction (PCR) from the corresponding plasmids p_m_ABHD6_YFP and p_h_CPT1C_mTurquoise2. And the gene cassette for ABHD6-mCherry was amplified in two steps: first, ABHD6 and mCherry were amplified separately by PCR from existing plasmids of our lab, and then, a second PCR was performed to obtain the complete cassette of ABHD6-mCherry. The primers used to amplify the different genes are described in *Table 7*.

Primer	Sequence (5'-3')	Purpose
Δ8ABHD6 F	CCGCGGGCCCGGGATCCATGTTTGTGATTGCGGG	Amplification of Δ8ABHD6 and Δ29ABHD6
Δ29ABHD6 F	CCGCGGGCCCGGGATCCATGTGGCCTTCAGCACTG	
Δ8/29ABHD6 R	GCGACCGGTGGATCCAAGTTCAGCTTCTTGTTGTCTGTGTT	

ABHD6ΔCter F	CCGCGGGCCCGGGATCCATGGATCTCGATGTGG	Amplification of ABHD6ΔCter
ABHD6ΔCter R	GCGACCGGTGGATCCAACAGGAGGAAAGACGCAAC	
Δ26CPT1C F	GCAGTCGACGGTACCGCGGGCCCGGGATCCATGGTGCTGCAGG AGATCTACCTCTCTGGC	Amplification of Δ26CPT1C and Δ52CPT1C
Δ52CPT1C F	GCAGTCGACGGTACCGCGGGCCCGGGATCCATGGGTGTGTTTC CTGCCAGCCCCCTCAG	
Δ26/52CPT1C R	GCTCACCATGGTGGCGACCGGTGGATCCAAGAAGTCGGTGGAT GTCATTGAGGCCTTGG	
pcDNA3.1-ABHD6 F[1]	CCGAGCTCGGATCCATGGATCTCGATGTGGTTAAC	Amplification of ABHD6 for ABHD6-mCherry
pcDNA3.1-ABHD6 R	CCTTGCTCACGGTGGCGACCGGTGGGTTCAGCTTCTTGTTGTCT G	
pcDNA3.1-mCherry F	GAAGCTGAACCCACCGGTCGCCACCGTGAGCAAGGGCGAGGA GG	Amplification of mCherry for ABHD6-mCherry
pcDNA3.1-mCherry R[1]	TGGACTAGTGGATCCCTACTTGTACAGCTCGTCC	

Table 7. Primers used to amplify the gene cassettes for ABHD6 and CPT1C. F: Forward, R: Revers. [1]Primers used in the second PCR of ABHD6-mCherry.

Gene cassettes were amplified using the PFU DNA polymerase (generated in our lab). The reagents used and the PCR conditions are detailed in *Table 8* (annealing and amplification conditions were adapted as required by base pair length and GC content of the primers).

Reaction mix		
Component	**Amount**	**Source or reference**
Forward primer (10 µM)	2 µl	*Table 7*
Reverse primer (10 µM)	2 µl	*Table 7*
10X PFU buffer	5 µl	Generated in our lab
10 mM dNTPs	1.5 µl	R0192, Thermo Fisher Scientific, Waltham, USA
50 mM MgCl$_2$	2 µl	
DNA template	50 ng	
PFU DNA polymerase	0.6 µl	Generated in our lab
ddH$_2$O	To 50 µl	
Total	50 µl	

Thermocycler conditions		
Cycle	**Temperature**	**Time**
1	95 ºC	2 min
2-30	95 ºC	30 s
	55-65 ºC	30 s
	72 ºC	2 min/kb
31	72 ºC	5 min
32	4 ºC	hold

Table 8. Reaction mix (up) and conditions (down) of PCR using PFU DNA polymerase.

After PCRs, the vectors were digested for 1h 30 min at 37 ºC by the restriction enzyme BamHI by mixing the components described in *Table 9*.

Component	Amount	Source or reference
Vector DNA	2 µg	*Table 6*
10X CutSmart® Buffer	5 µl	B6004, New England Biolabs, Ipswich, USA
BamHI	1 µl	R3136, New England Biolabs, Ipswich, USA
ddH$_2$O	To 50 µl	
Total	50 µl	

Table 9. Reaction mix for vector's digestion.

Then the digested vectors and amplicons were run and separated on an 1% agarose gel, purified with a Wizard® SV Gel and PCR Clean-up kit (Promega, Madison, USA) and cloned by homologous recombination using an In-fusion® HD cloning kit (102518, Takara Bio, Mountain View, USA).

2.2. Bacterial transformation

The recombination products were transformed into DH5α competent *E. coli* following the protocol explained in *Section 1.1.2*.

2.3. Plasmid isolation and sequencing

Isolation of plasmids was done as explained in *Section 1.1.3*. Then, the obtained plasmids were sequenced using the primers described in *Table 10*, and subsequent expression of recombinant proteins was confirmed by Western Blot.

Primer	Sequence (5'-3')	Purpose
YFP-BamHI_Seq F	CAGAGCTGGTTTAGTGAACCG	To verify the sequence of p_m_Δ8ABHD6_YFP, p_m_Δ29ABHD6_YFP, p_m_ABHD6ΔCter_YFP, p_h_Δ26CPT1C_mTurquoise2 and p_h_Δ52CPT1C_mTurquoise2
YFP-BamHI_Seq R	GTTTACGTCGCCGTCCAG	
hCPT1c_Seq F	GATGCTGTTCAGTTACCAGCGCTCCCTGCCAC	To verify the sequence of p_h_Δ26CPT1C_mTurquoise2 and p_h_Δ52CPT1C_mTurquoise2
pcDNA3.1-BamHI_Seq F	GCTTATCGAAATTAATACG	To verify the sequence of pcDNA3.1_myc-His_A_m_ABHD6_mCherry
mABHD6_Seq F	CGTGTGTCCTGCTGGCCTG	
pcDNA3.1-BamHI_Seq R	CGGGCCCTCTAGACTCGAG	

Table 10. Primers used for sequencing F: forward, R: revers.

3. Animals and procedures

Male (8–10 weeks old) CPT1C–KO mice and their WT littermates with the same genetic background (C57BL/6J) were used for the experiments (Pozo et al., 2017). Mice were housed on a 12 h/12 h light/dark cycle (light on at 8 am, light off 8 pm) in a temperature- and humidity-controlled room and were allowed free access to water and standard laboratory chow diet.

For the experiments in which mice were fed with fatty diets *(Table 11)*, mice were kept 1 week in the specific standard diet (SD) before the administration of the different fatty diets. Mice were randomly assigned to SD group or fatty diet group and diets were administrated for a period of 7 days.

Diet	% kcal from fat	Reference
Standard diet (SD)	10 %	D12450J, Research Diets, New Brunswick, USA
High-fat diet (HFD)	60 %	D12492, Research Diets, New Brunswick, USA
Monounsaturated fatty acid (MUFA) diet	49 %	D19121203, Research Diets, New Brunswick, USA. Customized (Fosch et al., 2023)
Saturated fatty acid (SFA) diet	49 %	D19121204, Research Diets, New Brunswick, USA. Customized (Fosch et al., 2023)

Table 11. Diets used in the experiments with animal models.

At the end of the studies mice were sacrificed by cervical dislocation and hypothalamus, hippocampus and liver were collected from each mouse for protein analyses and measurement of BMP levels or ABHD6 activity.

All animal care and experimental procedures were carried out in strict accordance with European guidelines (2010/63/EU) and Spanish legislation (BOE 252/34367-91, 2005) regulating animal research and were approved by the Clinical Research Ethics Committee of the Autonomous University of Barcelona (Procedure ref. CEEAH 5622_5623_5624_5881, Generalitat de Catalunya). All efforts were made to minimize animal suffering and to minimize the number of animals used.

4. Protein analyses

4.1. Protein extraction from cells and tissues

Total protein was obtained from cells or tissues, and all protein extraction process was performed at 4 ºC.

For cell protein extraction, cell medium was removed and cells were washed with ice-cold 1X PBS. Cells were then scraped and collected in 50-75 μl of lysis buffer, consisting of RIPA lysis buffer (20-188, Merck Millipore, Burlington, USA) supplemented with protease inhibitors (A32955, Thermo Fisher Scientific, Waltham, USA) and phosphatase inhibitors (32957, Thermo Fisher Scientific, Waltham, USA), in a ratio of 1/40 to RIPA buffer. Cell lysates were incubated for 1 h at 4 ºC and briefly sonicated, and protein extract was obtained by collecting the supernatant after centrifugation at 12000 rpm for 15 min at 4 ºC.

For tissue protein extraction, tissues were homogenated in screw tubes with ceramic beads and lysis buffer (composition above) using the homogenator Fast-Prep®-24 (MP Biomedicals, Irvine, USA). Homogenization was achieved by performing 3 cycles at 6.5 M/S in the Fast-Prep®-24, keeping the samples on ice between cycles. Then, homogenates were transferred into new tubes, placed in a wheel for 30 min at 4 ºC and sonicated briefly to break the remaining cell components. Afterwards, samples were centrifuged at 12,000 rpm for 15 min at 4 ºC and protein extract was obtained by collecting the supernatant into new tubes.

Finally, protein concentration from both cell and tissue samples was quantified by Pierce™ BCA Protein Assay Kit (23225, Thermo Fisher Scientific, Waltham, USA) following the manufacturer's instructions.

4.2. Western blot

Western blot technique was performed for the detection and quantification of proteins from cell and tissue samples.

First, protein samples were prepared to a final concentration of 0.5-1 µg/µl adding dH_2O and loading buffer (125 mM Tris pH 6.8, 25 % glycerol, 50 % SDS-20 %, 10 % β-mercapto-ethanol, 2.5 % dH2O and Bromophenol blue), and boiled at 95 ºC for 5 min.

Then, protein samples were loaded into the wells (10 µg/well) of a 10 % Criterion™ TGX™ Precast Midi Protein Gel (5671034, BioRad, Hercules, USA), and electrophoresis was run at 180-200 V for 60-90 min in electrophoresis buffer (25 mM Tris-HCl pH 8.3, 192 mM glycine and 0.05 % SDS-20 %).

After electrophoresis, proteins were transferred from acrylamide gels to PVDF membranes (IPVH00010, Merck Millipore, Burlington, USA). PVDF membranes were activated by immersion in 100 % methanol, and transfer was run at 400 mA for 90 min at 4 ºC in transfer buffer (25 mM Tris pH 8.3, 192 mM glycine and 10 % methanol). And once the proteins were transferred to the PVDF membranes, the membranes were rinsed with TBS-T and incubated for 1 h with blocking solution, consisting of 5 % fat-free powdered-milk diluted in TBS-T (0.1 % Tween 20 (P9416, Sigma-Aldrich, Madrid, Spain) in TBS (20 mM Tris, 137 mM NaCl and 3.9 mM HCl)).

Protein detection was done through the specific antibodies detailed in *Table 12*. First, membranes were incubated with primary antibodies overnight at 4 ºC under agitation. Then, the membranes were washed three times for 5 min with TBS-T under agitation and incubated with horseradish peroxidase-conjugated secondary antibodies for 1 h at room temperature under agitation. Membranes were washed again three times for 5 min with TBS-T under agitation before revealing.

Antibody	Host	Dilution	Source or reference
Anti mCPT1C	Rabbit	1:6000 in 2 % BSA	Kindly provided by Dr. Dolors Serra (Universitat de Barcelona)
Anti hCPT1C	Mouse	1:1000 in 2 % BSA	66072-1, Proteintech, Manchester, UK
Anti ABHD6	Rabbit	1:1000 in 2 % BSA	Kindly provided by Dr. Ken Mackie (Straiker et al., 2009)
Anti GFP	Mouse	1:20000 in 2 % BSA	66002-1, Proteintech, Manchester, UK
Anti β-actin	Mouse	1:10000 in 2 % BSA	MA191399, Thermo Fisher Scientific, Waltham, USA
Anti Rabbit – HRP	Goat	1:10000 in 2 % BSA	111-035-144, Jackson Immunoresearch, West Grove, USA

			515-035-003, Jackson Immunoresearch,
Anti Mouse – HRP	Goat	1:20000 in 2 % BSA	West Grove, USA

Table 12. Primary and secondary antibodies used for protein detection by western blot.

Finally, membranes were revealed using Luminata Forte Western HRP substrate (WBLUF0500, Merck Millipore, Burlington, USA). Images were collected by ChemiDoc (BioRad, Hercules, USA) and quantified by densitometry using Image Lab Software (BioRad, Hercules, USA).

5. Protein interaction

5.1. Sensitized emission FRET

FRET is a technique commonly applied to proof protein-protein interactions. FRET is a process of radiation-less energy transfer based on dipole-dipole interactions that can occur from an excited fluorescent molecule (donor) to a suitable acceptor molecule (acceptor) *(Figure 21A)*. The transfer of energy only occurs when the donor fluorescence emission spectrum overlaps with the acceptor excitation spectrum *(Figure 21B)* and donor and acceptor are within close proximity (usually <10 nm) (Hochreiter et al., 2019).
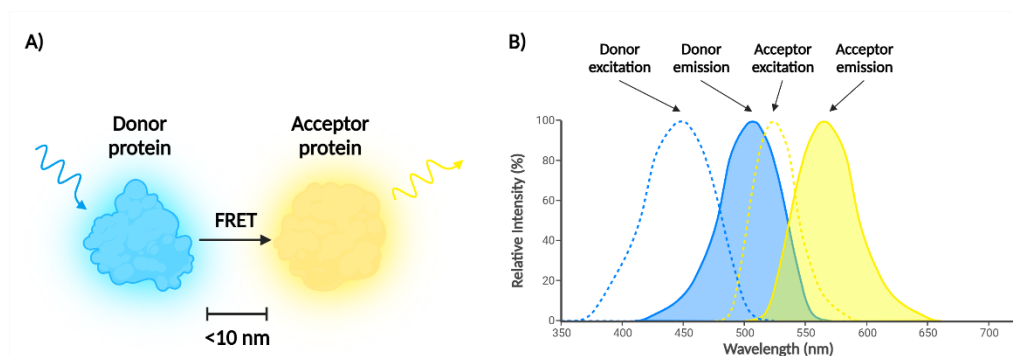
Figure 21. FRET diagram. A) Energy transfer from donor to acceptor protein if they are in close apposition (< 10 nm). B) Transfer of energy occurs when the donor emission spectrum overlaps with acceptor excitation spectrum.

There are different ways to determine FRET. The most frequently applied technique, named 3-filter FRET or sensitized emission FRET, is based on the measurement of three distinct combinations of excitation wavelengths and emission filters *(Figure 21)* (Hochreiter et al., 2019):

- Channel 1 (Ch1): donor detection channel combining donor-specific excitation with a donor-specific emission filter.
- Channel 2 (Ch2): FRET channel employing donor-specific excitation and an acceptor specific emission filter.

- Channel 3 (Ch3): acceptor channel using an acceptor-specific excitation and an acceptor-specific emission filter.

FRET is mostly used in microscopy but can be applied to other set-ups like fluorescence plate readers, which allow the assessment of FRET in entire live cell populations and allow plotting FRET-saturation curves. Here, we used the fluorescence plate reader approach, and the interaction of proteins was measured by FRET efficiency *(Formula below)*, which represents the total fraction of energy dissipated by the donor that is actually transferred to the acceptor.

$$FRET\ efficiency = \frac{Ch2}{Ch1} - \frac{Ch2\ for\ isolated\ donor}{Ch1\ for\ isolated\ donor}$$

For FRET sensitized emission saturation curves, HEK293T cells were seeded in 6-well plates and transiently co-transfected using calcium-phosphate (protocol described in *Section 1.2*) with both the donor protein (mTurquoise2-tagged protein) and the acceptor protein (YFP-tagged protein). Both proteins were transfected using a donor to acceptor ratio ranging from 0 to 10.

FRET assays were performed in live HEK293T cells 48 h after seeding based on the protocols conducted by Gemma Navarro's group (Navarro et al., 2009). Cells were collected from wells by resuspension in HBSS containing 1 % glucose and centrifuged at 3200 rpm for 5 min at room temperature. Then, cell pellets were resuspended in HBSS – 1 % glucose and protein concentration was quantified using a Bradford assay kit (Bio-Rad Protein Assay Dye Reagent Concentrate, 5000006, Bio-Rad, Hercules, USA) following the manufacturer's instructions. Finally, cell suspension (20 µg of protein) was loaded into black 96-well plates and fluorescence was read through 3 different channels in a Synergy HT microplate reader (BioTek, Winooski, USA) using excitation filters of 420/50 (Ch1 and Ch2) or 495/10 (Ch3) and emission filters of 485/20 (Ch1) and 530/25 (Ch2 and Ch3).

5.2. Proximity Ligation Assay

Proximity Ligation Assay (PLA) experiments were performed during the stay at Dr. Emily Eden's lab (Institute of Ophthalmology, University College London). PLA was used as a tool to quantify inter-organelle MCS. PLA utilizes complementary single-stranded DNA oligomers bound to secondary antibodies generated from different species that hybridize and complete a circular piece of DNA when the proteins of interest (membrane proteins on two different organelles) are in very close apposition (<40 nm), e.g., at MCS. These interactions can be detected by amplifying the circular DNA and adding fluorescent probes *(Figure 22)* (Ching et al., 2021). Here, PLA was used to quantify LE-ER MCS using the LE/Lys marker LAMP1 and the ER marker VAPA in WT and CPT1C-KO GT1-7 cells.
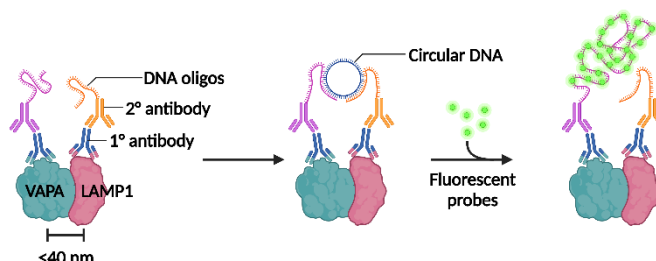
Figure 22. Proximity ligation assay diagram. The PLA probes (formed by single-stranded DNA oligomers bound to secondary antibodies) bind to the primary antibodies detecting the proteins of interest. If the proteins are in close apposition (<40 nm), the DNA probes hybridize to make a circular DNA, which can be amplified and visualized by adding fluorescent probes.

For the PLA experiments, WT and CPT1C-KO GT1-7 cells were cultured onto coverslips pre-coated with poly-L-Lysine (P4707, Sigma-Aldrich, Madrid, Spain) for 1 h at 37 ºC placed in wells of a 24-well plate. The day after seeding, cells were fixed with 4% paraformaldehyde (PFA) for 20 min at room temperature. Then PFA was quenched with 15 mM glycine for 10 min at room temperature, and cells were permeabilized in 0.05 % Triton (T8787, Sigma-Aldrich, Madrid, Spain) in PBS for 10 min on ice and blocked in 1 % BSA (10735078001, Roche, Basel, Switzerland) in PBS for 1 h at room temperature. After blocking, primary antibodies *(Table 13)* were incubated overnight at 4 ºC.

Antibody	Host	Dilution	Source or reference
Anti VAPA (4C12)	Mouse	1:100 in 1 % BSA	sc-293278, Santa Cruz Biotechnology, Dallas, USA
Anti LAMP1	Rabbit	1:200 in 1 % BSA	ab24170, Abcam, Cambridge, UK

Table 13. Primary antibodies used for PLA experiments.

The next day, PLA was performed using the Duolink® In Situ Red Starter Kit Mouse/Rabbit (DUO92101, Sigma-Aldrich, Sant Louis, USA) following the manufacturer's instructions and coverslips were mounted onto slides with ProLong™ Glass Antifade Mountant with NucBlue™ Stain (15808401, Thermo Fisher Scientific, Waltham, USA), and allowed to dry at 4 ºC. PLA images were acquired with a Leica TCS SP8 microscope and LAS X software.

6. Fluorescence-based ABHD6 activity assay

ABHD6 hydrolase activity was assessed by the 4-MUH-based activity assay developed and described by our group in (Miralpeix et al., 2021).

The ABHD6 activity assay is based on its natural capacity to hydrolyze 4-methylumbelliferyl-heptanoate (4-MUH) (M2514, Sigma-Aldrich, Madrid, Spain), a fluorogenic substrate whose

hydrolysis produces the fluorescent compound 4-methylumbelliferone (4-MU, λ_{ex} = 355 nm and λ_{em} = 460 nm) *(Figure 23)*.
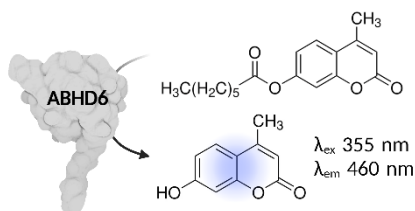

Figure 23. Principle of the fluorescence based ABHD6 activity assay. ABHD6 hydrolyses 4-MUH producing 4-MU, a highly florescent compound (excitation 355 nm; emission 460 nm).

This assay was conducted in both endogenous ABHD6-expressing models (GT1-7 cells and brain tissues) and ABHD6-overexpressing HEK293T cells.

6.1. 4-MUH assay for endogenous ABHD6 activity

Endogenous ABHD6 activity was measured in WT and CPT1C-KO GT1-7 cells and in brain tissue homogenates from WT and CPT1C-KO mice.

Regarding GT1-7 cells, they were plated onto 6-well plates and collected through trypsinization 48 h after seeding. After collection, cells were centrifuged at 3200 rpm for 5 min, resuspended in PBS to remove the remaining medium, and centrifugated again at 3200 rpm for 5 min. The resulting pellets were then frozen for 10 min at -80 ºC, resuspended in 100 µl of Tris-EDTA 50:1-mM buffer at pH 7.4, and briefly sonicated.

In the case of brain tissue, hypothalamus (6–8 mg) and hippocampus (11–12 mg) were quickly removed from mice after sacrifice and kept at 4 ºC for immediate processing. The tissue was then processed by dounce-homogenizing it in 200 µl of Tris-EDTA 50:1-mM buffer at pH 7.4, followed by a brief sonication.

Once processed, protein concentration from cell and tissue homogenates was quantified by Pierce™ BCA Protein Assay Kit (23225, Thermo Fisher Scientific, Waltham, USA) following the manufacturer's instructions.

The assay was performed in black 96-well plates. A total volume of 100 µl of Tris-EDTA 50:1-mM buffer at pH 7.4 containing 1 µg of protein from cell or tissue homogenates was added per well. The samples were then incubated with either WWL70 (a selective ABHD6 inhibitor) at a final concentration of 10 µM or DMSO (the vehicle of WWL70) for 30 min at 37 ºC. Subsequently, 4-MUH was added at a final concentration of 50 µM and fluorescence was immediately measured at 10-min intervals for a duration of 90-120 min using a Synergy H1 microplate reader (BioTek, Winooski, USA).

ABHD6 activity was calculated after subtracting the curve in the presence of the ABHD6 inhibitor WWL70, and 4-MU was used to conduct a standard curve to express ABHD6 activity as nmol/mg (Miralpeix et al., 2021).

6.2. 4-MUH assay for ABHD6-overexpressing cells

For the 4-MUH assay carried out in overexpressing cells, HEK293T cells were seeded on 6-well plates and transiently transfected with 3 µg per well of cDNAs encoding YFP, mTurquoise2, ABHD6-YFP, Δ29ABHD6-YFP, Δ8ABHD6-YFP, ABHD6ΔCter-YFP, CPT1C-mTurquoise2, Δ26CPT1C-mTurquoise2 or Δ52rCPT1C-mTurquoise2, alone or in combination, using calcium phosphate *(section 1.2)*. After 48h, cells were washed twice with ice-cold PBS and collected by resuspension in PBS. Once collected, cells were centrifuged at 3200 rpm for 5 min at 4 ºC. Pellets were then frozen for 10 min at -80 ºC, resuspended in 100 µl of Tris-EDTA 50:1-mM buffer at pH 7.4 and briefly sonicated.

Prior to MUH assay, protein concentration from cell and tissue homogenates was quantified by Pierce™ BCA Protein Assay Kit (23225, Thermo Fisher Scientific, Waltham, USA) following the manufacturer's instructions.

The assay was performed in black 96-well plates using 1 µg of protein in a total volume of 100 µl of Tris-EDTA 50:1-mM buffer at pH 7.4 per well. 4-MUH was added to each well at a final concentration of 50 µM and fluorescence was immediately measured at 5-min intervals for 30 min using a Synergy H1 microplate reader (BioTek, Winooski, USA).

ABHD6 activity was calculated after subtracting the curve of EV-expressing cells, and 4-MU was used to conduct a standard curve to express ABHD6 activity as nmol/mg (Miralpeix et al., 2021).

6.3. Substrate competition assay

To confirm that BMP is a substrate for ABHD6, we conducted a competitive substrate assay in HEK293T cells expressing ABHD6. This competitive assay was performed following the same procedure described in *Section 6.2*, with the exception that cell homogenates were incubated with BMP in a final concentration range from 0 to 500 µM for 20 min at 37 ºC before the addition of 4-MUH.

7. LC/MS analysis of BMP

BMP levels and composition were measured from hypothalamus, hippocampus and liver of WT and CPT1C-KO mice in collaboration with Dr. Robert Zimmermann at the University of Graz. WT and CPT1C-KO mice were exposed to SD or HFD for 7 days *(Section 3)*, sacrificed by

cervical dislocation and tissues were collected from each mouse, placed in dry ice and shipped to Dr. Robert Zimmermann for further processing. BMP analysis was conducted following the protocol described in (Grabner et al., 2020). Briefly, total lipids of weighed tissue explants were extracted using 4 ml chloroform-methanol containing butylated hydroxytoluene, acetic acid, and BMP as an internal standard. Extraction was performed under constant shaking for 90 min at RT and phase separation. Organic phase was dried under a stream of nitrogen and resolved in methanol/2-propanol/water for liquid chromatography-mass spectrometry (LC/MS) analysis. BMP species were measured using selected reaction monitoring, and the data were normalized and quantified using internal standards. The quantified results were expressed as nmol/g tissue.

8. Microscopy

8.1. Fluorescence microscopy

Fluorescence microscopy was used to determine the amount of BMP and cholesterol in cultured cells, to evaluate lysosomal activity and to determine the colocalization of proteins.

8.1.1. BMP quantification by immunocytochemistry

BMP levels were measured in WT and CPT1C-KO GT1-7 cells by immunocytochemistry. For these experiments, cells were cultured on 24-well plates onto coverslips pre-coated with poly-L-Lysine (P4707, Sigma-Aldrich, Madrid, Spain) for 1 h at 37 ºC. 24 h after seeding, or immediately after a treatment when specified, cells were fixed with 4% paraformaldehyde (PFA) for 15 min at 4 ºC and permeabilized in 0.05 % Saponin (84510, Sigma-Aldrich, Madrid, Spain) in PBS for 15 min at room temperature. Then, cells were incubated with the primary anti-LBPA antibody *(Table 14)* for 1 h 30 min at room temperature followed by incubation with the secondary antibody anti-mouse Alexa 633 *(Table 14)* for 1 h at room temperature. Both primary and secondary antibodies were washed three times with PBS before proceeding with the next steps. Finally, cell nuclei were stained with Hoechst (14530, Sigma-Aldrich, Madrid, Spain) diluted at 1:1000 in PBS, and coverslips were mounted onto slides using antifade Fluoromount-G® (0100-01, Southern Biotech, Birmingham, USA) and allowed to dry at 4 ºC. Images were acquired with a Leica DMi8 and LAS X software using the 63x objective.

8.1.2. Cholesterol quantification by staining

Free cholesterol was also measured in WT and CPT1C-KO GT1-7 cells by fluorescence microscopy. GT1-7 cells were cultured and fixed as described in *Section 8.1.1*. Fixed cells were incubated with glycine at 1.5 mg/ml in PBS for 10 min at room temperature to quench

the paraformaldehyde, and incubated afterwards with filipin at 0.05 mg/ml in PBS for 2 h. Then, coverslips were processed as described in the previous section.

8.1.3. Lysosomal Function by fluorescent dyes

Lysosomal function was assessed in WT and CPT1C-KO GT1-7 cells by the alteration of the lysosomal pH using LysoTracker Red DND-99 probe (L7528, Thermo Fisher Scientific, Waltham, USA) and by the activity of cathepsin B using the Magic Red kit (Immunochemistry Technologies, Bloomington, USA). In these experiments, cells were seeded on 24-well plates onto poly-L-Lysine pre-coated coverslips. Cells were incubated with either 50 nM LysoTracker or 1:250 Magic Red probes for 45 min at 37 ºC, and then washed twice with PBS. Following, cells were fixed, nuclei were counterstained and coverslips were processed as described in *Section 8.1.1*.

8.1.4. Colocalization of proteins by immunocytochemistry

Both the colocalization of CPT1C with ABHD6 and the colocalization of these proteins with organelle markers were studied in CPT1C- and ABHD6- overexpressing HeLa cells. HeLa cells were seeded on 24-well plates onto poly-L-Lysine pre-coated coverslips. The day after seeding, cells were transfected with 200 ng per well of cDNAs encoding CPT1C-EGFP and ABHD6-mCherry using FuGENE and fixed with PFA 48 h post-transfection. Following, cells were either mounted for imaging or immunostained with organelle markers. For immunostaining, cells were incubated with blocking solution (2.5 % goat serum (g-9023, Sigma-Aldrich, Madrid, Spain) and 0.05 % saponin (84510, Sigma-Aldrich, Madrid, Spain) in PBS) for 15 min at room temperature. Afterwards, cells were incubated with the primary anti-LAMP1 or anti-Calnexin antibody *(Table 14)* for 1 h at room temperature followed by incubation with the secondary antibody anti-rabbit Alexa 647 *(Table 14)* for 1 h at room temperature. Both primary and secondary antibodies were washed three times with PBS before proceeding with the next steps. Finally, coverslips were processed as described in *Section 8.1.1*. Colocalization was quantified using Manders coefficient.

Antibody	Host	Dilution	Source or reference
Anti LBPA (clone 6C4)	Mouse	1:1000 in PBS	MABT837, Sigma-Aldrich, Madrid, Spain
Anti LAMP1	Rabbit	1:1000 in 2.5 % goat serum / PBS	L1418, Sigma-Aldrich, Madrid, Spain
Anti Calnexin	Rabbit	1:2000 in 2.5 % goat serum / PBS	ab22595, Abcam, Cambridge, UK

Anti-mouse Alexa Fluor™ 633	Goat	1:1000 in PBS	A21052, Invitrogen, Waltham, USA
Anti-rabbit Alexa Fluor™ 647	Goat	1:1000 in 2.5 % goat serum / PBS	A21244, Invitrogen, Waltham, USA

Table 14. Primary and secondary antibodies used for immunocytochemistry.

8.2. Transmission electron microscopy (TEM)

TEM experiments were performed during the stay at Dr. Emily Eden's lab (Institute of Ophthalmology, University College London). TEM was done for studying endosome morphology and LE-ER MCS in WT and CPT1C-KO GT1-7 cells.

For TEM experiments, WT and CPT1C-KO GT1-7 cells were cultured onto coverslips pre-coated with poly-L-Lysine for 1 h at 37 ºC placed in wells of a 24-well plate. The day after seeding, cells were fixed in 2 % PFA/2 % Glutaraldehyde in 0.1 M sodium cacodylate buffer (AGR1501, Agar Scientific, Essex, UK) for 30min at room temperature, and post-fixed in 1 % osmium tetroxide (AGR1019, Agar Scientific, Essex, UK)/1.5 % potassium ferricyanide (P018, TAAB, Berkshire, UK) on ice for 1 h. Afterwards, cells were incubated in with UA-zero (AGR1000, Agar Scientific, Essex, UK) in dark for 1 h at room temperature, and dehydrated in ethanol following the sequence: 2 min in 70 % ethanol, 2 min in 90 % ethanol and 10 min in 100 % ethanol twice. Once dehydrated, cells were embedded in TAAB-812 resin by incubating them in 50 % Propylene Oxide (AGR1080, Agar Scientific)/50 % TAAB-812 resin for 1 h at room temperature followed by incubation in TAAB-812 resin for 1 h at room temperature. Finally, beam capsules were freshly filled with TAAB-812 resin, inverted onto coverslips and baked at 65 ºC overnight. The next day, baked capsules were plunged into liquid nitrogen to remove the coverslip and embedded samples were obtained from the beam capsules.

TAAB-812 resin: prepared by mixing 10 ml TAAB-812 (T022, TAAB, Berkshire, UK) with 9 ml dodecenylsuccinic anhydride (DDSA; AGR1051, Agar Scientific, Essex, UK), 12 ml methyl nadic anhydride (MNA; AGR1081, Agar Scientific, Essex, UK) and 0.8 ml Tri-Dimethylaminomethyl Phenol (DMP-30; AGR1065, Agar Scientific, Essex, UK) for 1-4 h rotating at room temperature.

Sample sectioning was performed using a Leica EM UC6 Ultramicrotome and cell sections of 70 nm were processed on a JEOL JEM-1400Plus transmission electron microscope.

Endosome area and ER-endosome MCS were analyzed using ImageJ Softwate (NIH, Wisconsin, USA). Contact sites were considered when apposing membranes were <30 nm apart, with no minimum length.

9. *In silico* modeling and energetic assessment

The structure of the complex formed by CPT1C and ABHD6 was modelled *in silico* to elucidate the potential regions involved in the interaction of both proteins. These studies were performed by Nostrum Biodiscovery. Detailed methodology can be found in the final report provided by the company *(Appendix I)*.

10. Data and statistical analyses

Data processing and statistical analyses were performed using Prism 9.0 (GraphPad Software). All results are expressed as mean ± SD. The number of replicates for each experiment is indicated in the figure caption. Student's t test was used to compare two groups and multiple comparisons were analyzed by one- or two-way ANOVA followed by Bonferroni's post hoc correction. Kinetics parameters were analyzed using nonlinear regression with variable slope and the Michaelis–Menten model, and compared by the extra sum-of-squares F-test. $P < 0.05$ was considered statistically significant.

RESULTS

Chapter I

Study of the role of CPT1C in BMP metabolism and endolysosomal function

In this chapter we aim to elucidate the role of hypothalamic CPT1C in BMP metabolism and endolysosomal function through the modulation of ABHD6 activity, and to determine whether this role depends on lipid sensing. To address these questions, we use the GT1-7 mouse hypothalamic neuronal cell line, which endogenously expresses both CPT1C and ABHD6, as well as WT and CPT1C-KO animal models.

In hypothalamic GT1-7 cells, we delete CPT1C using CRISPR-Cas9 technology to investigate how CPT1C regulates ABHD6 activity, BMP levels, cholesterol homeostasis, and endolysosomal morphology and activity. We also examine if these effects of CPT1C are impaired after exposure to FA. Then, WT and CPT1C-KO animal models are used to validate the role of CPT1C in BMP metabolism in the context of lipid overload from a more physiological perspective.

Importantly, the studies of endosome morphology and endosome MCS were conducted during the three-month research stay at Dr. Emily Eden's lab (Institute of Ophthalmology, University College London).

1. Generation of the hypothalamic cell models: WT and CPT1C-KO GT1-7 cells

To elucidate the implications of CPT1C in BMP metabolism, we knocked-out the gene of CPT1C from GT1-7 cells by using the CRISPR-Cas9 system. This system uses RNA-guided nucleases to promote gene KO (Ran et al., 2013), so in order to delete CPT1C from GT1-7 cells efficiently, we designed and tested 4 different plasmids bearing different sgRNA sequences to target different coding regions of CPT1C.

Generation of WT and CPT1C-KO GT1-7 cells was performed in two steps: i) lentiviral infection of GT1-7 cells with the different CRISPR plasmids (CRISPR_EV for WT cells, and CRISPR_exon1-mCpt1c, CRISPR_exon6-mCpt1c, CRISPR_exon9-mCpt1c and CRISPR_exon10-mCpt1c for CPT1C-KO cells); and ii) selection of infected cells by puromycin *(Figure 24)*.
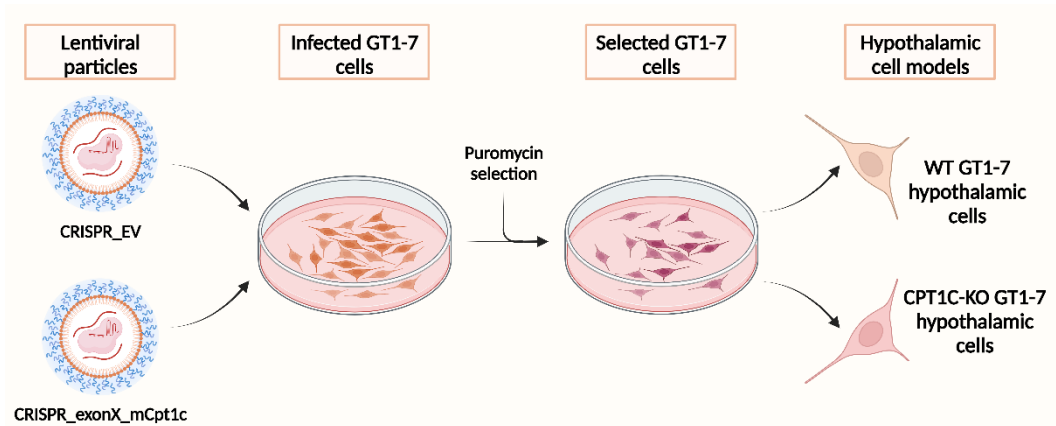
Figure 24. CRISPR workflow. Lentiviral particles containing CRISPR plasmids were used to generate the WT and CPT1C-KO hypothalamic neuronal cells. GT1-7 cells were infected with lentiviral vectors for 72 h. Then, selection of infected cells was performed by incubation with puromycin for other 72h. Infection of cells with CRISPR_EV was performed to obtain WT GT1-7 cells, whereas infection of cells with CRISPR plasmid targeting either Cpt1c exons was conducted to obtain CPT1C-KO GT1-7 cells.

The CRISPR plasmid contains a puromycin resistance gene that allows selection of cells that have been infected with the plasmid. To determine the optimal dose of puromycin required to effectively eliminate uninfected cells following lentiviral infection of CRISPR plasmids, we first tested puromycin resistance in non-infected GT1-7 cells. In order to do that, we exposed the cells to increasing concentrations of puromycin ranging from 0 to 5 µg/ml for 72 h, and then determined cell survival by doing an MTT viability assay. The results showed that 0.5 µg/ml was the lowest dose that killed almost all the non-infected cells *(Figure 25A)*. Therefore, 0.5 µg/ml was the dose of puromycin used to select the cells after lentiviral infection.

After determining the optimal puromycin dose for cell selection following lentiviral infection, we tested, for each CRISPR plasmid, the amount of virus needed to successfully infect all the cells. For that, GT1-7 cells were seeded in 24-well plates at a final concentration of 100,000 cells/well and infected with different volumes of virus, ranging from 0 µl to 12 µl. Then, infected cells were selected 72 h post-infection using 0.5 µg/ml puromycin and, another 72 h later, cell survival was assessed by an MTT viability assay to elucidate the volume of virus that infected the cells most efficiently. In all cases, the lowest amount of virus needed to infect all the cells was 2 µl per 100,000 cells *(Figure 25B-F)*. This dose was used in the following experiments.
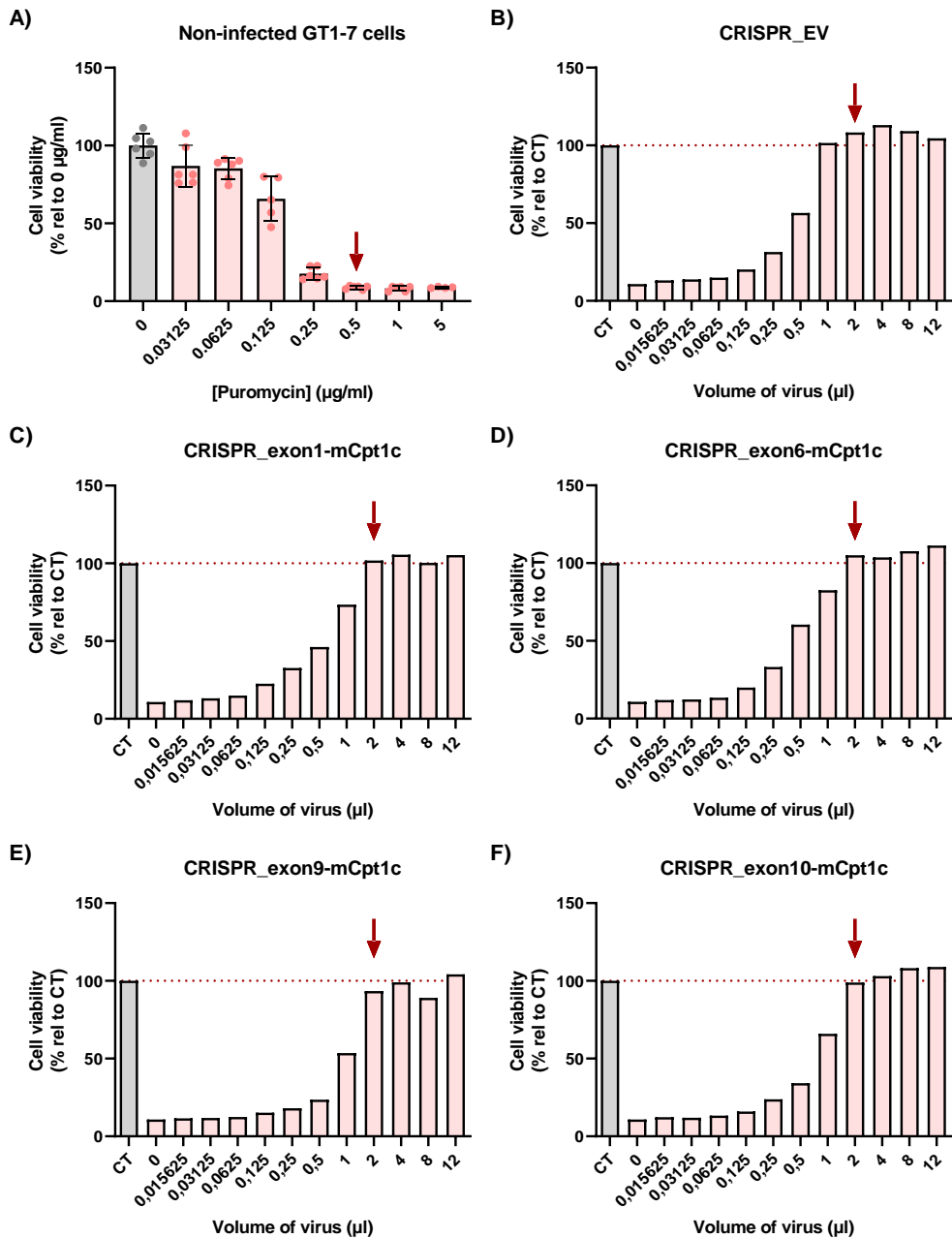
Figure 25. Cell viability after puromycin selection in non-infected and infected GT1-7 cells. A) MTT viability assay in non-infected GT1-7 cells after 72 h incubation of ranging doses of puromycin. Data are shown as mean ± SD (n ≥ 4 from 2 independent experiments); B-F) MTT viability assay in GT1-7 cells after infection with the different CRISPR plasmids and selection with 0.5 µg/ml puromycin. Non-infected and non-puromycin treated cells were used as control (CT). The red dotted line indicates 100% cell survival. Dara is shown as unique values (n = 1). CT: control.

GT1-7 cells were infected with lentivirus (2 µl per 100,000 cells) containing different plasmids: the empty one and the ones bearing the sgRNA sequences for exon 1, 6, 9 and 10 of Cpt1c gene. 72 h post-infection, GT1-7 cells were selected by 0.5 µg/ml puromycin for at least another 72 h. After that period of time, the efficiency of the different sgRNA sequences to KO Cpt1c was evaluated by analyzing CPT1C expression by Western Blot. Non-infected and non-puromycin treated GT1-7 cells were used as control. Results showed that targeting exon 6 resulted in the best KO of CPT1C by decreasing its expression to 27% *(Figure 26)*. The remaining CPT1C expression after targeting exons 6, 9 or 10 could be attributed to infected cells in which only one of the two alleles of the Cpt1c gene was KO, resulting in the sustained expression of CPT1C in those cells. Interestingly, when exon 1 was targeted, CPT1C protein expression was not affected, probably because exon 1 is a non-coding region of the Cpt1c gene (Price et al., 2002).

In line with the obtained results, the CRISPR_EV and the CRISPR_exon6-mCpt1c plasmids were the ones used to generate the WT and the CPT1C-KO hypothalamic cells, respectively.
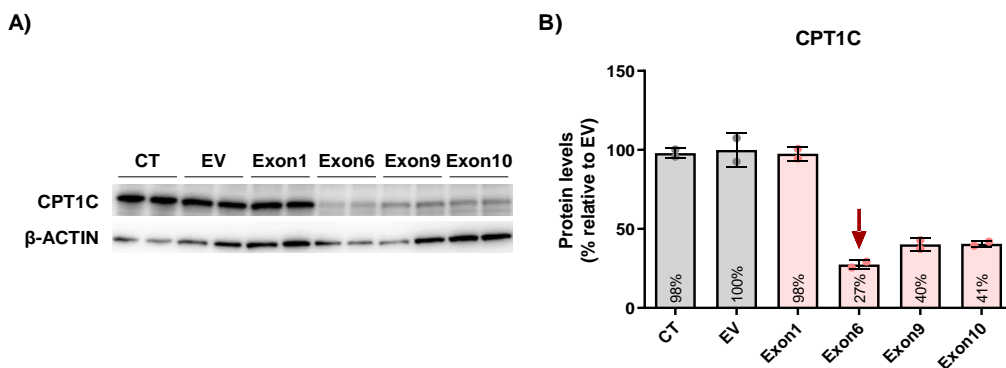
Figure 26. Expression of CPT1C in GT1-7 cells after lentiviral infection of CRISPR plasmid. A) Immunoblotting of CPT1C and β-actin. B) Immunoblot quantification of CPT1C. Data are shown as mean ± SD (n = 2 from 1 experiment). CT: control; EV: Empty vector.

2. Cell model validation

WT and CPT1C-KO hypothalamic cell models originated by the CRISPR-Cas9 technology were used to study the role of CPT1C on BMP metabolism. Our group previously demonstrated that CPT1C interacts with ABHD6 and inhibits its hydrolase activity (Miralpeix et al., 2021), so firstly we measured the ABHD6 activity by the 4-MUH assay to validate our model. As expected, ABHD6 activity was increased in CPT1C-KO cells *(Figure 27A-B)*. Afterwards, we analyzed if CPT1C deletion impaired the expression of ABHD6, and our results showed that there were no significant differences on ABHD6 protein levels after deleting CPT1C *(Figure 27C-E)*. Altogether, these results confirm that CPT1C modulates ABHD6 activity and that the

observed changes in ABHD6 activity are due to lack of inhibition by CPT1C rather than changes in protein expression.
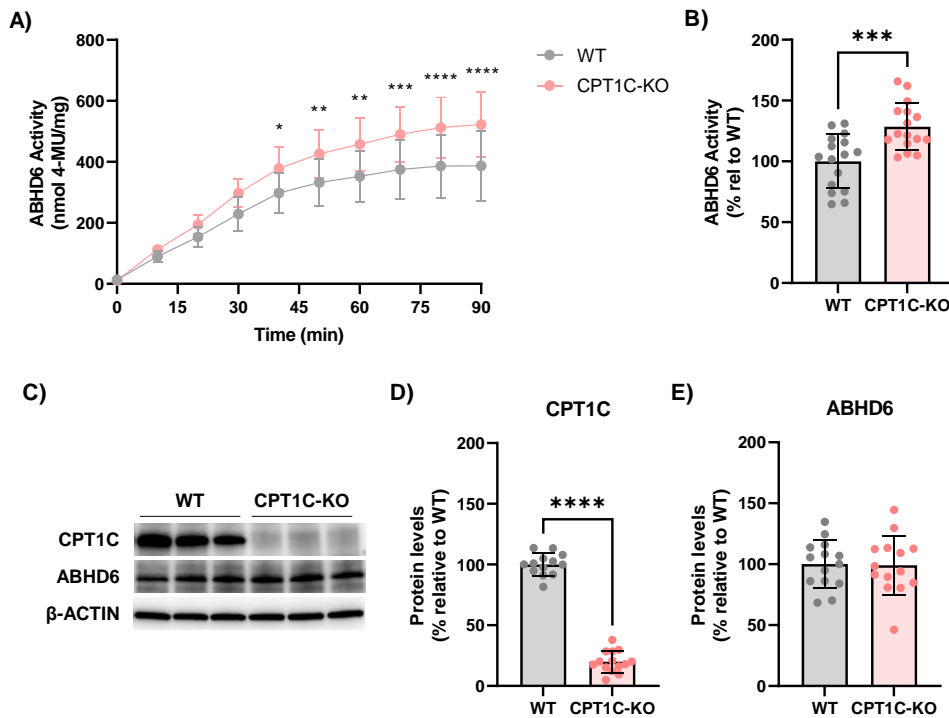
Figure 27. ABHD6 activity and expression in WT and CPT1C-KO GT1-7 cells. A-B) Kinetics (A) and quantification (B) of ABHD6 activity in WT and CPT1C-KO cells. Quantification of ABHD6 activity was calculated from the AUCs of WT and CPT1C-KO cells (n = 16 from 5 independent experiments). C) Representative image from immunoblotting of CPT1C, ABHD6 and β-actin in WT and CPT1C-KO cells. D-E) Immunoblot quantification of CPT1C and ABHD6 (n ≥ 13 from 5 independent experiments). Data are shown as mean ± SD. *$p < 0.05$, **$p < 0.01$, ***$p < 0.001$, ****$p < 0.0001$ vs WT. Statistical significance was determined by two-way ANOVA followed by Bonferroni's post hoc correction (A) and by t-student test (D-E).

3. CPT1C regulates BMP metabolism through modulation of ABHD6 activity

3.1. BMP levels depend on ABHD6 activity

The group of Dr. Zimmermann has previously demonstrated the role of ABHD6 in BMP catabolism (Grabner et al., 2019; Pribasnig et al., 2015). Since we observed significant changes on ABHD6 activity after deletion of CPT1C, we further explored the role of CPT1C in BMP metabolism.

We first confirmed the BMP hydrolase activity of ABHD6. In order to do that, we performed a competitive substrate assay in ABHD6-overexpressing HEK293T cells. We measured the 4-MUH hydrolysis while adding increasing concentrations of BMP. In accordance with what was expected, BMP displaced 4-MUH hydrolysis in a concentration-dependent manner, indicating that ABHD6 was hydrolyzing BMP instead of 4-MUH *(Figure 28)*.
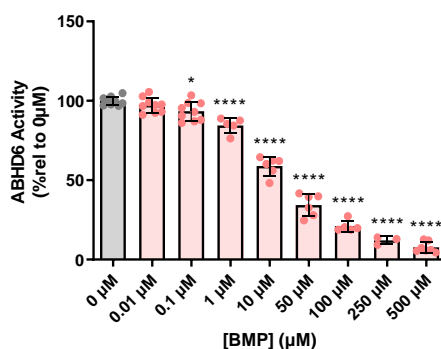
Figure 28. BMP competition with 4-MUH in ABHD6-overexpressing HEK293T cells. ABHD6 activity is measured in function of 4-MUH hydrolysis at t = 10 min after adding increasing concentrations of BMP in HEK293T cells overexpressing ABHD6 (n ≥ 3 from 3 independent experiments). Data shown are means ± SD. *$p < 0.5$, ****$p < 0.0001$ vs 0 µM. Statistical significance was determined by one-way ANOVA followed by Bonferroni's post hoc correction.

Afterwards, we proceeded to investigate how changes in ABHD6 activity affected BMP levels. To accomplish that, we modulated the hydrolase activity of ABHD6 in WT GT1-7 cells using its inhibitor, WWL70, and measured BMP levels thereafter. Notably, our findings showed that 1 h incubation with 10 µM WWL70 efficiently decreased ABHD6 activity in WT cells *(Figure 29A-B)*. Moreover, that decrease in ABHD6 activity was accompanied by an increase in BMP levels *(Figure 29C-D)*. These results, then, provide evidence for the dependence of BMP levels on ABHD6 activity in our hypothalamic model.
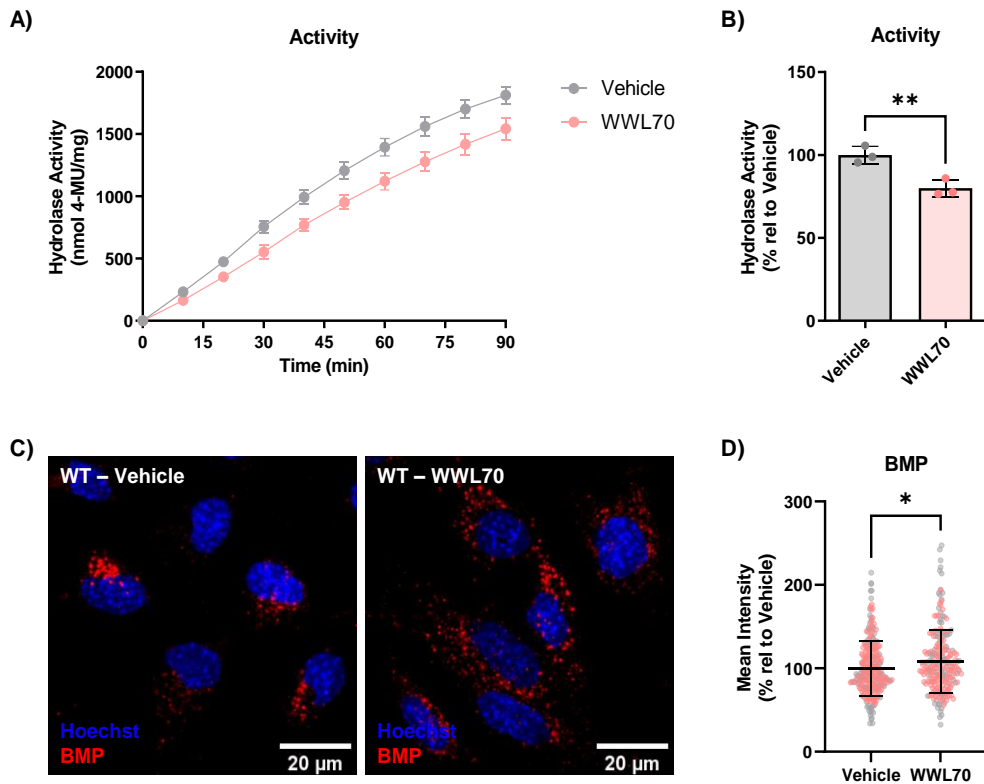
Figure 29. Modulation of ABHD6 activity results in changes in BMP levels in WT GT1-7 cells. A-B) Kinetics (A) and quantification (B) of hydrolase activity in WT cells after ABHD6 inhibition. WT cells were incubated with 10 µM WWL70 for 1 h and then processed for the 4-MUH assay. Quantification of hydrolase activity was calculated from the AUCs of WT cells incubated with vehicle or WWL70 (n = 3 from 1 experiment). C) Representative confocal images of BMP immunocytochemistry in WT cells incubated with vehicle or WWL70. D) Quantification of BMP levels per cell after treatment with WWL70 (n > 200 from 2 independent experiments represented in two different colors). Data are shown as mean ± SD. *p < 0.05, **p < 0.01. Statistical significance was determined by t-student test.

3.2. BMP levels in CPT1C-KO GT1-7 cells

Since CPT1C-KO GT1-7 cells had increased ABHD6 activity *(see Section 2)*, and ABHD6 is partly responsible for BMP hydrolysis (Pribasnig et al., 2015), we next measured the BMP levels of WT and CPT1C-KO cells by immunocytochemistry. As expected, BMP levels were significantly decreased in CPT1C-KO cells *(Figure 30)*.
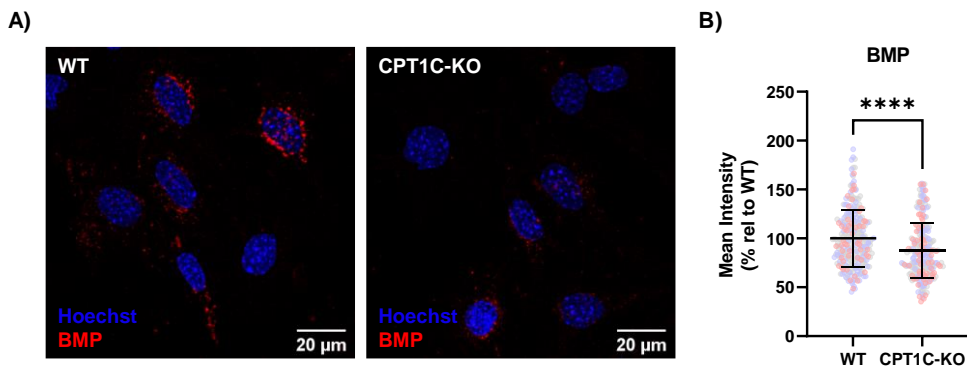
Figure 30. BMP levels in WT and CPT1C-KO GT1-7 cells. A) Representative confocal images of BMP immunocytochemistry in WT and CPT1C-KO cells. B) Quantification of BMP levels per cell in WT and CPT1C-KO cells (n > 200 from 3 independent experiments represented in three different colors). Data are shown as mean ± SD. ****p < 0.0001. Statistical significance was determined by t-student test.

The reduction in BMP levels observed in CPT1C-KO cells was probably associated with the increase in ABHD6 activity. To investigate this, we assessed if inhibiting ABHD6 activity in CPT1C-KO cells could restore BMP levels. As shown in *Figure 31*, inhibition of ABHD6 activity using WWL70 led to the restoration of BMP levels in CPT1C-KO cells, suggesting that the decreased levels observed in CPT1C-KO cells were a result of increased ABHD6 activity.
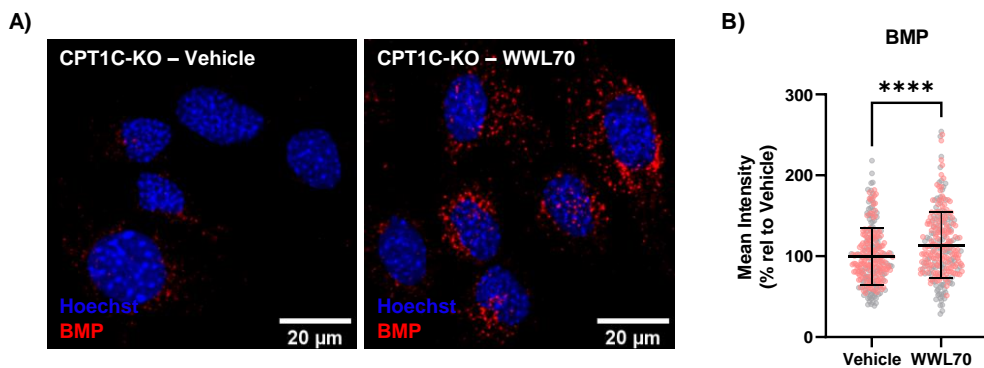
Figure 31. BMP levels after ABHD6 inhibition in CPT1C-KO GT1-7 cells. A) Representative confocal images of BMP immunocytochemistry in CPT1C-KO cells incubated with vehicle or 10 µM WWL70 for 1 h. B) Quantification of BMP levels per cell after treatment with WWL70 (n > 200 from 2 independent experiments represented in two different colors). Data are shown as mean ± SD. ****p < 0.0001. Statistical significance was determined by t-student test.

Taken together, these findings confirm the role of ABHD6 activity in controlling BMP levels and demonstrate that, in hypothalamic cells, CPT1C regulates BMP levels through ABHD6.

4. Cholesterol levels in CPT1C-KO GT1-7 cells

4.1. CPT1C-KO GT1-7 cells show lower intracellular cholesterol levels than WT cells

Different studies have provided evidence of a close correlation between cholesterol and BMP levels (Chevallier et al., 2008; Kobayashi et al., 1999; McCauliff et al., 2019). Consistently, when we assessed intracellular cholesterol levels by filipin staining in our hypothalamic cell lines, we observed that CPT1C-KO cells had lower intracellular cholesterol levels compared to WT cells *(Figure 32)*.
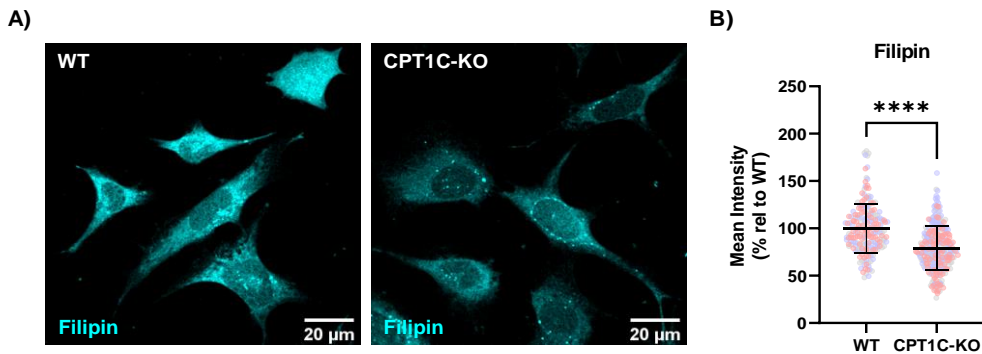
Figure 32. Cholesterol levels in WT and CPT1C-KO GT1-7 cells. A) Representative confocal images of Filipin staining in WT and CPT1C-KO cells. B) Quantification of filipin intensity per cell in WT and CPT1C-KO cells (n > 200 from 3 independent experiments represented in three different colors). Data are shown as mean ± SD. ****p < 0.0001. Statistical significance was determined by t-student test.

4.2. CPT1C-KO GT1-7 cells exhibit an impaired response to PG supplementation

Even though our results suggested a relationship between BMP and cholesterol levels, the dependence of cellular cholesterol on BMP levels was further confirmed by inducing the accumulation of BMP and subsequently analyzing the cholesterol levels in WT and CPT1C-KO cells. BMP enrichment was achieved by supplementing the cells with its biosynthetic precursor PG (McCauliff et al., 2019), and PC was used as a control. As expected, both BMP and intracellular cholesterol levels were reduced in CPT1C-KO cells compared to WT cells after incubation with control liposomes, made of 100 % PC *(Figure 33)*. Regarding PG supplementation, results in *Figure 33 (panels A and C)* show that incubation of the cells with 100 % PG liposomes led to the accumulation of BMP in both WT and CPT1C-KO cells. However, cellular cholesterol content increased in WT cells but remained unchanged in CPT1C-KO cells following PG supplementation *(Figure 33B, D)*. In summary, the results show that modulation of BMP levels leads to changes in intracellular cholesterol in WT cells, as previously described in Chevallier et al. (2008), but not in CPT1C-KO-cells. This suggest that CPT1C-regulation of cholesterol levels is not directly dependent on BMP.
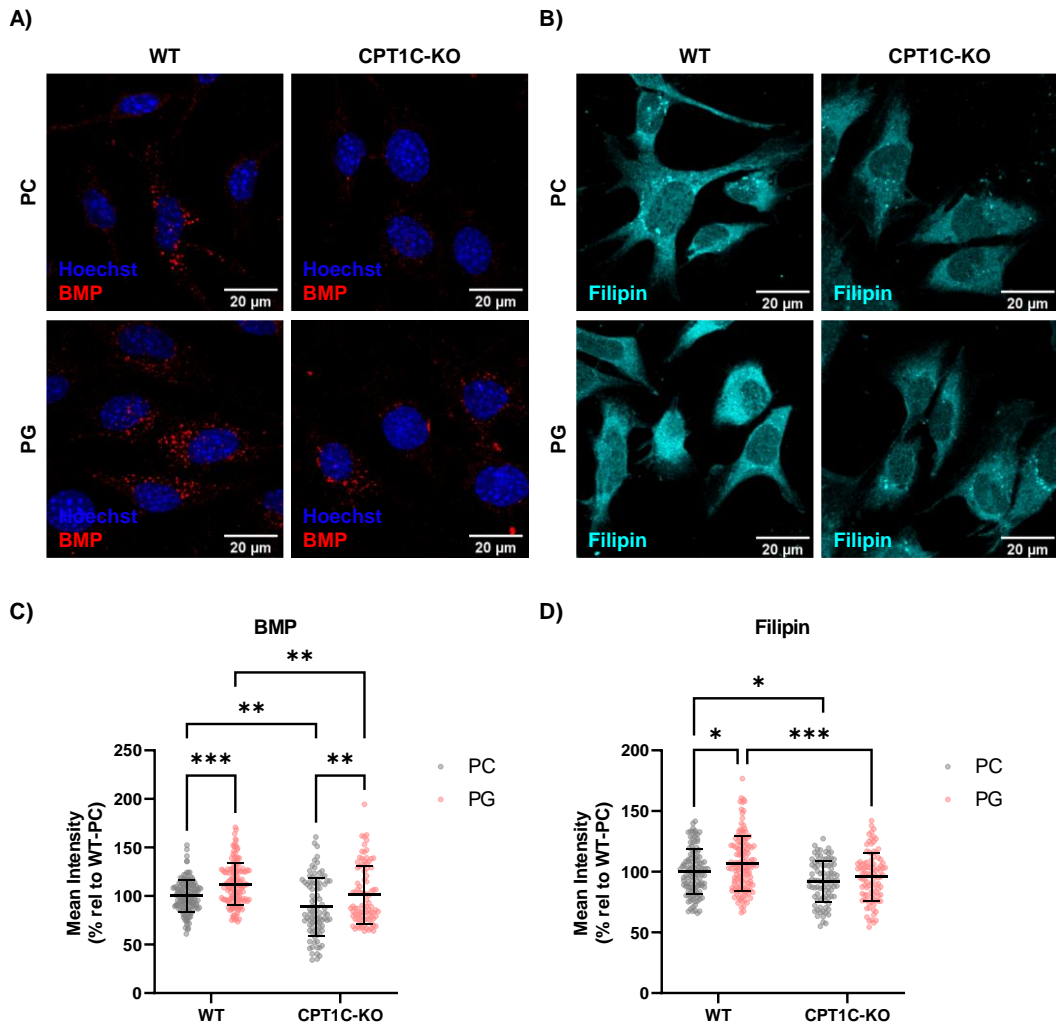
Figure 33. Response to PG supplementation in WT and CP1C-KO GT1-7 cells. A-B) Representative confocal images of BMP immunocytochemistry (A) and filipin staining (B) in WT and CPT1C-KO cells after supplementation with 100 µM PC or PG liposomes for 24 h. C-D) Quantification of BMP (C) and filipin (D) intensity per cell (n > 80 from 1 experiment). Data are shown as mean ± SD. *p < 0.05, ** p < 0.01, ***p < 0.001, ****p < 0.0001. Statistical significance determined by two-way ANOVA followed by Bonferroni's post hoc correction.

5. CPT1C-KO GT1-7 cells have smaller and more immature endosomes than WT cells

BMP is enriched in ILVs of LE, and has been characterized by its role to favor the formation of ILVs in these organelles (Pribasnig et al., 2015). Moreover, several studies have reported that agents that perturb cellular BMP caused cholesterol defects together with

morphological change of LEs (Chen et al., 2023; Chevallier et al., 2008; Kobayashi et al., 1999; Makino et al., 2006).

We have investigated the morphology of endosomes and endolysosomes from WT and CPT1C-KO cells by analyzing both the maturity of the endosomal population and the size of the endosomes and endolysosomes by conventional TEM. Identification and categorization of these organelles were based on their morphological features (i.e., presence of ILVs in EE and LE and presence of multilaminar structures), as represented in *Figure 34A*. In order to examine the maturity of endosomes, we looked for endosomes in different cell sections and catalogued them as early EE or LE depending on the ILVs density. The ones containing a high density of ILVs were considered as LE whereas the ones with very few ILVs were considered as EE. Then, the percentage of LE to EE across the endosomal population was calculated. The higher amount of LE versus EE, the more mature the endosomal population was considered.
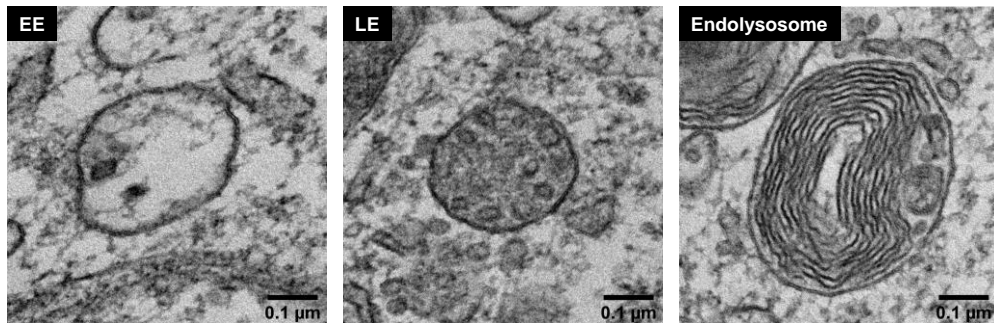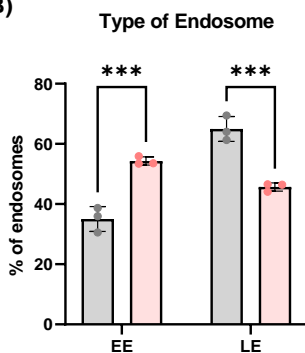
Figure 34. Analysis of endosome and endolysosome morphology in WT and CPT1C-KO GT1-7 cells by TEM. A) Representative electron microscopy images of an early endosome (EE), a late endosome (LE) and an endolysosome. B) Proportion of EE and LE within the analyzed endosomal population (n = 3 independent experiments). C) Area of EE, LE and endolysosomes of WT and CPT1C-KO cells (n > 50 from 3 independent experiments represented in three different colors). Data are shown as mean ± SD. **p < 0.01, ***p < 0.001, ****p < 0.0001. Statistical significance was determined by two-way ANOVA followed by Bonferroni's post hoc correction (B) and by t-student test (C).

Regarding the maturity of endosomes, our findings indicate that CPT1C-KO cells, which exhibit lower levels of BMP, contain a higher proportion of EE and a lower proportion of LE than WT cells *(Figure 34B)*, suggesting that CPT1C-KO cells are characterized by a more immature endosomal population compared to WT cells. Among the multiple mechanisms of ILV formation and endosome maturation identified, the BMP-driven is a crucial one (Gruenberg, 2020; Matsuo et al., 2004). Hence, the lower BMP content of CPT1C-KO cells could be the cause of the immaturity observed in their endosomal population. Nevertheless, the potential contributions of other mechanisms cannot be dismissed.

Regarding the size, we observed that the endosomal population in CPT1C-KO cells exhibited smaller EE, LE and endolysosomes in comparison to WT cells *(Figure 34C)*. The endosomes undergo a multitude of changes during the maturation process, including the exchange of membrane components, movement towards the perinuclear area, and changes in size (Huotari & Helenius, 2011). Therefore, the reduced size of endosomes observed in CPT1C-KO cells could serve as an indicator of their immaturity.

6. CPT1C is involved in the regulation of LE-ER contact sites formation

As previously reported, CPT1C is located at the ER (Casals et al., 2016) and ABHD6 co-localizes with LE/lysosomes and the ER, at the cytosolic side of membranes, while BMP is enriched in the ILVs of LE (Pribasnig et al., 2015). Altogether, it seems that the interaction of CPT1C with ABHD6 takes place in the membrane of the ER, and that ABHD6 is able to hydrolyze BMP when the ILVs, which are very dynamic vesicles, back-fuse with the limiting membrane of LE and BMP becomes accessible. Since this proposed model would imply MCS between the ER and the MVB, we decided to examine those contact sites in our hypothalamic model.

Within each endosomal population (EE, LE and endolysosomes), we assessed the proportion of endosomes that established MCS with the ER, mitochondria, or remained without contact with other organelles by conventional TEM. We considered MCS when the distance between membranes were less than 30 nm. Representative examples of a LE in contact or not with the ER are shown in *Figure 35A*.

After processing all the images, no significant differences were observed between WT and CPT1C-KO cells regarding MCS between EE and ER *(Figure35B)*. However, notable differences were found between the two cell types in the latter maturity stages of endosomes. CPT1C-KO cells exhibited less LE-ER and endolysosome-ER MCS and showed a more predominant population of LE and endolysosomes that remained without contact with organelles, in contrast to WT cells *(Figure 35C, D)*.

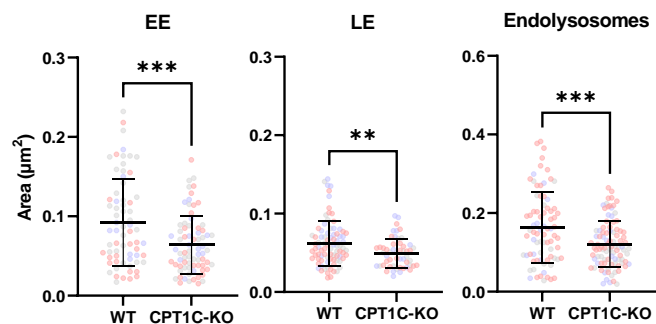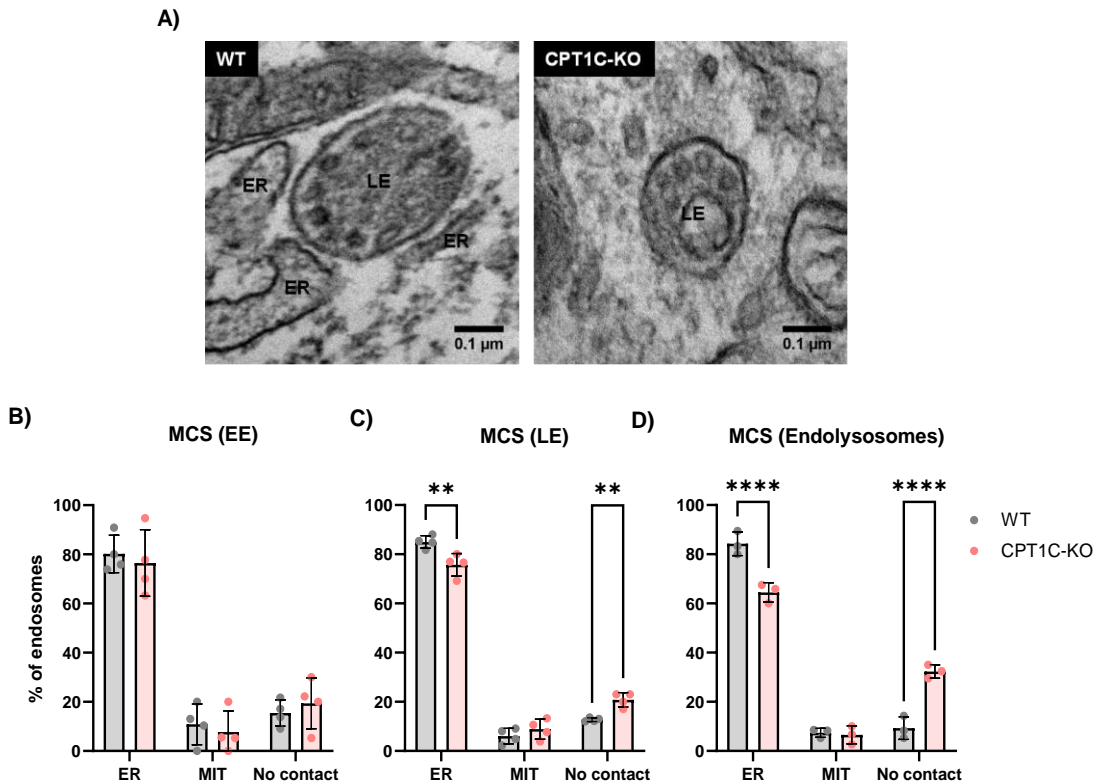**Figure 35. Analysis of endosome:ER contact sites in WT and CPT1C-KO GT1-7 cells by TEM.** A) Representative electron microscopy images of a LE in contact with the ER in a WT cell, and an LE with no contact in a CPT1C-KO cell. B-D) Proportion of EE (B) LE (C) and endolysosomes (D) in contact with ER, mitochondria or with no contact in WT and CPT1C-KO cells (n ≥ 3 independent experiments). Data are shown as mean ± SD. **p < 0.01, ****p < 0.0001. Statistical significance was determined by two-way ANOVA followed by Bonferroni's post hoc correction. ER: endoplasmic reticulum; MIT: mitochondria.

These results were confirmed when LE/lysosomes-ER MCS were quantified by PLA. In these experiments, the interaction between LAMP1, a marker of LE and lysosomes (Huotari & Helenius, 2011), and VAPA, a marker of ER (Eden, 2016), was examined in both WT and CPT1C-KO cells under basal conditions. The red dots observed in *Figure 36A* correspond to the sites of interaction between LAMP1 and VAPA, thus indicating the points of contact between LE/lysosomes and the ER. When quantifying the number of dots per cell, it was observed that the CPT1C-KO cells had less LE/lysosomes-ER contact sites compared to WT cells *(Figure 36A-B)*.
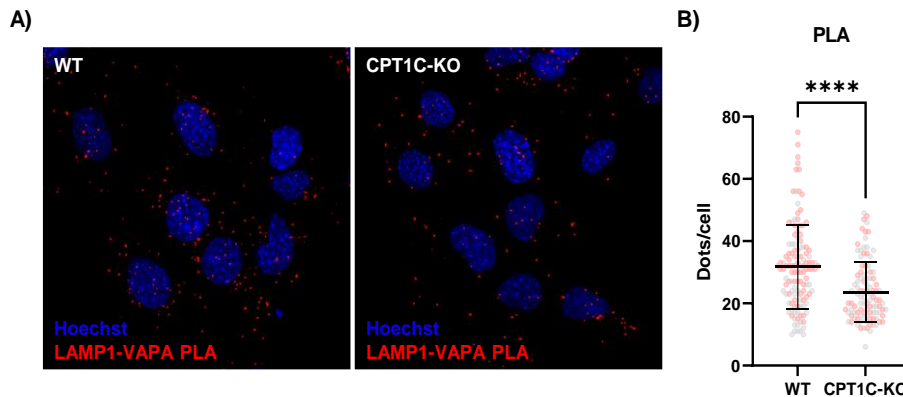
Figure 36. MCS between LE/lysosomes and ER in WT and CPT1C-KO GT1-7 cells by PLA. A) Representative confocal images of PLA experiment in WT and CPT1C-KO cells. B) Quantification of red dots per cell in WT and CPT1C-KO cells (n > 100 from 2 independent experiments represented in two different colors). Data are shown as mean ± SD. ****p < 0.0001. Statistical significance was determined by t-student test.

These findings indicate that CPT1C plays a role in the formation of MCS between the ER and LE/lysosomes. However, these results do not fully elucidate or exclude the necessity of these contacts for the hydrolysis of BMP.

7. CPT1C-KO GT1-7 cells have impaired lysosomal activity

Lysosomal size has been previously described as a morphological readout of the functionality of these organelles, ultimately influencing cellular homeostasis (de Araujo et al., 2020). Since our previous results showed a decrease in size of endolysosomes of CPT1C-KO cells compared to WT cells *(see Section 5)*, we further investigated the functionality of these organelles in our hypothalamic models.

We assessed lysosomal function by measuring the lysosomal pH using the LysoTracker Red DND-99 probe and the activity of cathepsin B using the Magic Red kit. LysoTracker is a cell permeable weak base dye that exhibits acidotrophic properties and accumulates in acidified organelles, commonly used for the analysis of lysosomal acidification (te Vruchte et al., 2015). The Magic Red kit, on the other hand, uses a permeable cathepsin substrate that, once hydrolyzed, liberates membrane-impermeable fluorescent cresyl violet within the organelles that contain a catalytically active cathepsin B (Pryor, 2012).
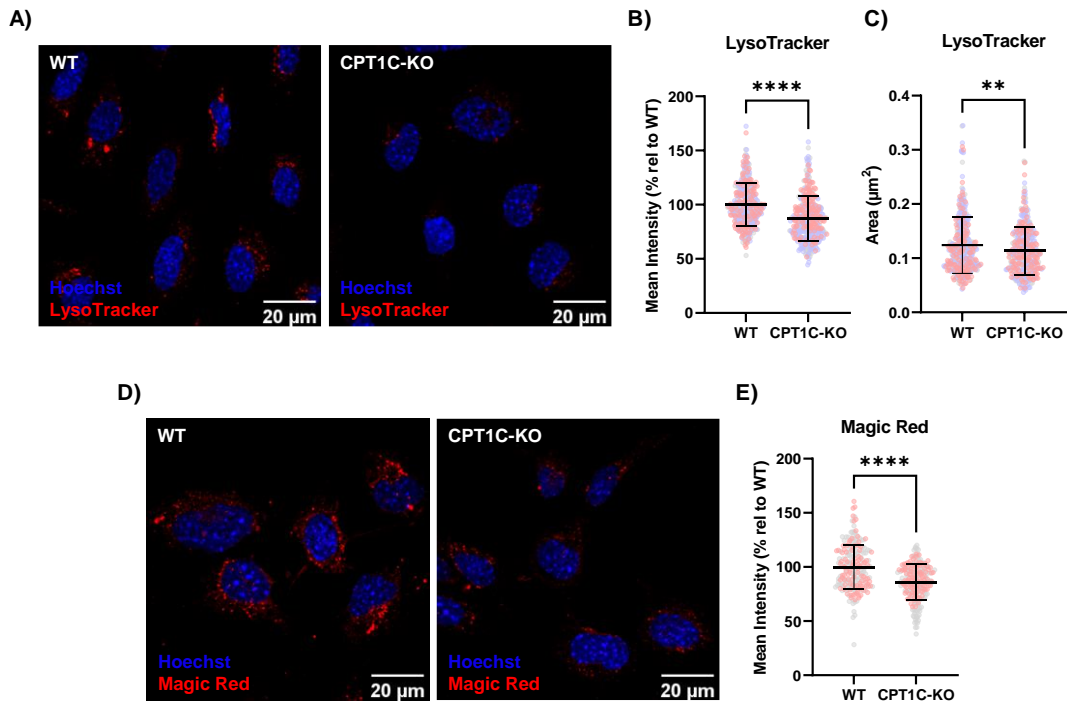
Figure 37. Lysosomal activity in WT and CPT1C-KO GT1-7 cells. A) Representative confocal images of LysoTracker dye in WT and CPT1C-KO cells. B-C) Quantification of LysoTracker average fluorescence intensity (B) and LysoTracker dots size (C) in WT and CPT1C-KO cells (n > 350 from 3 independent experiments represented in three different colors). D) Representative confocal images of Magic Red dye in WT and CPT1C-KO cells. E) Quantification of Magic Red intensity per cell in WT and CPT1C-KO cells (n > 200 from 2 independent experiments represented in two different colors). Data are shown as mean ± SD. **p < 0.01, ****p < 0.0001. Statistical significance was determined by t-student test.

As shown in *Figure 37*, experiments performed in WT and CPT1C-KO cells indicate that the deletion of CPT1C was associated with a decrease in both LysoTracker and Magic Red fluorescence intensity compared to WT cells *(Figure 37A, B, D, E)*. Additionally, in accordance with the data obtained from the conventional TEM experiments, the acidic organelles were smaller in CPT1C-KO cells than in WT cells *(Figure 37C)*. Collectively, these findings suggest that CPT1C plays a crucial role in preserving the homeostasis of the endocytic system.

8. CPT1C regulation of BMP metabolism and endolysosomal function is influenced by the nutritional status of the cell

8.1. CPT1C regulation of ABHD6 activity and BMP levels is impaired by PA

We have previously described that the negative regulation of ABHD6 activity by CPT1C is sensitive to the nutritional status of the cell (Miralpeix et al., 2021). Moreover, hypothalamic CPT1C has been characterized as a key mediator of lipid sensing in response to saturated or unsaturated LCFA (Fosch et al., 2023). According to this statement, we wanted to elucidate if the role of CPT1C regulating BMP levels and further endolysosomal activity was dependent on LCFA sensing.
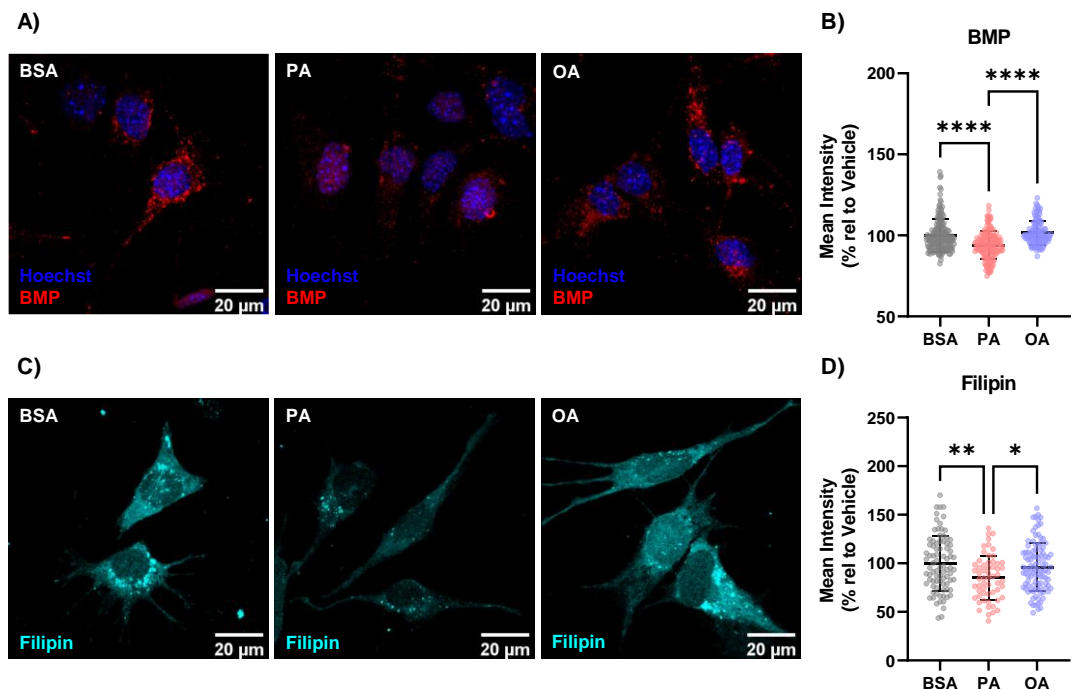
Figure 38. Response of WT GT1-7 cells to PA or OA in terms of BMP and cholesterols levels. A-B) Representative confocal images of BMP immunocytochemistry (A) and quantification of BMP levels per cell (B) in WT cells after 16 h treatment with BSA, 300 μM PA or 300 μM OA (n > 100 from 1 experiment). C-D) Representative confocal images of filipin staining (C) and quantification of filipin intensity per cell (D) in WT cells after 16 h treatment with BSA, 300 μM PA or 300 μM OA (n > 50 from 1 experiment). Data are shown as mean ± SD. *$p < 0.05$, **$p < 0.01$, ****$p < 0.0001$. Statistical significance was determined by one-way ANOVA followed by Bonferroni's post hoc correction.

First of all, we assessed whether BMP levels fluctuated in a context of saturated or unsaturated LCFA overload. We exposed WT cells to PA (saturated LCFA) or OA (unsaturated LCFA) for 16 h and then measured BMP levels by immunocytochemistry. The obtained data

showed that our hypothalamic cells responded differently to PA and OA. When cells were exposed to PA, BMP levels decreased notably, whereas no changes in BMP levels were observed in response to OA *(Figure 38A, B)*.

Since our prior findings demonstrated a correlation between BMP and cholesterol levels in WT cells *(see Section 4.1)*, we subsequently examined the cholesterol levels after PA or OA cell overload. Concerning total cholesterol levels, they fluctuated in agreement with BMP levels. Exposure to PA resulted in a reduction in cellular cholesterol that was not appreciated with OA *(Figure 38C, D)*.

Based on our observation of the effects of PA on BMP metabolism, we further investigated the involvement of CPT1C in this process. We measured BMP levels in both WT and CPT1C-KO cells after PA exposure and the results showed that PA decreased BMP levels in WT cells but not in CPT1C-KO cells, which already had low basal levels of BMP *(Figure 39A-B)*. Accordingly, exposure to PA resulted in increased ABHD6 activity in WT cells, but not in CPT1C-KO cells. Interestingly, CPT1C-KO cells exhibited similarly increased ABHD6 activity regardless of whether they were exposed to BSA or PA *(Figure 39C-D)*. Noteworthy is the fact that no significant differences in CPT1C or ABHD6 protein expression were observed between BSA or PA conditions in our hypothalamic cell line *(Figure 23E-F)*. Taken together, these findings provide evidence that the inhibitory effect of CPT1C on ABHD6 activity and its subsequent modulation of BMP levels are blunted under PA overload. This therefore suggests that CPT1C plays a role in regulating BMP metabolism in response to LCFA sensing.
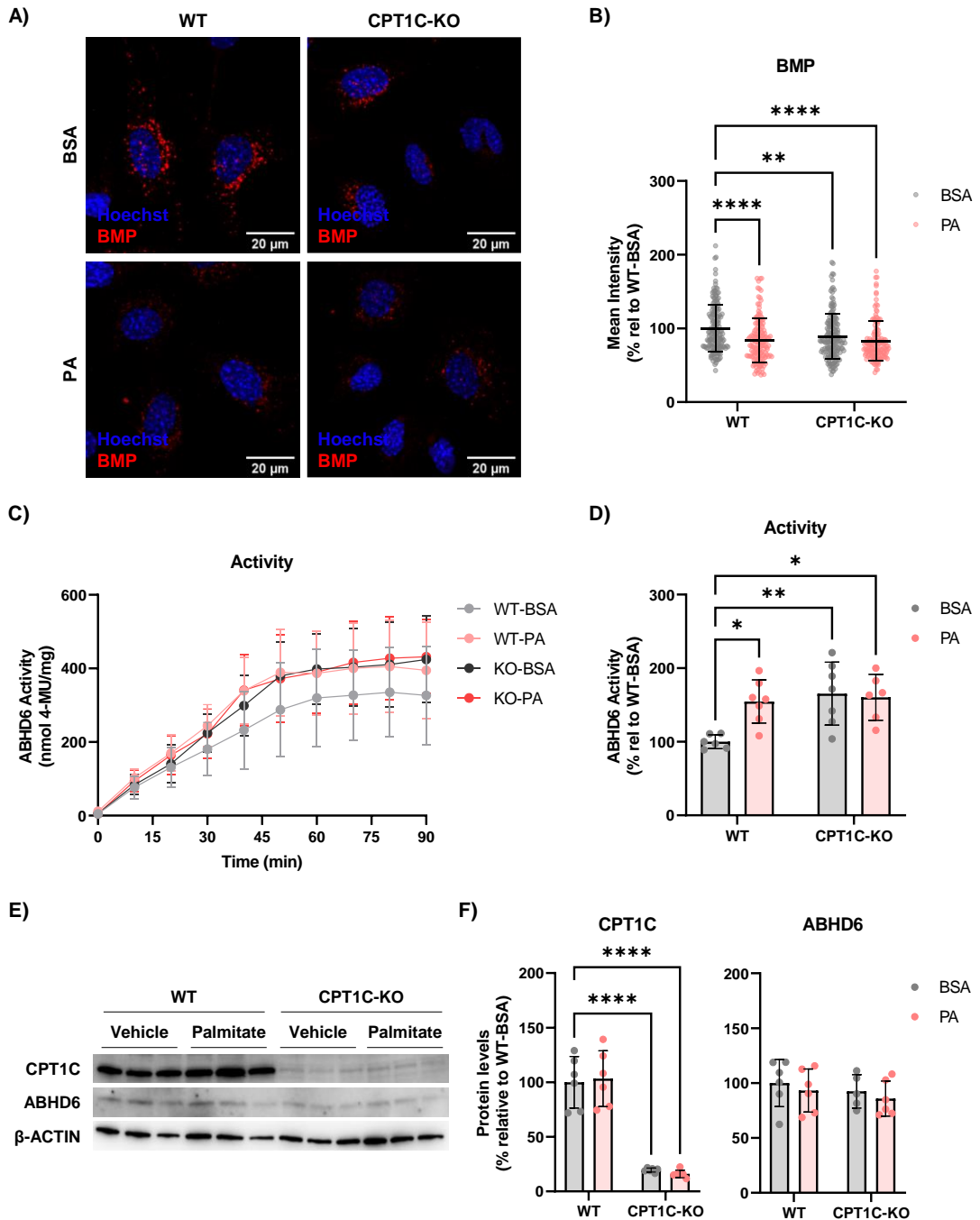
Figure 39. Effects of PA in BMP metabolism in WT and CPT1C-KO GT1-7 cells. A) Representative confocal images of BMP immunocytochemistry in WT and CPT1C-KO cells after treatment with BSA or 300 µM PA for 16 h. B) Quantification of BMP intensity per cell of WT and CPT1C-KO cells treated with BSA or PA (n > 100 from 1 experiment). C-D) Kinetics (C) and quantification (D) of ABHD6 activity in WT and CPT1C-KO cells after treatment with BSA or PA. Quantification of hydrolase activity was calculated from the AUCs of graph shown in (C) (n ≥ 6

from 3 independent experiments). E) Representative image from immunoblotting of CP1C, ABHD6 and β-actin in WT and CPT1C-KO cells treated with BSA or PA. F) Immunoblot quantification of CPT1C and ABHD6 (n ≥ 5 from 2 independent experiments). Data are shown as mean ± SD. *p < 0.05, **p < 0.01, ****p < 0.0001. Statistical significance was determined by two-way ANOVA followed by Bonferroni's post hoc correction.

8.2. Impact of PA on the role of CPT1C in endolysosomal function

We also explored the involvement of CPT1C in the PA-mediated endolysosomal function. After exposing WT and CPT1C-KO cells to PA overload, PA did not decrease LysoTracker fluorescence intensity but instead promoted the acidification and the formation of larger puncta in both WT and CPT1C-KO cells when compared to BSA treated cells *(Figure 40)*. These data indicate that PA induces the accumulation of enlarged endolysosomal structures, increasing their acidity, and that CPT1C might not be involved in the process since cells lacking CPT1C respond equally than WT cells. In both cell models, PA overload induced an increase in acidity and endolysosomal size, although both acidity and size remained consistently lower in CPT1C-KO cells compared to WT cells. This process would be rather explained by the impact of PA on the reduction of autophagic flux, since PA is known to decrease the autophagosome-lysosome fusion, consequently leading to the swelling of endolysosomal compartments (Hernández-Cáceres et al., 2020).However, we cannot rule out the involvement of the CPT1C-ABHD6 axis, as its regulation on lysosomal function could be masked by the potent role of PA in autophagy.
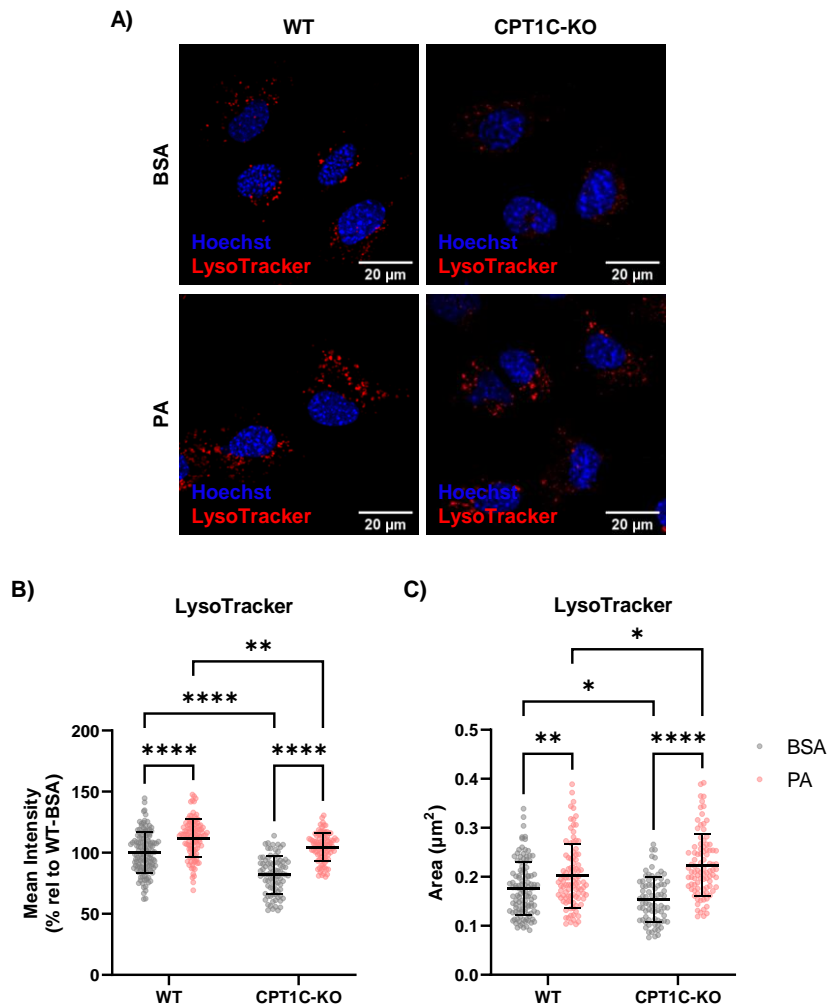
Figure 40. Effects of PA in lysosomal function in WT and CPT1C-KO GT1-7 cells. A) Representative confocal images of WT and CPT1C-KO cells treated with BSA or 300 µM PA for 16 h and stained with LysoTracker. B-C) Quantification of LysoTracker average fluorescence intensity per cell (B) and LysoTracker dots size (C) in WT and CPT1C-KO cells after treatment with BSA or PA (n > 75 from 1 experiment). Data are shown as mean ± SD. *p < 0.05, **p < 0.01, ****p < 0.0001. Statistical significance was determined by two-way ANOVA followed by Bonferroni's post hoc correction.

9. Confirmation of the hypothalamic CPT1C-ABHD6-BMP axis in animal models

To further validate the regulatory role of CPT1C in BMP metabolism and confirm whether this function is compromised under a context of lipid overload, we conducted additional experiments in animal models. First, we measured BMP levels and composition in

hypothalamus, hippocampus and liver from WT and CPT1C-KO mice after short-term (7 days) SD or HFD, and then, we explored the relationship between BMP levels and ABHD6 activity.

9.1. Hypothalamic response to a dietary lipid overload

Regarding the hypothalamus, exposure to a HFD resulted in decreased BMP levels in WT mice, while it did not induce significant changes in total BMP levels in CPT1C-KO mice *(Figure 41A)*. When comparing BMP levels between WT and CPT1C-KO mice under a SD, a trend to decrease (p = 0.0631) was observed, consistently with the findings observed in hypothalamic cell models *(see Section 3.2)*.

Regarding BMP species, exposure to HFD led to changes in the composition of BMP in both WT and CPT1C-KO mice. The most notable alterations were observed in BMP species esterified with arachidonic acid (present in 40:8) and DHA (present in 44:12) *(Figure 41B)*.

The variations in BMP levels correlated with changes in ABHD6 activity. Under a SD, CPT1C-KO mice exhibited higher ABHD6 activity in the hypothalamus compared to WT mice. When comparing the response of ABHD6 activity to a HFD within each genotype, the results demonstrated that short-term exposure to HFD increased ABHD6 activity in hypothalamic homogenates of WT, while no significant differences were observed between HFD and SD-fed CPT1C-KO mice *(Figure 41C-D)*. Furthermore, no significant differences were observed in CPT1C or ABHD6 protein expression levels in hypothalamic homogenates after HFD *(Figure 41E-F)*, indicating that changes in activity are not due to changes in ABHD6 or CPT1C protein levels. Hence, these results provide further support for the conclusion that hypothalamic CPT1C regulates BMP levels through the modulation of ABHD6 activity in response to a dietary overload.

Figure 41. Effects of short-term HFD on hypothalamic BMP levels and ABHD6 activity in WT and CPT1C-KO mice.
A-B) Total hypothalamic BMP content of WT and CPT1C-KO mice fed a SD or HFD for 7 days (A) and respective BMP subspecies (B) (n ≥ 8 animals). C-D) Kinetics (C) and respective quantification (D) of hypothalamic ABHD6 activity in WT and CPT1C-KO mice after short-term HFD. Quantification of hydrolase activity was calculated from the AUCs of graph shown in (C) (n ≥ 5 animals). E) Representative image from immunoblotting of hypothalamic CP1C, ABHD6 and β-actin in WT and CPT1C-KO mice after short-term HFD. F) Immunoblot quantification of CPT1C and ABHD6 (n ≥ 4 animals). Data are shown as mean ± SD. *$p < 0.05$, **$p < 0.01$, ***$p < 0.001$, ****$p < 0.0001$. Statistical significance was determined by two-way ANOVA followed by Bonferroni's post hoc correction.

9.2. Hippocampal response to a dietary lipid overload

The hippocampal response to a HFD was also explored in terms of BMP levels and ABHD6 activity. Unlike the results observed in hypothalamus of WT and CPT1C-KO mice exposed to a dietary overload, no significant differences were found in total BMP levels either when comparing WT and CPT1C-KO mice under the SD or when comparing the effects of a HFD versus SD within each genotype *(Figure 42A)*. Regarding BMP species, the most present within the hippocampus and in which small variations were observed, were those esterified with arachidonic acid and DHA *(Figure 42B)*.

The analysis of ABHD6 activity in the hippocampus revealed distinct findings compared to the results observed in the hypothalamus. CPT1C-KO mice exhibited increased ABHD6 activity when compared to WT mice, both under a SD and a HFD. However, within each genotype, HFD did not induce any significant changes in ABHD6 activity compared to SD *(Figure 42C-D)*. As shown in the hypothalamus, no significant differences were observed in CPT1C or ABHD6 protein expression levels in hippocampal homogenates after HFD *(Figure 42E-F)*, meaning that changes in ABHD6 activity were not due to changes in protein expression.

Altogether, these findings suggest that CPT1C regulates ABHD6 activity in both the hypothalamus and hippocampus, but only in hypothalamus CPT1C is able to modulate ABHD6 activity and BMP levels in response to lipid sensing.
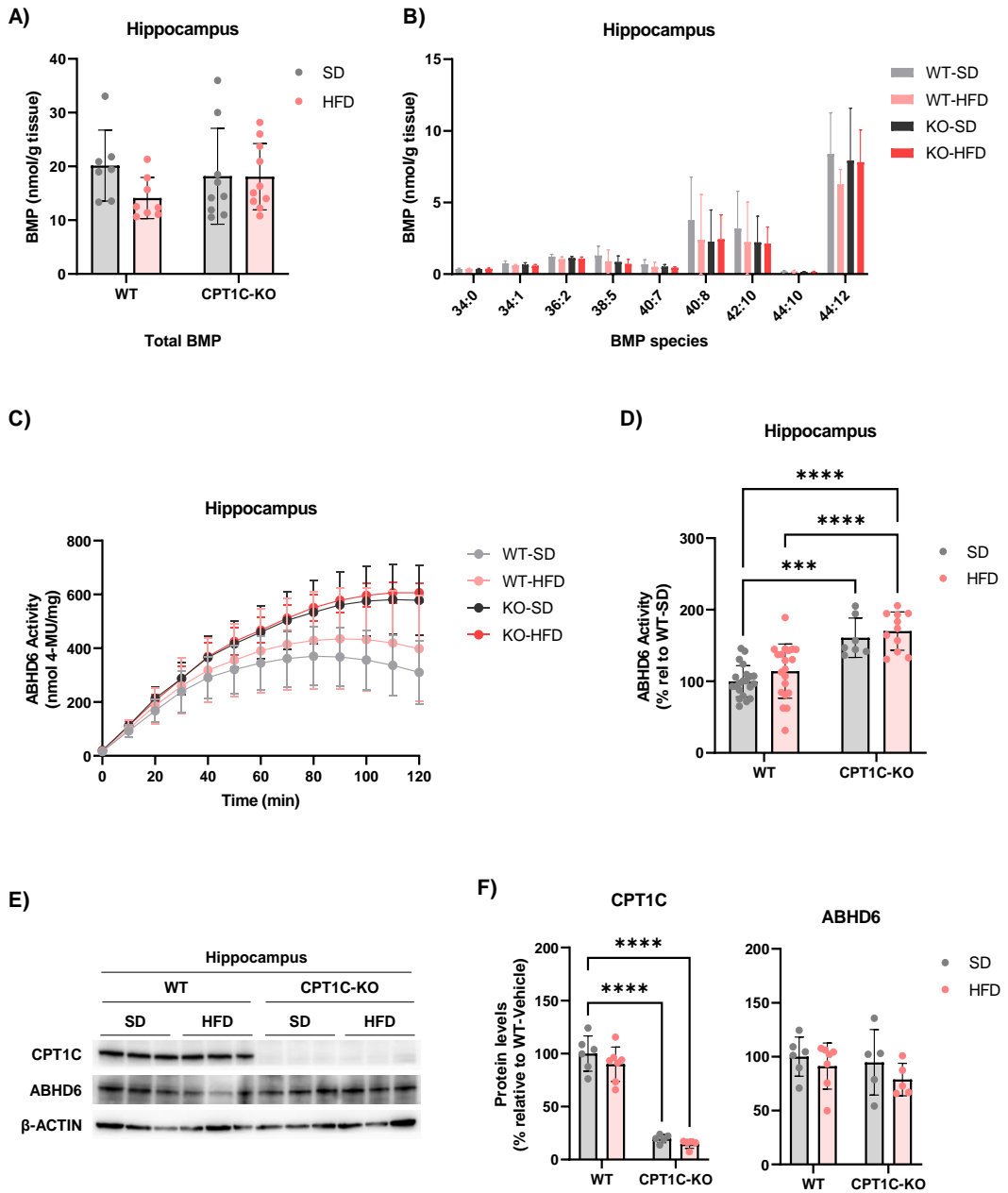
Figure 42. Effects of short-term HFD on hippocampal BMP levels and ABHD6 activity in WT and CPT1C-KO mice.
A-B) Total hippocampal BMP content of WT and CPT1C-KO mice fed a SD or HFD for 7 days (A) and respective BMP subspecies (B) (n ≥ 8 animals). C-D) Kinetics (C) and respective quantification (D) of hippocampal ABHD6 activity in WT and CPT1C-KO mice after short-term HFD. Quantification of hydrolase activity was calculated from the AUCs of graph shown in (C) (n ≥ 7 animals). E) Representative image from immunoblotting of hippocampal CP1C, ABHD6 and β-actin in WT and CPT1C-KO mice after short-term HFD. F) Immunoblot quantification of CPT1C and ABHD6 (n ≥ 5 animals). Data are shown as mean ± SD. ***$p < 0.001$, ****$p < 0.0001$. Statistical significance was determined by two-way ANOVA followed by Bonferroni's post hoc correction.

9.3. Liver response to a dietary lipid overload

Interestingly, liver homogenates of both WT and CPT1C-KO mice exhibited a different response from brain homogenates after HFD exposure. Total BMP levels under SD were increased in CPT1C-KO compared to WT mice, but decreased under HFD in both WT and CPT1C-KO mice when compared to SD-fed mice *(Figure 43A)*. In addition, the most significant alterations in BMP composition were found in BMP species esterified with OA (present in 36:2) and DHA (present in 44:12) *(Figure 43B)*.

Regarding ABHD6 activity, similar to the results observed in the hippocampus, in both the SD and HFD conditions CPT1C-KO mice displayed increased ABHD6 activity compared to WT mice. However, the HFD did not lead to significant alterations in ABHD6 activity when compared to the SD within each genotype *(Figure 43C-D)*.

Given that CPT1C is not expressed in the liver, these findings suggest the presence of a brain-liver crosstalk mechanism involved in the modulation of ABHD6 activity and BMP levels in the liver.
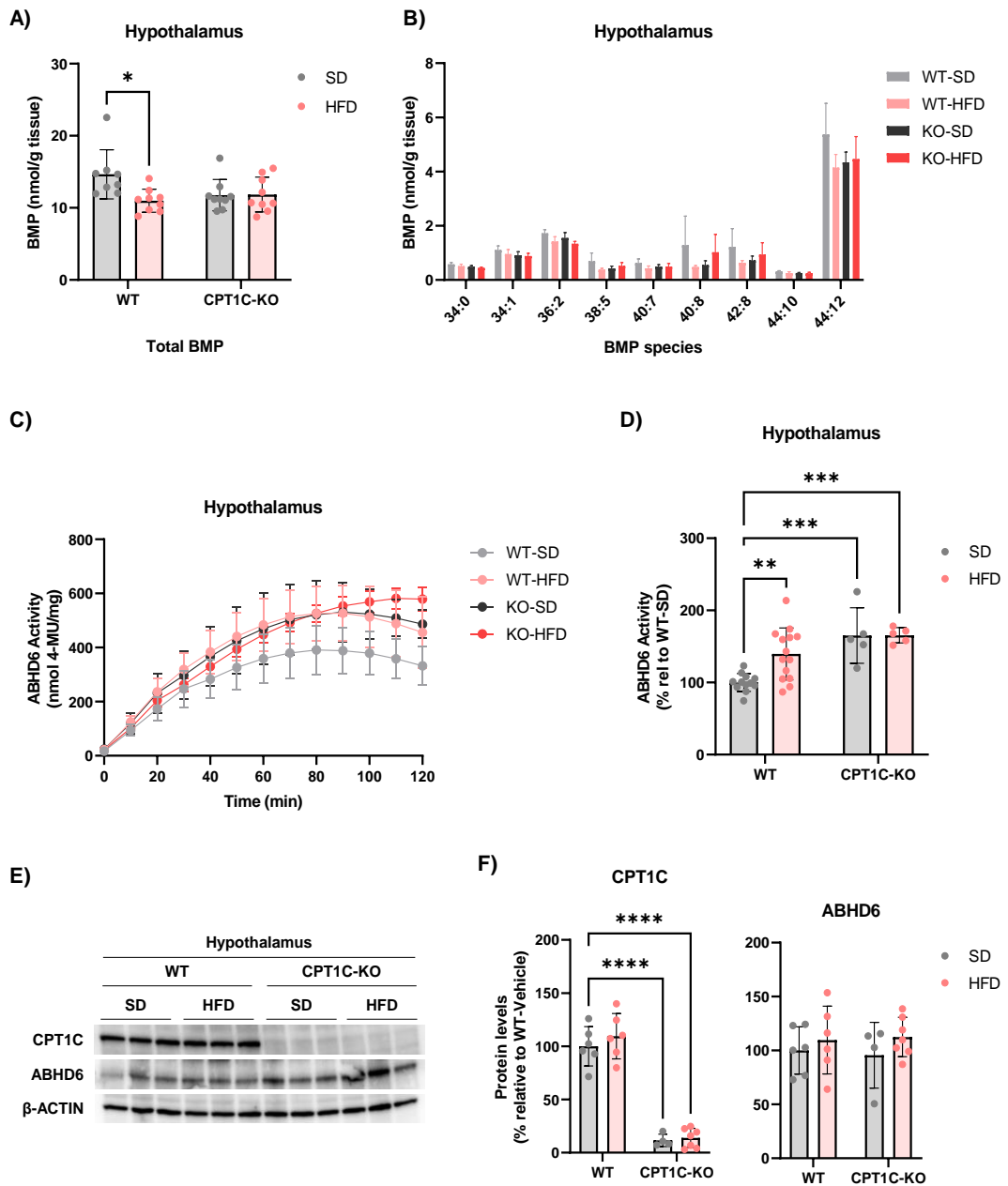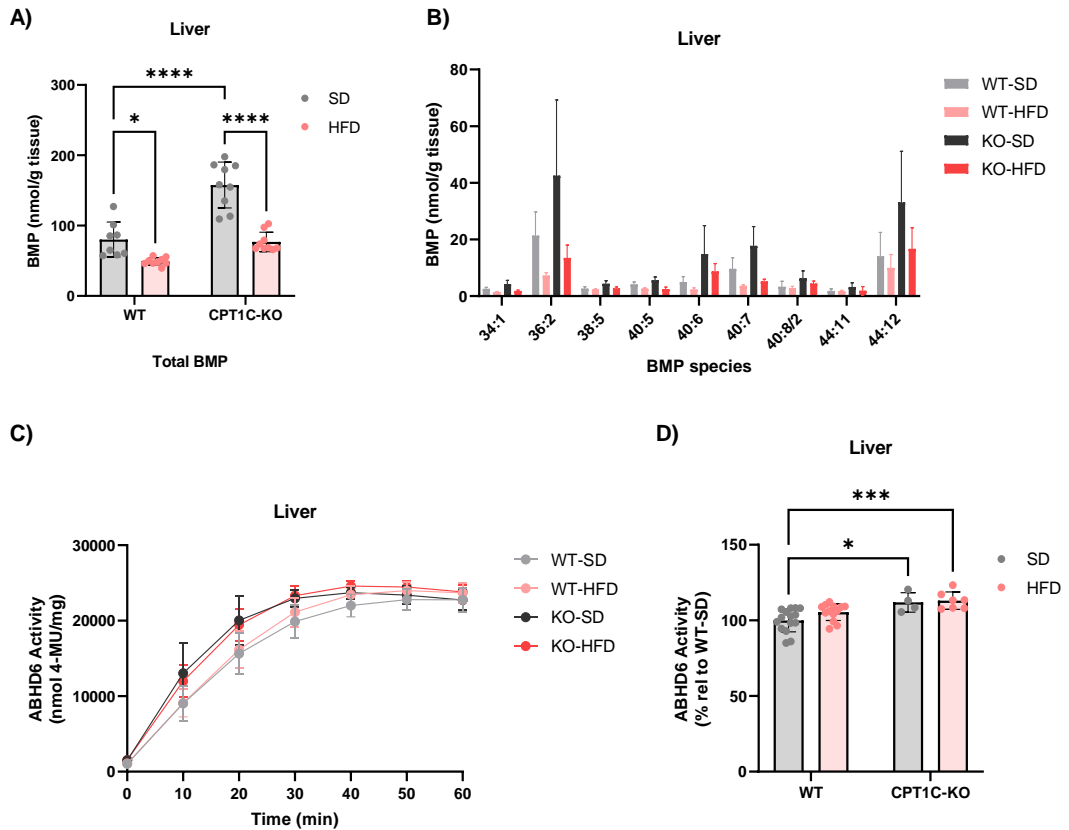
Figure 43. Effects of short-term HFD on hepatic BMP levels and ABHD6 activity in WT and CPT1C-KO mice. A-B) Total hepatic BMP content of WT and CPT1C-KO mice fed a SD or HFD for 7 days (A) and respective BMP subspecies (B) (n ≥ 8 animals). C-D) Kinetics (C) and respective quantification (D) of hepatic ABHD6 activity in WT and CPT1C-KO mice after short-term HFD. Quantification of hydrolase activity was calculated from the AUCs of graph shown in (C) (n ≥ 4 animals). Data are shown as mean ± SD. *p < 0.05, ***p < 0.001, ****p < 0.0001. Statistical significance was determined by two-way ANOVA followed by Bonferroni's post hoc correction.

9.4. Confirmation of hypothalamic modulation of ABHD6 activity by CPT1C in response to lipid sensing

Our previous findings in cells demonstrated differential responses of hypothalamic GT1-7 cells to saturated or unsaturated LCFA in terms of BMP levels *(see Section 8)*. Here, our aim was to confirm whether the increase of ABHD6 activity following a short-term exposure to HFD was dependent on the lipid composition of the diet. To investigate this, we exposed WT mice to SD, SFA or MUFA diets for 7 days, and then measured ABHD6 activity in hypothalamic homogenates. Results shown in *Figure 44* demonstrate that hypothalamic ABHD6 activity increased in mice exposed to SFA but not in those exposed to MUFA. These findings suggest that the altered ABHD6 activity and subsequent changes in BMP levels observed in *Section*

9.1 are primarily influenced by the presence of saturated lipids in the HFD, providing support for the statement that hypothalamic CPT1C serves as the key mediator of lipid sensing.
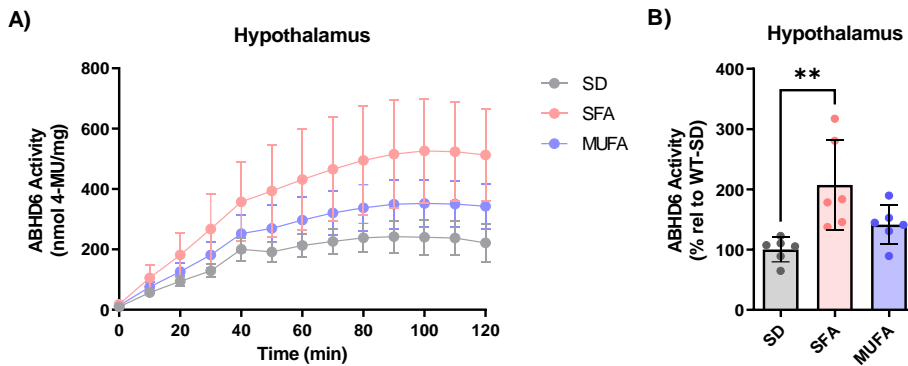
Figure 44. Hypothalamic ABHD6 activity is dependent on lipid sensing. A-B) Kinetics (A) and respective quantification (B) of hypothalamic ABHD6 activity in WT mice after short-term SD, SFA or MUFA. Quantification of hydrolase activity was calculated from the AUCs of graph shown in (A) (n = 6 animals). Data are shown as mean ± SD. **p < 0.01. Statistical significance was determined by one-way ANOVA followed by Bonferroni's post hoc correction.

10. Results summary of Chapter I

The main results obtained from the study of the role of CPT1C in BMP metabolism and endolysosomal function are represented in *Figure 45*.
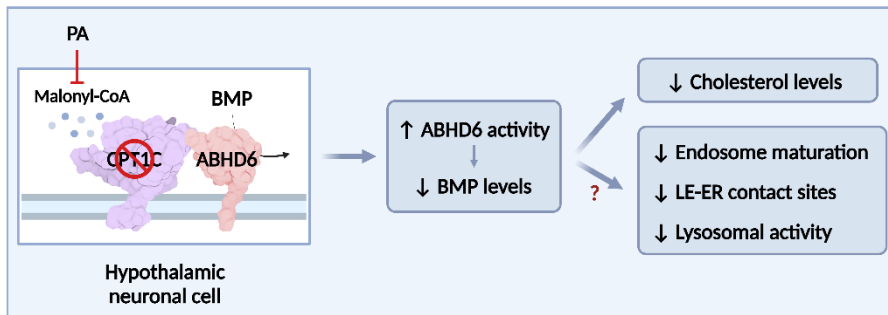
Figure 45. Graphical abstract of chapter I. Deletion of CPT1C or exposure to PA results in increased ABHD6 activity and decreased BMP levels in hypothalamic neuronal cells, which leads to a decrease in cholesterol levels. CPT1C-KO cells also exhibit a decrease in endosome maturation, in MCS between LE and ER, and in lysosomal activity. However, whether these latter are a consequence of reduced BMP remains to be elucidated.

Chapter II

Study of the subcellular localization and interaction of CPT1C and ABHD6 proteins

In this chapter, we aim to characterize the interaction between CPT1C and ABHD6 by addressing i) the subcellular localization where the CPT1C-ABHD6 interaction likely takes place, ii) the structural domains of both proteins involved in their interaction, and iii) whether these domains are also responsible for the modulation of ABHD6 activity by CPT1C.

We use HeLa cells to overexpress CPT1C and ABHD6, and analyze their colocalization with organelle markers and with each other. Additionally, HEK293T cells are employed to overexpress CPT1C and ABHD6 constructs lacking specific structural domains to investigate which of them are responsible for the CPT1C-ABHD6 interaction and modulation of ABHD6 activity. Finally, in silico modeling is conducted to provide insights into the potential amino acids forming the interaction between CPT1C and ABHD6.

1. Subcellular localization of CPT1C and ABHD6

It is well known that CPT1C is an ER-resident protein (Casals et al., 2016), and as for ABHD6, it was described to colocalize with the ER and LE/Lys (Pribasnig et al., 2015). The first aim of this chapter was to confirm the subcellular localization of CPT1C and ABHD6 and explore where the interaction between both proteins takes place by analyzing the colocalization of these proteins with ER and LE/Lys markers.

1.1. CPT1C and ABHD6 colocalize in the ER

We first confirmed the localization of CPT1C and ABHD6 in the ER and explored whether these proteins colocalize within the cell. To that end, we transfected HeLa cells with CPT1C-EGFP or ABHD6-mCherry plasmids, immunostained the ER for calnexin, and analyzed the colocalization between CPT1C or ABHD6 and calnexin by confocal microscopy. The acquired images showed that both CPT1C and ABHD6 colocalized with the ER marker *(Figure 46A)*. In addition, when CPT1C and ABHD6 were co-expressed in HeLa cells, a similar degree of colocalization was observed between CPT1C and ABHD6 *(Figure 46B)*, comparable to the colocalization observed between these proteins and the ER marker. Therefore, these results confirm the colocalization of CPT1C and ABHD6 in the ER.
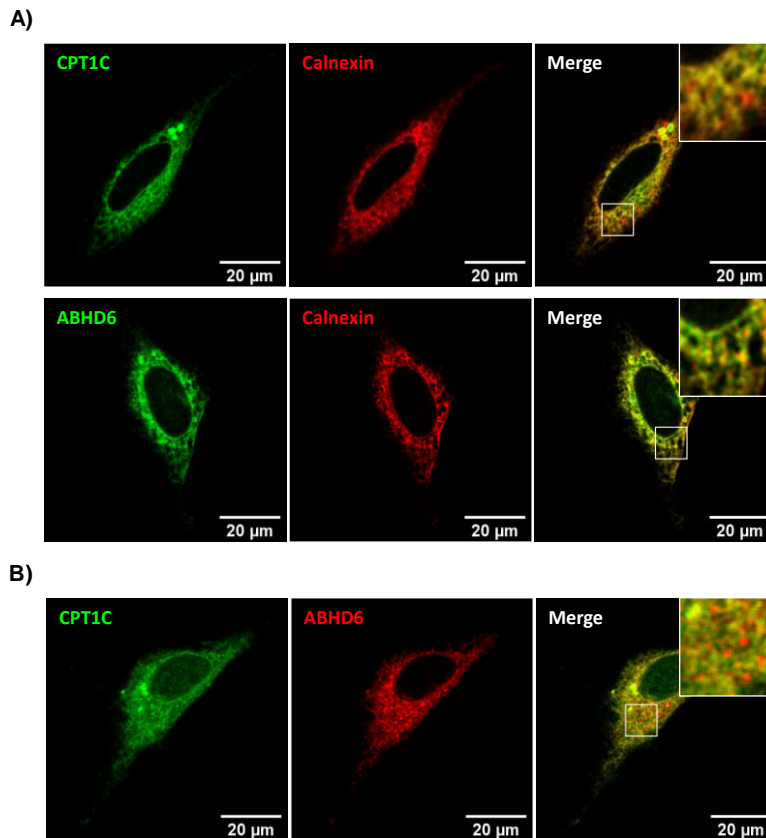
Figure 46. CPT1C and ABHD6 colocalize in the ER. A) Representative confocal images of HeLa cells transfected with plasmids encoding for CPT1C-EGFP or ABHD6-mCherry and immunostained for Calnexin. B) Representative confocal images of HeLa cells overexpressing CPT1C-EGFP and ABHD6-mCherry.

1.2. Colocalization of CPT1C and ABHD6 with LEs

In the previous chapter we presented evidence for the presence of contacts between the ER and LE, and the involvement of CPT1C in these contacts, as well as the role of ABHD6 in BMP catabolism. To further investigate the interplay between these components, we examined the colocalization of CPT1C and ABHD6 with either the LE/Lys marker LAMP1 or its specific phospholipid BMP.

To study the colocalization with LE/Lys or BMP, HeLa cells were transfected with CPT1C or ABHD6 and immunolabeled for LAMP1 or BMP. The results presented in *Figure 47A-B* demonstrate that both CPT1C and ABHD6 showed some degree of colocalization with LAMP1, as indicated by the white arrows, with a significantly higher degree observed in ABHD6 expressing cells. Approximately 30 % of the LE/Lys signal overlapped with CPT1C, while the percentage of LE/Lys signal overlapping with ABHD6 increased to 37%. Regarding

the interplay of CPT1C and ABHD6 with BMP, similar results were observed compared to those of LAMP1. The fraction of BMP signal overlapping with ABHD6 was significantly higher than that overlapping with CPT1C *(Figure 47C-D)*. Furthermore, we confirmed the presence of BMP in LE/Lys. Almost 60% of the BMP signal was found to be localized in LE/Lys *(Figure 47C-D)*.

Altogether, we can conclude that the interaction between CPT1C and ABHD6 occurs within the ER and in close approximation of LE/lysosomes, where BMP is located and can be accessed and hydrolyzed by ABHD6, which seems to be closer to LE/lysosomes than CPT1C.
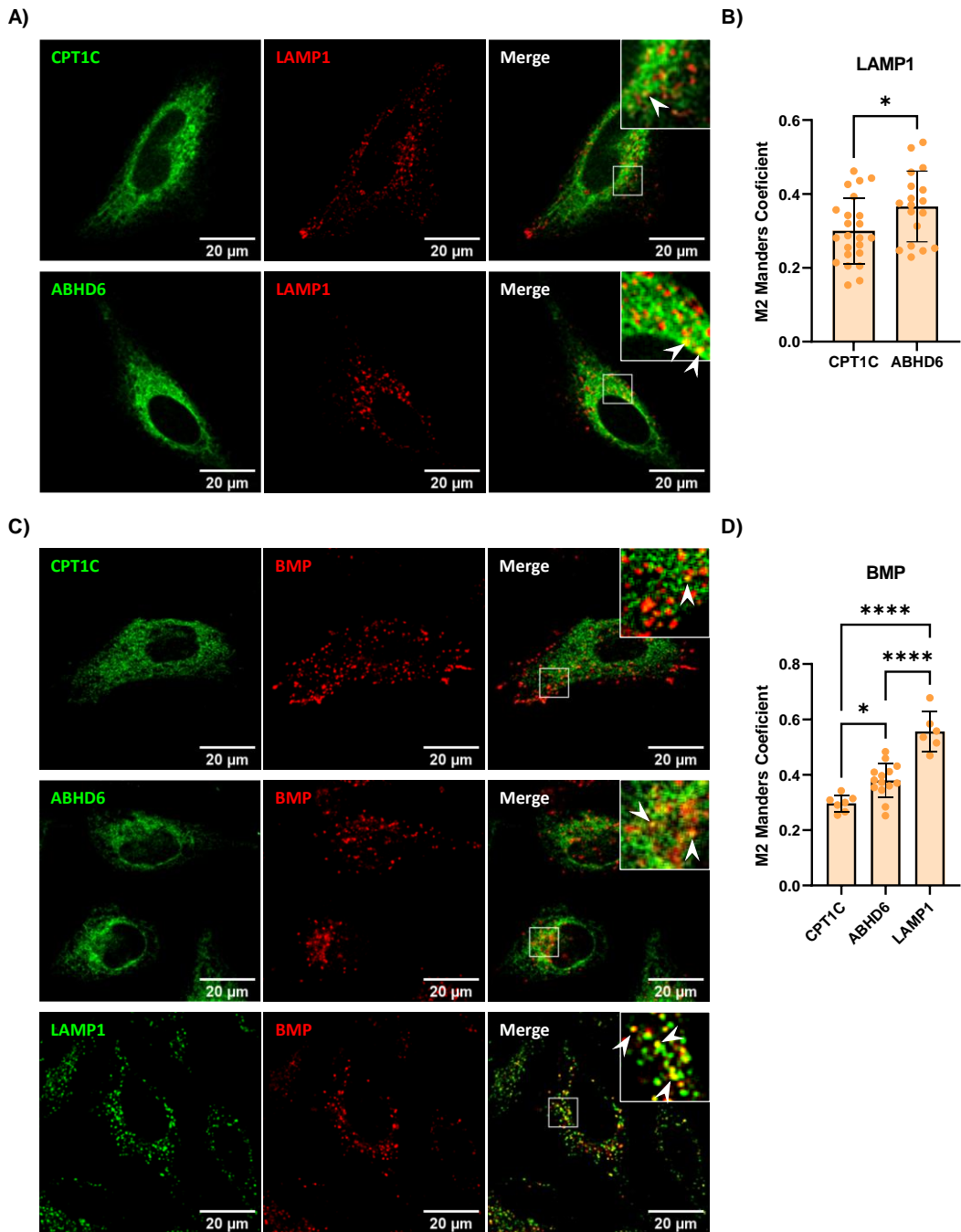
Figure 47. Colocalization analysis of CPT1C and ABHD6 in LE/Lys. A-B) Representative confocal images (A) and respective quantification results (B) of colocalization between CPT1C or ABHD6 and the LE/Lys marker LAMP1 in HeLa cells. Plasmids for CPT1C or ABHD6 overexpression were transfected in HeLa cells and colocalization with LAMP1 was analyzed by immunostaining. Results are given as M2 Manders overlap coefficient (fraction of LAMP1 overlapping with CPT1C or ABHD6) (n ≥ 18 cells). C-D) Representative confocal images (C) and respective

quantification results (D) of colocalization between CPT1C, ABHD6 or LAMP1 and BMP. HeLa cells were either transfected with CP1C or ABHD6 overexpressing plasmids and immunostained for BMP, or co-immunostained for LAMP1 and BMP. Results are given as M2 Manders overlap coefficient (fraction of BMP overlapping with CPT1C, ABHD6 or LAMP1) (n ≥ 6 cells). Statistical significance was determined by t-student test (B) and by one-way ANOVA followed by Bonferroni's post hoc correction (D). White arrows indicate colocalization points.

2. Characterization of the CPT1C-ABHD6 interaction

The second aim of this chapter was to elucidate which structural motifs of CPT1C and ABHD6 are responsible for their interaction and the subsequent modulation of ABHD6 activity. To accomplish that, we designed different constructs of the proteins lacking some of their structural motifs *(Figure 48A)*, and studied thereafter whether their absence had any impact on the interaction between the proteins and the modulation of ABHD6 activity.

2.1. Validation of CPT1C and ABHD6 mutated constructs

Regarding CPT1C, we generated two constructs, the one lacking the first 52 amino acids corresponding to the whole N-terminal tail of CPT1C (Δ52CPT1C-mTurq2), and the other lacking only the first 26 amino acids (Δ26CPT1C-mTurq2). The second construct was generated just in case the deletion of the entire N-terminal tail impaired the expression of CPT1C. And referring to ABHD6, we generated three constructs, the first one lacking the N-terminal tail of ABHD6 (Δ8ABHD6-YFP), the second one lacking the first 29 amino acids corresponding to the N-terminal tail together with the transmembrane domain (Δ29ABHD6-YFP), and the last one lacking the whole C-terminal domain (ABHD6ΔCter-YFP) comprised by the last 307 amino acids. The CPT1C constructs were fluorescently tagged with mTurquoise2, while the ABHD6 constructs were tagged with YFP, enabling them to be used for FRET assays.

Before performing the interaction and activity analyses, we validated our mutated proteins by ensuring that both the CPT1C and ABHD6 constructs were properly expressed and that the ABHD6 constructs had hydrolase activity. In order to do that, we transfected HEK293T cells by calcium-phosphate with the different constructs separately, and then analyzed protein expression and ABHD6 activity by Western Blot and the 4-MUH assay, respectively.
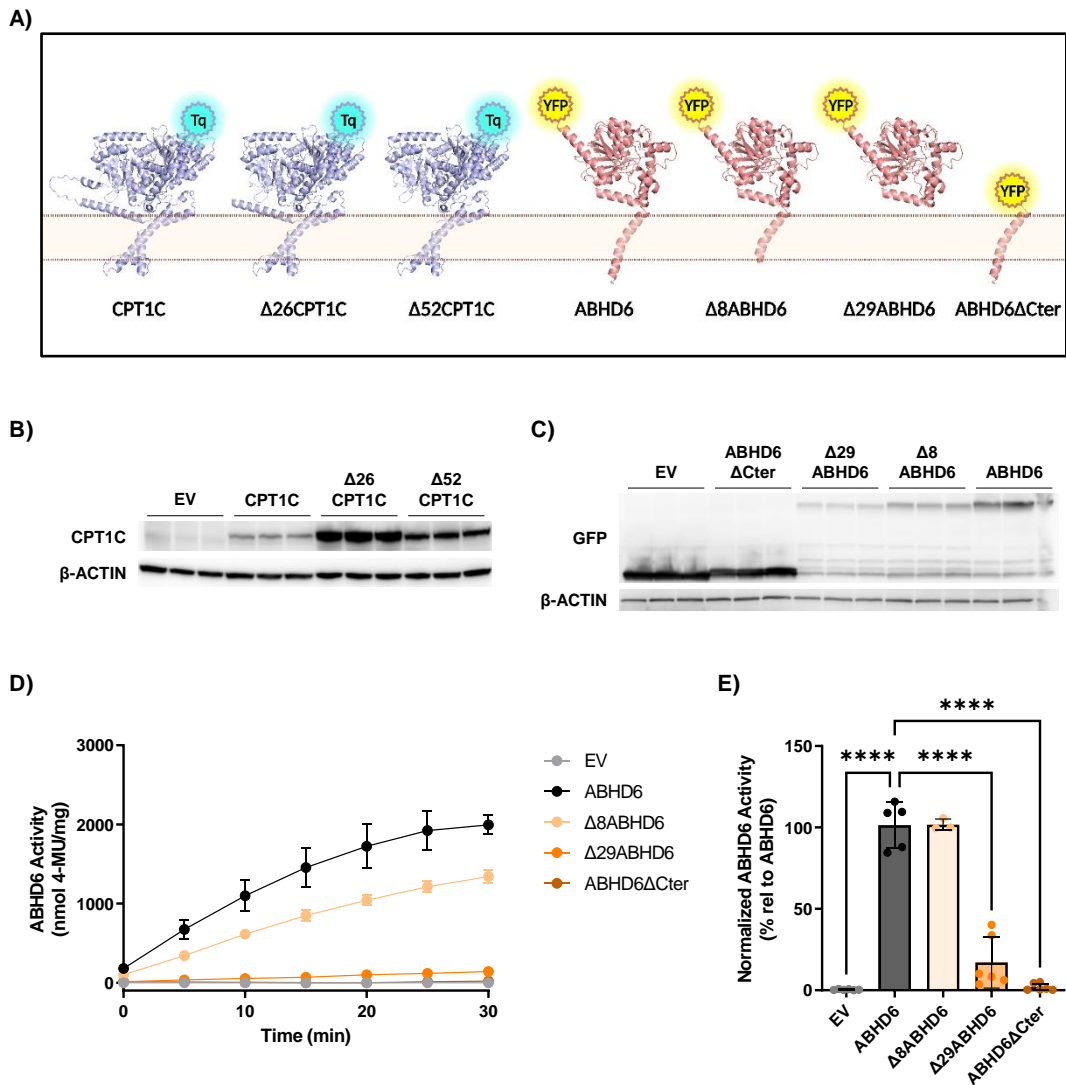
Figure 48. Expression and activity of the CPT1C and ABHD6 mutated proteins. A) Structural representation of generated mutated proteins. B) Immunoblotting of CP1C constructs and β-actin in transfected HEK293T cells. C) Immunoblotting of ABHD6 constructs and β-actin in transfected HEK293T cells. ABHD6 constructs were detected by their fluorescent tag using the GFP antibody. D-E) Kinetics (D) and quantification (E) of ABHD6 activity in HEK293T cells transfected with the EV or the different ABHD6 constructs. Quantification of ABHD6 activity was normalized to ABHD6 protein expression (n ≥ 3 from 2 independent experiments). Data shown are means ± SD. ****$p < 0.0001$. Statistical significance was determined by one-way ANOVA followed by Bonferroni's post hoc correction. Tq: mTurquoise; YFP: yellow fluorescence protein.

As shown in *Figure 48*, Δ26CPT1C and Δ52CPT1C were effectively expressed when transfected to HEK293T cells *(Figure 48B)*. Regarding the expression and activity of ABHD6, all constructs were expressed upon transfection into HEK293T cell *(Figure 48C)*. However, not all of the constructs displayed hydrolase activity *(Figure 48D-E)*. ABHD6 functions through a catalytic triad (Ser[148], Asp[278] and His[306]) located in its C-terminal tail (Shields et al., 2019). As expected, the ABHD6 construct lacking the C-terminal tail (ABHD6ΔCter) showed no activity. Surprisingly, the protein lacking the N-terminal and transmembrane domains (Δ29ABHD6), which was expected to retain hydrolase activity due to the presence of the C-terminal region, also demonstrated a very low activity compared to full-length ABHD6. Lastly, the construct without the N-terminal tail (Δ8ABHD6) retained hydrolase activity.

The absence of activity in Δ29ABHD6 despite having the C-terminal tail, could be due to a conformational change caused by the removal of the N-terminal and transmembrane domains. This conformational change could affect the disposition of the catalytic triad, thereby impairing the hydrolase ability of the protein, even though it was expressed properly. For that reason, we no longer included this construct in the following studies.

2.2. Structural motifs involved in CPT1C-ABHD6 interaction

Based on the previous findings, Δ26CPT1C, Δ52CPT1C, Δ8ABHD6 and ABHD6ΔCter were the final constructs selected for conducting the interaction and activity assays. Interaction assays were done by FRET sensitized emission, performed in HEK293T cells.

First, we assessed which motif of ABHD6 was part of the CPT1C-ABHD6 interaction by co-transfecting the cells with CPT1C-mTurq2 (donor) and Δ8ABHD6-YFP or ABHD6ΔCter-YFP (acceptors). The pair of plasmids encoding for CPT1C-mTurq2 and ABHD6-YFP were used as a positive interaction control (Miralpeix et al., 2021) while, as a negative interaction control, we used calnexin-mTurq2 with ABHD6-YFP *(Figure 49A)*. Results showed that the FRET efficiency of CPT1C/Δ8ABHD6 was similar to the FRET efficiency of CPT1C/ABHD6 *(Figure 49B)*, meaning that the first 8 amino acids of the N-terminal tail of ABHD6 was not relevant for the interaction with CPT1C. Interestingly, the FRET efficiency of CPT1C/ABHD6ΔCter was significantly lower than the FRET efficiency of CPT1C/ABHD6 *(Figure 49C)* but similar to the FRET efficiency of the negative interaction control, Calnexin/ABHD6 *(Figure 49D)*, which suggested that the structural motif responsible for the interaction with CPT1C is the C-terminal region of ABHD6.

Then, we tested if the N-terminal region of CPT1C was involved in the CPT1C-ABHD6 interaction by co-transfecting the HEK293T cells with the donor proteins Δ26CPT1C-mTurq2 or Δ52CPT1C-mTurq2 and the acceptor protein ABHD6-YFP. On the one hand, the comparison of FRET efficiencies of Δ26CPT1C/ABHD6 and CPT1C/ABHD6 revealed a significant difference between the two protein pairs *(Figure 49E)*, indicating that the deletion of the first 26 amino acids of CPT1C affected somehow the interaction between CPT1C and ABHD6. Notably, this deletion did not result in the loss of interaction but rather appeared to facilitate it, since the curve seems to saturate earlier. And on the other hand, no differences were observed when the FRET efficiency of Δ52CPT1C/ABHD6 was compared with the FRET efficiency of CPT1C/ABHD6 *(Figure 49F)*. Taken together, these results suggested that the N-terminal motif of CPT1C is not essential for the CPT1C-ABHD6 interaction.
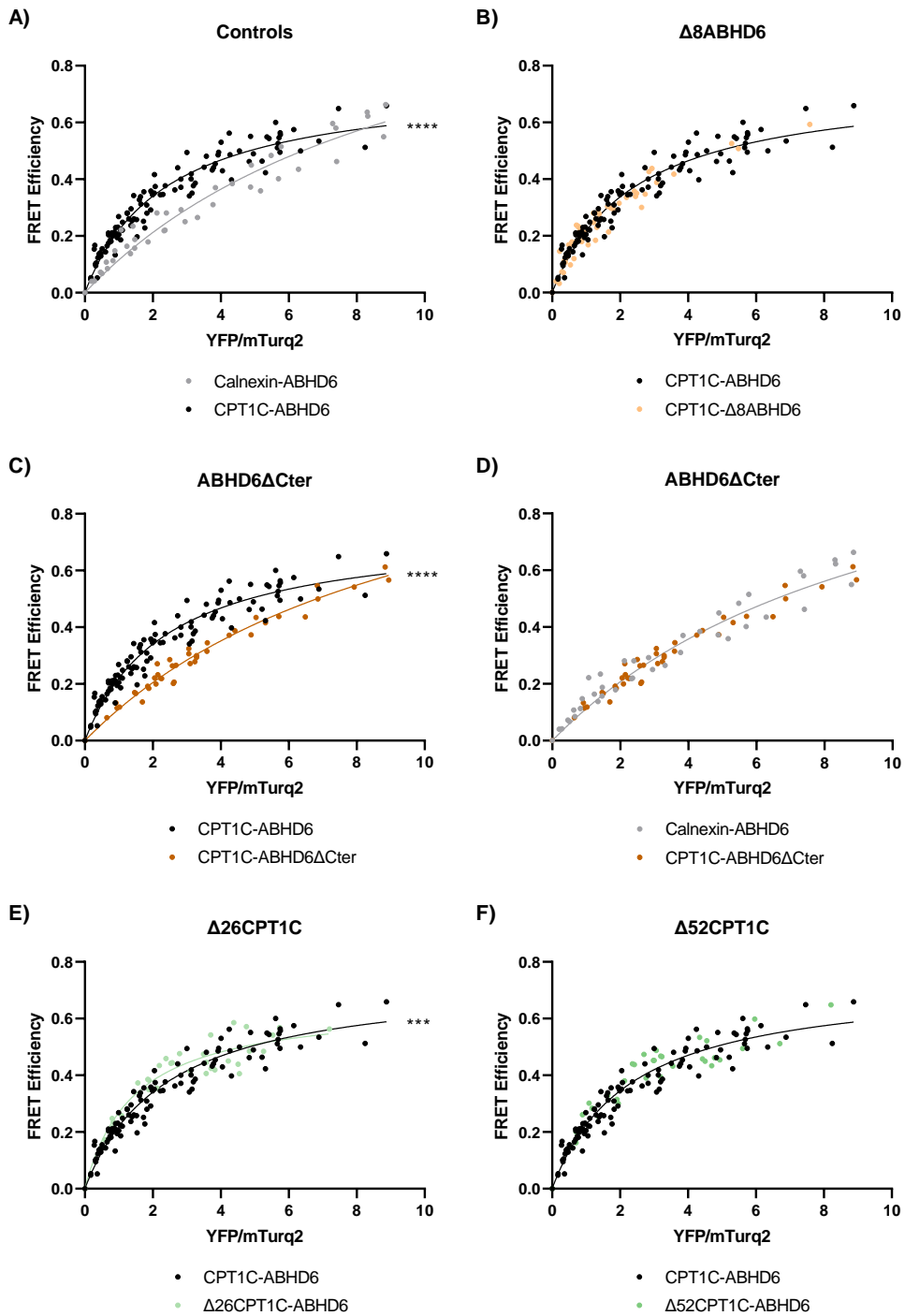
Figure 49. Interaction between ABHD6 and CPT1C constructs. A-F) FRET sensitized emission of CPT1C or ABHD6 with either calnexin or CPT1C/ABHD6 constructs in transfected living HEK293T cells. The calnexin-ABHD6 pair and the CPT1C-ABHD6 pair (A) were used as negative and positive interaction controls, respectively. The different

ABHD6 constructs were tested for interaction with CPT1C (B-D) and the different CPT1C constructs were tested for interaction with ABHD6 (E-F). Assays were performed 48 h post transfection in HEK293T cells expressing the donor protein (calnexin, CPT1C and CPT1C constructs) with increasing amounts of acceptor protein (ABHD6 and ABHD6 constructs). FRET saturation curves were fit by nonlinear regression. ***p < 0.001, ****p < 0.0001. Statistical significance was determined by testing if one curve fit all the data by the extra sum-of-squares F-test.

As ABHD6 appears to interact with CPT1C via the C-terminal region, it suggests that the interaction occurs in the cytosolic face of the cell. Furthermore, excluding the N-terminal region of CPT1C from the interaction leads us to conclude that the interaction must occur between the C-terminal tails of both proteins.

2.3. Structural motifs involved in CPT1C-mediated ABHD6 inhibition

Then, we were interested in evaluating whether the N-terminal regions of CPT1C and ABHD6, even not being part of the interaction, were involved in the CPT1C-modulation of ABHD6 activity. For that, ABHD6 activity was assessed in HEK293T cells expressing either ABHD6 with the different constructs of CPT1C lacking the N-terminal domain, or the construct of ABHD6 lacking the N-terminal domain with CPT1C. In these experiments, the ABHD6ΔCter construct was excluded since it does not have hydrolytic activity.

Our results demonstrated that both Δ26CPT1C and Δ52CPT1C decreased ABHD6 activity as efficiently as CPT1C *(Figure 50A-B)*, and that Δ8ABHD6 activity was also decreased in the presence of CPT1C *(Figure 50C-D)*.
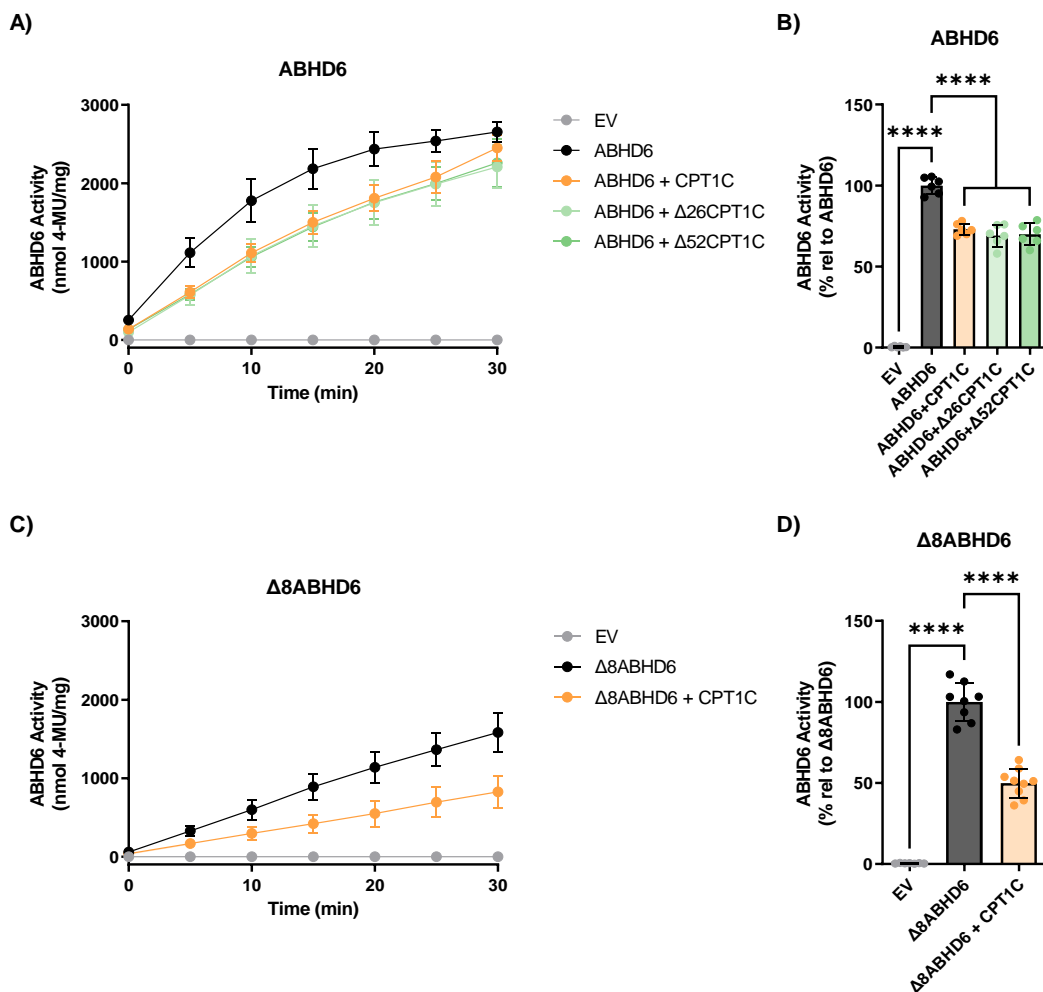
Figure 50. Modulation of ABHD6 or Δ8ABHD6 activity by CPT1C constructs. A-B) Kinetics (A) and quantification (B) of ABHD6 activity in HEK293T cells transfected with ABHD6 alone or together with CPT1C constructs (n ≥ 7 from 3 independent experiments). C-D) Kinetics (C) and quantification (D) of Δ8ABHD6 activity in HEK293T cells transfected with ABHD6 alone or with CPT1C (n = 6 from 3 independent experiments). Data shown are means ± SD. ****$p < 0.0001$. Statistical significance was determined by one-way ANOVA followed by Bonferroni's post hoc correction.

Furthermore, the decrease in hydrolase activity could be attributed to the inhibitory effect of CPT1C rather than changes in protein expression since *Figure 51* shows that there were no significant differences in the expression of ABHD6 or Δ8ABHD6 when expressed alone or in the presence of the CPT1C constructs.
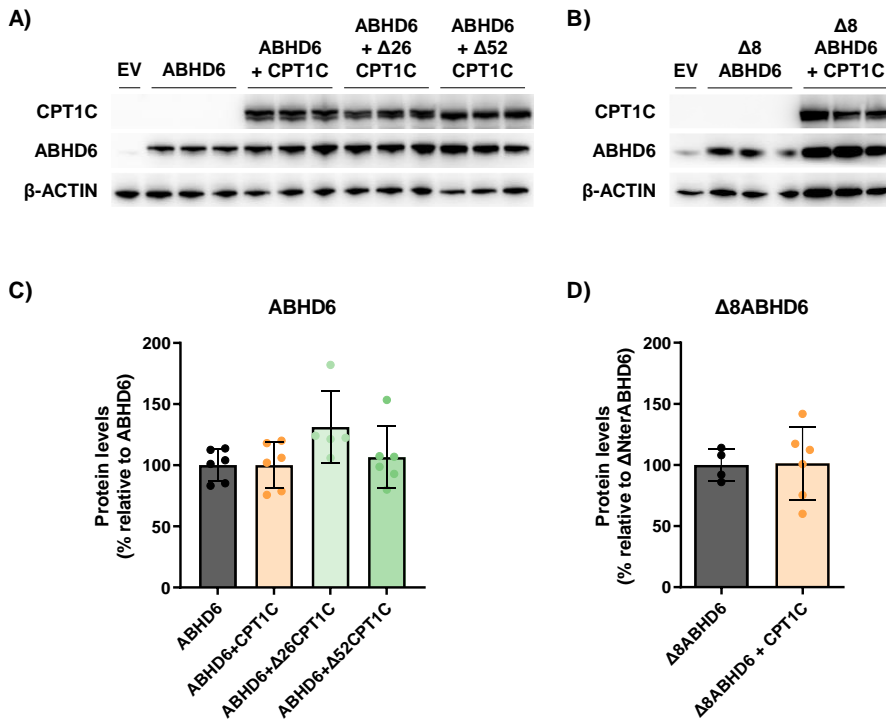
Figure 51. Protein expression of ABHD6 and CPT1C constructs. A-B) Immunoblotting of ABHD6 with CPT1C constructs (A) or Δ8ABHD6 with CPT1C (B) and β-actin in co-transfected HEK293T cells. C-D) Quantification of ABHD6 and CPT1C protein levels when co-transfected to HEK293T cells alone or together (n ≥ 4 from 2 independent experiments). Data shown are means ± SD. ****$p < 0.0001$. Statistical significance was determined by one-way ANOVA followed by Bonferroni's post hoc correction.

Altogether, these results indicate that the N-terminal tails of both proteins are not implicated in either the interaction between CPT1C and ABHD6 or the modulation of ABHD6 activity by CPT1C. Therefore, the regulation of ABHD6 activity by CPT1C must be exerted by the C-terminal region of the protein.

3. *In silico* modeling of the human CPT1C-ABHD6 protein complex

In order to delve deeper into the domains or amino acids involved in the CPT1C-ABHD6 interaction, an extensive *in silico* study was carried out by Nostrum Biodiscovery. Here, we present the key outcomes. For a more comprehensive understanding, please refer to the company's final report with detailed results attached in *Appendix I*.

3.1. Protein structure prediction

To identify the structural motifs involved in the CPT1C-ABHD6 interaction, the first approach was to assess the structural models of the isolated CPT1C and ABHD6 proteins. The crystal

structure of CPT1C protein is not yet available, so it was used the AlphaFold model of CPT1C protein already available in the AlphaFold web server (https://alphafold.ebi.ac.uk/) *(Figure 52A)*. After extensive analysis, it could be confirmed that the CPT1C protein structure predicted by AlphaFold should correspond to a reasonably accurate representation of the native CPT1C protein structure. Regarding ABHD6, it was used both the protein X-ray structure currently available in the PDB Data Bank (PDB ID 7OTS) comprising only the C-terminal region of the protein and the AlphaFold model comprising the whole protein already build and stored in the AlphaFold web server *(Figure 52B)*. The published X-ray structure was assessed with an OA to visualize the FA channel for the binding of the substrate.
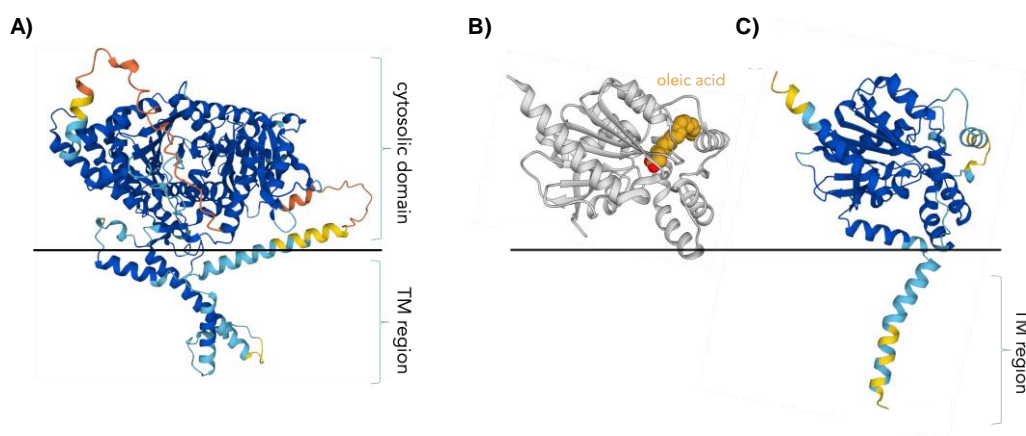
Figure 52. Structure predictions of CPT1C and ABHD6 proteins. A) CPT1C protein structure predicted by AlphaFold color-coded according to the pLDDT (per-residue confidence metric) values: very high confidence (pLDDT > 90) in dark blue, confidence (70 < pLDDT < 90) in light blue, low confidence (50 < pLDDT < 70) in yellow, very low confidence (pLDDT < 50) in orange. B) ABHD6 protein X-ray structure with oleic acid. C) ABHD6 protein structure predicted by AlphaFold color-coded according to the pLDDT (per-residue confidence metric) values.

3.2. CPT1C/ABHD6 protein complex modelling

Once CPT1C and ABHD6 structures were predicted, it was proceeded with the identification of the interaction sites by performing docking experiments. After a highly exhaustive conformational search, four potential CPT1C-ABHD6 binding models, named C1.1, C1.2, C2.1 and C2.2, were identified. Interestingly, all the four models selected shared the same binding region within the ABHD6 protein surface that perfectly overlaps with the OA binding site entrance *(Figure 53)*, which agree with the inhibitory activity of CPT1C against ABHD6 protein previously demonstrated by our group (Miralpeix et al., 2021) and further studied in this chapter.
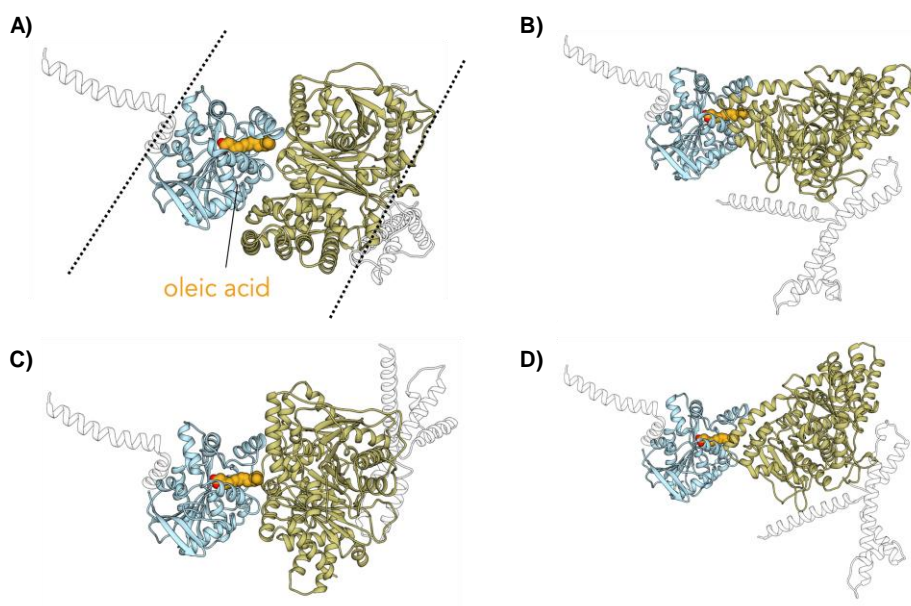
Figure 53. The most promising CPT1C-ABHD6 protein complex models. A) C1.1 model. B) C1.2 model. C) C2.1 model. D) C2.2 model. CPT1C and ABHD6 cytosolic domains are shown in khaki and light blue, respectively.

3.3. Critical binding residues identification

Finally, the most relevant hotspots residues for CPT1C-ABHD6 recognition were predicted by two computational approaches, per-residue energy decomposition and *in silico* alanine scanning. As shown in *Table 15*, at least one pair of residues were identified as hotspots for each protein complex model.

Complex	Protein	Residue	Per residue Binding Energy ΔG (Kcal/mol)	AlaScanning ΔΔG (Kcal/mol)
C1.1	**CPT1C**	Asp518	-3,2	-11,7
	ABHD6	Lys245	-2,3	-6,7
C1.2	**CPT1C**	Pro374	-2,6	-2,9
		Asp521	-2,8	-7,4
		Ser528	-2,5	-7,5
	ABHD6	Glu198	-7,0	-14,9
		Arg244	-3,0	-3,9
		Leu248	-3,2	-4,0
C2.1	**CPT1C**	His715	-2,4	-3,0
	ABHD6	Ser252	-2,7	-4,4

C2.2	**CPT1C**	Thr672	-4,7	-6,3
		Gln673	-2,4	-3,7
	ABHD6	Asp122	-2,1	-2,3
		Lys265	-7,6	-7,6

Table 15. Hotspots residues resulted from C1.1, C1.2, C2.1 and C2.2 model analysis.

In model C1.1, two residues, Asp518 and Lys245, were identified forming a salt bridge between their side chains *(Figure 54A)*. In model C1.2, six residues appeared particularly promising, namely Pro374 and Leu248, forming extensive hydrophobic interactions between their side chains, Asp521 and Arg244 interacting each other through a salt bridge, and finally Glu198 and Ser528 forming a hydrogen bond *(Figure 54B)*. In model C2.1, two residues were found as hotspots, the Ser252 and His715, forming a hydrogen bond between their side chains *(Figure 54C)*. And in model C2.2, the four residues Thr672, Lys265, Gln673 and Asp122, which interact with each other through hydrogen bonds, were found to be promising *(Figure 54D)*.
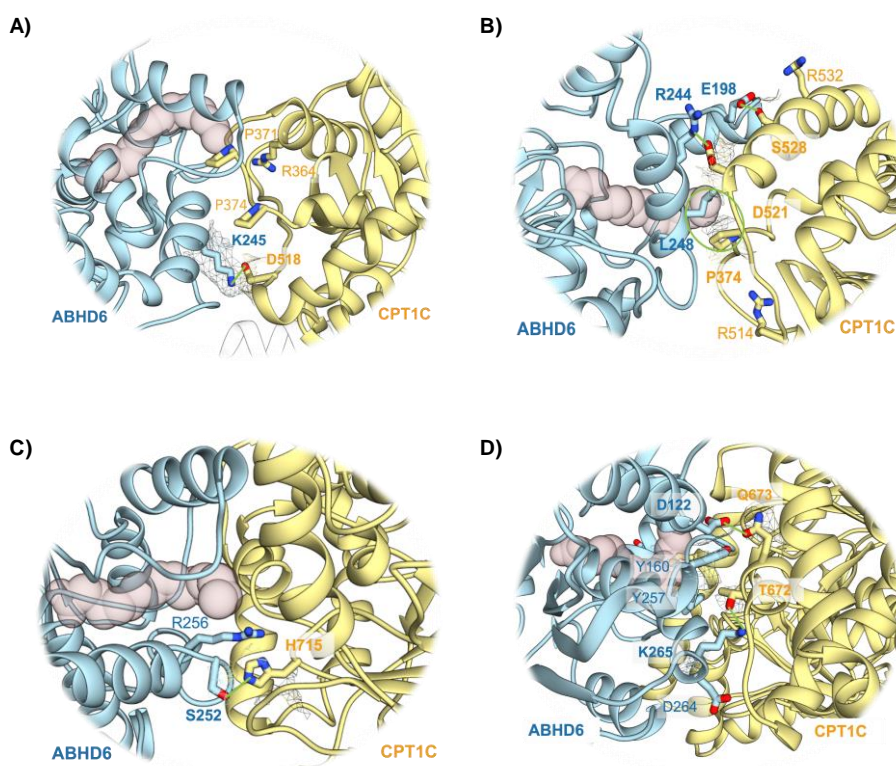
Figure 54. Hotspot residues for ABHD6-CPT1C interaction. A-D) Zoom-up of the C1.1 (A), C1.2 (B), C2.1 (C) and C2.2 (D) models interface region. CPT1C and ABHD6 cytosolic domains are shown in khaki and light blue, respectively. Hotspots residues are shown in sticks.

Based on these results, our next steps will be to elucidate which of these predicted models correspond to the CPT1C-ABHD6 interacting complex. We intend to perform directed mutagenesis on the amino acids described in *Table 15* and assess whether the interaction between both proteins is disrupted in any of these complexes.

4. Results summary of Chapter I

The main results obtained from the study of the subcellular localization and interaction of CPT1C and ABHD6 are represented in *Figure 55*.
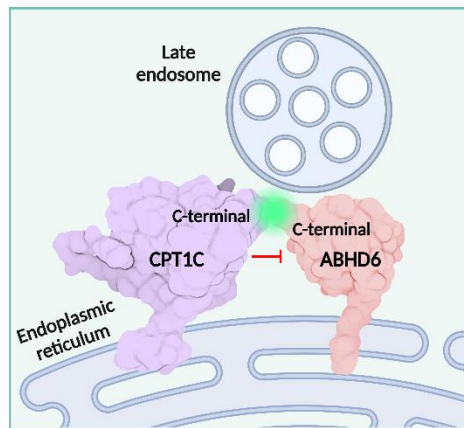
Figure 55. Graphical abstract of chapter II. CPT1C and ABHD6 colocalize in the ER, in close proximity to LEs. The C-terminal domains of CPT1C and ABHD6 are responsible for both their interaction and the inhibition of ABHD6 activity by CPT1C. -

DISCUSSION

Given the crucial role of the endolysosomal system in maintaining neuronal homeostasis and its association with numerous neurological diseases, research over the past few years has aimed to identify the fundamental players and mechanisms responsible for its function. Among these, the CPT1C-ABHD6 complex appears to play a significant role, particularly in the hypothalamus. Previous findings from our group have demonstrated that CPT1C negatively regulates the hydrolase activity of ABHD6 depending on nutrient status (Miralpeix et al., 2021). Additionally, ABHD6 hydrolyzes BMP, which is crucial for many endolysosomal processes (Pribasnig et al., 2015). Thus, this thesis delves into how the CPT1C-ABHD6 interaction in the hypothalamus might regulate BMP metabolism and subsequently endolysosomal function, and how this regulation is influenced by nutrients, especially saturated fatty acids. Importantly, understanding the impact of nutrients on endolysosomal function and neuronal homeostasis in the hypothalamus could provide new insight into the mechanisms underlying diet-induced obesity.

The role of the CPT1C-ABHD6 complex in BMP metabolism and endolysosomal function within the hypothalamus, particularly in response to LCFA, has been explored in the first chapter of this thesis. For the first time, we have demonstrated in both hypothalamic neuronal cells and brain tissues that CPT1C inhibition of ABHD6 activity is able to regulate BMP levels, and that such regulation is abolished upon exposure to saturated fatty acids. Considering the association of BMP metabolism with cholesterol trafficking and endolysosomal dynamics (Showalter et al., 2020), it is noteworthy that cells lacking CPT1C exhibit decreased cholesterol levels, an immature endolysosomal system, and impaired lysosomal activity.

Furthermore, the characterization of the subcellular location and the interaction between ABHD6 and CPT1C has been addressed in the second chapter. Importantly, we have found that both proteins colocalize in the ER, being ABHD6 in close proximity to LE/lysosomes, where it can both interact with CPT1C and hydrolyze BMP.

Altogether, and in accordance to the hypothesis of this thesis, we have demonstrated that CPT1C plays a role on BMP metabolism and endolysosomal function through its interaction with ABHD6, and this role is dependent on nutrients availability. In addition, our results suggest that CPT1C modulation of ABHD6 activity depends on their interaction by the cytoplasmic C-terminal tail, and that both proteins are located in the ER, with ABHD6 probably located in MCS with LEs/lysosomes.

1. CPT1C regulates BMP metabolism and endolysosomal functionality

Our group has recently uncovered an intriguing role for CPT1C as a negative regulator of ABHD6 activity, particularly within the hypothalamus (Miralpeix et al., 2021). ABHD6 was first identified as the newest 2-AG hydrolase of the eCB system (Cao et al., 2019), but further studies revealed its key function as a BMP hydrolase. Indeed, whereas ABHD6 is only responsible for 4% of the 2-AG hydrolysis in the brain, it hydrolyzes 50% and 90% of the BMP in the brain and liver, respectively (Pribasnig et al., 2015). Consistent with this, our hypothalamic CPT1C-KO cell model generated by CRISPR-Cas9 technology exhibited increased ABHD6 activity and decreased BMP levels when compared to WT cells. This modulation of hypothalamic BMP levels through the regulation of ABHD6 activity by CPT1C was further confirmed by measuring ABHD6 activity and BMP levels in hypothalamic homogenates from WT and CPT1C-KO mice. In hypothalamus of mice under SD conditions, the lack of CPT1C led to an increase in ABHD6 activity in CPT1C-KO mice and, although the difference was not significant ($p = 0.0631$), a tendency to decrease in BMP levels was also observed.

To confirm that the changes in hypothalamic BMP levels were due to CPT1C-mediated modulation of ABHD6 activity rather than the absence of CPT1C itself, the correlation between BMP levels and ABHD6 activity was demonstrated in our cell models using two different experimental approaches. First, a substrate competition assay in ABHD6 overexpressing HEK293T cells confirmed the specificity of ABHD6 for the BMP substrate, as previously performed in Miralpeix et al. (2021) for the 2-AG substrate. Then, we assessed BMP levels after pharmacological inhibition of ABHD6 activity with WWL70, a specific inhibitor of ABHD6 hydrolase activity (Blankman et al., 2007). This compound has been used by several researchers to demonstrate the involvement of ABHD6 in different functions. For instance, it was used by Fisette et al. to demonstrate that inhibition of ABHD6 activity in the VMH alters fasting-induced feeding in a 2-AG dependent manner (Fisette et al., 2016), or by Zhao et al. to determine that inhibition of ABHD6 induces insulin secretion in a MAG-dependent manner (Zhao et al., 2015). In our case, pharmacological inhibition of ABHD6 by WWL70 was conducted to elucidate whether the decrease in BMP levels observed in CPT1C-KO neuronal cells (GT1-7) was a consequence of the increased ABHD6 activity in these cells. We found that pharmacological inhibition of ABHD6 restored BMP levels in CPT1C-KO neurons, hence confirming that CPT1C regulates BMP levels through its interaction with ABHD6. Of note, treatment with WWL70 also increased BMP levels in WT cells, but to a lesser extent than in CPT1C-KO cells. In WT neuronal cells, ABHD6 activity is already inhibited by CPT1C, and therefore they start from higher BMP basal levels. Consequently, the increase in BMP levels after pharmacological inhibition of ABHD6 is not as significant as in CPT1C-KO

cells, where BMP basal levels are reduced due to the increased activity of ABHD6. These results support the role of CPT1C in BMP metabolism by modulating ABHD6 activity. Since BMP metabolism is poorly characterized, this finding sheds light on how BMP levels may be regulated in hypothalamic neurons. However, other mechanisms may be also involved.

The fact that ABHD6, being a cytosolic-faced protein (Pusch et al., 2022), is able to hydrolyze BMP that is present in the ILVs of endosomes (Kobayashi et al., 1998), is still a matter of debate. There is evidence that ILVs can fuse with the limiting membrane of LEs through a process known as "back-fusion". For instance, this phenomenon has been proposed for the recycling of mannose-6-phosphate receptors or EGF receptors, which are found to be enriched in ILVs (Eden & Futter, 2021). As a result, the lipids present in the ILV membrane become part of the endosomal limiting membrane. Therefore, as suggested by Zimmermann's group, ABHD6 would hydrolyze BMP when it becomes available after the back-fusion of ILVs with the limiting membrane of endosomes (Pribasnig et al., 2015).

Given that BMP is crucial for the correct function of the endolysosomal system, particularly by regulating cholesterol trafficking, ILV formation, and lysosomal proteins activity (Showalter et al., 2020), we explored the implications of an attenuation of BMP levels in hypothalamic CPT1C-KO neurons concerning these BMP-related functions. Importantly, our results clearly show that CPT1C-KO GT1-7 cells exhibited decreased intracellular cholesterol levels, reduced ILV density within endosomes and impaired lysosomal activity when compared to WT cells.

Intracellular cholesterol levels are dynamically regulated through various mechanisms, including *de novo* biosynthesis, exogenous uptake, storage, and export (Shi et al., 2022). In general, cells acquire cholesterol through endocytosis of LDL. After LDL internalization, endosomes play a key role in regulating the fate of endocytosed cholesterol. The majority of cholesterol is delivered to the PM, while some of it is transported to the ER to enable feedback control or undergoes esterification for storage in lipid droplets (Enrich et al., 2015). Within endosomes, BMP has been suggested to control their cholesterol capacity by the formation of ILVs (Chevallier et al., 2008), and to facilitate the export of cholesterol from endosomes through the interaction with NPC2 (Enkavi et al., 2017; McCauliff et al., 2019). These functions are further supported by the fact that both BMP and cholesterol are abundant within intralumenal membranes of endosomes (Kobayashi et al., 1998; Möbius et al., 2003), and that BMP and cholesterol accumulate in NPC cells concomitantly with an increase in the size of LEs as a compensatory mechanism to accommodate excess cholesterol (Sobo et al., 2007). In the study conducted by Chevallier et al. (2008), they observed that decreasing BMP levels by downregulating Alix led to a concomitant decrease in ILVs within endosomes and intracellular cholesterol levels, both of which were restored upon incubation

with exogenous BMP. Our findings in hypothalamic cells align with their observations, as the decrease in BMP levels observed in CPT1C-KO neuronal cells is accompanied by reduced ILV density within endosomes and decreased cholesterol levels. Importantly, cholesterol levels were measured by filipin staining, which stains free cholesterol (present in biological membranes), not esterified cholesterol (Maxfield & Wüstner, 2012), meaning that the decrease observed corresponds to total membrane cholesterol levels. However, it should be noted that we have not specifically measured cholesterol in endosomes. Therefore, to fully confirm that in our hypothalamic model BMP is regulating the capacity of endosomes to accommodate cholesterol, it would be necessary to assess whether the decreased cholesterol observed in CPT1C-KO cells corresponds to endosomal cholesterol.

Notably, Incubation with PG, the precursor of BMP, increased BMP levels in both WT and CPT1C-KO neuronal cells, but only led to an increase in intracellular cholesterol levels in WT cells. The advantages of PG or BMP supplementation have been widely explored in cell models characterized by pathological cholesterol accumulation (i.e., NPC cells) (Chevallier et al., 2008; Ilnytska et al., 2021; McCauliff et al., 2019; Moreau et al., 2019), but less is known about the effects on cholesterol trafficking after inducing BMP increase in non-NPC cells. Interestingly, one recent study found that while U18666A, a drug that inhibits NPC1 activity, induced cholesterol accumulation and consequently increased BMP levels in common cell lines (e.g., HeLa cells), another drug named thioperamide increased BMP levels without causing cholesterol accumulation (Moreau et al., 2019). These findings are particularly interesting, as they not only suggest the potential utility of thioperamide for NPC treatment but also indicate that in cells without pathological cholesterol accumulation, an increase in BMP does not necessarily result in elevated cholesterol levels.

Taking that into consideration, our findings after PG supplementation suggest two important points. Firstly, the increase in BMP levels following PG supplementation indicates that the biosynthesis of BMP is not impaired in either WT or CPT1C-KO cells, further supporting the idea that cells lacking CPT1C have reduced BMP levels due to increased BMP hydrolysis rather than decreased BMP synthesis. Secondly, the fact that the increase in BMP results in a slight rise in intracellular cholesterol in WT but not in CPT1C-KO cells aligns with the proposed role of BMP in accommodating cholesterol in control neuronal cells, and also suggest that mechanisms other than the cholesterol accommodation function by BMP may be occurring in CPT1C KO cells. For instance, given that CPT1C-KO neuronal cells contain less basal cholesterol than WT cells, CPT1C could be influencing intracellular cholesterol by regulating its uptake through other pathways. In this context, even though BMP levels rise in CPT1C-KO cells following PG supplementation, intracellular cholesterol levels would not increase due to their lack of uptake. Nonetheless, to our knowledge, the role of CPT1C in regulating cholesterol trafficking remains unknown to date.

The reduced content of ILVs within endosomes of CPT1C-KO cells suggests that deleting CPT1C have an impact in the maturation process of endosomes. Considering the roles that ILVs play in the endolysosomal system, defects in their formation derive in important alterations in the signaling and degradation functions of the endolysosomal system. ILVs are formed through the invagination of the endosomal membrane and, once formed, ILVs can follow different pathways. ILVs containing cargoes destined for degradation are delivered to lysosomes, where they are degraded together with their cargo, whereas other ILVs may be released into the extracellular space upon fusion of LEs with the PM as exosomes (Gruenberg, 2020). Exosomes are considered critical mediators of intercellular communication. They can carry specific proteins, lipids, nucleic acids and other cargoes to mediate a wide range of effects in target cells, including synaptic plasticity, nutritional metabolic support, nerve regeneration or inflammatory responses, among others (reviewed in Huo et al., 2021). Moreover, exosome production is crucial in preserving the flux through the neuronal endosomal pathway by decompressing "traffic jams", especially by delivering endosomal-lysosomal material into the extracellular space, where other cell types can assist in its degradation (reviewed in Mathews & Levy, 2019). Considering the important function of exosomes in intercellular communication and endosomal pathway integrity, alterations in exosome secretion could lead to important disruptions in neuronal functions, potentially contributing to the pathogenesis of neuronal disorders. In fact, secretion of exosomes containing BMP has been reported to serve as a homeostatic response to counteract lysosomal dysfunction (Miranda et al., 2018). Furthermore, a very recent study suggested that hypothalamic neuronal exosomes may play a role in the control of energy homeostasis. They found that hypothalamic NPY/AgRP neurons secreted exosomes able to mediate anorexigenic effects through the modulation of target genes in POMC neurons, and that this effect was absent after exposure to palmitate, thereby unraveling another route by which palmitate promotes obesity (McIlwraith & Belsham, 2023). Since CPT1C-KO cells contain less ILVs within endosomes, it would be very interesting to analyze if these cells release less exosomes to the extracellular space than WT cells.

Besides the low density of ILVs within endosomes, CPT1C-KO cells also showed smaller endosome and lysosomal compartments. As stated by the title of the review authored by de Araujo et al. (2020), "lysosomal size matters", the size of these organelles has a strong impact on lysosomal activity, ultimately influencing cellular homeostasis. Accordingly, endolysosomes and lysosomes of CPT1C-KO cells exhibited less acidified lysosomes and decreased activity of cathepsin B, one of the main proteases responsible for lysosomal activity (Appelqvist et al., 2013), when compared to WT cells. The role of BMP in lysosomal activity is further supported by the fact that treatment of NPC1 fibroblasts with PG induced

a reacidification of lysosomes and an improvement of lysosomal homeostasis (Ilnytska et al., 2021).

Formation of ILVs, change in endosome size and morphology, acidification of endolysosomal compartments, and gain of lysosomal hydrolases are processes that occur during endosome maturation and are critical for the correct function of the endolysosomal system (Huotari & Helenius, 2011). Taken together, our findings reveal a new potential role for CPT1C in the endolysosomal system, most likely associated with its involvement in BMP metabolism via ABHD6 interaction. To fully elucidate whether the maturation and function of endosomes and lysosomes depends on the CPT1C-ABHD6-BMP axis, it would be of significant interest to explore if the content of ILVs within endosomes, as well as the acidity and activity of lysosomes, are restored by increasing BMP levels in CPT1C-KO cells, either through pharmacological inhibition of ABHD6 or PG supplementation. Furthermore, considering that CPT1C also regulates protrudin activity regarding LE/lysosome transport, the possibility exists that CPT1C may also modulate some functions of the endolysosomal system independently of ABHD6.

Endosomes and lysosomes establish MCS with most organelles of the cell, including the ER, the Golgi, peroxisomes and mitochondria. The most widely studied MCS population formed by endocytic organelles is the ER-endosome contact. These contacts are dynamic and increase during endosome maturation, and have been found to be involved in different process (Friedman et al., 2013). Particularly, MCS between endosomes and the ER have a key role in cholesterol trafficking and endosome dynamics (Cabukusta & Neefjes, 2018; Eden, 2016; Enrich et al., 2019; Martello et al., 2020; Raiborg et al., 2016).

Regarding cholesterol trafficking, MCS between LE and ER have a very important role in mediating cholesterol egress from endocytic compartments. Different studies have identified interactions between LE/lysosome sterol-binding proteins and ER proteins at MCS, leading to propose these MCS as conduits for cholesterol transport from LE/lysosomes to the ER (reviewed in Martello et al., 2020; Phillips & Voeltz, 2016; Ridgway & Zhao, 2018). For instance, ORP1L or NPC1, located at the limiting membrane of LEs, have been reported to be involved in the formation of MCS with the ER to mediate cholesterol clearance (Höglinger et al., 2019; Meneses-Salas et al., 2019; Zhao & Ridgway, 2017).

MCS between ER and LEs also regulate endosome positioning. Importantly, they are involved in LE translocation and neurite outgrowth through a mechanism mediated by protrudin and FYCO. The ER-resident protein protrudin forms MCS with LEs via interaction with Rab7. This allows the transfer of kinesin-1 from protrudin to FYCO1, which in turn mediates the anterograde transport of LEs along microtubules. Close to the tip of the forming neurite, LEs fuse with the plasma membrane to induce protrusion formation and neurite outgrowth

(Raiborg et al., 2015). Our group demonstrated later that this anterograde transport of LEs mediated by protrudin was dependent on the nutritional status of the cell, sensed by CPT1C. When malonyl-CoA levels drop due to glucose deprivation, the anterograde transport of these organelles is paralyzed, and they remain in the perinuclear area. Similarly, in the absence of CPT1C, protrudin-dependent transport of LEs is less efficient, resulting in reduced axonal growth (Palomo-Guerrero et al., 2019).

Additionally, endosome maturation also depends on MCS between ER and LEs. A recent study identified that tethering of LEs to the ER via a VAP-protrudin-PDZD8 complex increased the size and the formation of ILVs within LEs, due to the role of PDZD8 in lipid transfer from ER to LEs (Shirane et al., 2020).

Considering the diverse range of functions mediated by LE-ER MCS, many questions arise from our findings. How is CPT1C influencing the formation of MCS between LE and ER? What repercussions does the decrease in LE-ER MCS have? Are these contacts influencing the CPT1C-ABHD6-dependent BMP hydrolysis?

In accordance with the role of CPT1C in regulating LE/lysosome anterograde transport through its interaction with protrudin (Palomo-Guerrero et al., 2019), one plausible interpretation of our findings is that CPT1C might be modulating both protrudin's function in facilitating kinesin-1 transfer to LEs and its involvement in MCS formation through its interaction with Rab7. Additionally, since mutations in both CPT1C and protrudin have been linked to HSP (Hashimoto et al., 2014; Rinaldi et al., 2015), impaired transport of LEs could be one of the underlying mechanisms mediating the pathogenesis of the disease.

Importantly, the reduction in MCS between endosomes and the ER observed in CPT1C-KO cells was only significant in the later stages of endosome maturation, being even more pronounced in endolysosomes than in LEs. Given that MCS formation increases as endosomes traffic and mature (Friedman et al., 2013), and that these MCS contribute to the formation of ILVs (Shirane et al., 2020), our results suggest that CPT1C, through its role in mediating MCS, may assist in endosome maturation, thus providing another potential mechanism through which the absence of CPT1C results in less mature endosomes.

In our hypothalamic cell model, the lack of CPT1C resulted in reduced MCS between mature endosomes and the ER, but not in cholesterol accumulation, thus suggesting that the decrease in MCS between endosomes and ER does not impair cholesterol efflux in CPT1C-KO cells. Transport of cholesterol within CPT1C-KO cells is probably mediated by other mechanisms rather than by MCS. In fact, it is estimated that direct transport mechanisms between LE/lysosomes and ER via MCS contribute to roughly 30% of LDL-derived cholesterol delivery to the ER (Martello et al., 2020). Another possibility, as mentioned earlier, could be

that CPT1C-KO cells do not accumulate cholesterol because they might have impaired cholesterol uptake.

The interaction of CPT1C and ABHD6 seems to occur at the cytosolic facing membrane of the ER, while BMP is primarily found in LEs. These facts suggest that BMP hydrolysis requires the presence of MCS between LEs and the ER. However, whether its hydrolysis is dependent on MCS formation is not elucidated in our results. Deletion of CPT1C in hypothalamic cells increases BMP hydrolysis as well as decreases the formation of LE-ER MCS. These findings seem to be contradictory. Nevertheless, it is worth noting that a significant proportion of MCS persist between LE and ER even in the absence of CPT1C, which would be enough for ABHD6 to access and efficiently hydrolyze BMP.

After confirming the role of CPT1C in BMP metabolism and endolysosomal function, we observed that this regulation of CPT1C is dependent on lipid sensing, since some of the effects described for CPT1C in BMP metabolism and in endolysosomal function appeared to be blunted upon exposure to saturated fatty acids. We have previously reported that CPT1C modulates the activity of ABHD6 depending on malonyl-CoA sensing. When malonyl-CoA levels decrease, CPT1C is not able to inhibit ABHD6 activity (Miralpeix et al., 2021). Malonyl-CoA levels fluctuate in response to different stimulus (Fadó et al., 2021). For instance, palmitoyl-CoA, as an allosteric inhibitor of ACC, decreases the synthesis of malonyl-CoA (Hunkeler et al., 2018). Moreover, unsaturated FAs decrease the synthesis of FAs, presumably leading to the accumulation of its precursor malonyl-CoA, whereas saturated FAs have the contrary effect (Fosch et al., 2023). Accordingly, exposure to PA but not OA induced a decrease in BMP levels in hypothalamic WT cells. The decrease in BMP levels after PA treatment was explained by the increase in ABHD6 activity. Such events were not observed in CPT1C-KO neuronal cells, thereby confirming the lipid sensing-dependent role of CPT1C in BMP metabolism. Moreover, the decrease in BMP levels was accompanied by a decrease in cholesterol present in cellular membranes, which further supported the role of BMP in cholesterol homeostasis, as discussed above. To our knowledge, the impact of PA in hypothalamic neurons regarding cholesterol has not been previously reported.

Regarding lysosomal function under PA treatment, we would expect that, similarly to the BMP levels decrease by PA, it would also decrease lysosomal activity. However, what we observe is that PA treatment increases the acidity and the size of lysosomes in both WT and CPT1C-KO cells, casting doubt on the role of CPT1C in lysosomal function through the regulation of BMP under exposure to PA. As stated by Hernández-Cáceres et al. (2020), PA reduces the autophagic flux by inhibiting the fusion of autophagosomes with lysosomes, leading to the swelling of endocytic compartments. Interestingly, even though PA induced the same effects in both WT and CPT1C-KO cells, we observe significant differences between

WT and CPT1C-KO cells under the same conditions. Under PA exposure, acidity increases in both WT and CPT1C-KO cells compared to the BSA condition, but the increase in CPT1C-KO cells is not as pronounced as that in WT cells. Furthermore, the enlargement of vesicles is greater in CPT1C-KO cells than in WT cells after PA incubation. These findings suggest that CPT1C might play a role in PA-mediated endolysosomal function, likely through the regulation of autophagy rather than by modulating BMP levels. To date, the involvement of CPT1C in autophagy has not been described in neuronal cells. However, in human mesenchymal stem cells, overexpression of CPT1C has been found to enhance autophagy (Roa-Mansergas et al., 2018). The role of CPT1C in favoring autophagy would explain why the inhibition of the autophagic flux by PA is more pronounced in CPT1C-KO cells. Nevertheless, further experiments, such as the analysis of autophagic markers in WT and CPT1C-KO cells following exposure to PA, are needed to confirm this hypothesis.

Finally, the role of CPT1C in BMP metabolism in response to lipid sensing was also evaluated in animal models. BMP levels and ABHD6 activity were measured in the hypothalamus, hippocampus and liver of both WT and CPT1C-KO mice under short-term SD or HFD intake. In line with our observations in hypothalamic cells, 7 days HFD caused a slight decrease in hypothalamic BMP levels in WT mice, accompanied by an increase in ABHD6 activity, while no significant differences were detected in hypothalamus of CPT1C-KO animals following HFD. Notably, we found that the increase in ABHD6 activity in the hypothalamus was triggered by the presence of SFAs in the diet rather than MUFAs, which blunted the inhibitory effect of CPT1C on ABHD6 activity probably by inducing a reduction in malonyl-CoA levels.

In the hippocampus, BMP levels under SD showed no significant differences between WT and CPT1C-KO mice, despite the increase in ABHD6 activity, and remained unchanged following HFD. Unlike in the hypothalamus, hippocampal ABHD6 activity did not increase in WT mice under HFD, aligning with our previous observations in Miralpeix et al. (2021), in which fasting induced a significant increase in ABHD6 activity in the hypothalamus of WT mice but not in the hippocampus. These changes in ABHD6 activity are attributed to CPT1C's sensing of malonyl-CoA, whose levels are presumably decreased after both fasting and HFD. Therefore, the observed differences between the analyzed brain tissues suggests that the role of CPT1C in modulating BMP levels and ABHD6 activity is more evident in the hypothalamus than in the hippocampus. One possible explanation for this difference is that the hypothalamus is especially permeable to nutrients (Haddad-Tóvolli et al., 2017), hence being more sensible to dietary changes.

Zimmermann's group conducted a very interesting study in which they described how different tissues exhibit distinct BMP profiles regulated by the nutritional state in a tissue-specific manner. Interestingly, they observed that BMP levels decreased in most tissues

following refeeding but increased in the brain (Grabner et al., 2020). In this context, the role of CPT1C in BMP metabolism in response to nutrient sensing could potentially explain their findings. During fasting, malonyl-CoA levels decrease and CPT1C is no longer able to inhibit ABHD6 activity (Miralpeix et al., 2021), presumably resulting in increased BMP hydrolysis and reduced BMP levels. Conversely, refeeding would restore malonyl-CoA levels and CPT1C's inhibitory capacity on ABHD6 activity, allowing BMP levels to recover. However, it is important to highlight that this assumption needs further validation, given that Zimmermann's study analyzed BMP levels in the whole brain, while our findings are primarily focused on the hypothalamus.

Regarding hepatic BMP and ABHD6 activity in WT and CPT1C-KO mice under SD or HFD, the liver displayed a quite different pattern compared to brain tissues, which was already expected as CPT1C expression is limited to the brain. In contrast to brain tissues, BMP levels under SD are higher in CPT1C-KO mice than in WT mice. This finding suggests that CPT1C may have an impact on BMP metabolism in peripheral tissues, but not through its direct interaction with ABHD6, as CPT1C is not reported to be expressed in the liver, and furthermore, the activity of ABHD6 does not correlate with BMP levels. Moreover, exposure to HFD decreased BMP levels in both WT and CPT1C-KO mice, indicating that lipid overload has a direct impact on hepatic BMP independently of CPT1C. Surprisingly, other studies have reported that HFD increases hepatic BMP content in mice (d'Avignon et al., 2018; Grabner et al., 2019; Pribasnig et al., 2015), which contradicts our findings. However, it is important to note that these studies assessed BMP levels after feeding mice a HFD for 12 weeks (Grabner et al., 2019; Pribasnig et al., 2015) or 35 weeks (d'Avignon et al., 2018), whereas our results are derived from mice fed a HFD for only 1 week. Collectively, these findings suggest that HFD induces a transient decrease in hepatic BMP content, followed by an increase with long-term HFD exposure, revealing for the first time a potential dynamic of BMP throughout the development of obesity. The lack of correlation between BMP levels and ABHD6 activity suggests that, even though ABHD6 plays a key role as a BMP hydrolase in the liver (Pribasnig et al., 2015), hepatic BMP content is likely influenced by other mechanisms, possibly involving export into the circulation. Indeed, ABHD6-KO mice exhibited a significant decrease in BMP hydrolase activity but showed no changes in total BMP levels in the liver. Instead, BMP was found to be released into the circulation, even to a greater extent under lipid overload, thus becoming a marker in obesity development (Grabner et al., 2019). Therefore, it would be very interesting to analyze the circulating BMP profile in our animal models under SD and HFD, as BMP content within the different tissues might not fully reflect the dynamic changes in BMP metabolism. Nonetheless, the mechanism of BMP release into the circulation remains poorly understood.

We also observed distinct BMP FA compositions in the different tissues, and consistent with the findings of Grabner et al. (2020), HFD affected BMP levels in a tissue-specific manner. Hypothalamus and hippocampus predominantly contained BMP esterified with DHA, and the most notable alterations following HFD were observed in BMP species esterified with arachidonic acid and DHA. In contrast, BMP in liver was mostly esterified with oleic acid and DHA, and accordingly, the most remarkable alterations after HFD were observed in BMP species containing oleic acid, linoleic acid and DHA. The importance of identifying BMP species resides in the characterization of BMP as a biomarker in disease, since different circulating BMP profiles have been associated with diseases of different degrees and origin (Grabner et al., 2019).

Altogether, our findings in animal models demonstrate that various tissues exhibit distinct responses to short-term HFD concerning BMP metabolism, supporting the importance of BMP in the functional adaptation to changing metabolic conditions (Grabner et al., 2020). Moreover, the different responses observed in brain tissues, where CPT1C is expressed, in comparison to peripheral tissues, underscore the role of CPT1C in BMP metabolism, particularly in the hypothalamus. Nevertheless, further investigation is needed to fully understand how CPT1C is regulating BMP dynamics in the context of obesity.

In conclusion, these results position CPT1C within the intricate network of molecular mechanisms that regulate the endolysosomal system in the hypothalamus. CPT1C, through its interaction with ABHD6, regulates BMP levels depending on the sensing of lipids, particularly in hypothalamic neurons. Moreover, CPT1C is necessary for cholesterol trafficking and for the correct function of the endolysosomal system. Nevertheless, whether the role of CPT1C in endolysosomal function is modulated through the ABHD6-BMP axis remains to be elucidated. Altogether, these findings highlight the significance of CPT1C in maintaining neuronal homeostasis, especially in the hypothalamus, and could contribute to a better understanding of the pathogenesis of conditions associated with endolysosomal dysfunction, such as obesity or neurodegeneration.

2. CPT1C and ABHD6 colocalize in the ER and interact by their C-terminal domain

The first evidence reporting the association between CPT1C and ABHD6 came from Fakler's group. They discovered that both CPT1C and ABHD6 are present in native AMPAR complexes, where they play a crucial role in the ER assembly line of AMPAR (Brechet et al., 2017; Schwenk et al., 2012, 2019). Subsequently, we reported that CPT1C interacts with ABHD6 and negatively regulates its hydrolase activity (Miralpeix et al., 2021). Consistent with these findings, we observed that both proteins, when overexpressed in HeLa cells, exhibited a

reticular pattern and a high degree of colocalization with calnexin, considered an ER marker, as well as with each other.

Interestingly, nearly the entire CPT1C signal overlapped with the signal of ABHD6, but not the other way around. A small proportion of ABHD6 did not colocalize with CPT1C, appearing as small red dots within the cell. This suggests that ABHD6 might be also located elsewhere apart from interacting with CPT1C. Indeed, when analyzing the colocalization of CPT1C or ABHD6 with LAMP1 or BMP, which are present in LE/lysosomes, we observed that a higher fraction of both LAMP1 and BMP colocalized with ABHD6 compared to CPT1C. Although further analysis is required for confirmation, this finding could indicate that a portion of ABHD6 protein might be in close approximation with LE/lysosomes where it can hydrolyze BMP, aligning with the study of Pribasnig et al. (2015) in which they described the presence of ABHD6 in LE/lysosomes and its role degrading BMP. Furthermore, it is worth noting that our results show that not all BMP signal colocalizes with LAMP1. This may be explained by the heterogeneity of the endocytic organelles. While both LAMP1 and BMP are considered LE/lysosomal markers, they has been associated with different subpopulations of these organelles (Cheng et al., 2018; White et al., 2006; Yap et al., 2018). Therefore, there are LE/lysosomes containing BMP but not LAMP1, and vice versa.

While it is widely accepted that CPT1C is localized in the ER (Casals et al., 2016), there has been more discrepancies regarding the localization of ABHD6. One first study reported the presence of endogenous ABHD6 in cellular fractions enriched in mitochondria obtained from BV-2 cells (Marrs et al., 2010). In this study, though, it was not specified if other organelles or membranes associated to mitochondria were present in that mitochondria-enriched fraction. Years later, a second study explored the subcellular localization of ABHD6 in both endogenous and overexpressing models (Pribasnig et al., 2015). When analyzing endogenous ABHD6 protein levels in liver lysates from mice after subcellular fractionation, they observed that ABHD6 was detected in cellular fractions containing LE/lysosomes, while when overexpressing ABHD6 in COS-7 cells, ABHD6 emerged enriched in ER membrane structures and on vesicles positive for Rab7 (marker of LE/lysosomes) but not Rab5 (marker of EEs). Furthermore, the colocalization of ABHD6 with LE/lysosomes was more prominent under low ABHD6 overexpression, indicating that overexpression of proteins has an impact on their subcellular localization. Finally, the study of Fakler's group detected the endogenous presence of ABHD6 together with CPT1C in ER membranes after subcellular fractionation from whole mouse brains (Schwenk et al., 2019).

Here, it is worth noting that our findings are based on overexpression cell models and, therefore, may not reflect the real subcellular distribution of the proteins. Nonetheless, what we can conclude from contrasting our findings with previous literature regarding CPT1C and

ABHD6 localization, is that CPT1C is an ER-resident protein and ABHD6 might be located dynamically between ER and LE/lysosomes, maybe at MCS between these two organelles, where it can both interact with CPT1C and hydrolyze BMP. In fact, preliminary results of our group derived from subcellular fractionation of mouse brain homogenates align with this hypothesis, since ABHD6 expression was found in cellular fractions containing ER and endosomes *(Figure attached in Appendix II)*.

To study the interaction of CPT1C with ABHD6, we generated different protein constructs lacking specific structural domains. The last 39 amino acids and the N-terminal domain of CPT1C are the regions that most differ from the canonical isoforms, CPT1A and CPT1B (Casals et al., 2016). Given that in our previous study we reported that the removal of the last 39 amino acids from the CPT1C C-terminal tail did not affect its interaction with ABHD6 (Miralpeix et al., 2021), we explored whether the responsible domain for this interaction was located in its N-terminal region. Therefore, we deleted either the first 26 amino acids of the N-terminal domain or the whole N-terminal domain of CPT1C to analyze its repercussions on the CPT1C-ABHD6 interaction. Importantly, the deletion of the first amino acids of CPT1C did not impair its expression in cells.

Regarding ABHD6, there have been no previous studies shedding light on which structural domains of ABHD6 might be involved in its interaction with CPT1C. For that reason, we decided to explore both the involvement of the N-terminal domain and the C-terminal domain in its interaction. Additionally, based on the proteomic characterization of a recombinant ABHD6 (Shields et al., 2019), we also generated a construct in which the first 29 amino acids, comprising the N-terminal and transmembrane domains of ABHD6, were deleted. However, this latter construct was poorly expressed in cells and did not exhibit an equivalent hydrolytic activity to the full-size ABHD6 protein, probably due to changes in protein localization and conformation derived from the deletion of the transmembrane domain. Consequently, we only included the ABHD6 protein constructs lacking the N-terminal or the C-terminal domain in the subsequent interaction analyses.

The interaction analyses were conducted by FRET assays, which allow the assessment of protein interactions in living cells. Our results suggested that the interaction between CPT1C and ABHD6 likely occurs through their C-terminal domains, as deletion of the N-terminal domain in both proteins did not affect their interaction. As previously mentioned, the last 39 amino acids of the C-terminal domain of CPT1C have not been found to be necessary for the interaction with ABHD6 (Miralpeix et al., 2021). Therefore, based on the data reported so far, it is probable that CPT1C interacts with ABHD6 through other residues present in the C-terminal domain.

The fact that the N-terminal domains of CPT1C and ABHD6 are not responsible for their interaction does not exclude the possibility of these domains being involved in the regulation of ABHD6 activity by CPT1C. Our group has previously reported that CPT1C interacts with and regulates the activity of protrudin, SAC1, or ABHD6 depending on malonyl-CoA sensing (Casas et al., 2020; Miralpeix et al., 2021; Palomo-Guerrero et al., 2019). In all three studies, malonyl-CoA sensing affected the regulatory role of CPT1C on its partners' activity but not their interaction. It has been proposed that the N-terminal domain of CPT1C undergoes a conformational change depending on malonyl-CoA binding (Palomo-Guerrero et al., 2019; Rao et al., 2011; Samanta et al., 2014), which led us to hypothesize that this mechanism is how CPT1C regulates the function of the other proteins while still interacting with them. However, no significant differences were observed in ABHD6 activity, regardless of whether it was co-expressed with full-size CPT1C or CPT1C lacking the N-terminal domain. These findings indicate that the N-terminal domain of CPT1C is not responsible for the regulation of ABHD6 activity, thus dismissing the hypothesis of the N-terminal conformational change, at least in the context of the CPT1C-ABHD6 interaction. Furthermore, the deletion of the ABHD6 N-terminal domain did not prevent its inhibition by CPT1C, leading us to conclude that both the CPT1C-ABHD6 interaction and activity regulation are mediated by their respective C-terminal domains.

Finally, *in silico* modeling of the CPT1C-ABHD6 interaction identified four potential interacting complexes. According to our findings, only the C-terminal domains of both proteins were considered for this study. In all the four models, the substrate binding pocket of ABHD6 is located within the interaction interface, suggesting a potential mechanism through which CPT1C would inhibit ABHD6 activity by interfering with its binding region. Given that CPT1C modulates ABHD6 activity depending on malonyl-CoA sensing, we hypothesize that malonyl-CoA depletion due to fasting or exposure to saturated FAs would induce a conformational change in CPT1C, making the ABHD6 substrate binding pocket more accessible, thus leading to increased ABHD6 hydrolase activity. Additionally, different residues located at the predicted interacting interface were identified as relevant hotspots for the CPT1C-ABHD6 interaction within each complex. However, further research is needed in order to clarify whether the interaction of CPT1C with ABHD6 occurs through one of the proposed models. For instance, an interesting approach would be analyzing the interaction of both proteins after conducting directed mutagenesis on the predicted amino acids.

In conclusion, these findings provide new insights into the subcellular localization and the interaction of CPT1C and ABHD6. Unraveling the subcellular localization of these proteins could enhance our understanding of CPT1C's role in both the formation of MCS between the ER and LE/lysosomes and the modulation of BMP metabolism through its interaction with ABHD6, as discussed in chapter I. Moreover, given that ABHD6 is associated with various

pathologies, including epilepsy, traumatic brain injury, multiple sclerosis and obesity (Cao et al., 2019), a deeper understanding of how CPT1C interacts with and modulates ABHD6 activity could help develop novel therapeutic strategies to address these conditions.

3. Concluding remarks

Overall, this thesis has described for the first time the involvement of the CPT1C-ABHD6 interaction in BMP metabolism and has reaffirmed that CPT1C's functions are specifically linked to the nutritional status of the cell. Furthermore, this thesis has unveiled novel roles for CPT1C in cholesterol trafficking and endolysosomal function, although it remains to be elucidated whether these roles are dependent on its interaction with ABHD6. Regarding the interaction between CPT1C and ABHD6, this thesis has also shed light into the motifs responsible for the interaction and where this interaction might be taking place within the cell.

Based on our findings, we propose that CPT1C regulates BMP levels in both hypothalamic cells and tissues by modulating ABHD6 activity depending on malonyl-CoA sensing, whose levels fluctuate in response to nutrients. This regulation, in turn, impacts BMP-related functions within the endolysosomal system, such as cholesterol trafficking, the formation of ILVs and endolysosomal activity. Furthermore, we propose that CPT1C is involved in the formation of MCS between the ER and LEs, where its interaction with ABHD6 through their C-terminal domains likely takes place *(Figure 56)*.

Collectively, these findings reveal the importance of the CPT1C-ABHD6-BMP axis for the proper function of the endolysosomal system in hypothalamic neurons. Given the critical role of this system in neuronal homeostasis and its association with various neurological diseases, including obesity, our results provide new insights into understanding the impact of nutrients within the hypothalamus and into the future development of therapeutic strategies to address these conditions.
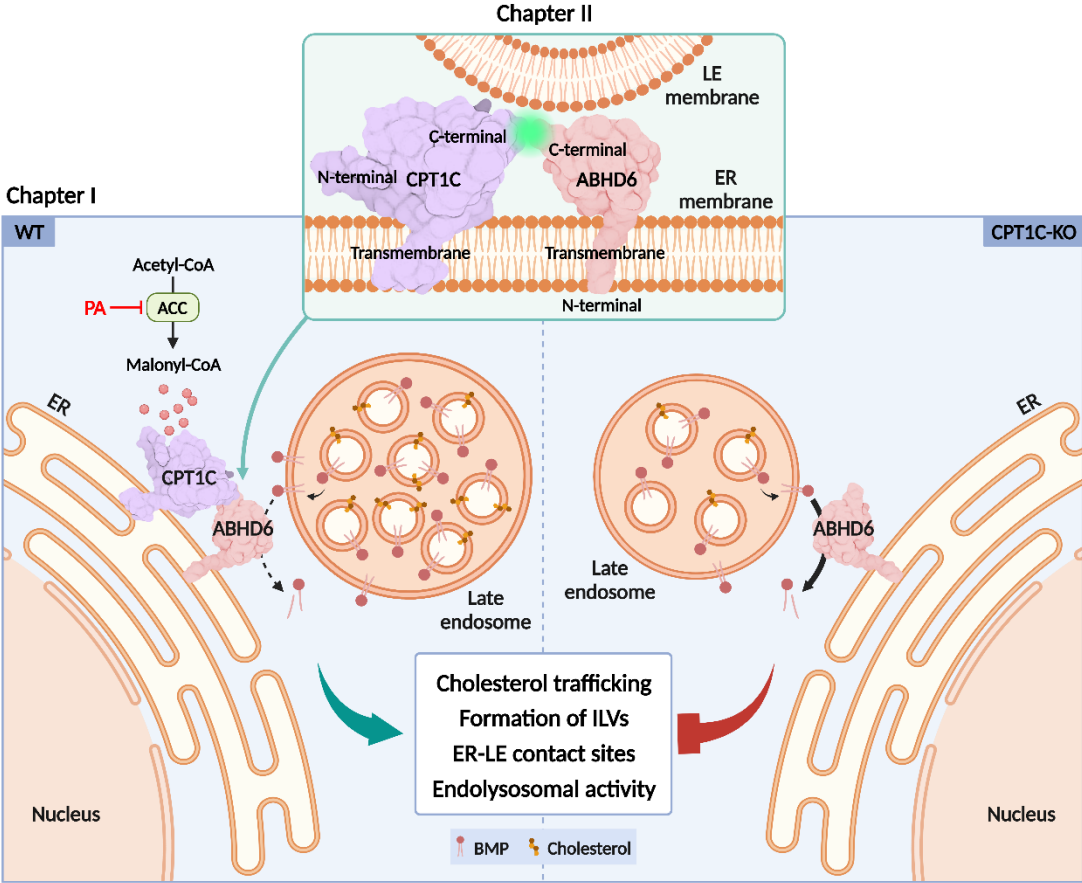
Figure 56. Graphical abstract of thesis concluding remarks. CPT1C modulates BMP metabolism, cholesterol trafficking and endolysosomal function (Chapter I) through its interaction with ABHD6, which occurs between their C-terminal domains (Chapter II). ER: Endoplasmic reticulum; LE: Late endosome; PA: palmitic acid.

CONCLUSIONS

1. CPT1C regulates BMP hydrolysis by modulating ABHD6 activity in hypothalamic neuronal cells.

2. Deletion of CPT1C decreases cholesterol levels in hypothalamic neuronal cells.

3. CPT1C is relevant for the endolysosomal function since the lack of CPT1C in hypothalamic neuronal cells results in endosomal immaturity, reduced LE-ER contact sites, less acidic lysosomes, and decreased lysosomal activity.

4. The function of CPT1C on BMP metabolism and cholesterol trafficking in hypothalamic neuronal cells depends on malonyl-CoA sensing, whose synthesis is affected by saturated fatty acids like PA.

5. The CPT1C-ABHD6-BMP axis found in the hypothalamus is dysregulated after short-term exposure to a HFD, primarily due to the presence of saturated fatty acids in it.

6. CPT1C and ABHD6 colocalize in the ER. They also colocalize with LE/lysosome markers, showing ABHD6 a higher degree of colocalization than CPT1C, indicating that the CPT1C-ABHD6 interaction takes place in the ER in close proximity to LE/lysosomes, where ABHD6 can hydrolyze BMP.

7. The interaction between CPT1C and ABHD6, as well as the inhibition of ABHD6 activity by CPT1C, is mediated through their respective C-terminal domains.

REFERENCES

Abe, A., & Shayman, J. A. (2009). The role of negatively charged lipids in lysosomal phospholipase A2 function. *Journal of Lipid Research*, *50*(10), 2027–2035. https://doi.org/10.1194/jlr.M900008-JLR200

Afghah, Z., Chen, X., & Geiger, J. D. (2020). Role of endolysosomes and inter-organellar signaling in brain disease. *Neurobiol Dis*, *134*, 104670. https://doi.org/10.1016/j.nbd.2019.104670

Alhouayek, M., Masquelier, J., Cani, P. D., Lambert, D. M., & Muccioli, G. G. (2013). Implication of the anti-inflammatory bioactive lipid prostaglandin D2-glycerol ester in the control of macrophage activation and inflammation by ABHD6. *Proceedings of the National Academy of Sciences of the United States of America*, *110*(43), 17558–17563. https://doi.org/10.1073/pnas.1314017110

Appelqvist, H., Wäster, P., Kågedal, K., & Öllinger, K. (2013). The lysosome: From waste bag to potential therapeutic target. *Journal of Molecular Cell Biology*, *5*(4), 214–226. https://doi.org/10.1093/jmcb/mjt022

Bissig, C., Lenoir, M., Velluz, M. C., Kufareva, I., Abagyan, R., Overduin, M., & Gruenberg, J. (2013). Viral Infection Controlled by a Calcium-Dependent Lipid-Binding Module in ALIX. *Developmental Cell*, *25*(4), 364–373. https://doi.org/10.1016/j.devcel.2013.04.003

Blankman, J. L., Long, J. Z., Trauger, S. A., Siuzdak, G., & Cravatt, B. F. (2013). ABHD12 controls brain lysophosphatidylserine pathways that are deregulated in a murine model of the neurodegenerative disease PHARC. *Proceedings of the National Academy of Sciences of the United States of America*, *110*(4), 1500–1505. https://doi.org/10.1073/pnas.1217121110

Blankman, J. L., Simon, G. M., & Cravatt, B. F. (2007). A Comprehensive Profile of Brain Enzymes that Hydrolyze the Endocannabinoid 2-Arachidonoylglycerol. *Chemistry and Biology*, *14*(12), 1347–1356. https://doi.org/10.1016/j.chembiol.2007.11.006

Body, D. R., & Gray, G. M. (1967). The isolation and characterisation of phosphatidylglycerol and a structural isomer from pig lung. *Chemistry and Physics of Lipids*, *1*(3), 254–263. https://doi.org/10.1016/0009-3084(67)90032-1

Bononi, G., Tuccinardi, T., Rizzolio, F., & Granchi, C. (2021). α/β-Hydrolase Domain (ABHD) Inhibitors as New Potential Therapeutic Options against Lipid-Related Diseases. *Journal of Medicinal Chemistry*, *64*(14), 9759–9785. https://doi.org/10.1021/acs.jmedchem.1c00624

Brechet, A., Buchert, R., Schwenk, J., Boudkkazi, S., Zolles, G., Siquier-Pernet, K., Schaber, I., Bildl, W., Saadi, A., Bole-Feysot, C., Nitschke, P., Reis, A., Sticht, H., Al-Sanna'a, N., Rolfs, A., Kulik, A., Schulte, U., Colleaux, L., Abou Jamra, R., & Fakler, B. (2017). AMPA-receptor specific biogenesis complexes control synaptic transmission and intellectual ability. *Nature Communications*, *8*(15910). https://doi.org/10.1038/ncomms15910

Brotherus, J., & Renkonen, O. (1977). Subcellular distributions of lipids in cultured BHK cells: evidence for the enrichment of lysobisphosphatidic acid and neutral lipids in lysosomes. *Journal of Lipid Research*, *18*(2), 191–202. https://doi.org/10.1016/s0022-2275(20)41698-0

Brownsey, R. W., Boone, A. N., Elliott, J. E., Kulpa, J. E., & Lee, W. M. (2006). Regulation of acetyl-CoA carboxylase. *Biochemical Society Transactions*, *34*(2), 223. https://doi.org/10.1042/BST20060223

Cabukusta, B., & Neefjes, J. (2018). Mechanisms of lysosomal positioning and movement. *Traffic*, *19*(10), 761–769. https://doi.org/10.1111/tra.12587

Cao, J. K., Kaplan, J., & Stella, N. (2019). ABHD6: Its Place in Endocannabinoid Signaling and Beyond. *Trends in Pharmacological Sciences*, *40*(4), 267–277. https://doi.org/10.1016/j.tips.2019.02.002

Carrasco, P., Jacas, J., Sahún, I., Muley, H., Ramírez, S., Puisac, B., Mezquita, P., Pié, J., Dierssen, M., & Casals, N. (2013). Carnitine palmitoyltransferase 1C deficiency causes motor impairment and hypoactivity. *Behavioural Brain Research*, *256*, 291–297. https://doi.org/10.1016/j.bbr.2013.08.004

Carrasco, P., Sahún, I., McDonald, J., Ramírez, S., Jacas, J., Gratacós, E., Sierra, A. Y., Serra, D., Herrero, L., Acker-Palmer, A., Hegardt, F. G., Dierssen, M., & Casals, N. (2012). Ceramide levels regulated by carnitine palmitoyltransferase 1C control dendritic spine maturation and cognition. *Journal of Biological Chemistry*, *287*(25), 21224–21232. https://doi.org/10.1074/jbc.M111.337493

Casals, N., Zammit, V., Herrero, L., Fadó, R., Rodríguez-Rodríguez, R., & Serra, D. (2016). Carnitine palmitoyltransferase 1C: From cognition to cancer. *Progress in Lipid Research*, *61*, 134–148. https://doi.org/10.1016/j.plipres.2015.11.004

Casas, M., Fadó, R., Domínguez, J. L., Roig, A., Kaku, M., Chohnan, S., Solé, M., Unzeta, M., Miñano-Molina, A. J., Rodríguez-Álvarez, J., Dickson, E. J., & Casals, N. (2020). Sensing of nutrients by CPT1C controls SAC1 activity to regulate AMPA receptor trafficking. *The Journal of Cell Biology*, *219*(10). https://doi.org/10.1083/jcb.201912045

Chen, J., Cazenave-Gassiot, A., Xu, Y., Piroli, P., Hwang, R., DeFreitas, L., Chan, R. B., Di Paolo, G., Nandakumar, R., Wenk, M. R., & Marquer, C. (2023). Lysosomal phospholipase A2 contributes to the biosynthesis of the atypical late endosome lipid bis(monoacylglycero)phosphate. *Communications Biology*, *6*(1), 1–11. https://doi.org/10.1038/s42003-023-04573-z

Cheng, X. T., Xie, Y. X., Zhou, B., Huang, N., Farfel-Becker, T., & Sheng, Z. H. (2018). Characterization of LAMP1-labeled nondegradative lysosomal and endocytic compartments in neurons. *Journal of Cell Biology*, *217*(9), 3127–3139. https://doi.org/10.1083/jcb.201711083

Chevallier, J., Chamoun, Z., Jiang, G., Prestwich, G., Sakai, N., Matile, S., Parton, R. G., & Gruenberg, J. (2008). Lysobisphosphatidic acid controls endosomal cholesterol levels.

Journal of Biological Chemistry, *283*(41), 27871–27880. https://doi.org/10.1074/jbc.M801463200

Chia, P. Z. C., Gunn, P., & Gleeson, P. A. (2013). Cargo trafficking between endosomes and the trans-Golgi network. In *Histochemistry and Cell Biology* (Vol. 140, Issue 3, pp. 307–315). https://doi.org/10.1007/s00418-013-1125-6

Ching, J., Osborne, A., Eva, R., Prudent, J., & Yu-Wai-Man, P. (2021). Quantifying inter-organelle membrane contact sites using proximity ligation assay in fixed optic nerve sections. *Experimental Eye Research*, *213*(June), 108793. https://doi.org/10.1016/j.exer.2021.108793

Cochran, F. R., Roddick, V. L., Connor, J. R., Thornburg, J. T., & Waite, M. (1987). Regulation of arachidonic acid metabolism in resident and BCG-activated alveolar macrophages: role of lyso(bis)phosphatidic acid. *The Journal of Immunology*, *138*(6), 1877–1883. https://doi.org/10.4049/jimmunol.138.6.1877

Cristofori, A. Di, Ferrero, S., Bertolini, I., Gaudioso, G., Russo, M. V., Berno, V., Vanini, M., Locatelli, M., Zavanone, M., Rampini, P., Vaccari, T., Caroli, M., & Vaira, V. (n.d.). The vacuolar H+ ATPase is a novel therapeutic target for glioblastoma. In *Oncotarget* (Vol. 6, Issue 19). www.impactjournals.com/oncotarget/

d'Avignon, D. A., Puchalska, P., Ercal, B., Chang, Y. J., Martin, S. E., Graham, M. J., Patti, G. J., Han, X., & Crawford, P. A. (2018). Hepatic ketogenic insufficiency reprograms hepatic glycogen metabolism and the lipidome. *JCI Insight*, *3*(12), 1–19. https://doi.org/10.1172/jci.insight.99762

Dai, Y., Wolfgang, M. J., Cha, S. H., & Lane, M. D. (2007). Localization and effect of ectopic expression of CPT1c in CNS feeding centers. *Biochemical and Biophysical Research Communications*, *359*(3), 469–474. https://doi.org/10.1016/j.bbrc.2007.05.161

de Araujo, M. E. G., Liebscher, G., Hess, M. W., & Huber, L. A. (2020). Lysosomal size matters. *Traffic*, *21*(1), 60–75. https://doi.org/10.1111/tra.12714

Deng, H., & Li, W. (2020). Therapeutic potential of targeting α/β-Hydrolase domain-containing 6 (ABHD6). *European Journal of Medicinal Chemistry*, *198*. https://doi.org/10.1016/j.ejmech.2020.112353

Eden, E. R. (2016). The formation and function of ER-endosome membrane contact sites. *Biochimica et Biophysica Acta - Molecular and Cell Biology of Lipids*, *1861*(8), 874–879. https://doi.org/10.1016/j.bbalip.2016.01.020

Eden, E. R., & Futter, C. E. (2021). Membrane trafficking: Retrofusion as an escape route out of the endosome. *Current Biology*, *31*(17), R1037–R1040. https://doi.org/10.1016/j.cub.2021.07.055

Enkavi, G., Mikkolainen, H., Güngör, B., Ikonen, E., & Vattulainen, I. (2017). Concerted regulation of NPC 2 binding to endosomal/lysosomal membranes by bis (monoacylglycero)phosphate and sphingomyelin. *PLoS Computational Biology*, *13*(10),

1–21. https://doi.org/10.5281/zenodo.1035202.Funding

Enrich, C., Rentero, C., Grewal, T., Futter, C. E., & Eden, E. R. (2019). Cholesterol Overload: Contact Sites to the Rescue! *Contact*, *2*, 251525641989350. https://doi.org/10.1177/2515256419893507

Enrich, C., Rentero, C., Hierro, A., & Grewal, T. (2015). Role of cholesterol in SNARE-mediated trafficking on intracellular membranes. *Journal of Cell Science*, *128*(6), 1071–1081. https://doi.org/10.1242/jcs.164459

Fadó, R., Rodríguez-Rodríguez, R., & Casals, N. (2021). The return of malonyl-CoA to the brain: Cognition and other stories. *Progress in Lipid Research*, *81*. https://doi.org/10.1016/j.plipres.2020.101071

Fadó, R., Soto, D., Miñano-Molina, A. J., Pozo, M., Carrasco, P., Yefimenko, N., Rodríguez-Álvarez, J., & Casals, N. (2015). Novel regulation of the synthesis of α-Amino-3-hydroxy-5-methyl-4-isoxazolepropionic Acid (ampa) receptor subunit glua1 by carnitine palmitoyltransferase 1C (CPT1C) in the Hippocampus. *Journal of Biological Chemistry*, *290*(42), 25548–25560. https://doi.org/10.1074/jbc.M115.681064

Falguières, T., Luyet, P. P., & Gruenberg, J. (2009). Molecular assemblies and membrane domains in multivesicular endosome dynamics. *Experimental Cell Research*, *315*(9), 1567–1573. https://doi.org/10.1016/j.yexcr.2008.12.006

Ferguson, S. M. (2019). Neuronal Lysosomes. *Neuroscience Letters*, *697*, 1–9. https://doi.org/10.1016/j.neulet.2018.04.005

Fisette, A., Tobin, S., Décarie-Spain, L., Bouyakdan, K., Peyot, M. L., Madiraju, S. R. M., Prentki, M., Fulton, S., & Alquier, T. (2016). α/β-Hydrolase Domain 6 in the Ventromedial Hypothalamus Controls Energy Metabolism Flexibility. *Cell Reports*, *17*(5), 1217–1226. https://doi.org/10.1016/j.celrep.2016.10.004

Fosch, A., Rodriguez-Garcia, M., Miralpeix, C., Zagmutt, S., Larrañaga, M., Reguera, A. C., Garcia-Chica, J., Herrero, L., Serra, D., Casals, N., & Rodriguez-Rodriguez, R. (2023). Central Regulation of Brown Fat Thermogenesis in Response to Saturated or Unsaturated Long-Chain Fatty Acids. *International Journal of Molecular Sciences*, *24*(2), 1697. https://doi.org/10.3390/ijms24021697

Friedman, J. R., DiBenedetto, J. R., West, M., Rowland, A. A., & Voeltz, G. K. (2013). Endoplasmic reticulum-endosome contact increases as endosomes traffic and mature. *Molecular Biology of the Cell*, *24*(7), 1030–1040. https://doi.org/10.1091/mbc.E12-10-0733

Gallala, H. D., & Sandhoff, K. (2011). Biological function of the cellular lipid bmp-bmp as a key activator for cholesterol sorting and membrane digestion. *Neurochemical Research*, *36*(9), 1594–1600. https://doi.org/10.1007/s11064-010-0337-6

Gao, S., Zhu, G., Gao, X., Wu, D., Carrasco, P., Casals, N., Hegardt, F. G., Moran, T. H., & Lopaschuk, G. D. (2011). Important roles of brain-specific carnitine

palmitoyltransferase and ceramide metabolism in leptin hypothalamic control of feeding. *Proceedings of the National Academy of Sciences of the United States of America*, *108*(23), 9691–9696. https://doi.org/10.1073/pnas.1103267108

Gao, X. F., Chen, W., Kong, X. P., Xu, A. M., Wang, Z. G., Sweeney, G., & Wu, D. (2009). Enhanced susceptibility of Cpt1c knockout mice to glucose intolerance induced by a high-fat diet involves elevated hepatic gluconeogenesis and decreased skeletal muscle glucose uptake. *Diabetologia*, *52*(5), 912–920. https://doi.org/10.1007/s00125-009-1284-0

Garver, W., & Heidenreich, R. (2005). The Niemann-Pick C Proteins and Trafficking of Cholesterol Through the Late Endosomal / Lysosomal System. *Current Molecular Medicine*, *2*(5), 485–505. https://doi.org/10.2174/1566524023362375

Giovedì, S., Ravanelli, M. M., Parisi, B., Bettegazzi, B., & Guarnieri, F. C. (2020). Dysfunctional Autophagy and Endolysosomal System in Neurodegenerative Diseases: Relevance and Therapeutic Options. *Frontiers in Cellular Neuroscience*, *14*(December). https://doi.org/10.3389/fncel.2020.602116

Goursot, A., Mineva, T., Bissig, C., Gruenberg, J., & Salahub, D. R. (2010). Structure, dynamics, and energetics of lysobisphosphatidic acid (LBPA) isomers. *Journal of Physical Chemistry B*, *114*(47), 15712–15720. https://doi.org/10.1021/jp108361d

Grabner, G. F., Fawzy, N., Pribasnig, M. A., Trieb, M., Taschler, U., Holzer, M., Schweiger, M., Wolinski, H., Kolb, D., Horvath, A., Breinbauer, R., Rülicke, T., Rabl, R., Lass, A., Stadlbauer, V., Hutter-Paier, B., Stauber, R. E., Fickert, P., Zechner, R., … Zimmermann, R. (2019). Metabolic disease and ABHD6 alter the circulating bis(monoacylglycerol)phosphate profile in mice and humans. *Journal of Lipid Research*, *60*(5), 1020–1031. https://doi.org/10.1194/jlr.M093351

Grabner, G. F., Fawzy, N., Schreiber, R., Pusch, L. M., Bulfon, D., Koefeler, H., Eichmann, T. O., Lass, A., Schweiger, M., Marsche, G., Schoiswohl, G., Taschler, U., & Zimmermann, R. (2020). Metabolic regulation of the lysosomal cofactor bis(monoacylglycero)phosphate in mice. *Journal of Lipid Research*, *61*(7), 995–1003. https://doi.org/10.1194/jlr.RA119000516

Gratacòs-Batlle, E., Yefimenko, N., Cascos-García, H., & Soto, D. (2015). AMPAr interacting protein CPT1C enhances surface expression of GLuA1-containing receptors. *Frontiers in Cellular Neuroscience*, *8*(FEB), 1–17. https://doi.org/10.3389/fncel.2014.00469

Gruenberg, J. (2020). Life in the lumen: The multivesicular endosome. *Traffic*, *21*(1), 76–93. https://doi.org/10.1111/tra.12715

Grüner, B. M., Schulze, C. J., Yang, D., Ogasawara, D., Dix, M. M., Rogers, Z. N., Chuang, C.-H., McFarland, C. D., Chiou, S.-H., Brown, J. M., Cravatt, B. F., Bogyo, M., & Winslow, M. M. (2016). An in vivo multiplexed small-molecule screening platform. *Nature Methods*, *13*(10), 883–889. https://doi.org/10.1038/nmeth.3992

Haddad-Tóvolli, R., Dragano, N. R. V., Ramalho, A. F. S., & Velloso, L. A. (2017). Development

and function of the blood-brain barrier in the context of metabolic control. *Frontiers in Neuroscience*, *11*(APR), 1–12. https://doi.org/10.3389/fnins.2017.00224

Halcrow, P., Datta, G., Ohm, J. E., Soliman, M. L., Chen, X., & Geiger, J. D. (2019). Role of endolysosomes and pH in the pathogenesis and treatment of glioblastoma. In *Cancer Reports* (Vol. 2, Issue 6). Wiley-Blackwell Publishing Ltd. https://doi.org/10.1002/cnr2.1177

Hardie, D. G. (2015). AMPK: Positive and negative regulation, and its role in whole-body energy homeostasis. *Current Opinion in Cell Biology*, *33*, 1–7. https://doi.org/10.1016/j.ceb.2014.09.004

Hashimoto, Y., Shirane, M., Matsuzaki, F., Saita, S., Ohnishi, T., & Nakayama, K. I. (2014). Protrudin regulates endoplasmic reticulum morphology and function associated with the pathogenesis of hereditary spastic paraplegia. *Journal of Biological Chemistry*, *289*(19), 12946–12961. https://doi.org/10.1074/jbc.M113.528687

Heravi, J., & Waite, M. (1999). Transacylase formation of bis(monoacylglycerol)phosphate. *Biochimica et Biophysica Acta - Molecular and Cell Biology of Lipids*, *1437*(3), 277–286. https://doi.org/10.1016/S1388-1981(99)00021-9

Hernández-Cáceres, M. P., Cereceda, K., Hernández, S., Li, Y., Narro, C., Rivera, P., Silva, P., Ávalos, Y., Jara, C., Burgos, P. V. P. P. V. P., Toledo-Valenzuela, L., Lagos, P., Cifuentes Araneda, F., Perez-Leighton, C., Bertocchi, C., Clegg, D. J., Criollo, A., Tapia-Rojas, C., Burgos, P. V. P. P. V. P., & Morselli, E. (2020). Palmitic acid reduces the autophagic flux in hypothalamic neurons by impairing autophagosome-lysosome fusion and endolysosomal dynamics. *Molecular and Cellular Oncology*, *7*(5). https://doi.org/10.1080/23723556.2020.1789418

Hochreiter, B., Kunze, M., Moser, B., & Schmid, J. A. (2019). Advanced FRET normalization allows quantitative analysis of protein interactions including stoichiometries and relative affinities in living cells. *Scientific Reports*, *9*(1), 1–16. https://doi.org/10.1038/s41598-019-44650-0

Höglinger, D., Burgoyne, T., Sanchez-Heras, E., Hartwig, P., Colaco, A., Newton, J., Futter, C. E., Spiegel, S., Platt, F. M., & Eden, E. R. (2019). NPC1 regulates ER contacts with endocytic organelles to mediate cholesterol egress. *Nature Communications*, *10*(1), 1–14. https://doi.org/10.1038/s41467-019-12152-2

Hostetler, K. Y. (1982). Polyglycerophospholipids: Phosphatidylglycerol, diphosphatidylglycerol and bis (monoacylglycero) phosphate. *New Comprehensive Biochemistry*, *4*(C), 215–261. https://doi.org/10.1016/S0167-7306(08)60010-1

Hu, Y. B., Dammer, E. B., Ren, R. J., & Wang, G. (2015). The endosomal-lysosomal system: From acidification and cargo sorting to neurodegeneration. *Translational Neurodegeneration*, *4*(1), 1–10. https://doi.org/10.1186/s40035-015-0041-1

Hullin-Matsuda, F., Kawasaki, K., Delton-Vandenbroucke, I., Xu, Y., Nishijima, M., Lagarde, M., Schlame, M., & Kobayashi, T. (2007). De novo biosynthesis of the late endosome

lipid, bis(monoacylglycero) phosphate. *Journal of Lipid Research*, *48*(9), 1997–2008. https://doi.org/10.1194/jlr.M700154-JLR200

Hullin-Matsuda, F., Luquain-Costaz, C., Bouvier, J., & Delton-Vandenbroucke, I. (2009). Bis(monoacylglycero)phosphate, a peculiar phospholipid to control the fate of cholesterol: Implications in pathology. *Prostaglandins Leukotrienes and Essential Fatty Acids*, *81*(5–6), 313–324. https://doi.org/10.1016/j.plefa.2009.09.006

Hunkeler, M., Hagmann, A., Stuttfeld, E., Chami, M., Guri, Y., Stahlberg, H., & Maier, T. (2018). Structural basis for regulation of human acetyl-CoA carboxylase. *Nature*, *558*(7710), 470–474. https://doi.org/10.1038/s41586-018-0201-4

Huo, L., Du, X., Li, X., Liu, S., & Xu, Y. (2021). The Emerging Role of Neural Cell-Derived Exosomes in Intercellular Communication in Health and Neurodegenerative Diseases. *Frontiers in Neuroscience*, *15*(August). https://doi.org/10.3389/fnins.2021.738442

Huotari, J., & Helenius, A. (2011). Endosome maturation. *EMBO Journal*, *30*(17), 3481–3500. https://doi.org/10.1038/emboj.2011.286

Ilnytska, O., Lai, K., Gorshkov, K., Schultz, M. L., Tran, B. N., Jeziorek, M., Kunkel, T. J., Azaria, R. D., McLoughlin, H. S., Waghalter, M., Xu, Y., Schlame, M., Altan-Bonnet, N., Zheng, W., Lieberman, A. P., Dobrowolski, R., & Storch, J. (2021). Enrichment of NPC1-deficient cells with the lipid LBPA stimulates autophagy, improves lysosomal function, and reduces cholesterol storage. *Journal of Biological Chemistry*, *297*(1), 100813. https://doi.org/10.1016/j.jbc.2021.100813

Ito, M., Tchoua, U., Okamoto, M., & Tojo, H. (2002). Purification and properties of a phospholipase A2/lipase preferring phosphatidic acid, bis(monoacylglycerol) phosphate, and monoacylglycerol from rat testis. *Journal of Biological Chemistry*, *277*(46), 43674–43681. https://doi.org/10.1074/jbc.M202817200

Ivanova, D., & Cousin, M. A. (2022). Synaptic Vesicle Recycling and the Endolysosomal System: A Reappraisal of Form and Function. *Frontiers in Synaptic Neuroscience*, *14*(February), 1–21. https://doi.org/10.3389/fnsyn.2022.826098

Jin, E. J., Kiral, F. R., Ozel, M. N., Burchardt, L. S., Osterland, M., Epstein, D., Wolfenberg, H., Prohaska, S., & Hiesinger, P. R. (2018). Live Observation of Two Parallel Membrane Degradation Pathways at Axon Terminals. *Current Biology*, *28*(7), 1027-1038.e4. https://doi.org/10.1016/j.cub.2018.02.032

Jumper, J., Evans, R., Pritzel, A., Green, T., Figurnov, M., Ronneberger, O., Tunyasuvunakool, K., Bates, R., Žídek, A., Potapenko, A., Bridgland, A., Meyer, C., Kohl, S. A. A., Ballard, A. J., Cowie, A., Romera-Paredes, B., Nikolov, S., Jain, R., Adler, J., … Hassabis, D. (2021). Highly accurate protein structure prediction with AlphaFold. *Nature*, *596*(7873), 583–589. https://doi.org/10.1038/s41586-021-03819-2

Kaushik, S., Arias, E., Kwon, H., Lopez, N. M., Athonvarangkul, D., Sahu, S., Schwartz, G. J., Pessin, J. E., & Singh, R. (2012). Loss of autophagy in hypothalamic POMC neurons impairs lipolysis. *EMBO Reports*, *13*(3), 258–265.

https://doi.org/10.1038/embor.2011.260

Kobayashi, T., Beuchat, M. H., Chevallier, J., Makino, A., Mayran, N., Escola, J. M., Lebrand, C., Cosson, P., Kobayashi, T., & Gruenberg, J. (2002). Separation and characterization of late endosomal membrane domains. *Journal of Biological Chemistry*, *277*(35), 32157–32164. https://doi.org/10.1074/jbc.M202838200

Kobayashi, T., Beuchat, M. H., Lindsay, M., Frias, S., Palmiter, R. D., Sakuraba, H., Parton, R. G., & Gruenberg, J. (1999). Late endosomal membranes rich in lysobisphosphatidic acid regulate cholesterol transport. *Nature Cell Biology*, *1*(2), 113–118. https://doi.org/10.1038/10084

Kobayashi, T., Stang, E., Fang, K. S., De Moerloose, P., Parton, R. G., & Gruenberg, J. (1998). A lipid associated with the antiphospholipid syndrome regulates endosome structure and function. *Nature*, *392*(6672), 193–197. https://doi.org/10.1038/32440

Kobayashi, T., Startchev, K., Whitney, A. J., & Gruenberg, J. (2001). Localization of lysobisphosphatidic acid-rich membrane domains in late endosomes. *Biological Chemistry*, *382*(3), 483–485. https://doi.org/10.1515/BC.2001.059

Kuijpers, M., Azarnia Tehran, D., Haucke, V., & Soykan, T. (2021). The axonal endolysosomal and autophagic systems. *Journal of Neurochemistry*, *158*(3), 589–602. https://doi.org/10.1111/jnc.15287

Langemeyer, L., Fröhlich, F., & Ungermann, C. (2018). Rab GTPase Function in Endosome and Lysosome Biogenesis. *Trends in Cell Biology*, *28*(11), 957–970. https://doi.org/10.1016/j.tcb.2018.06.007

Li, F., Fei, X., Xu, J., & Ji, C. (2009). An unannotated α/β hydrolase superfamily member, ABHD6 differentially expressed among cancer cell lines. *Molecular Biology Reports*, *36*(4), 691–696. https://doi.org/10.1007/s11033-008-9230-7

Lie, P. P. Y., & Nixon, R. A. (2019). Lysosome trafficking and signaling in health and neurodegenerative diseases. *Neurobiology of Disease*, *122*, 94–105. https://doi.org/10.1016/j.nbd.2018.05.015

Linke, T., Wilkening, G., Lansmann, S., Moczall, H., Bartelsen, O., Weisgerber, J., & Sandhoff, K. (2001). Stimulation of Acid Sphingomyelinase Activity by Lysosomal Lipids and Sphingolipid Activator Proteins. *Biological Chemistry*, *382*(2), 283–290. https://doi.org/10.1515/BC.2001.035

Linke, T., Wilkening, G., Sadeghlar, F., Mozcall, H., Bernardo, K., Schuchman, E., & Sandhoff, K. (2001). Interfacial Regulation of Acid Ceramidase Activity: Stimulation of ceramide degradation by lysosomal lipids and sphingolipid activator proteins. *Journal of Biological Chemistry*, *276*(8), 5760–5768. https://doi.org/10.1074/jbc.M006846200

Lord, C. C., Thomas, G., & Brown, J. M. (2013). Mammalian alpha beta hydrolase domain (ABHD) proteins: Lipid metabolizing enzymes at the interface of cell signaling and energy metabolism. *Biochimica et Biophysica Acta - Molecular and Cell Biology of*

Lipids, *1831*(4), 792–802. https://doi.org/10.1016/j.bbalip.2013.01.002

Luquain, C., Dolmazon, R., Enderlin, J. M., Laugier, C., Lagarde, M., & Pageaux, J. F. (2000). Bis(monoacylglycerol) phosphate in rat uterine stromal cells: Structural characterization and specific esterification of docosahexaenoic acid. *Biochemical Journal*, *351*(3), 795–804. https://doi.org/10.1042/0264-6021:3510795

Maier, S., Staffler, G., Hartmann, A., Höck, J., Henning, K., Grabusic, K., Mailhammer, R., Hoffmann, R., Wilmanns, M., Lang, R., Mages, J., & Kempkes, B. (2006). Cellular Target Genes of Epstein-Barr Virus Nuclear Antigen 2. *Journal of Virology*, *80*(19), 9761–9771. https://doi.org/10.1128/jvi.00665-06

Makino, A., Ishii, K., Murate, M., Hayakawa, T., Suzuki, Y., Suzuki, M., Ito, K., Fujisawa, T., Matsuo, H., Ishitsuka, R., & Kobayashi, T. (2006). D-threo-1-phenyl-2-decanoylamino-3-morpholino-1-propanol alters cellular cholesterol homeostasis by modulating the endosome lipid domains. *Biochemistry*, *45*(14), 4530–4541. https://doi.org/10.1021/bi052104y

Manterola, A., Bernal-Chico, A., Cipriani, R., Ruiz, A., Pérez-Samartín, A., Moreno-Rodríguez, M., Hsu, K. L., Cravatt, B. F., Brown, J. M., Rodríguez-Puertas, R., Matute, C., & Mato, S. (2018). Re-examining the potential of targeting ABHD6 in multiple sclerosis: Efficacy of systemic and peripherally restricted inhibitors in experimental autoimmune encephalomyelitis. *Neuropharmacology*, *141*, 181–191. https://doi.org/10.1016/j.neuropharm.2018.08.038

Marques, A. R. A., & Saftig, P. (2019). Lysosomal storage disorders – challenges, concepts and avenues for therapy: Beyond rare diseases. *Journal of Cell Science*, *132*(2). https://doi.org/10.1242/jcs.221739

Marrs, W. R., Blankman, J. L., Horne, E. A., Thomazeau, A., Lin, Y. H., Coy, J., Bodor, A. L., Muccioli, G. G., Hu, S. S. J., Woodruff, G., Fung, S., Lafourcade, M., Alexander, J. P., Long, J. Z., Li, W., Xu, C., Möller, T., MacKie, K., Manzoni, O. J., … Stella, N. (2010). The serine hydrolase ABHD6 controls the accumulation and efficacy of 2-AG at cannabinoid receptors. *Nature Neuroscience*, *13*(8), 951–957. https://doi.org/10.1038/nn.2601

Martello, A., Platt, F. M., & Eden, E. R. (2020). Staying in touch with the endocytic network: The importance of contacts for cholesterol transport. *Traffic*, *21*(5), 354–363. https://doi.org/10.1111/tra.12726

Mathews, P. M., & Levy, E. (2019). Exosome Production Is Key to Neuronal Endosomal Pathway Integrity in Neurodegenerative Diseases. *Frontiers in Neuroscience*, *13*(December), 1–14. https://doi.org/10.3389/fnins.2019.01347

Matsuo, H., Chevallier, J., Mayran, N., Le Blanc, I., Ferguson, C., Fauré, J., Blanc, N. S., Matile, S., Dubochet, J., Sadoul, R., Parton, R. G., Vilbois, F., & Gruenberg, J. (2004). Role of LBPA and Alix in Multivesicular Liposome Formation and Endosome Organization. *Science*, *303*(5657), 531–534. https://doi.org/10.1126/science.1092425

Matsuzawa, Y., & Hostetler, K. Y. (1979). Degradation of bis(monoacylglycero)phosphate by

an acid phosphodiesterase in rat liver lysosomes. *Journal of Biological Chemistry*, *254*(13), 5997–6001. https://doi.org/10.1016/s0021-9258(18)50510-x

Max, D., Hesse, M., Volkmer, I., & Staege, M. S. (2009). High expression of the evolutionarily conserved α/β hydrolase domain containing 6 (ABHD6) in Ewing tumors. *Cancer Science*, *100*(12), 2383–2389. https://doi.org/10.1111/j.1349-7006.2009.01347.x

Maxfield, F. R., & Wüstner, D. (2012). Analysis of cholesterol trafficking with fluorescent probes Frederick. *Methods in Cell Biology*, *108*, 367–393. https://doi.org/10.1038/jid.2014.371

Mayor, S., & Pagano, R. E. (2007). Pathways of clathrin-independent endocytosis. *Nature Reviews Molecular Cell Biology*, *8*(8), 603–612. https://doi.org/10.1038/nrm2216

Mayr, J. A. (2015). Lipid metabolism in mitochondrial membranes. *Journal of Inherited Metabolic Disease*, *38*(1), 137–144. https://doi.org/10.1007/s10545-014-9748-x

McCauliff, L. A., Langan, A., Li, R., Ilnytska, O., Bose, D., Waghalter, M., Lai, K., Kahn, P. C., & Storch, J. (2019). Intracellular cholesterol trafficking is dependent upon NPC2 interaction with lysobisphosphatidic acid. *ELife*, *8*, 1–31. https://doi.org/10.7554/eLife.50832

McGarry, J. D., & Brown, N. F. (1997). The mitochondrial carnitine palmitoyltransferase system. From concept to molecular analysis. *European Journal of Biochemistry*, *244*(1), 1–14. https://doi.org/10.1111/j.1432-1033.1997.00001.x

McIlwraith, E. K., & Belsham, D. D. (2023). Palmitate alters miRNA content of small extracellular vesicles secreted from NPY/AgRP-expressing hypothalamic neurons. *Brain Research*, *1810*, 148367. https://doi.org/10.1016/j.brainres.2023.148367

Meneses-Salas, E., García-Melero, A., Kanerva, K., Blanco-Muñoz, P., Morales-Paytuvi, F., Bonjoch, J., Casas, J., Egert, A., Beevi, S. S., Jose, J., Llorente-Cortés, V., Rye, K. A., Heeren, J., Lu, A., Pol, A., Tebar, F., Ikonen, E., Grewal, T., Enrich, C., & Rentero, C. (2019). Annexin A6 modulates TBC1D15/Rab7/StARD3 axis to control endosomal cholesterol export in NPC1 cells. *Cellular and Molecular Life Sciences*, *0123456789*. https://doi.org/10.1007/s00018-019-03330-y

Miralpeix, C., Reguera, A. C., Fosch, A., Casas, M., Lillo, J., Navarro, G., Franco, R., Casas, J., Alexander, S. P. H., Casals, N., & Rodríguez-Rodríguez, R. (2021). Carnitine palmitoyltransferase 1C negatively regulates the endocannabinoid hydrolase ABHD6 in mice, depending on nutritional status. *British Journal of Pharmacology*, *178*(7), 1507–1523. https://doi.org/10.1111/bph.15377

Miranda, A. M., & Di Paolo, G. (2018). Endolysosomal dysfunction and exosome secretion: Implications for neurodegenerative disorders. *Cell Stress*, *2*(5), 115–118. https://doi.org/10.15698/cst2018.05.136

Miranda, A. M., Lasiecka, Z. M., Xu, Y., Neufeld, J., Shahriar, S., Simoes, S., Chan, R. B., Oliveira, T. G., Small, S. A., & Di Paolo, G. (2018). Neuronal lysosomal dysfunction

releases exosomes harboring APP C-terminal fragments and unique lipid signatures. *Nature Communications*, *9*(1). https://doi.org/10.1038/s41467-017-02533-w

Möbius, W., van Donselaar, E., Ohno-Iwashita, Y., Shimada, Y., Heijnen, H. F. G., Slot, J. W., & Geuze, H. J. (2003). Recycling compartments and the internal vesicles of multivesicular bodies harbor most of the cholesterol found in the endocytic pathway. *Traffic*, *4*(4), 222–231. https://doi.org/10.1034/j.1600-0854.2003.00072.x

Moreau, D., Vacca, F., Vossio, S., Scott, C., Colaco, A., Paz Montoya, J., Ferguson, C., Damme, M., Moniatte, M., Parton, R. G., Platt, F. M., & Gruenberg, J. (2019). Drug-induced increase in lysobisphosphatidic acid reduces the cholesterol overload in Niemann–Pick type C cells and mice. *EMBO Reports*, *20*(7), 1–15. https://doi.org/10.15252/embr.201847055

Morselli, E., Criollo, A., Rodriguez-Navas, C., & Clegg, D. J. (2015). Chronic High Fat Diet Consumption Impairs Metabolic Health of Male Mice. *Inflammation and Cell Signaling*. https://doi.org/10.14800/ics.561

Muley, H., Valencia, K., Casas, J., Moreno, B., Botella, L., Lecanda, F., Fadó, R., & Casals, N. (2023). Cpt1c Downregulation Causes Plasma Membrane Remodelling and Anthracycline Resistance in Breast Cancer. *International Journal of Molecular Sciences*, *24*(2), 1–18. https://doi.org/10.3390/ijms24020946

Napolitano, G., & Ballabio, A. (2016). TFEB at a glance. *Journal of Cell Science*, *129*(13), 2475–2481. https://doi.org/10.1242/jcs.146365

Naslavsky, N., & Caplan, S. (2018). The enigmatic endosome - Sorting the ins and outs of endocytic trafficking. *Journal of Cell Science*, *131*(13). https://doi.org/10.1242/jcs.216499

Navarro, G., Aymerich, M. S., Marcellino, D., Cortés, A., Casadó, V., Mallol, J., Canela, E. I., Agnati, L., Woods, A. S., Fuxe, K., Lluís, C., Lanciego, J. L., Ferré, S., & Franco, R. (2009). Interactions between calmodulin, adenosine A2A, and dopamine D2 receptors. *Journal of Biological Chemistry*, *284*(41), 28058–28068. https://doi.org/10.1074/jbc.M109.034231

Navia-Paldanius, D., Savinainen, J. R., & Laitinen, J. T. (2012). Biochemical and pharmacological characterization of human α/β-hydrolase domain containing 6 (ABHD6) and 12 (ABHD12). *Journal of Lipid Research*, *53*(11), 2413–2424. https://doi.org/10.1194/jlr.M030411

Nawrotek, A., Talagas, A., Vuillard, L., & Miallau, L. (2021). Crystal structure of human Monoacylglycerol Lipase ABHD6 in complex with oleic acid and octyl glucoside. *PDB*. https://www.rcsb.org/structure/7OTS

Naydenov, A. V, Horne, E. A., Cheah, C. S., Swinney, K., Hsu, K., Cao, J. K., Marrs, W., Blankman, J. L., Tu, S., Cherry, A. E., Fung, S., Wen, A., Li, W., Saporito, M. S., Selley, D. E., Cravatt, B. F., Oakley, J. C., & Stella, N. (2014). ABHD6 blockade exerts antiepileptic activity in PTZ-induced seizures and in spontaneous seizures in R6/2 mice. *Neuron*,

83(2), 361–371. https://doi.org/10.1016/j.neuron.2014.06.030.ABHD6

Okamoto, S., Sato, T., Tateyama, M., Kageyama, H., Maejima, Y., Nakata, M., Hirako, S., Matsuo, T., Kyaw, S., Shiuchi, T., Toda, C., Sedbazar, U., Saito, K., Asgar, N. F., Zhang, B., Yokota, S., Kobayashi, K., Foufelle, F., Ferré, P., … Minokoshi, Y. (2018). Activation of AMPK-Regulated CRH Neurons in the PVH is Sufficient and Necessary to Induce Dietary Preference for Carbohydrate over Fat. *Cell Reports*, *22*(3), 706–721. https://doi.org/10.1016/j.celrep.2017.11.102

Oninla, V. O., Breiden, B., Babalola, J. O., & Sandhoff, K. (2014). Acid sphingomyelinase activity is regulated by membrane lipids and facilitates cholesterol transfer by NPC2. *Journal of Lipid Research*, *55*(12), 2606–2619. https://doi.org/10.1194/jlr.M054528

Padamsey, Z., McGuinness, L., Bardo, S. J., Reinhart, M., Tong, R., Hedegaard, A., Hart, M. L., & Emptage, N. J. (2017). Activity-Dependent Exocytosis of Lysosomes Regulates the Structural Plasticity of Dendritic Spines. *Neuron*, *93*(1), 132–146. https://doi.org/10.1016/j.neuron.2016.11.013

Palomo-Guerrero, M., Fadó, R., Casas, M., Pérez-Montero, M., Baena, M., Helmer, P. O., Domínguez, J. L., Roig, A., Serra, D., Hayen, H., Stenmark, H., Raiborg, C., & Casals, N. (2019). Sensing of nutrients by CPT1C regulates late endosome/lysosome anterograde transport and axon growth. *ELife*, *8*, 1–26. https://doi.org/10.7554/eLife.51063

Phillips, M. J., & Voeltz, G. K. (2016). Structure and function of ER membrane contact sites with other organelles. *Nature Reviews Molecular Cell Biology*, *17*(2), 69–82. https://doi.org/10.1038/nrm.2015.8

Poursharifi, P., Madiraju, S. R. M., & Prentki, M. (2017). Monoacylglycerol signalling and ABHD6 in health and disease. *Diabetes, Obesity and Metabolism*, *19*(March), 76–89. https://doi.org/10.1111/dom.13008

Pozo, M., Rodrguez-Rodrguez, R., Raḿrez, S., Seoane-Collazo, P., López, M., Serra, D., Herrero, L., & Casals, N. (2017). Hypothalamic regulation of liver and muscle nutrient partitioning by brain-specific carnitine palmitoyltransferase 1c in male mice. *Endocrinology*, *158*(7), 2226–2238. https://doi.org/10.1210/en.2017-00151

Pribasnig, M. A., Mrak, I., Grabner, G. F., Taschler, U., Knittelfelder, O., Scherz, B., Eichmann, T. O., Heier, C., Grumet, L., Kowaliuk, J., Romauch, M., Holler, S., Anderl, F., Wolinski, H., Lass, A., Breinbauer, R., Marsche, G., Brown, J. M., & Zimmermann, R. (2015). α/β hydrolase domain-containing 6 (ABHD6) degrades the late Endosomal/Lysosomal lipid Bis(Monoacylglycero)phosphate. *Journal of Biological Chemistry*, *290*(50), 29869–29881. https://doi.org/10.1074/jbc.M115.669168

Price, N. T., Van Der Leij, F. R., Jackson, V. N., Corstorphine, C. G., Thomson, R., Sorensen, A., & Zammit, V. A. (2002). A novel brain-expressed protein related to carnitine palmitoyltransferase I. *Genomics*, *80*(4), 433–442. https://doi.org/10.1006/geno.2002.6845

Prinz, W. A., Toulmay, A., & Balla, T. (2020). The functional universe of membrane contact

sites. *Nature Reviews Molecular Cell Biology*, *21*(1), 7–24. https://doi.org/10.1038/s41580-019-0180-9

Pryor, P. R. (2012). Analyzing lysosomes in live cells. In *Methods in Enzymology* (1st ed., Vol. 505). Elsevier Inc. https://doi.org/10.1016/B978-0-12-388448-0.00016-4

Pryor, P. R., & Luzio, J. P. (2009). Delivery of endocytosed membrane proteins to the lysosome. *Biochimica et Biophysica Acta - Molecular Cell Research*, *1793*(4), 615–624. https://doi.org/10.1016/j.bbamcr.2008.12.022

Pusch, L. M., Riegler-Berket, L., Oberer, M., Zimmermann, R., & Taschler, U. (2022). α/β-Hydrolase Domain-Containing 6 (ABHD6)— A Multifunctional Lipid Hydrolase. *Metabolites*, *12*(8). https://doi.org/10.3390/metabo12080761

Raiborg, C., Wenzel, E. M., Pedersen, N. M., Olsvik, H., Schink, K. O., Schultz, S. W., Vietri, M., Nisi, V., Bucci, C., Brech, A., Johansen, T., & Stenmark, H. (2015). Repeated ER–endosome contacts promote endosome translocation and neurite outgrowth. *Nature*, *520*(7546), 234–238. https://doi.org/10.1038/nature14359

Raiborg, C., Wenzel, E. M., Pedersen, N. M., & Stenmark, H. (2016). ER-endosome contact sites in endosome positioning and protrusion outgrowth. *Biochemical Society Transactions*, *44*(2), 441–446. https://doi.org/10.1042/BST20150246

Ramírez, S., Martins, L., Jacas, J., Carrasco, P., Pozo, M., Clotet, J., Serra, D., Hegardt, F. G., Diéguez, C., López, M., & Casals, N. (2013). Hypothalamic ceramide levels regulated by cpt1c mediate the orexigenic effect of ghrelin. *Diabetes*, *62*(7), 2329–2337. https://doi.org/10.2337/db12-1451

Rampanelli, E., Ochodnicky, P., Vissers, J. P. C., Butter, L. M., Claessen, N., Calcagni, A., Kors, L., Gethings, L. A., Bakker, S. J. L., de Borst, M. H., Navis, G. J., Liebisch, G., Speijer, D., van den Bergh Weerman, M. A., Jung, B., Aten, J., Steenbergen, E., Schmitz, G., Ballabio, A., … Leemans, J. C. (2018). Excessive dietary lipid intake provokes an acquired form of lysosomal lipid storage disease in the kidney. *Journal of Pathology*, *246*(4), 470–484. https://doi.org/10.1002/path.5150

Ran, F. A., Hsu, P. D., Wright, J., Agarwala, V., Scott, D. A., & Zhang, F. (2013). Genome engineering using the CRISPR-Cas9 system. *Nature Protocols*, *8*(11), 2281–2308. https://doi.org/10.1038/nprot.2013.143

Rao, J. N., Warren, G. Z. L., Estolt-Povedano, S., Zammit, V. A., & Ulmer, T. S. (2011). An environment-dependent structural switch underlies the regulation of carnitine palmitoyltransferase 1A. *Journal of Biological Chemistry*, *286*(49), 42545–42554. https://doi.org/10.1074/jbc.M111.306951

Reilly, P. T., & Mak, T. W. (2012). Molecular pathways: Tumor cells Co-opt the brain-specific metabolism gene CPT1C to promote survival. *Clinical Cancer Research*, *18*(21), 5850–5855. https://doi.org/10.1158/1078-0432.CCR-11-3281

Ridgway, N. D., & Zhao, K. (2018). Cholesterol transfer at endosomal-organelle membrane

contact sites. *Current Opinion in Lipidology*, *29*(3), 212–217. https://doi.org/10.1097/MOL.0000000000000506

Rinaldi, C., Schmidt, T., Situ, A. J., Johnson, J. O., Lee, P. R., Chen, K., Bott, L. C., Fadó, R., Harmison, G. H., Parodi, S., Grunseich, C., Renvoisé, B., Biesecker, L. G., De Michele, G., Santorelli, F. M., Filla, A., Stevanin, G., Dürr, A., Brice, A., … Fischbeck, K. H. (2015). Mutation in CPT1C Associated With Pure Autosomal Dominant Spastic Paraplegia. *JAMA Neurology*, *72*(5), 561–570. https://doi.org/10.1001/jamaneurol.2014.4769

Roa-Mansergas, X., Fadó, R., Atari, M., Mir, J. F., Muley, H., Serra, D., & Casals, N. (2018). CPT1C promotes human mesenchymal stem cells survival under glucose deprivation through the modulation of autophagy. *Scientific Reports*, *8*(1), 1–13. https://doi.org/10.1038/s41598-018-25485-7

Rodríguez-Rodríguez, R., Miralpeix, C., Fosch, A., Pozo, M., Calderón-Domínguez, M., Perpinyà, X., Vellvehí, M., López, M., Herrero, L., Serra, D., & Casals, N. (2019). CPT1C in the ventromedial nucleus of the hypothalamus is necessary for brown fat thermogenesis activation in obesity. *Molecular Metabolism*, *19*, 75–85. https://doi.org/10.1016/j.molmet.2018.10.010

Roney, J. C., Cheng, X. T., & Sheng, Z. H. (2022). Neuronal endolysosomal transport and lysosomal functionality in maintaining axonostasis. *Journal of Cell Biology*, *221*(3), 1–16. https://doi.org/10.1083/jcb.202111077

Samanta, S., Situ, A. J., & Ulmer, T. S. (2014). Structural Characterization of the Regulatory Domain of Brain Carnitine Palmitoyltransferase 1. *Biopolymers*, *101*(4), 398–405. https://doi.org/10.1002/bip.22396.

Sanjana, N. E., Shalem, O., & Zhang, F. (2014). Improved vectors and genome-wide libraries for CRISPR screening. *Nature Methods*, *11*(8), 783–784. https://doi.org/10.1038/nmeth.3047

Schwenk, J., Boudkkazi, S., Kocylowski, M. K., Brechet, A., Zolles, G., Bus, T., Costa, K., Kollewe, A., Jordan, J., Bank, J., Bildl, W., Sprengel, R., Kulik, A., Roeper, J., Schulte, U., & Fakler, B. (2019). An ER Assembly Line of AMPA-Receptors Controls Excitatory Neurotransmission and Its Plasticity. *Neuron*, *104*(4), 680-692.e9. https://doi.org/10.1016/j.neuron.2019.08.033

Schwenk, J., Harmel, N., Brechet, A., Zolles, G., Berkefeld, H., Müller, C. S., Bildl, W., Baehrens, D., Hüber, B., Kulik, A., Klöcker, N., Schulte, U., & Fakler, B. (2012). High-Resolution Proteomics Unravel Architecture and Molecular Diversity of Native AMPA Receptor Complexes. *Neuron*, *74*(4), 621–633. https://doi.org/10.1016/j.neuron.2012.03.034

Scott, C. C., Vacca, F., & Gruenberg, J. (2014). Endosome maturation, transport and functions. *Seminars in Cell and Developmental Biology*, *31*, 2–10. https://doi.org/10.1016/j.semcdb.2014.03.034

Settembre, C., Fraldi, A., Medina, D. L., & Ballabio, A. (2013). Signals from the lysosome: a

control centre for cellular clearance and energy metabolism. *Nature Reviews Molecular Cell Biology*, *14*(5), 283–296. https://doi.org/10.1038/nrm3565

Shi, Q., Chen, J., Zou, X., & Tang, X. (2022). Intracellular Cholesterol Synthesis and Transport. *Frontiers in Cell and Developmental Biology*, *10*(March), 1–12. https://doi.org/10.3389/fcell.2022.819281

Shields, C. M., Zvonok, N., Zvonok, A., & Makriyannis, A. (2019). Biochemical and Proteomic Characterization of Recombinant Human α/β Hydrolase Domain 6. *Scientific Reports*, *9*(1), 1–12. https://doi.org/10.1038/s41598-018-36633-4

Shirane, M., Wada, M., Morita, K., Hayashi, N., Kunimatsu, R., Matsumoto, Y., Matsuzaki, F., Nakatsumi, H., Ohta, K., Tamura, Y., & Nakayama, K. I. (2020). Protrudin and PDZD8 contribute to neuronal integrity by promoting lipid extraction required for endosome maturation. *Nature Communications*, *11*(1). https://doi.org/10.1038/s41467-020-18413-9

Showalter, M. R., Berg, A. L., Nagourney, A., Heil, H., Carraway, K. L., & Fiehn, O. (2020). The emerging and diverse roles of bis(Monoacylglycero) phosphate lipids in cellular physiology and disease. *International Journal of Molecular Sciences*, *21*(21), 1–19. https://doi.org/10.3390/ijms21218067

Sierra, A. Y., Gratacós, E., Carrasco, P., Clotet, J., Ureña, J., Serra, D., Asins, G., Hegardt, F. G., & Casals, N. (2008). CPT1c is localized in endoplasmic reticulum of neurons and has carnitine palmitoyltransferase activity. *Journal of Biological Chemistry*, *283*(11), 6878–6885. https://doi.org/10.1074/jbc.M707965200

Sobo, K., Le Blanc, I., Luyet, P. P., Fivaz, M., Ferguson, C., Parton, R. G., Gruenberg, J., & Van der Goot, F. G. (2007). Late endosomal cholesterol accumulation leads to impaired intra-endosomal trafficking. *PLoS ONE*, *2*(9). https://doi.org/10.1371/journal.pone.0000851

Straiker, A., Hu, S. S., Long, J. Z., Arnold, A., Wager-miller, J., Cravatt, B. F., & Mackie, K. (2009). Monoacylglycerol Lipase Limits the Duration of Suppression of Excitation in Autaptic Hippocampal Neurons. *Molecular Pharmacology*, *76*(6), 1220–1227. https://doi.org/10.1124/mol.109.059030.cannabinoid

Sun, A. (2018). Lysosomal storage disease overview. *Annals of Translational Medicine*, *6*(24), 476.-476. https://doi.org/10.21037/atm.2018.11.39

Tang, Z., Xie, H., Heier, C., Huang, J., Zheng, Q., Eichmann, T. O., Schoiswohl, G., Ni, J., Zechner, R., Ni, S., & Hao, H. (2020). Enhanced monoacylglycerol lipolysis by ABHD6 promotes NSCLC pathogenesis. *EBioMedicine*, *53*, 102696. https://doi.org/10.1016/j.ebiom.2020.102696

Tchantchou, F., & Zhang, Y. (2013). Selective inhibition of alpha/beta-hydrolase domain 6 attenuates neurodegeneration, alleviates blood brain barrier breakdown, and improves functional recovery in a mouse model of traumatic brain injury. *Journal of Neurotrauma*, *30*(7), 565–579. https://doi.org/10.1089/neu.2012.2647

te Vruchte, D., Wallom, K. L., & Platt, F. M. (2015). Measuring relative lysosomal volume for monitoring lysosomal storage diseases. In *Methods in Cell Biology* (Vol. 126). Elsevier Ltd. https://doi.org/10.1016/bs.mcb.2014.10.027

Thomas, G., Betters, J. L., Lord, C. C., Brown, A. L., Marshall, S., Ferguson, D., Sawyer, J., Davis, M. A., Melchior, J. T., Blume, L. C., Howlett, A. C., Ivanova, P. T., Milne, S. B., Myers, D. S., Mrak, I., Leber, V., Heier, C., Taschler, U., Blankman, J. L., … Brown, J. M. (2013). The Serine Hydrolase ABHD6 Is a Critical Regulator of the Metabolic Syndrome. *Cell Reports*, *5*(2), 508–520. https://doi.org/10.1016/j.celrep.2013.08.047

Varadi, M., Anyango, S., Deshpande, M., Nair, S., Natassia, C., Yordanova, G., Yuan, D., Stroe, O., Wood, G., Laydon, A., Zídek, A., Green, T., Tunyasuvunakool, K., Petersen, S., Jumper, J., Clancy, E., Green, R., Vora, A., Lutfi, M., … Velankar, S. (2022). AlphaFold Protein Structure Database: Massively expanding the structural coverage of protein-sequence space with high-accuracy models. *Nucleic Acids Research*, *50*(D1), D439–D444. https://doi.org/10.1093/nar/gkab1061

Wang, C., Telpoukhovskaia, M. A., Bahr, B. A., Chen, X., & Gan, L. (2018). Endo-lysosomal dysfunction: a converging mechanism in neurodegenerative diseases. In *Current Opinion in Neurobiology* (Vol. 48, pp. 52–58). Elsevier Ltd. https://doi.org/10.1016/j.conb.2017.09.005

Wei, M., Jia, M., Zhang, J., Yu, L., Zhao, Y., Chen, Y., Ma, Y., Zhang, W., Shi, Y. S., & Zhang, C. (2017). The inhibitory effect of α/β-hydrolase domain-containing 6 (ABHD6) on the surface targeting of GluA2- and GluA3-containing AMPA receptors. *Frontiers in Molecular Neuroscience*, *10*(March), 1–12. https://doi.org/10.3389/fnmol.2017.00055

Wei, M., Zhang, J., Jia, M., Yang, C., Pan, Y., Li, S., Luo, Y., Zheng, J., Ji, J., Chen, J., Hu, X., Xiong, J., Shi, Y., & Zhang, C. (2016). α/β-Hydrolase domain-containing 6 (ABHD6) negatively regulates the surface delivery and synaptic function of AMPA receptors. *Proceedings of the National Academy of Sciences of the United States of America*, *113*(19), E2695–E2704. https://doi.org/10.1073/pnas.1524589113

Westenbroek, R., Kaplan, J., Viray, K., & Stella, N. (2023). The serine hydrolase ABHD6 controls survival and thermally induced seizures in a mouse model of Dravet syndrome. *Neurobiology of Disease*, *180*. https://doi.org/10.1016/j.nbd.2023.106099

White, I. J., Bailey, L. M., Aghakhani, M. R., Moss, S. E., & Futter, C. E. (2006). EGF stimulates annexin 1-dependent inward vesiculation in a multivesicular endosome subpopulation. *EMBO Journal*, *25*(1), 1–12. https://doi.org/10.1038/sj.emboj.7600759

Wilkening, G., Linke, T., Uhlhorn-Dierks, G., & Sandhoff, K. (2000). Degradation of membrane-bound ganglioside GM1: Stimulation by bis(monoacylglycero)phosphate and the activator proteins SAP-B and GM2-AP. *Journal of Biological Chemistry*, *275*(46), 35814–35819. https://doi.org/10.1074/jbc.M006568200

Winckler, B., Faundez, V., Maday, S., Cai, Q., Almeida, C. G., & Zhang, H. (2018). The endolysosomal system and proteostasis: From development to degeneration. *Journal*

of *Neuroscience*, *38*(44), 9364–9374. https://doi.org/10.1523/JNEUROSCI.1665-18.2018

Wolfgang, M. J., Kurama, T., Dai, Y., Suwa, A., Asaumi, M., Matsumoto, S. I., Cha, S. H., Shimokawa, T., & Lane, M. D. (2006). The brain-specific carnitine palmitoyltransferase-1c regulates energy homeostasis. *Proceedings of the National Academy of Sciences of the United States of America*, *103*(19), 7282–7287. https://doi.org/10.1073/pnas.0602205103

Woodman, P. G., & Futter, C. E. (2008). Multivesicular bodies: co-ordinated progression to maturity. *Current Opinion in Cell Biology*, *20*(4), 408–414. https://doi.org/10.1016/j.ceb.2008.04.001

Wubbolts, R., Leckie, R. S., Veenhuizen, P. T. M., Schwarzmann, G., Möbius, W., Hoernschemeyer, J., Slot, J. W., Geuze, H. J., & Stoorvogel, W. (2003). Proteomic and biochemical analyses of human B cell-derived exosomes: Potential implications for their function and multivesicular body formation. *Journal of Biological Chemistry*, *278*(13), 10963–10972. https://doi.org/10.1074/jbc.M207550200

Yakovlev, A. A. (2023). Neuronal Exosomes as a New Signaling System. *Biochemistry (Moscow)*, *88*(4), 457–465. https://doi.org/10.1134/S0006297923040028

Yap, C. C., Digilio, L., McMahon, L. P., Garcia, A. D. R., & Winckler, B. (2018). Degradation of dendritic cargos requires Rab7-dependent transport to somatic lysosomes. *Journal of Cell Biology*, *217*(9), 3141–3159. https://doi.org/10.1083/jcb.201711039

Yu, C. B., Zhu, L. Y., Wang, Y. G., Li, F., Zhang, X. Y., & Dai, W. J. (2016). Systemic transcriptome analysis of hepatocellular carcinoma. *Tumor Biology*, *37*(10), 13323–13331. https://doi.org/10.1007/s13277-016-5286-5

Zaugg, K., Yao, Y., Reilly, P. T., Kannan, K., Kiarash, R., Mason, J., Huang, P., Sawyer, S. K., Fuerth, B., Faubert, B., Kalliomäki, T., Elia, A., Luo, X., Nadeem, V., Bungard, D., Yalavarthi, S., Growney, J. D., Wakeham, A., Moolani, Y., … Mak, T. W. (2011). Carnitine palmitoyltransferase 1C promotes cell survival and tumor growth under conditions of metabolic stress. *Genes and Development*, *25*(10), 1041–1051. https://doi.org/10.1101/gad.1987211

Zhao, K., & Ridgway, N. D. (2017). Oxysterol-Binding Protein-Related Protein 1L Regulates Cholesterol Egress from the Endo-Lysosomal System. *Cell Reports*, *19*(9), 1807–1818. https://doi.org/10.1016/j.celrep.2017.05.028

Zhao, S., Mugabo, Y., Ballentine, G., Attane, C., Iglesias, J., Poursharifi, P., Zhang, D., Nguyen, T. A., Erb, H., Prentki, R., Peyot, M. L., Joly, E., Tobin, S., Fulton, S., Brown, J. M., Madiraju, S. R. M., & Prentki, M. (2016). α/β-Hydrolase Domain 6 Deletion Induces Adipose Browning and Prevents Obesity and Type 2 Diabetes. *Cell Reports*, *14*(12), 2872–2888. https://doi.org/10.1016/j.celrep.2016.02.076

Zhao, S., Mugabo, Y., Iglesias, J., Xie, L., Delghingaro-Augusto, V., Lussier, R., Peyot, M. L., Joly, E., Taïb, B., Davis, M. A., Brown, J. M., Abousalham, A., Gaisano, H., Madiraju, S.

R. M., & Prentki, M. (2014). α/β-Hydrolase Domain-6-accessible monoacylglycerol controls glucose-stimulated insulin secretion. *Cell Metabolism*, *19*(6), 993–1007. https://doi.org/10.1016/j.cmet.2014.04.003

Zhao, S., Poursharifi, P., Mugabo, Y., Levens, E. J., Vivot, K., Attane, C., Iglesias, J., Peyot, M. line, Joly, E., Madiraju, S. R. M., & Prentki, M. (2015). α/β-Hydrolase domain-6 and saturated long chain monoacylglycerol regulate insulin secretion promoted by both fuel and non-fuel stimuli. *Molecular Metabolism*, *4*(12), 940–950. https://doi.org/10.1016/j.molmet.2015.09.012

ABBREVIATIONS

1-MAG	1-monoacylglycerol
2-AG	2-arachidonoylglycerol
4-MU	4-methylumbelliferone
4-MUH	4-methylumbelliferyl-heptanoate
ABHD6	α/β-hydrolase domain-containing 6
ACC	Acetyl-Coa carboxylase
AD	Alzheimer's disease
AgRP	Agouti-related protein
AMPAR	α-amino-3-hydroxy-5- methyl-4-isoxazolepropionic acid receptor
AMPK	AMP-activated protein kinase
AUC	Area under curve
BAT	Brown adipose tisssue
BMP	Bis(monoacylglycero)phosphate
BSA	Bovine serum albumin
BW	Body weight
CNS	Central nervous system
CPT1	Carnitine palmitoyltransferase 1
CT	Control
DHA	Docosahexaenoic acid
DIO	Diet-induced obesity
DOPG	1,2-dioleoyl-sn-glycero-3-phospho-(1'-rac-glycerol)
DSB	Double-stranded break
EE	Early endosome
EEA1	Early endosomal antigen 1
EGFP	Enhanced green fluorescent protein
EGFR	Epidermal growth factor receptor
ER	Endoplasmic reticulum

ESCRT	Endosomal sorting complexes required for transport
EV	Empty vector
F	Forward
FA	Fatty acids
FAO	Fatty acid oxidation
FAS	Fatty acid synthase
FBS	Fetal bovine serum
FI	Food intake
FRET	Fluorescence resonance energy transfer
GBM	Glioblastoma multiforme
GSIS	Glucose-stimulated insulin secretion
HFD	High-fat diet
HSP	Hereditary spastic paraplegia
ILV	Intraluminal vesicle
KO	Knock-out
LAMP1	Lysosome-associated membrane protein 1
LBPA	Lyso-bis-phosphatidic acid
LC/MS	Liquid chromatography-mass spectrometry
LCFA	Long-chain fatty acids
LDL	Low-density lipoprotein
LE	Late endosome
LPG	Lysophosphatidylglycerol
LPLA1	Lysosomal phospholipase A1
LPLA2	Lysosomal phospholipase A2
LSD	Lysosomal storage disorders
MCS	Membrane contact sites
MMP-9	Matrix metalloproteinase 9

mTORC1	Mammalian target of rapamycin complex 1
MUFA	Monounsaturated fatty acids
Munc13-1	Mammalian Uc13-1 protein
NPC	Niemann-Pick type C
NPY	Neuropeptide Y
OA	Oleic acid
PA	Palmitic acid
PAc	Phosphatidic acid
PAM	Protospacer adjacent motif
PBS	Phosphate-buffered saline
PC	Phosphatidylcholine
PCR	Polymerase chain reaction
PD	Parkinson's disease
PG	Phosphatidylglycerol
PI(4)P	Phosphatidylinositol-4-phosphate
PLA	Proximity ligation assay
PM	Plasma membrane
POMC	Pro-opiomelanocortin
PUFA	Polyunsaturated fatty acids
R	Revers
RE	Recycling endosome
SD	Standard diet
SFA	Saturated fatty acids
TEM	Transmission electron microscopy
TFEB	Transcription factor EB
TGN	Trans-Golgi network
VMH	Ventromedial hypothalamus

| **WT** | Wild-type |
| **YFP** | Yellow fluorescent protein |

APPENDIX I

Nostrum Biodiscovery report

CPT1C/ABHD6 protein-protein interaction *in silico* modeling and energetic assessment

Nostrum Biodiscovery S.L.

Project Name:	CPT1C/ABHD6 protein-protein interaction in silico modeling and energetic assessment
Client:	Núria Casals Farré (Universitat Internacional de Catalunya)
Project Managers:	Lucía Díaz Chiara Pallara
Date:	January 27, 2023
Project Participants:	Lucía Díaz Chiara Pallara

Background

The group of Prof. Núria Casals at Universitat Internacional de Catalunya (UIC) is currently working with Carnitine palmitoyltransferase I (CPT1), an enzyme responsible for the formation of acyl carnitines that has three isoforms (CPT1A, CPT1B, and CPT1C).

UIC particularly aims to elucidate the structure of the complex formed by CPT1C and ABHD6 proteins. Experimental studies suggest that both proteins are interacting through their cytosolic domains.

Objective

The overall aim of this project was the *in silico* modeling and energetic assessment of the CPT1C/ABHD6 protein-protein interaction.

This main goal was divided into three different steps:
1. Selection/prediction of the isolated docking protein partners 3D structures and their consequent insertion into a bilayer lipid membrane.
2. *In silico* modelling of the CPT1C/ABHD6 protein interaction consisting in the prediction of the complex 3D structure and its final full-atom refinement.
3. Final stability assessment and validation of the selected complex models based on explicit solvent MD simulation and critical binding residues identification.

Deliverables

As agreed between NBD and UIC, the following deliverables were provided by NBD:
1. Up to 3 possible complex structures for CPT1C/ABHD6 interaction for UIC experimental assessment.
2. A list of potential mutations located at the predicted complex interface for UIC confirmation studies.

Methods

Protein preparation

The 1.80 Å resolution X-ray structure of the human monoacylglycerol lipase ABHD6 in complex with oleic acid and octyl glucoside (PDB 7OTS[1]) was downloaded from the RCSB PDB Data Bank (http://www.rcsb.org).

As first preparation step all the co-crystallized ligands, ions, solvent molecules and structure-stabilizing agents were removed, thus the ABHD6 protein structure was properly prepared using the Protein Preparation Wizard (PPW) tool from Schrödinger[2]. More specifically, PPW adds missing hydrogen atoms, reconstructs incomplete side chains and short missing loops using Prime module of Maestro[3] (if any), adds an acetyl and an amide group to the N- and C-terminus, assigns the ionization states at physiological pH, sets the orientation of any misoriented groups (Asparagine, Glutamine, and Histidine residues) and optimizes the hydrogen bond network. Finally, a restrained minimization allowing hydrogen atoms to be freely minimized was performed using OPLS2005 force field[4].

Moreover, both the CPT1C and ABHD6 AlphaFold[5] models were downloaded from the AlphaFold web server (https://alphafold.ebi.ac.uk/) and thus the CPT1C cytosolic domain (namely residues 123-763) was extracted from the full-length AlphaFold model. Finally, all the resulting structures were properly prepared with PPW, as previously described and the full-length AF models, both of ABHD6 and CPT1C proteins, were inserted in a bilayer lipid membrane.

Protein-protein interaction sites identification

The identification of potential protein-protein interaction sites on CPT1C and ABHD6 proteins was performed by the Optimal Docking Area (ODA) pyDock module[7] and MaSIF (Molecular Surface Interaction Fingerprinting) framework[8].

ODA enables the examination of any protein surface looking for areas with favorable energy change when buried upon protein-protein association. For this purpose, surface patches with optimal desolvation energy are identified. Such desolvation energy is based on atomic solvation parameters, derived from octanol/water transfer experiments, and finely adjusted for protein-protein docking[9]. All the regions with lower ODA score (i.e., lower than -10 a.u.) were selected as protein-protein interaction sites.

MaSIF is a recently developed framework based on a geometric deep learning method to capture fingerprints that are important for specific biomolecular interactions, hypothesizing that proteins participating in similar interactions may share common fingerprints, independent of their evolutionary history.

Artificial intelligence (AI)-based protein complex modelling

The artificial intelligence-based algorithm AlphaFold Multimer[10] was used to predict the 3D structure of the complex formed by CPT1C and ABHD6 proteins. To this aim, only the sequence of the cytosolic domain of both proteins (namely residues 123-763 and 43-337 for CPT1C and ABHD6, respectively) were used and the default parameters were set.

Ab initio rigid body protein-protein docking

For the CPT1C/ABHD6 complex modelling, two independent *ab initio* rigid body docking simulations were performed. Thus, in the first simulation (herein referred as Docking-1) the original CPT1C AlphaFold model was used (after removal of the C-terminal residues 764-800) while in the second simulation (herein referred as Docking-2), the most representative structure within the last 500ns of the MD refinement of the original CPT1C AlphaFold model was used. In both cases, the crystal structure of ABHD6 was used as a docking counterpart.

In both simulations, FTDock docking program[11] was used to generate 94,200 rigid-docking poses based on surface complementary and electrostatics at 0.7 Å grid resolution, and then, each docking solution was evaluated by the energy-based pyDock scoring scheme[12], based on desolvation, electrostatics and Van der Waals energy contributions. After scoring, the full CPT1C/ABHD6 protein complex was built by superimposition of each protein to the corresponding protein structure inserted into the bilayer lipid membrane and all the docking solutions in which CPT1C (or ABHD6) protein was clashing with the bilayer lipid membrane or the C-terminal residues of CPT1C (namely residues 780-800) were removed. Protein-protein superimposition, atomic clashes and distances were computed with ICM-Browser program[13] (www.molsoft.com)

Full-atoms flexible protein complex model refinement

The protein-protein complex refinement was performed using Protein Energy Landscape Exploration (PELE) software[14], which combines a Monte Carlo (MC)-based stochastic approach with different protein structure prediction techniques. Briefly, in PELE each MC step is composed by three processes: a) initial perturbation, where the ligand protein is randomly rotated and translated and the atoms of the backbone are displaced using normal modes; b) side chain sampling, where an experimental rotamer library is used to reposition side chains in response to the initial perturbation; c) final minimization, where the overall structure is relaxed.

Explicit solvent unrestrained Molecular Dynamic (MD) simulation

The AlphaFold model of the isolated CPT1C cytoplasmic domain as well as the CPT1C/ABHD6 complex structures, as previously modeled by the *ab initio* rigid body docking and full atom local refinement, were solvated in an octahedral TIP3P water box spanning 12 Å around the

system and neutralized, thus the optimal number of counterions (Na+ and Cl-) were added to reach a salt concentration of 0.1 M.

In brief, MD simulations were carried out using AMBER program (Case et. al., 2020) with the AMBER ff14SB force field[15]. The system was initially minimized with all heavy protein atoms restrained at their initial position and then fully equilibrated by gradually increasing the temperature from 0 to 298 K while reducing the harmonic constraint on the heavy atoms from 50 to 0 kcal/mol $Å^2$.

Finally, an unrestrained MD simulation was run during 1µs keeping positional restraints of 0.1 kcal/mol $Å^2$ on all the N- and C-terminal capping residues.

Root Mean Square Deviation (RMSD), per-residue root mean square fluctuations (RMSF) and clustering analysis along the trajectory were computed using CPPTRAJ module[16] from AmberTool.

Key interaction residues identification

Both per-residue energy decomposition and *in silico* alanine scanning techniques were applied on the MD simulations of the selected docking models to identify the key residues responsible for the binding process. The MMPBSA.py script[17] in AMBER16 was used to perform all binding energy calculation using the MM-GBSA method and all energy components (van der Waals contribution extracted from the MM force field, the electrostatic contribution to the solvation free energy calculated by GB method, nonpolar contribution to the solvation free energy calculated by an empirical model) were calculated using 100 snapshots extracted from the last 500 ns of each MD trajectory and then averaged.

Within the per-residue energy decomposition, the energetic contribution of each single residue in the interface was calculated by summing its interactions over all the residues in the system. Besides, in the *in silico* alanine scanning, each interface residue (located on both CPT1C and ABHD6 proteins) was mutated to alanine and then the binding free energy change ($\Delta\Delta G$) was estimated as the difference between the binding energy ($\otimes G$) of the wild type and the mutated complex.

In both calculations, all the residues with a ΔG or a $\Delta\Delta G$ lower than -2 kcal/mol were selected as hotspot residues. Moreover, the conformational entropy contribution to binding was not included, given the difficulty of computing it for a large protein-protein complex, and the small effect when calculating relative system free energies.

Finally, to summarize the results of the key interaction residues identification a priority scale was used, defining as *low-priority* (*) the residues identified as hotspots by only one technique (either per-residues energy decomposition or *in silico* alanine scanning), *medium-priority* (**) the residues identified as hotspots by both techniques (both per-residues

energy decomposition and *in silico* alanine scanning), and finally *high-priority* (***) the residues identified as hotspots by both techniques and interacting with each other.

Results

CPT1C protein structure prediction

The crystal structure of CPT1C protein (of any of its isoforms) is not yet available, so initially we planned to model it using both homology modeling techniques based on close templates and the AI-based AlphaFold algorithm.

Generally, the quality of the predicted structure by homology modeling depends on the degree of similarity between the model and template sequences. Thus, if the similarity is very low, the homology modeling of the query protein does not yield a meaningful result.

Indeed, given the lack of high sequence identity template structures available in the BLAST database (mostly lower than 30%), this approach was discarded.

Besides, the AlphaFold model of CPT1C protein as already available in the AlphaFold web server (https://alphafold.ebi.ac.uk/) was downloaded and thoroughly analyzed. As shown in Figure 1, the model shows a rather significant confidence especially within the cytosolic domain (colored in dark blue), apart from the C-terminal residues 763-800 corresponding to a rather disordered region (colored in orange).
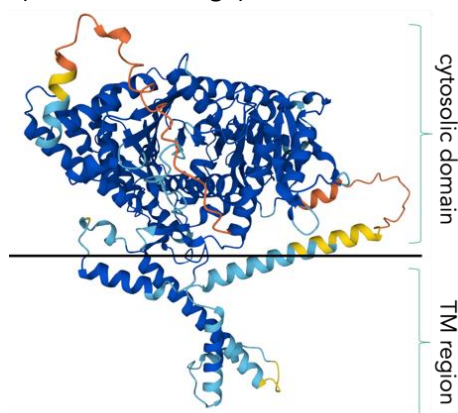

Figure 1. CPT1C protein structure predicted by AlphaFold color-coded according to the pLDDT *(per-residue confidence metric) values: very high confidence (pLDDT > 90) in dark blue, confidence (70 < pLDDT < 90) in light blue, low confidence (50 < pLDDT < 70) in yellow, very low confidence (pLDDT < 50) in orange.*

Thus, in order to validate the CPT1C protein structure as predicted by AlphaFold and also assess the overall stability of the cytosolic domain, we performed a 1 µs-long explicit solvent MD simulation using the model generated by the AlphaFold model as starting structure after removal of both the transmembrane (TM) region (residues 1-122) and the C-terminal tail (residues 763-800).

All in all, the above-mentioned 3D structure was rather confirmed by the MD simulation (Figure 2).
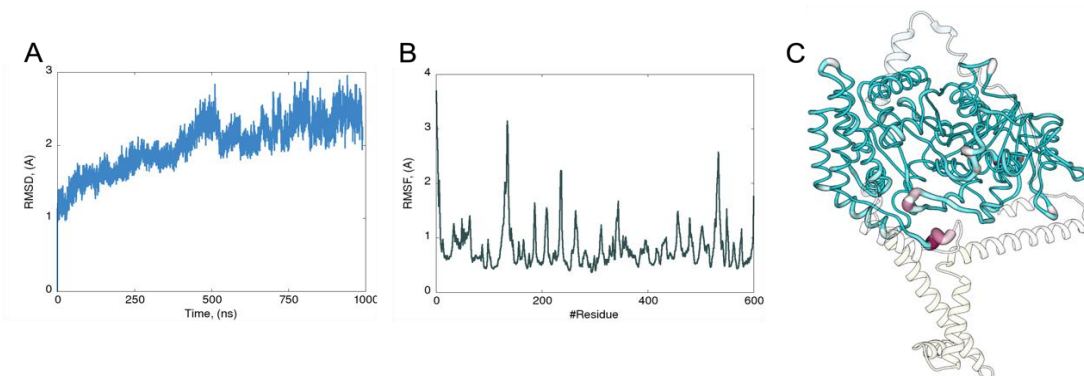

Figure 2. CPT1C protein AlphaFold model validation through MD simulation. Plots of (A) RMSD of the protein backbone and (B) RMSF along the trajectory. (C) Per-residue fluctuation values mapping on CPT1C cytosolic domain. The per-residue fluctuations are shown as worms with variable thickness and color according to their corresponding value (lower fluctuations in thin cyan worms and higher fluctuations in thick violet worms).

The overall structure appeared stable along the trajectory, and there was no evidence of large-scale reorganization or denaturation processes (Figure 2A). Likewise, the average fluctuations of each residue calculated along the MD simulation were rather low (Figure 2B and 2C) implying that the AlphaFold model should correspond to a reasonably accurate representation of the native CPT1C protein structure.

A cluster analysis was finally performed on the last 500 ns of the trajectory and the most representative structure was finally extracted and used as input for one of the *ab initio* rigid body docking simulations.

ABHD6 protein structure selection

First, the only ABHD6 protein X-ray structure currently available in the PDB Data Bank (PDB ID 7OTS) and the AlphaFold model already built and stored in the AlphaFold web server were downloaded and structurally compared. As shown in Figure 3, the X-ray structure lacks the TM domain (Figure 3A) while the full-length AF model shows a rather similar structure with an overall significant confidence especially within the cytosolic domain (Figure 3B).
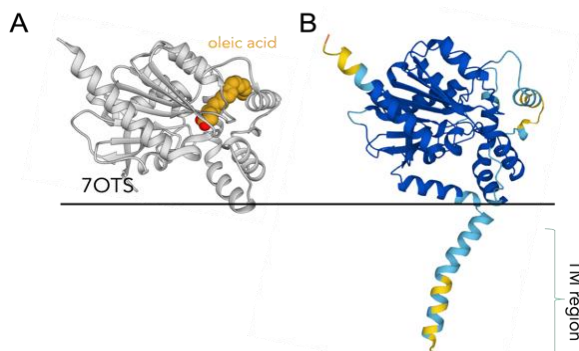
Figure 3. Structure comparison of (A) the ABHD6 protein X-ray structure and (B) the protein structure predicted by AF color-coded according to the pLDDT *(per-residue confidence metric) values. Same color code as described in Figure 1.*

Thus, the ABHD6 X-ray structure and the AlphaFold model were selected as input for the *ab initio* rigid body docking simulations and the protein/bilayer lipid membrane system building, respectively.

CPT1C and ABHD6 protein/membrane system building

The full-length AlphaFold models of both ABHD6 and CPT1C proteins were inserted in a bilayer lipid membrane. As shown in Figure 4, the generated models appear quite reliable and in agreement with both the data available in the UniProt (https://www.uniprot.org/) and OPM databases (https://opm.phar.umich.edu/).
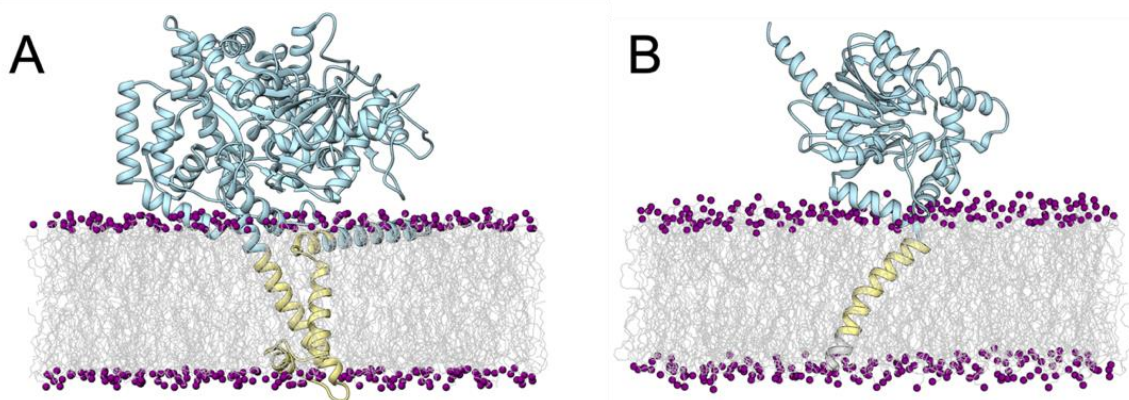

Figure 4: Protein/bilayer lipid membrane system building of (A) CPT1C and (B) ABHD6 protein.

Protein-protein interaction sites identification

To gain further insights into CPT1C and ABHD6 protein hot spots involved in protein-protein binding process, all the potential protein-protein interface sites were explored using ODA pyDock module and MaSIF.

On CPT1C protein, ODA signal mainly clustered on two rather large regions located on two opposite faces of the cytosolic domain (Figure 5A) while MaSIF identifies many patches spread across the entire surface (Figure 5B).
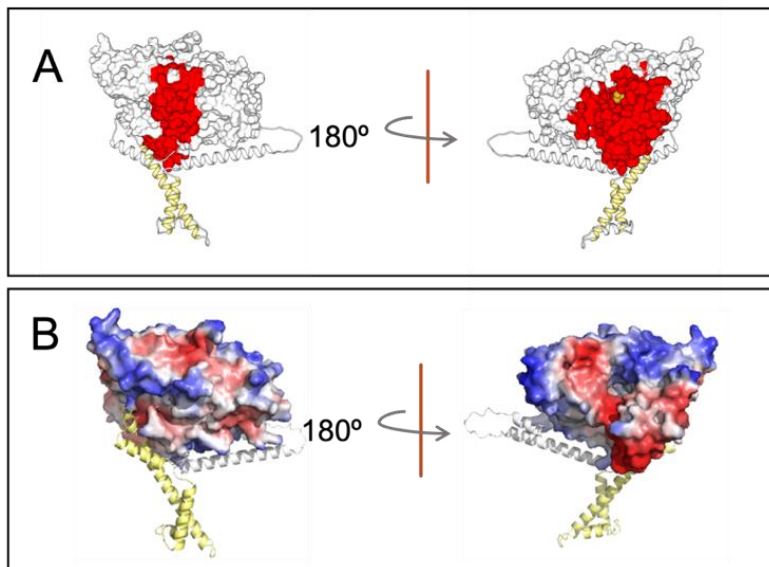

Figure 5. Protein-protein interaction sites on CPT1C cytosolic domain: (A) ODA and (B) MaSIF predictions (shown in red).

On ABHD6 protein, ODA showed no significant protein-protein interaction sites (Figure 6A) while MaSIF identifies two regions, one of them overlapping the oleic acid binding site entrance (Figure 6B), which would agree with the inhibiting activity of CPT1C against ABHD6 protein, as experimentally observed by the UIC team.
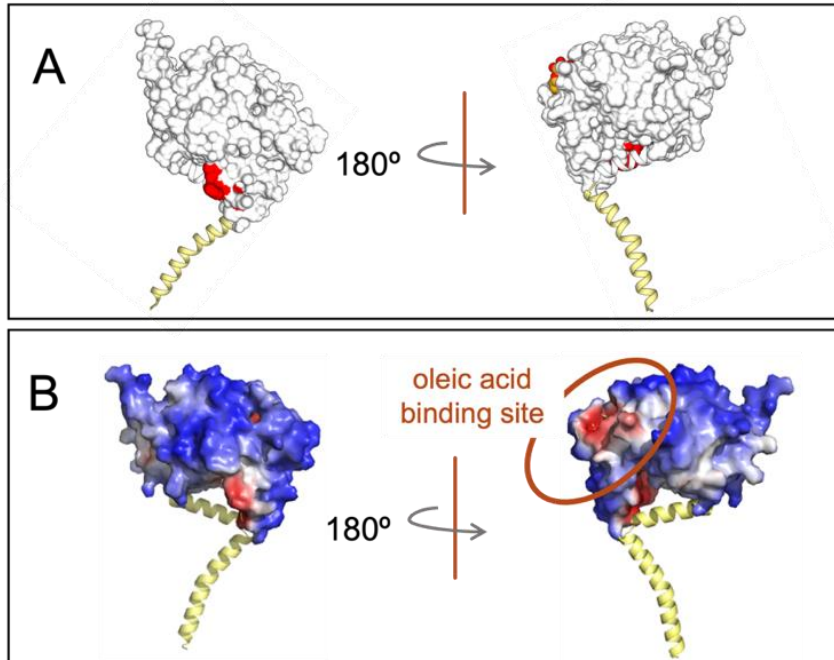
Figure 6. Protein-protein interaction sites on ABHD6 cytosolic domain: (A) ODA and (B) MaSIF predictions (shown in red).

All in all, no strong agreement was found between the two predicting methods used, thus the herein predicted protein-protein interaction sites were not used as filtering for docking poses selection within the consequent protein-protein docking simulation.

CPT1C/ABHD6 protein complex modelling

A total of five CPT1C/ABHD6 complex models were firstly generated using AlphaFold Multimer, setting as input exclusively the sequence of the corresponding cytosolic domain. After that, the membrane-embedded CPT1C/ABHD6 protein complex was built by superimposing each protein to the corresponding protein structure inserted into the bilayer lipid membrane. As a result, no AlphaFold complex structures were found to be compatible with the corresponding membrane-embedded protein complex and thus they were all discarded.
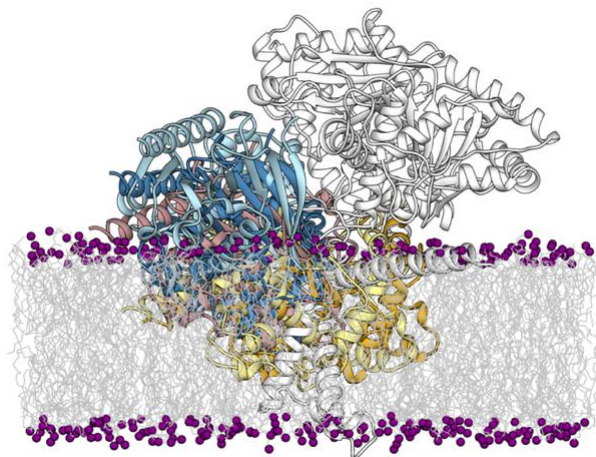
Figure 7. CPT1C/ABHD6 complex models generated by AlphaFold2 Multimer: CPT1C protein is shown in white, ABHD6 alternative poses are shown in colors.

In addition, we also explored the interaction between CPT1C and ABHD6 proteins by performing two energy-based rigid-body docking experiments, herein referred as Docking-1 and Docking-2 (as described in the Methods session), consisting in the generation of the docking poses, their energy evaluation, and the final filtering (Figure 8).
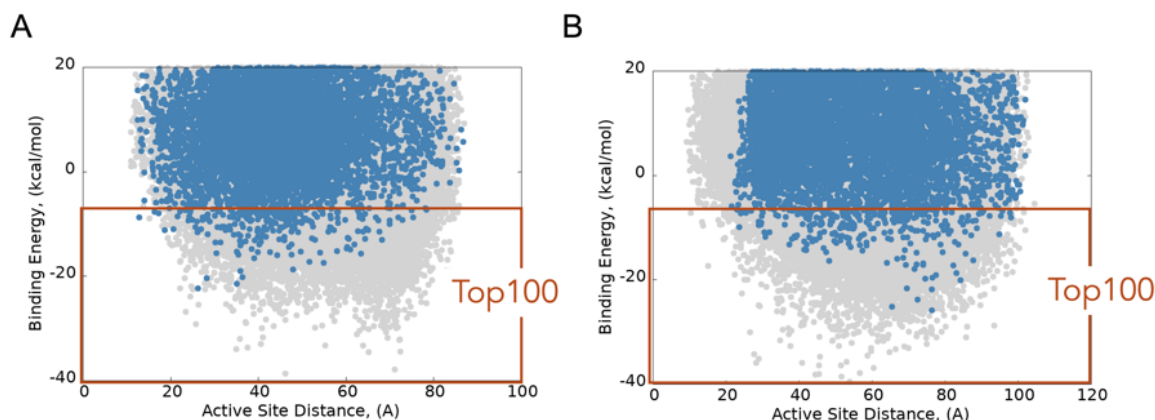

Figure 8. Unrestrained rigid-body docking results for the (A) Docking-1 and (B) Docking-2 simulation. All the generated docking poses are shown in gray, the filtered docking poses are shown in blue. The active site distance is computed as the minimum distance between CPT1C Ser243 and ABHD6 Arg256.

All in all, these results showed that the rigid-body simulations enabled the identification of alternative ABHD6 docking orientations compatible with the membrane-embedded CPT1C/ABHD6 protein complex. Nevertheless, they did not show any specific low energy docking pose, demonstrating the need of more accurate computational techniques, such as a full-atom flexible protein complex model refinement, to recognize the most energetically favored binding mode.

For this reason, the top100 ranked poses were extracted from each docking simulation and subject to a full-atoms flexible protein complex model refinement.

Full-atoms flexible protein complex model refinement

To refine the docking models previously selected and distinguish the possible preferred CPT1C/ABHD6 binding modes, a highly exhaustive conformational search was performed using PELE software involving small translations and rotations of ABHD6 protein with respect to the CPT1C protein, allowed to freely reorient but not to move away.

Thus, the best 20 ranked poses were extracted from each system (namely Docking-1 and Docking-2). As shown in Figure9, in Docking-1 simulation ABHD6 protein binding modes appeared equally distributed within the CPT1C protein cytosolic domain while in Docking-2 simulation, they clustered in a specific region within the CPT1C protein cytosolic domain surface.
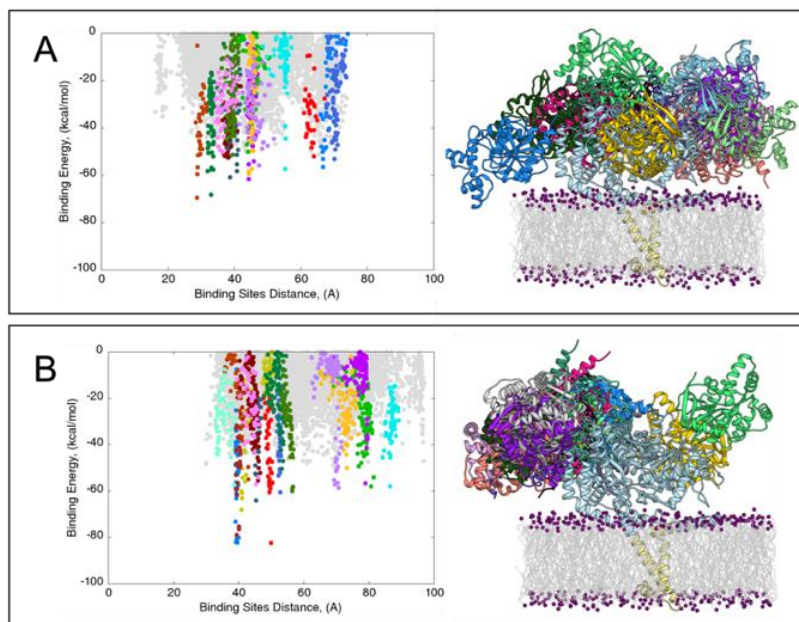
Figure 9. Full-atoms flexible protein complex model refinement using PELE of (A) Docking-1 and (B) Docking-2 system. On the left, binding energy profile of the PELE refinement. The energy profile of the top 20 ranked models is highlighted in color and the rest of the models in gray. On the right, the selected top20 *CPT1C/ABHD6 complex models. ABHD6 protein binding potential modes are shown in different colors, CPT1C cytosolic domain is shown in light blue.*

Protein complex model stability assessment

To assess the overall stability of the 40 protein complexes previously selected (20 from each system), unrestrained MD simulations in explicit solvent were performed during a maximum of 1μs.

As shown in Figure10, among all the models examined, we identified two from each system that showed rather low RMSD values along all the simulation and that were thus selected as the potential CPT1C/ABHD6 binding modes. For the sake of clarity, the two potential CPT1C/ABHD6 binding modes obtained from Docking-1 simulation were called C1.1 and C1.2 models, while the ones from Docking-2 simulation were called C2.1 and C2.2 models.
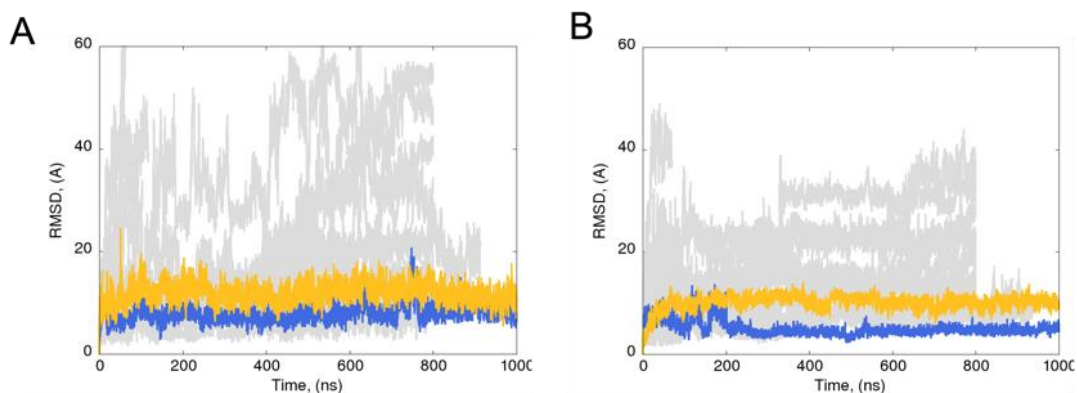
Figure 10. CPT1C/ABHD6 binding mode validation through MD simulation. RMSD of the protein backbone along the MD simulation for the (A) Docking-1 and (B) Docking-2 models. For each system, the RMSD profiles of the most stable systems are highlighted in yellow and blue, and the rest of the models are shown in gray.

Interestingly, all the four models selected shared the same binding region within the ABHD6 protein surface that perfectly overlaps with the oleic acid binding site entrance (Figure 11), which did agree with both the MaSIF prediction and the inhibiting activity of CPT1C against ABHD6 protein as experimentally observed by the UIC team.

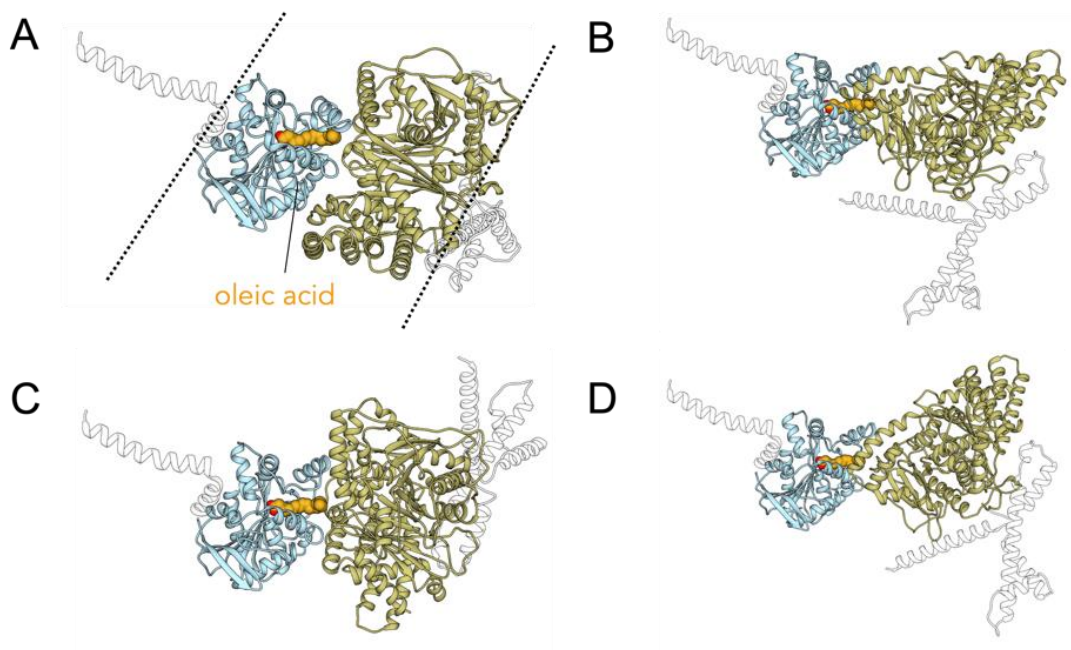*Figure 11. The most promising CPT1C/ABHD6 protein complex models: (A) C1.1 model, (B) C1.2 model, (C) C2.1 model and (D) C2.2 model. CPT1C and ABHD6 cytosolic domains are shown in khaki and light blue respectively.*

Critical binding residues identification

With the aim of predicting the most relevant hotspots residues for CPT1C/ABHD6 recognition, each CPT1C/ABHD6 protein complex model previously selected was used as input for both per-residue energy decomposition and *in silico* alanine scanning.

C1.1 model analysis

As shown in Table 1, a total of eight interface residues were identified as hotspots by at least one of the two computational approaches and five by both.

Protein	#Residue	Per residue Binding Energy ΔG (Kcal/mol)	AlaScanning ΔΔG (Kcal/mol)	Priority
CPT1C	ARG 364	-2,6	-5,3	**
	PRO 371	-3,5	-2,3	**
	PRO 374	-2,9	-2,8	**
	GLN 511	-	-2,4	*
	ASP 518	**-3,2**	**-11,7**	***

	LYS 245	**-2,3**	**-6,7**	*******
ABHD6	GLU 253	-	-2,9	*
	LEU 248	-2,3	-	*

Table 1. All the hotspot residues as resulted from C1.1 model analysis. In the "Priority" column, "***" corresponds to "high priority", "**" corresponds to "medium priority" and "*" corresponds to "low priority".

Among all the hotspots identified, we found two particularly promising residues, namely Asp518 and Lys 245, forming a salt bridge between their side chains (Figure 12).
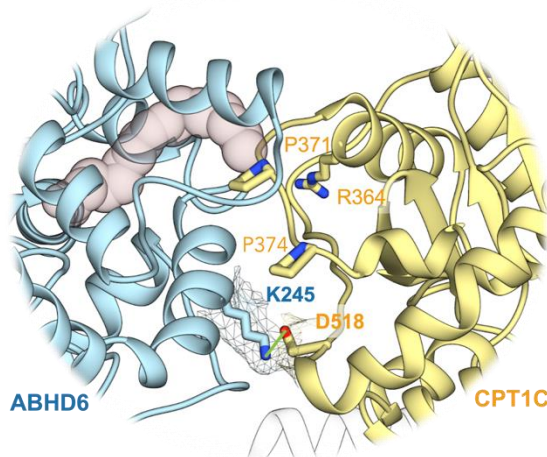

Figure 12. Zoom-up of the C1.1 model interface region. CPT1C and ABHD6 cytosolic domains are shown in khaki and light blue, respectively. Hotspots residues are shown in sticks.

C1.2 model analysis

As shown in Table 2, a total of 13 interface residues were identified as hotspots by at least one of the two computational approaches and eight by both.

Protein	#Residue	Per residue Binding Energy ΔG (Kcal/mol)	AlaScanning ΔΔG (Kcal/mol)	Priority
CPT1C	SER 370	-	-4,4	*
	PRO 371	-5,6	-	*
	CYS 373	-	-3,3	*
	PRO 374	**-2,6**	**-2,9**	*******
	ARG 514	-6,9	-8,4	**
	ASP 521	**-2,8**	**-7,4**	*******
	SER 528	**-2,5**	**-7,5**	*******

	ARG 532	-4,7	-8,4	**
ABHD6	ALA 195	-3,0	-	*
	GLU 198	**-7,0**	**-14,9**	***
	ARG 244	**-3,0**	**-3,9**	***
	LEU 248	**-3,2**	**-4,0**	***
	ARG 256	-	-12,4	*

*Table 2. All the hotspot residues as resulted from C1.2 model analysis. In the "Priority" column, "***" corresponds to "high priority", "**" corresponds to "medium priority" and "*" corresponds to "low priority".*

Among all the hotspots identified, six residues appeared particularly promising: namely Pro374 and Leu248, forming extensive hydrophobic interactions between their side chains, Asp521 and Arg244 interacting each other through a salt bridge, and finally Glu198 and Ser528 forming a hydrogen bond (Figure 13).
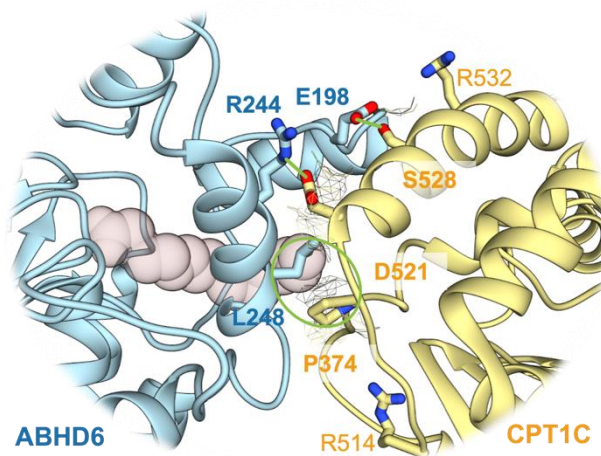

Figure 13. Zoom-up of the C1.2 model interface region. CPT1C and ABHD6 cytosolic domains are shown in khaki and light blue, respectively. Hotspots residues are shown in sticks.

C2.1 model analysis

As shown in Table 3, a total of 14 interface residues were identified as hotspots by at least one of the two computational approaches and three by both.

Protein	#Residue	Per residue Binding Energy ΔG (Kcal/mol)	AlaScanning ΔΔG (Kcal/mol)	Priority
CPT1C	TRP 201	-3,2	-	*

	PRO 386	-	-4,1	*
	THR 672	-2,5	-	*
	GLN 678	-	-2,3	*
	ASP 714	-	-7,8	*
	HIS 715	**-2,4**	**-3,0**	*******
	LYS 741	-	-2,4	*
ABHD6	GLN 177	-	-3,5	*
	GLY 193	-2,0	-	*
	VAL 197	-	-3,5	*
	GLU 198	-	-5,7	*
	GLU 249	-	-8,7	*
	SER 252	**-2,7**	**-4,4**	*******
	ARG 256	-2,1	-6,4	**

Table 3. All the hotspot residues as resulted from C2.1 model analysis. In the "Priority" column, "***" corresponds to "high priority", "**" corresponds to "medium priority" and "*" corresponds to "low priority".

Among all the hotspots identified, we found two particularly promising residues, namely Ser252 and His715, forming a hydrogen bond between their side chains (Figure 14).
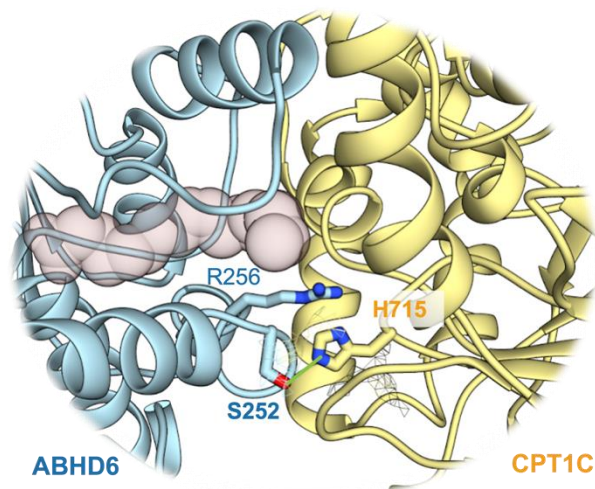

Figure 14. Zoom-up of the C2.1 model interface region. CPT1C and ABHD6 cytosolic domains are shown in khaki and light blue, respectively. Hotspots residues are shown in sticks.

C2.2 model analysis

As shown in Table 4, a total of 20 interface residues were identified as hotspots by at least one of the two computational approaches and nine by both.

Protein	#Residue	Per residue Binding Energy ΔG (Kcal/mol)	AlaScanning ΔΔG (Kcal/mol)	Priority
CPT1C	TRP 201	-3,7	-	*
	ARG 532	-5,1	-	*
	ILE 536	-2,3	-2,4	**
	TYR 658	-2,1	-	*
	GLN 667	-	-7,1	*
	PRO 669	-2,7	-	*
	THR 672	**-4,7**	**-6,3**	*******
	GLN 673	**-2,4**	**-3,7**	*******
	ASP 713	-	-6,9	*
	ASP 714	-	-9,4	*
	THR 740	-	-2,3	*
ABHD6	**ASP 122**	**-2,1**	**-2,3**	*******
	LYS 126	-	-7,3	*
	TYR 160	-3,5	-5,6	**
	GLU 190	-2,3	-5,4	**
	SER 252	-2,2	-	*
	LYS 254	-	-10,0	*
	TYR 257	-2,6	-2,4	**
	ASP 264	-8,2	-8,2	**
	LYS 265	**-7,6**	**-7,6**	*******

Table 4. All the hotspot residues as resulted from C2.2 model analysis. In the "Priority" column, "***" corresponds to "high priority", "**" corresponds to "medium priority" and "*" corresponds to "low priority".

Among all the hotspots identified, four residues appeared particularly promising (namely Thr672, Lys265, Gln673 and Asp122) interacting with each other through hydrogen bonds (Figure 15).
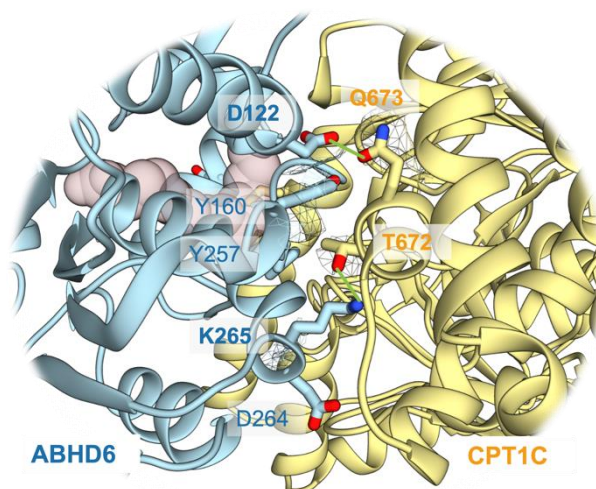

Figure 15. Zoom-up of the C2.2 model interface region. CPT1C and ABHD6 cytosolic domains are shown in khaki and light blue, respectively. Hotspots residues are shown in sticks.

As an initial recommendation, we recommend to mutate all the high-priority residues to alanine in order to test their contribution to the native complex binding and thus validate the correspondent complex models proposed.

References

1. Nawrotek, A., Talagas, A., Vuillard, L. & Miallau, L. Crystal structure of human Monoacylglycerol Lipase ABHD6 in complex with oleic acid and octyl glucoside. *(To be published)*

2. Sastry, G. M., Adzhigirey, M., Day, T., Annabhimoju, R. & Sherman, W. Protein and ligand preparation: parameters, protocols, and influence on virtual screening enrichments. *J. Comput. Aided Mol. Des.* **27**, 221–234 (2013).

3. Jacobson, M. P. *et al.* A hierarchical approach to all-atom protein loop prediction. *Proteins* **55**, 351–367 (2004).

4. Robertson, M. J., Qian, Y., Robinson, M. C., Tirado-Rives, J. & Jorgensen, W. L. Development and Testing of the OPLS-AA/M Force Field for RNA. *J. Chem. Theory Comput.* **15**, 2734–2742 (2019).

5. Jumper, J. *et al.* Highly accurate protein structure prediction with AlphaFold. *Nature* **596**, 583–589 (2021).

6. Jo, S., Kim, T., Iyer, V. G. & Im, W. CHARMM-GUI: a web-based graphical user interface for CHARMM. *J. Comput. Chem.* **29**, 1859–1865 (2008).

7. Fernandez-Recio, J., Totrov, M., Skorodumov, C. & Abagyan, R. Optimal docking area: a new method for predicting protein-protein interaction sites. *Proteins* **58**, 134–143 (2005).

8. Gainza, P. *et al.* Deciphering interaction fingerprints from protein molecular surfaces using geometric deep learning. *Nat. Methods* **17**, 184–192 (2020).

9. Fernández-Recio, J., Totrov, M. & Abagyan, R. Identification of protein-protein interaction sites from docking energy landscapes. *J. Mol. Biol.* **335**, 843–865 (2004).

10. Evans, R., el al. Protein complex prediction with AlphaFold-Multimer. *bioRxiv*. (2022).

11. Gabb, H. A., Jackson, R. M. & Sternberg, M. J. Modelling protein docking using shape complementarity, electrostatics and biochemical information. *J. Mol. Biol.* **272**, 106–120 (1997).

12. Cheng, T. M.-K., Blundell, T. L. & Fernandez-Recio, J. pyDock: electrostatics and desolvation for effective scoring of rigid-body protein-protein docking. *Proteins* **68**, 503–515 (2007).

13. Abagyan, R. *et al.* Disseminating structural genomics data to the public: from a data dump to an animated story. *Trends Biochem. Sci.* **31**, 76–78 (2006).

14. Borrelli, K. W., Vitalis, A., Alcantara, R. & Guallar, V. PELE: Protein Energy Landscape Exploration. A Novel Monte Carlo Based Technique. *J. Chem. Theory Comput.* **1**, 1304–1311 (2005).

15. Maier, J. A. *et al.* ff14SB: Improving the Accuracy of Protein Side Chain and Backbone Parameters from ff99SB. *J. Chem. Theory Comput.* **11**, 3696–3713 (2015).

16. Roe, D. R. & Cheatham, T. E., 3rd. PTRAJ and CPPTRAJ: Software for Processing and Analysis of Molecular Dynamics Trajectory Data. *J. Chem. Theory Comput.* **9**, 3084–3095 (2013).

17. Genheden, S. & Ryde, U. The MM/PBSA and MM/GBSA methods to estimate ligand-binding affinities. *Expert Opin. Drug Discov.* **10**, 449–461 (2015).

182

APPENDIX II

Supplementary figure

Expression of ABHD6 in different cellular fractions was analyzed by western blot after subcellular fractionation of mouse brain homogenates. As shown in attached figure, ABHD6 is expressed in the same fractions as the ER marker calreticulin.

Appendix II figure. Expression of ABHD6 in different cellular fractions after subcellular fractionation of mouse brain homogenates. TH: total homogenate; Cyt: cytoplasm; CM: crude mitochondria (contains ER and endosomes as well); ER: Endoplasmic reticulum; MAM: mitochondria-associated membranes, FM: free mitochondria; MER: mitochondria-associated ER membrane.